THE UNIVERSITY OF READING

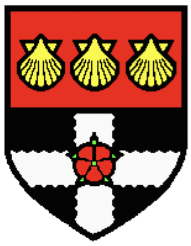

The membrane binding peptides of Middle East Respiratory Syndrome-related coronavirus and Mouse Hepatitis Virus

A thesis submitted for the degree of Doctor of Philosophy in Microbiology / Virology

By

ENTEDAR ALSAADI

Supervisor: Prof. Ian M. Jones

March 2019

Declaration

I confirm that this is my own work and that it has not been previously submitted for any dissertation or PhD degree at any other university or institution. The use of all materials from other sources has been properly and fully acknowledged. All drawings not cited are original artwork by the author.

ENTEDAR ALSAADI

Abstract

Coronaviruses infect many species causing a variety of diseases with a range of severities. Their members include zoonotic viruses with pandemic potential where therapeutic options are currently limited. Despite this diversity coronaviruses share some common features including the production, in infected cells, of elaborate membrane structures. Membranes represent both an obstacle and aid to coronavirus replication and in consequence virus encoded structural and nonstructural proteins have membrane binding properties. The structural proteins S, E and M encounter cellular membranes at both entry and exit of the virus while the nonstructural proteins nsp3, nsp4 and nsp6 reorganize cellular membranes to benefit virus replication. MERS CoV is responsible for sporadic infections in countries focused on the Middle East with occasional transfer elsewhere. A key step in the MERS CoV replication cycle is the fusion of the virus and host cell membranes mediated by the virus spike protein, S. The location of the fusion peptide within MERS S protein has not been precisely mapped. The coronavirus envelope protein by contrast has defined functions in virus assembly, production and release. It may also induce membrane curvature in the endoplasmic reticulum Golgi intermediate compartment (ERGIC) leading to scission of budding virions. M is located among the S proteins in the virus envelope along with the small amounts of E and is the primary driver of the virus budding process. Nsp3, nsp4 and nsp6 may also have roles in the creation of double-membrane vesicles (DMVs) that are considered the site for viral RNA synthesis although their more precise role is not understood. Thus, S, E, M, nsp3, nsp4 and nsp6 potentially all contain membrane-modifying peptides. To search for such peptides, parameters such as amino acid conservation, and proximity to the membrane and/or Amphipaseek amphipathic helix prediction were used on the

requisite open reading frames of both *Mouse Hepatitis Virus* (MHV) and *Middle Eastern Respiratory Syndrome Virus*. Peptides identified *in silico* were synthesised and tested for membrane-modifying activity in the presence of giant unilamellar vesicles (GUVs) consisting of 1, 2-dipalmitoyl-sn-glycero-3-phosphocholine (DPPC), sphingomyelin and cholesterol. A putative fusion peptide located near the N-terminus of the S2 domain was shown to change the shape and size of the GUVs membrane leading to extensive deformation. Key residues required for activity were mapped by amino acid replacement and their relevance *in vitro* tested by their introduction into recombinant MERS S protein expressed in mammalian cells. Mutations preventing membrane binding *in vitro* also abolished S mediated syncytium formation consistent with the identified peptide acting as the fusion peptide for the S protein of MERS-CoV. Peptides from E, nsp3, nsp4 and nsp6 were also found to change the size and shape of vesicle membranes in a manner consistent with membrane insertion. Select peptides from nsp4 and nsp6 caused pore formation in GUVs. To assess the roles of the identified E *in vivo*, MHV E protein was expressed in insect cells using the baculovirus expression system and the relevant peptide sequence mutated. Mutant expression levels were modified compared to wild type with evidence for a redistribution within the expressing cell confirming a role for the MHV-E post transmembrane region in membrane binding *in vitro* and *in vivo*. The overall findings identify several conserved sequences as *bona fide* membrane binding motifs in the structural and non structural proteins of MERS-CoV and MHV. While some were validated by assay in physiologically relevant systems, the precise mechanism of action of others remains to be investigated.

Dedication

This thesis is dedicated to my country, Iraq, as well, my parents, Mr. Alioy Jafer Alsaadi and Mrs. Kefah Alsaadi, my beloved husband Atheer Alshweli and my children, Zahraa and Ali for their endless love and support. This work is also dedicated to all my big family and friends without whom all my success would be impossible.

Acknowledgments

Firstly, I would like to express my sincere gratitude to my supervisor Prof. Ian Jones for his continuous support during my PhD study, for his immense knowledge, his motivation and patience. I could not have imagined having a better supervisor and mentor for my PhD study.

Beside my supervisor, I would like to thank Dr. Benjamin W. Neuman for his valued contribution to this study and his continuous encouragement and support.

I gratefully acknowledge the funding received toward my PhD study from the Higher Committee for Education Development “HCED” in Iraq, which gave me the opportunity to perform this study.

My sincere thanks also go to Dr. Silvia, Dr. Geraldine, Dr. Sinead and Dr. Sophie for their help and support. My deep thanks also to all staff and PhD students at the Knight building and my lab colleagues for their continued help and kindness.

Last but not least, I would like to thank my husband Atheer, my children Zahraa and Ali for their patience and understanding over the past four years, and my whole big family for supporting me spiritually throughout this study, writing this thesis and my life in general.

Publication and conference presentations

1- Membrane binding proteins of coronaviruses. *Future Virol*: Volume 14, Issue 4, pages 275-286. April 2019. Entedar A J Alsaadi & Ian M Jones.

2- "Investigating membrane viral bending proteins in coronavirus replication". Alsaadi, E.A, Neuman, B.W.

Society of Microbiology, 3-6 April 2017. Edinburgh, UK. Presented poster

3- "Investigating membrane viral bending proteins in coronavirus replication". Alsaadi, E.A, Neuman, B.W.

The annual symposium at School of Biological Sciences University of Reading, 16 June 2017. Presentation.

4- "Investigating membrane viral bending proteins in coronavirus replication". Alsaadi, E.A, Neuman, B.W.

The Doctoral Research Conference at School of Biological Sciences University of Reading, UK, 20 June 2017. Presented poster.

5- "Investigating membrane viral bending proteins in coronavirus replication". Alsaadi, E.A, Neuman, B.W.

The emerging viruses of zoonotic and veterinary importance's symposium at Churchill College, Cambridge, UK 24 July 2017. Presented poster.

6- "Investigating membrane viral bending proteins in coronavirus replication". Alsaadi, E.A, Neuman, B.W.

The emerging viruses' symposium at St Hilda's College, Oxford, UK 4-5 September 2017. Presented poster.

7- "Investigating membrane viral bending proteins in coronavirus replication". Alsaadi, E.A, Neuman, B.W, Jones, I.M.

Society of Microbiology 10-13 April 2018. Birmingham, UK. Presented poster

8- “Investigating membrane viral bending proteins in coronavirus replication”.

Alsaadi, E.A, Neuman, B.W, Jones, I.M.

The Doctoral Research Conference at School of Biological Sciences University of Reading, UK, 20 June 2018. Presented poster.

9- Investigating membrane viral bending proteins in coronavirus replication.

Alsaadi, E.A, Neuman, B.W, Jones, I.M.

The 37th annual meeting of the American Society for Virology (ASV) 14-18 July 2018. University of Maryland, College Park, USA. Presented poster.

Table of contents

List of Figures

List of Tables

Abbreviations

°C Degree Celsius

Ab Antibody

bp Base pair

COPII Coat protein complex II

Cryo-EM Cryo-electron microscopy

ddiH_2O Distilled water

DNA Deoxyribonucleic acid

E. coli Escherichia coli

ECL Enhanced chemiluminescence

EDTA Ethylene Diamine Tetra Acetic acid

FBS Fetal bovine serum

FCS Foetal calf serum

Fw Forward primer

HAE Human airway epithelial cell

HSP High speed pellets

HSV Herpes simplex virus

IBV Infectious Bronchitis Virus

IDT Integrated DNA Technology

kb Kilo base pairs

kDa Kilo Daltons

MOI Multiplicity of infection

Oligo Oligonucleotides

PBS Phosphate Buffer Saline

PC Phosphatidylcholine

PE Phosphatidylethanolamine

pH Potential Hydrogen

PI Phosphatidylinositol

PS Phosphatidylserine

PVDF Polyvinylidene fluoride

RNA Ribonucleic acid

rpm Revolutions per minute

SOC Super Optimal Broth

Tm Transition temperature

1. Introduction

Coronaviruses (CoVs) are enveloped +ve sense RNA viruses causing a variety of diseases in man and animals and are considered to be the largest of the RNA viruses, with genomes ranging from 27-32 kb (Coleman and Frieman, 2014; Brandão et al 2016). Viruses of zoonotic potential are found within the coronaviruses as exemplified by Severe Acute Respiratory Syndrome- related coronavirus (SARS-CoV) which emerged in Southern China in 2003 (Drosten, 2003) and Middle East Respiratory Syndrome (MERS) CoV, which appeared more recently in Saudi Arabia in 2012 (Zaki et al 2012). In both cases infection of man is thought to have arisen by contact with an intermediate host which in turn acquired the virus from the original reservoir, presumed to be bats (Bolles, Donaldson and Baric, 2011; Hu et al 2015). The basis of cross species infection lies primarily in the ability of the virus major surface spike protein, S, to bind to cell surface receptors and initiate infection. Coronaviruses use a variety of receptors ranging from sugars to extended cell surface proteins (reviewed in (Li, 2015) and the receptor for MERS infection has been identified as Dipeptidyl peptidase-4 (DPP4) found on a variety of cell types including epithelial cells of the respiratory tract (Boheemen et al 2012; Raj et al 2013). More recently, sialic acid has been shown to be an additional low affinity receptor whose binding might precede that of DPP4 suggesting that its distribution may also contribute to virus tropism (Li et al 2017). There is no effective treatment or licensed vaccine for either virus emphasizing the need to further understand CoV biology as a route to improved future intervention (van Doremalen and Munster 2015; Baseler et al 2016).

1.1Taxonomy of coronaviruses

Coronaviruses belong to the *Coronaviridae* family and contain two subfamilies *Orthocoronavirinae* and *Letovirinae*. Along with six other families, *Abnidovirineae, Arnidovirineae, Cornidovirineae, Mesnidovirineae, Monidovirineae, Ronidovirineae,* and *Tornidovirineae*, they form the *Nidovirales* order (Gorbalenya et al 2006; Masters, 2006) so named for the overlapping set of transcripts used by all members to encode viral proteins. The Coronaviridae are further subdivided phylogenetically into four genera, α, β, γ and δ (Adams and Carstens 2012). The *Alphacoronavirus* genus is represented by alpha coronavirus 1, human coronaviruses HCoV-229E, human coronaviruses NL63, Miniopterus bat coronavirus1, Miniopterus bat coronavirus HKU8, porcine epidemic diarrhea virus, Rhinolophus bat coronavirus HKU2 and Scotophilius bat coronavirus 512, while the *Betacoronavirus* genus includes Betacoronavirus 1, Human coronavirus HKU1, murine coronavirus, pipistrellus bat coronavirus HKU5, Rousettus bat coronavirus HKU9, Severe Acute Respiratory syndrome-related coronavirus and Tylonyctrus bat coronavirus HKU4. The *Deltacoronavirus* genus is composed of Bulbul coronavirus HKU11, Munia coronavirus HKU13, and Thrush coronavirus HKU12. The last genus *Gamma coronavirus* is represented by Avian coronavirus and Beluga whale coronavirus SW1 (Adams and Carstens 2012).

1.2 Coronavirus genome

Coronaviruses are enveloped positive strand non-segmented RNA viruses. They have the largest RNA genome of the RNA viruses ranging from 25.4 kb (Porcine deltacoronavirus HKU15) to 31.8 kb (Bottlenose dolphin coronavirus HKU22) (Neuman and Buchmeier, 2016). The genome has a 5′cap and a polyadenylate tail at

the 3` end. This structure makes this genome similar to the cellular mRNA and is consistent with it acting as an mRNA following cell entry in common with all Baltimore Class IV viruses. Despite their complexity and range of function however (Reguera et al 2014; Li, 2015) the structural proteins of coronaviruses occupy only about one third of the coding capacity of the genome, some two thirds located at the 5′ end encode two long open reading frames (ORFs), ORFs 1a and 1b, which together encode the non-structural proteins of the virus **Figure 1.1**.

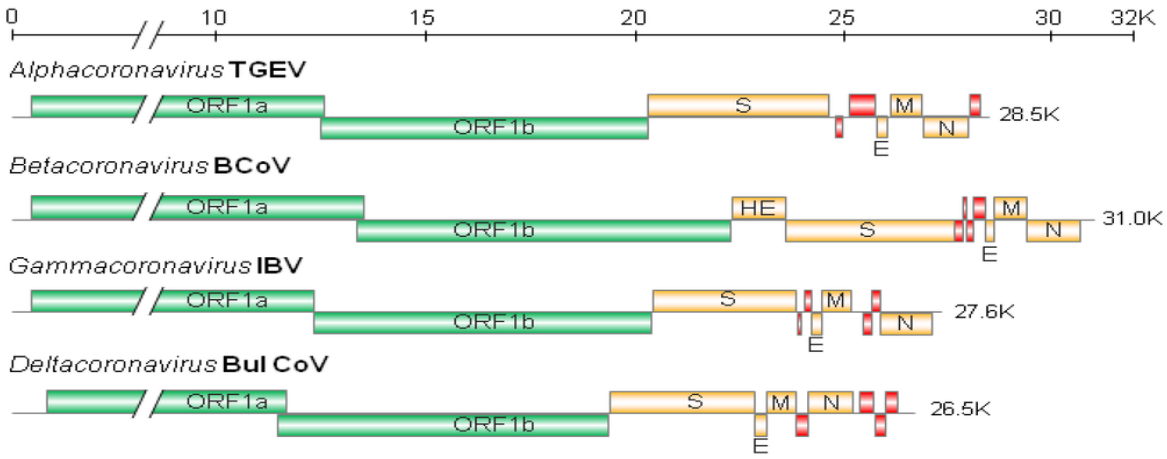

Figure 1.1 :Organisation of coronavirus genome in various coronaviruses.

TGEV: -, Transmissible gastroenteritis virus; BCoV: Bovine coronavirus; IBV: -infectious bronchitis virus; Bul CoV: -Bulbul coronavirus. Open reading frame (ORF 1a/b) is represents by green, S, M, E, N and HE genes colored in orange. Accessory proteins encode by ORFs are colored red. Figure adapted from (Ujike and Taguchi, 2015).

1.3 Overview of the Coronavirus replication cycle

Coronavirus infection starts by the binding of the virus spike proteins onto particular receptors such as DPP4 as in MERS-CoV or mCEACAM1 on the surface of target cells susceptible to infection by MHV-A59 (Williams, Jiang and Holmes, 1991; Boheemen et al 2012; Raj et al 2013). Recently, sialic acid has been shown to be an additional low affinity attachment receptor whose binding might precede that of DPP4 suggesting that its distribution may also contribute to virus tropism (Li et al 2017).

This binding leads to conformational changes in the S protein which allows the fusion of viral and cellular membranes (Zelus et al 2003) leading to release of the viral genome into the cystol and initiation of the translation of the replicase gene translation from viral genomic RNA. ORF1a and ORF1b are translated into replicase polyprotein 1a (pp1a) and replicase polyprotein 1ab (pp1ab). The polyprotein 1ab is translated by a -1 ribosomal frameshift mechanism (Bredenbeek et al 1990). These poly proteins are cleaved by viral proteinases such as the papin-like proteases (PLpro1 and PLpro2) and chymotrypsin-like cysteine proteinase (3CLpro) or main protease (Mpro) which are situated in nsp3 and nsp5 respectively leading to the generation of 16 nonstructural proteins (Ziebuhr et al 2000; Lee et al 1991; Ziebuhr et al 2001). Subsequently, numerous nonstructural proteins are assembled into a replicase-transcriptase complex (RTC) to produce an appropriate environment for RNA synthesis and these structures are essentially responsible for RNA replication and the transcription of sub-genomic RNAs which provide the mRNAs for virus structural protein translation (Fehr and Perlman, 2015).

The genomic positive sense RNA is copied into a negative sense template by the virion encoded RNA-dependent RNA-polymerase (RdRp) and negative sense RNAs

act as a template for the synthesis of the positive sense subgenomic RNAs (sgRNAs). These positive sense sgRNAs are formed by discontinuous transcription during subgenomic length minus-strand RNA synthesis to produce overlapping transcripts all of which have a common 3` terminus. This “nested set” of mRNAs is the characteristic of the *Nidovirales* which gives the order its name (Sawicki, Sawicki and Siddell, 2007). Translation of the nested mRNAs leads to the expression of the structural and accessory proteins of coronaviruses needed for the assembly of new virus particles (Sawicki and Sawicki 1995; Zúñiga et al 2004). After replication, the synthesis of subgenomic RNA and the translation of the structural proteins, the process of virus assembly begins. The structural proteins are incorporated into the endoplasmic reticulum then transported to the ERGIC (Klumperman et al 1994; Hurst et al 2005) via the secretory pathway, where encapsidation of the viral genome with the virus N protein is accomplished and where budding of the mature virions occurs into vesicles which migrate to the plasma membrane where true virus release takes place **Figure 1.2**.

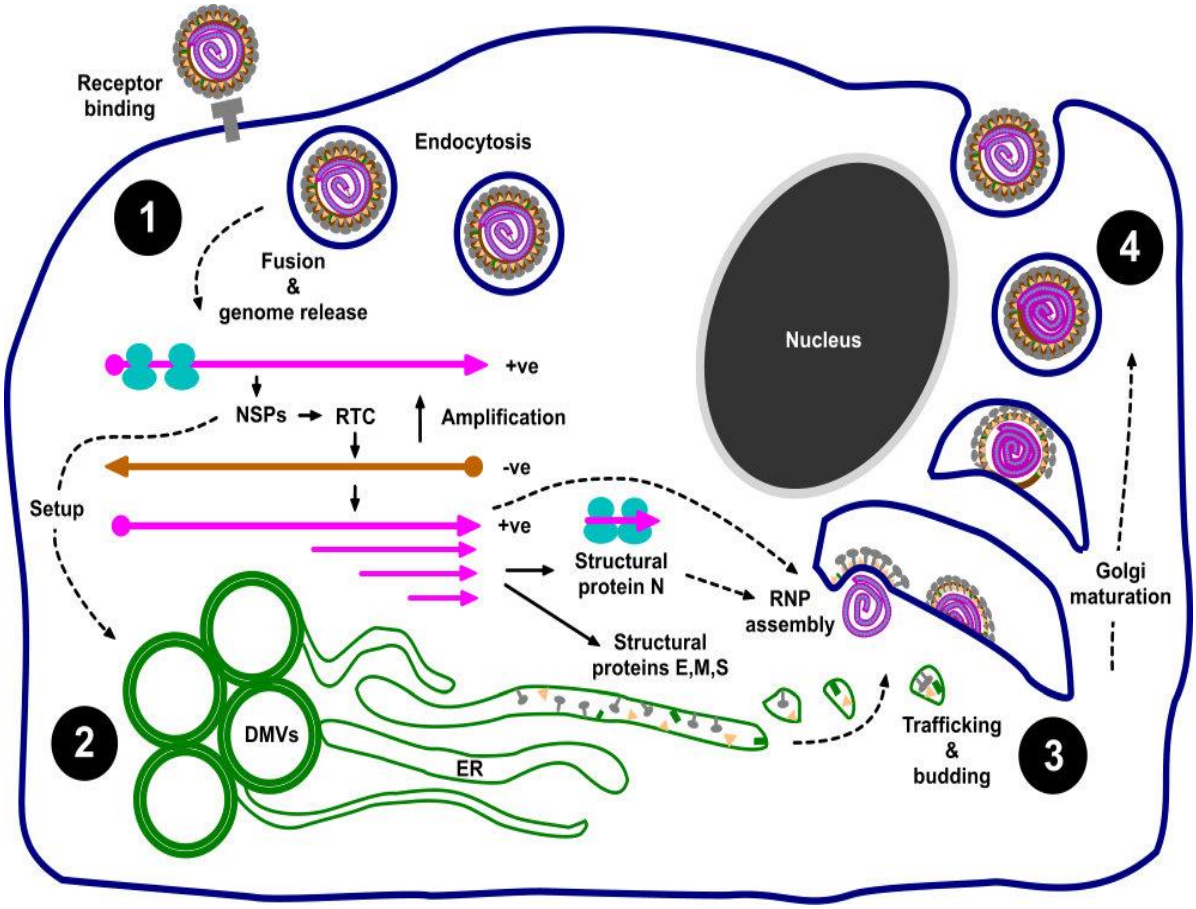

Figure 1.2: Coronavirus replication.1. Most coronaviruses enter by receptor mediated endocytosis. The +ve sense genomic RNA is released into the cytoplasm and translated into the initial virus polyproteins, which encode the non-structural proteins (NSPs). 2. NSPs stimulate the production of DMVs and establish the replication transcription complexes (RTC), which produce the-ve strand replicative intermediate from which more +ve strand genomes and mRNAs are produced. Translation of the N mRNA produces the N protein in the cytoplasm which combines with the new genomes to form RNPs while translation of the remaining structural proteins, M, E and S occurs in the ER where they accumulate in the ERGIC and cis-Golgi. 3. Virus assembly begins and completes as the protein cargoes migrate through the Golgi stacks resulting in new virus particles in vesicles (4), which eventually fuse with the plasma membrane.

1.4 Coronavirus proteins and membrane interaction

1.4.1 Structural proteins

1.4.1.1 Spike protein

The coronavirus spike protein (S) is a large fusion protein that is responsible for virus binding to target cells through different receptors on the host cells. Thus, it mediates cell entry, tissue tropism and viral infectivity as well as host range (Bosch et al 2003). Spike proteins exist as protrusions on the surface of the virus and due to assembling into trimers, give the viruses a distinctive shape under the electron microscope, the crown-like structure, which the virus name is derived from **Figure 1.3**. S protein is a large protein of approximately 1160 to 1400 amino acids in size. It has many potential N-linked glycosylation sites, up to 23 sites in some cases (Zheng et al 2018). S consists of two subunits, S1 and S2. S1 is considered to be the receptor binding subunit and is located at the N-terminus of the complete protein. S2 is the fusion subunit and it is located in the C-terminal half of the molecule (Belouzard et al 2012). S1 contains a receptor binding domain (RBD) and this region varies in sequence among coronaviruses, even among viruses in the same genus. The RBD is usually composed of a N-terminal domain (NTD) and C-terminal domain **Figure 1.4**. The N-terminal domain of the RBD has been reported to have some similarity with host cell proteins such as galectin-like domain proteins and as a result it has been suggested that the virus gained this domain from the host (Peng et al 2011; Belouzard et al 2012). S2 comprises a fusion peptide, two conserved heptad regions (HR), heptad 1 and heptad 2, located N-terminal and C-terminal, respectively, and a transmembrane domain (Supekar et al 2004) **Figure 1.4**. The HR consists of a distinctive pattern of seven amino acid pattern **a**bc**d**efg in which **a** and **d**

are hydrophobic amino acids on one side of an α helical configuration. HR1 and HR2 are brought together during the structural changes involved in membrane fusion to form a coiled-coil structure (Millet and Whittaker, 2015), which brings the viral and cellular membranes into such close proximity that fusion occurs (Eckert and Kim, 2001). Heptad repeat regions are a characteristic motifs in several viral fusion proteins (Skehel and Wiley, 1998). A number of studies have shown that the two HR regions have roles in viral fusion and several studies have proposed that the putative fusion peptide may be situated close to (Chambers, Pringle and Easton, 1990), or inside of HR1 (Luo and Weiss, 1998). Similarly, mutations in membrane-proximal HR2 in some viruses has shown subsequent disorder in viral fusion and spike oligomerization consistent with a role in S conformation (Luo, Matthews and Weiss, 1999).

1.4.1.2 Host cell proteases and spike protein activation

As noted during description of their spike proteins there are different entry strategies for coronaviruses and this could be one of the reasons for their success in infecting a wide range of hosts (Bosch, Bartelink and Rottier, 2008; Belouzard et al 2012). Entry is driven by the S protein as it contains the receptor binding domain, fusion peptide and fusion domain (Li, 2016) but several stimulators have been noted that lead to activation of S protein and are so also important components of cell entry steps. Two noted factors are a drop in pH and proteolytic activation. Cleavage of S protein can occur at several sites depending on the infected cell type and virus species, and cleavage can occur at different time points in the coronavirus life cycle during virus entry or during S protein biosynthesis in the infected cell. In some coronaviruses, it has been reported that there are two different cleavage sites for S

protein, the first site being situated at the S1/S2 boundary and the second located within S2 just before the putative fusion peptide, termed S2` (Belouzard, Chu and Whittaker, 2009; Millet and Whittaker, 2015). At these sites many different proteases have been shown to be capable of activating S protein, for example trypsin, furin and cathepsin.

1.4.1.2.1 Trypsin

Trypsin is one of the cellular proteases that cleave S proteins. It is known to be non-selective in substrate recognition as a result there are several sites on S protein mapped as being cleaved by trypsin (Millet and Whittaker, 2015). Trypsin is expressed in the respiratory tract as well as in the small intestine, mainly expressed in the acinar cells of the pancreas (Swift et al 1989), consistent with infection by coronaviruses at both of these sites. It seems to cleave many intestinal coronaviruses such as Porcine epidemic diarrhea virus (PEDV) (Park, Cruz and Shin, 2011) and although trypsin readily cleaves after runs of arginine or lysine residues, the most commonly used viral cleavage site is a single arginine (R) with cleavage occurring on the carboxyl-side (Millet and Whittaker, 2015).

1.4.1.2.2 Furin and the proprotein convertases (PC) family

Furin is considered as a member of the subgroup of proprotein convertases family (PC), nine serine proteases mainly localized in the trans-Golgi network (TGN) that can cleave a high number of cellular and microbial substrates (Misumi et al 1991; Seidah and Prat, 2012). Furin is the enzyme most commonly involved in cleaving coronavirus S proteins as it has been shown that furin or furin-like proteases cleave S protein at S1/S2 site in many different coronaviruses. But some coronaviruses are different, for example MERS and IBV, and their cleavage site appears to be

immediately prior to the putative fusion peptide- a site known as S2` (Millet and Whittaker, 2015).

1.4.1.2.3 Cathepsins

Cathepsins consist of a group of proteases, including serine, cysteine, and aspartyl proteases, that are usually located in endosomes and lysosomes where they work normaly as degradatives enzymes. In general, cathepsins have a wide range of substrates (Millet and Whittaker, 2015) and biochemical studies show that the favored substrate for cathepsins is at the carboxyl side of arginine residues, R (Choe et al 2006; Rawlings and Barrett 2013). Two types of cathepsins are associated with coronaviruses activation, cathepsin L and cathepsin B. Cathepsin L activates a number of different coronavirus S glycoproteins including SARS, HCoV-229E, MERS and MHV-2. Cathepsin L has a pH ranging from 3.0-6.5 (Simmons et al 2005; Qiu et al 2006; Kawase et al 2009; Shirato, Kawase and Matsuyama, 2013). In contrast cathepsin B has some different features including a requirement for higher pH than cathepsin L and and it has been shown to prefer to process di-basic substrates. Coronaviruses known to be processed by cathepsin B include MHV-2 and feline coronavirus (Choe et al 2006; Regan et al 2008).

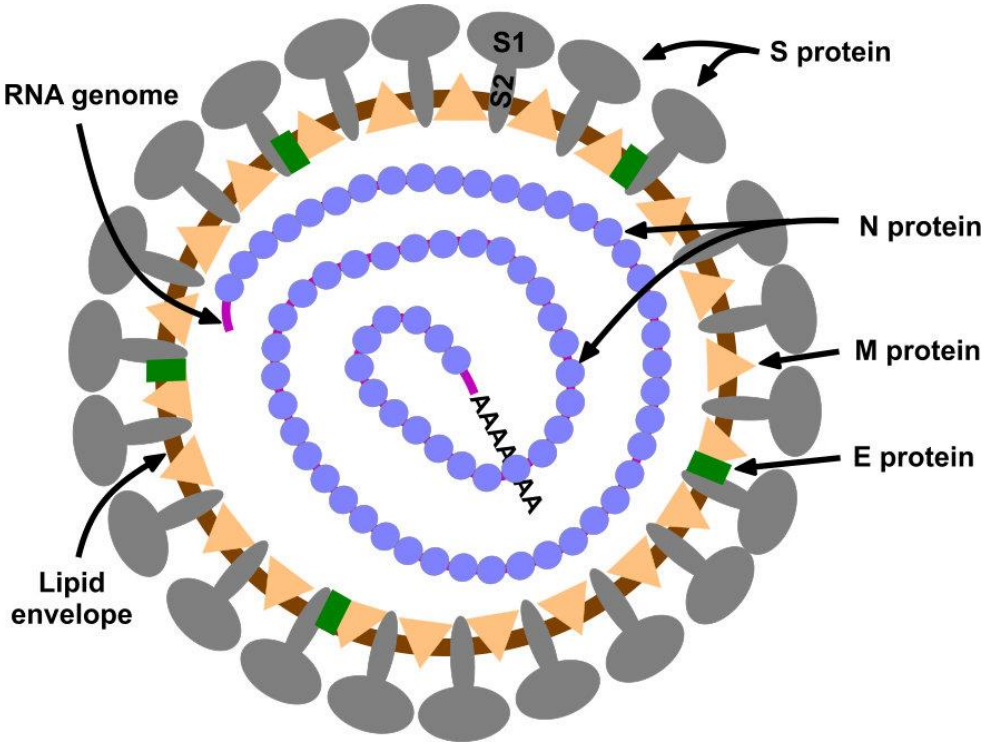

Figure 1.3: Schematic representation of a Coronavirus particle. The structural components of the virus are indicated. Small amounts of host cell and virus nonstructural proteins, presumed to be captured non-specifically during the budding process, are also found in virions but are not illustrated.

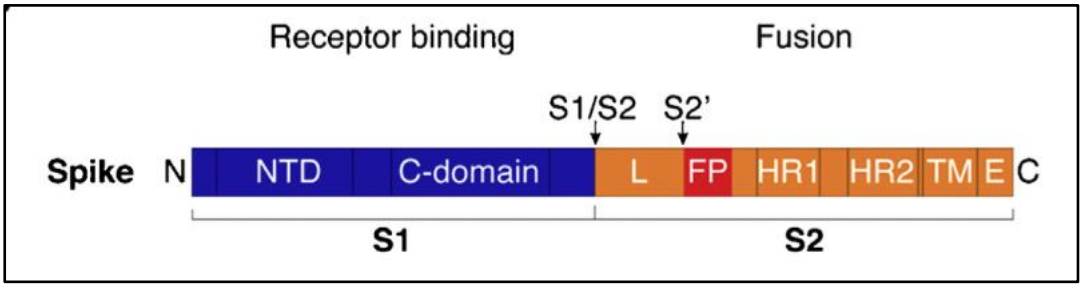

Figure 1.4: Diagram of coronavirus S protein with the two cleavage sites, S1/S2 and S2′ indicated by arrows.

The S protein consists of two subunits, the S1 receptor-binding subunit, and the S2 fusion subunit. NTD: N-terminal domain of S1, C-domain: C-terminal domain of S1, L: linker region between S1/S2 and S2′ sites, FP: putative fusion peptide, HR1: heptad repeat 1, HR2: heptad repeat 2, TM: transmembrane domain, E: endodomain. Not drawn to scale. Figure adapted from (Millet and Whittaker, 2015).

1.4.1.3 Envelope protein

The envelope protein (E) is a small hydrophobic integral viroporin ranging from 74 – 109 amino acids (Raamsman et al 2000; Arbely et al 2004). It has an N-terminal domain, a long alpha helical transmembrane domain, and a C-terminal hydrophilic domain and is found at low levels of incorporation in all coronavirus groups (Wilson et al 2006; Torres et al 2007; Narayanan et al 2000; Ruch and Machamer 2012; Hogue and Machamer 2008). The E protein is palmitoylated at all 3 of its Cys residues (Liao et al 2006) but the role of this secondary modification is debated. For MHV-CoV single Cys residue changes do not significantly impair virus growth but modification of all three residues results in severe attenuation (Lopez et al 2008; Boscarino et al 2008). For SARS-CoV however, triple mutation of the conserved Cys does not impact secretion of virus antigen from expressing cells, suggesting no dependence on palmitoylation (Tseng et al 2014). Two membrane topologies have been demonstrated for E protein: hairpin or transmembrane (Ruch and Machamer 2012; Lopez et al 2008) and it has been suggested that the level of palmitoylation may moderate their relative proportion, in turn allowing modified membrane curvature (Ruch and Machamer 2012; Lopez et al 2008).

E protein also interacts with the M protein and mutants of M that are unable to bud from cells can be complemented by forms of E (Chen et al 2009; Kuo et al 2016). The membrane curving properties of E are such that co-expression of M and E is adequate for the efficient formation of virus-like particles (VLP) (Vennema *et al*, 1996; Corse and Machamer, 2002a) and these can also incorporate the S protein if it is co-expressed (Mortola and Roy, 2004). For many coronaviruses, including MHV, E protein has also been shown to have a role as an ion channel, a viroporin (Madan et al 2005; Ye and Hogue, 2007). E function as a viroporin is thought to include the

trafficking of virions in the secretory pathways and membrane permeability, both of which are essential for virus growth (Ruch and Machamer 2012; Nieva et al 2012; Castaño-Rodriguez et al 2018). E also interacts with host cellular proteins (Castaño-Rodriguez et al 2018) including PALS1 (Proteins Associated with Lin Seven 1) which is known to maintain the epithelial cell junction, with clear implications for the virus assembly site in the Golgi (Teoh et al 2010; Cohen, Lin and Machamer, 2011). While E function is critical for virus assembly its viroporin activity in mobilizing calcium ions and its interactions with host tight junction cell proteins have been also implicated as mediators of pathology in some coronavirus infections (Teoh et al 2010; Castaño-Rodriguez et al 2018). An additional role for E in viral pathogenesis may also be exerting an anti-apoptotic effect on host cells during virus replication (Ruch and Machamer, 2012). The connection of the E encoded ion channel activity to virus morphogenesis, as opposed to its structural role in binding M, is still uncertain, but its role as a virulence factor, demonstrated by many studies on SARS-CoV E protein, have shown an impact on pathogenesis in a mouse model study, part of which could be an effect of virus production and part on its direct properties in the expressing cells (Wilson, Gage and Ewart, 2006; DeDiego et al 2014; Regla-Nava et al 2015). Whatever it's primary role, the many possible functions of E make it an attractive target for the development of antiviral therapies.

1.4.1.4 Membrane protein (M)

Coronavirus M protein is a type III transmembrane glycoprotein and is the most abundant glycoprotein in coronavirus particles. Despite variability in the primary sequence their predicted secondary structures are similar (Arndt, Larson and Hogue, 2010). The M protein is ~230 amino acids in length and is composed of three parts; a short N-terminal domain situated outside the virion membrane, three transmembrane

domains and a carboxy-terminal domain situated inside the particle (Hogue and Machamer 2008; Ujike and Taguchi 2015) **Figure 1.5**. An amphipathic region is situated at the end of the third transmembrane domain and is well conserved in almost all *Coronaviridae* members (Arndt, Larson and Hogue, 2010). Coronavirus M proteins are characterized by N-linked glycosylation in the α and δ coronaviruses and O-linked glycosylation in the β coronaviruses (de Haan, Cornelis & Rottier et al 1998; Oostra et al 2006) and study of chimeric M proteins has shown that the type of glycosylation is not critical for virus assembly and growth at 37°C (Kuo et al 2016). It seems more likely that, as for many virus glycoproteins, glycosylation has a more general significance in maintaining bioactive conformation and antigenic character (Alexander and Elder 1984; de Haan et al 2003; Braakman and van Anken 2000; Wissink et al 2004).

M is located among the S proteins in the virus envelope along with the small amounts of E (Arndt, Larson and Hogue, 2010) and is the primary driver of the virus budding process (Vennema *et al*, 1996; Corse and Machamer, 2002a). During assembly of the authentic virion M interacts with itself, with the nucleocapsid protein N, with E and with the S protein (Kuo and Masters, 2002; Boscarino et al 2008; Arndt, Larson and Hogue, 2010). M protein is present as a dimer in the virion and high resolution imaging has suggested it presents as two conformations, long and compact (M_{LONG} and $M_{COMPACT}$), which together induce membrane curvature as well as binding to the nucleocapsid (Neuman et al 2011; Neuman and Buchmeier, 2016).

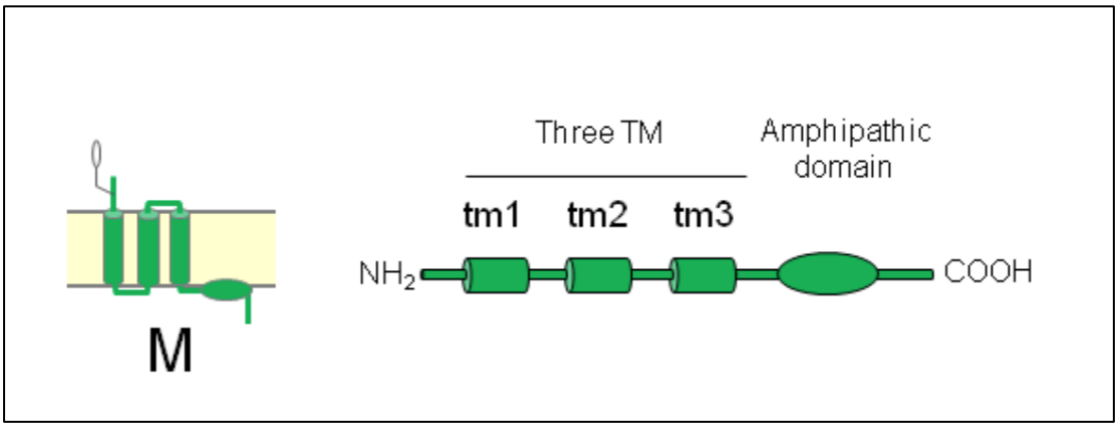

Figure 1.5: Topology and schematic diagram of coronavirus M protein.

M protein is composed of short glycosylated amino terminal ectodomain, three transmembrane domains (TM1, TM2, TM3), an amphipathic domain after the third TM domain and a long carboxy terminus. Adapted from (Ujike and Taguchi, 2015).

1.4.1.5 Nucleocapsid protein (N)

Nucleocapsid protein (N) is located inside the viral envelope in association with the viral RNA forming the helical ribonucleoprotein (RNP), its length ranging from 350-450 amino acids. Its function is to package the genome of the virus to protect it within the capsid and, later, during the replication phase, to ensure replication initiates and switches at the right time (Zhou et al 2008; de Haan & Rottier 2005). Amino acid conservation patterns and structural studies have revealed that N protein has three conserved regions represented by two structurally folded regions called the N-terminal domain (domain1) and a RNA-binding domain (domain2), connected an intrinsically disordered central region, and lastly a C-terminal domain (domain3). These three domains are conserved, as is the function of binding with viral RNA, in all coronaviruses (Masters, 1992; Yu, 2004). N-protein is heavily phosphorylated (Surjit et al 2005; Peng, Lee and Tarn, 2008; Wu et al 2009) and phosphorylation has been suggested to activate a structural change in the molecule which promotes the affinity for viral RNA rather than non-viral RNA. Binding of N-protein with the viral genome occurs with a bead-on-a-string like conformation (Fehr

and Perlman, 2015) and this binding is significant not only for the encapsidation of the genome but also for discontinuous transcription and polymerase template switching (Zúñiga et al 2010; Mateos-Gomez et al 2011). In addition, the protein alters cellular physiology through influence on the cell cycle, transcription of genes, triggering apoptosis and organization of the cytoskeleton (Hsieh et al 2005; Surjit et al 2006; Zhao et al 2006). As a result of its abundance N protein is an immunodominant antigen during virus infection and a host immune response is mounted to it. N thus acts as an essential diagnostic marker and its high level of conservation means diagnosis is not affected by antigenic drift (Tang et al 2005; Mourez et al 2007). The multiple functions of N during the viral life cycle mean that it too has been suggested as an important antiviral target (Lin et al 2014).

1.6 Nonstructural proteins

Roughly two thirds of the coronavirus genome are occupied by two open reading frames (ORFs), ORF1a and ORF1b. ORF1a and ORF1b translation leads to the formation of polyprotein1a (pp1a) and polyprotein 1ab (pp1ab) respectively. Processing of polyprotein1a (pp1a) or polyprotein 1ab (pp1ab) by viral proteases including papin-like proteases (PLpro 1 and PLpro 2) and the chymotrypsin-like cysteine proteinase (3CLpro) or main protease (Mpro) lead to the generation of sixteen nonstructural proteins nsps (nsp 1-16 nsp) with various role during the virus replication cycle (Ziebuhr et al 2000; Prentice et al 2004b).

Coronavirus nsp 3, 4, and 6 have fundamental functions in the rearrangement of host cell membranes that are required for the establishment of the viral replication-transcription complexes (RTCs) (Hagemeijer et al 2011), also called replication organelles (RO) (van der Hoeven et al 2016). Indeed, expression of just

these proteins will induce the formation of the double-membrane vesicles (DMVs) and other structures that are characteristic of coronavirus infected cells (Oudshoorn et al 2017). Replication complexes intimately bound up with convoluted membrane structures derived from the host cell are a feature of all positive stand RNA viruses and serve at least three functions, probably connected. Firstly, they serve to concentrate viral proteins in a microenvironment where all necessary replication factors are closely associated with the genomic RNA. Secondly, they exclude host factors so that the competition for resources can be focused on the virus, and thirdly they act to separate, as far as possible, the intermediates of replication, which are necessarily double stranded RNA molecules, from the host innate sensors such as Toll Like Receptor 7 (TLR7) and Melanoma differentiation gene-5 (MDA-5) (Angelini and Akhlaghpour 2013; Paul 2013; den Boon and Ahlquist 2010a; Zalinger et al 2015).

1.6.1 nsp3

Coronavirus nsp3 has two transmembrane regions and ~10-16 identifiable domains (depending on the virus) within the ~200kDa predicted primary translation product, eight of which are conserved **Figure 1.6** (Ziebuhr, Thiel and Gorbalenya, 2001; Neuman, 2016). It is co-translationally inserted into the endoplasmic reticulum resulting in the majority of the domains being tethered to the cytosolic side of the membrane (Kanjanahaluethai et al 2007; Woo et al 2012). Nsp3 function is integral to coronavirus replication and the domains include many predicted or demonstrated to act as accessories in RNA replication, such as ssRNA binding and unwinding domains, as well as those for which no distinct function has yet been determined (Lei, Kusov and Hilgenfeld, 2018).

1.6.2 nsp4

CoV nsp4 is also a transmembrane protein, having four transmembrane helices and an internal C-terminal domain **Figure 1.6** (Oostra et al 2007). With nsp3 it has been shown that nsp4 is an indispensable component required to produce DMVs (Angelini and Akhlaghpour, 2013). All CoV-nsp4 molecules encode at least one predicted glycosylation site and in the case of MHV, it has been shown that mutation of the glycosylation site results in loss of virus fitness suggesting that nsp4 glycosylation is necessary for virus replication or the organization of the DMVs (Beachboard, Anderson-Daniels and Denison, 2015). In an electron micrographic study, transfection of SARS-nsp3 and nsp4 alone caused considerable membrane deformation, producing a perinuclear double walled maze-like body (MLB) (Angelini and Akhlaghpour, 2013) and the nsp3-nsp4 interaction has been shown to be absolutely necessary for such membrane rearrangement (Sakai et al 2017). However, the interaction of these two nsps alone was not enough to trigger membrane rearrangement and host factors such as ER degradation-enhancing α mannosidase-like protein 1 (EDEM1) and osteosarcoma amplified protein 9 (OS9) of the ER-associated degradation (ERAD) system have been implicated as cofactors (Reggiori et al 2010; Sakai et al 2017). Despite them being a universal feature of coronaviruses the size and number of DMVs does not appear to correlate directly with viral fitness, at least when virus is grown at reduced temperatures (Al-Mulla et al 2014) nor are they a determinant of pathogenicity (Maier et al 2016).

1.6.3 nsp6

Coronavirus nsp6 is a membrane protein with six transmembrane helices including, in almost all viruses, a highly conserved C-terminus **Figure 1.6** (Baliji et al 2009). Although internal cellular membrane rearrangement is observed with only nsp3 and nsp4, nsp6 also causes membrane proliferation (Angelini and Akhlaghpour, 2013), including the formation of Atg5 and LC3II-positive vesicles classically observed in autophagy (Cottam et al 2011). The autophagosomes produced are somewhat different from those induced by starvation however as although their number is higher their size is reduced (Cottam, Whelband and Wileman, 2014). Along with nsp3 and nsp4, nsp6 thus functions to produce the canonical DMVs as well as many other types of intracellular vesicles observed in coronavirus infected cells such as convoluted membranes (CMs), vesicle package (VPs), tubular bodies (TBs), large virion-containing vacuoles (LVCVs), cubic membrane structures, (CMSs) and zippered ER spherules in the case of IBV (Knoops et al 2008; Maier et al 2013). An attenuated form of an IBV vaccine includes mutations in a nsp6 TM domain, confirming its role in virulence and replication (Quinteros et al 2015).

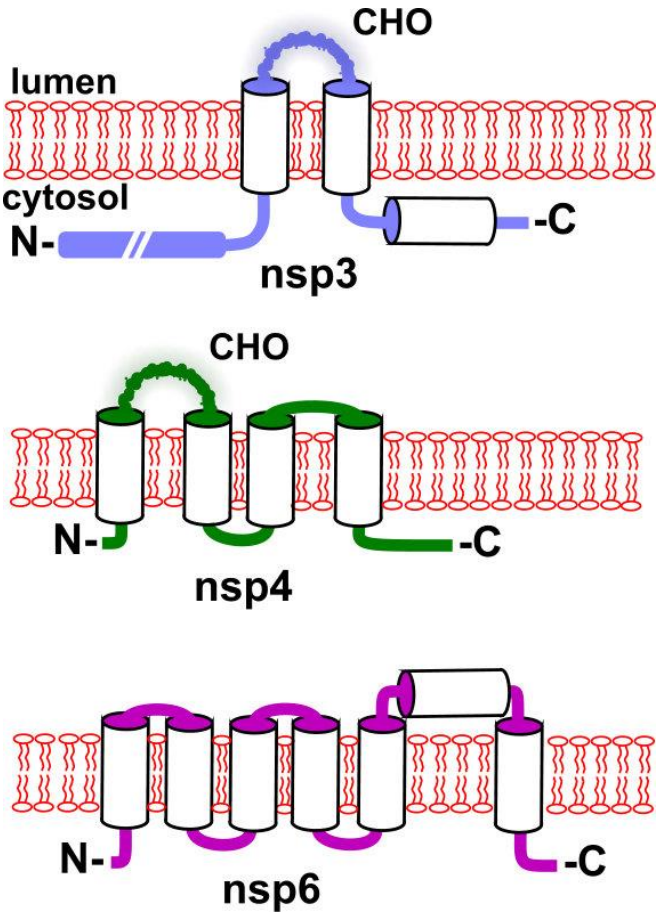

Figure 1.6: The suggested topology for the coronavirus non-structural proteins associated with membrane deformation. Three proteins, nsp 3, 4 and 6 are implicated in membrane curvature and the formation of sub-cellular membrane organelles. The topologies suggested within the lipid bilayer (red) are supported by experimental evidence but may not be the same for all coronaviruses. In all cases the white cylinders represent hydrophobic stretches of amino acids that are consistent with transmembrane domains although all may not be used as such (see nsp6). Only the region of the protein that interacts with the membrane is shown. N-the amino terminus of the protein, C-the carboxyl terminus of the protein, CHO- the addition of carbohydrate. The cartoon is not to scale.

1.7. Recruitment and modification of membranes by coronaviruses

As noted, the membranous vesicles or organelles of different morphologies induced by coronaviruses act as a platform for the formation of replication and transcription complexes (RTCs) and sequester newly formed RNAs away from host immune sensors (den Boon and Ahlquist 2010a; den Boon et al 2010b). Both viral and hijacked host proteins are used in this process, taking advantage of cellular pathways and lipid modifying enzymes to benefit the virus (Miller and Krijnse-locker 2008; den Boon et al 2010a; den Boon and Ahlquist 2010b; Hagemeijer et al 2012; Delang et al 2012). This usurping comes about through the commandeering of normal secretory pathways used by non-infected cells to transport and deliver protein cargos. Rather than encode proteins to build new DMVs, coronaviruses redirect and reorganize the cellular processes already in place (Strating and van Kuppeveld, 2017).

Two principle mechanisms have been described for moving and delivering cargo proteins through the cellular secretory pathway; cisternal maturation (Morré and Ovtracht, 1977) and the formation of megavesicles (Volchuk et al 2000). In both cases detail remains incomplete (Mironov et al 2001). During coronavirus infection, such as for MHV, virions have been observed in large vesicle depots resembling megavesicles derived from Golgi/ERGIC membranes, indicating that remodeling of the Golgi complex is crucial for virion trafficking (Ulasli et al 2010). As noted, nsp6 may initiate cellular autophagy and a general ER stress response also occurs during the formation of DMVs (Prentice et al 2004a; Cottam et al 2014; Cottam et al 2011; Fung et al 2016) and if Atg5, necessary for formation of the crescent membranes, is knocked out MHV yield is reduced (Suzuki and Ohsumi 2007; Prentice et al 2004a) although this is not a universal finding (Snijder et al 2006; Stertz et al 2007).

Although precise mechanisms are ill defined, biological bilayers of proteins and lipids (Engelman, 2005) are key to the separation and control of biological processes and their composition is dynamic (Derganc, Antonny and Čopič, 2013). Bending, that is positive or negative membrane curvature, is driven by acquisition and loss of peripheral membrane proteins, integral membrane proteins and by lipid composition (Kooijman et al 2005; McMahon and Gallop, 2005). Membrane wrapping may occur around intrinsically curved proteins in which positively charged amino acids interact with negatively charged lipid head groups, for example in the dynamin and BAR domain interactions, also known as scaffolding (Sweitzer and Hinshaw, 1998; Peter et al 2004). Alternatively, crowding mechanisms may be the effector of membrane curvature as a result of the asymmetric distribution of proteins either side of a cellular membrane (Stachowiak *et al*, 2012; Derganc, Antonny and Čopič, 2013) and the insertion of an amphipathic helix which acts as a wedge to expand one side of the membrane more than the other can also cause curvature as revealed by studies on influenza virus M2 protein, Epsins and Sar 1p **Figure 1.7** (Rossman et al 2010; Boucrot et al 2012; Lee et al 2005; Kirchhausen 2012).

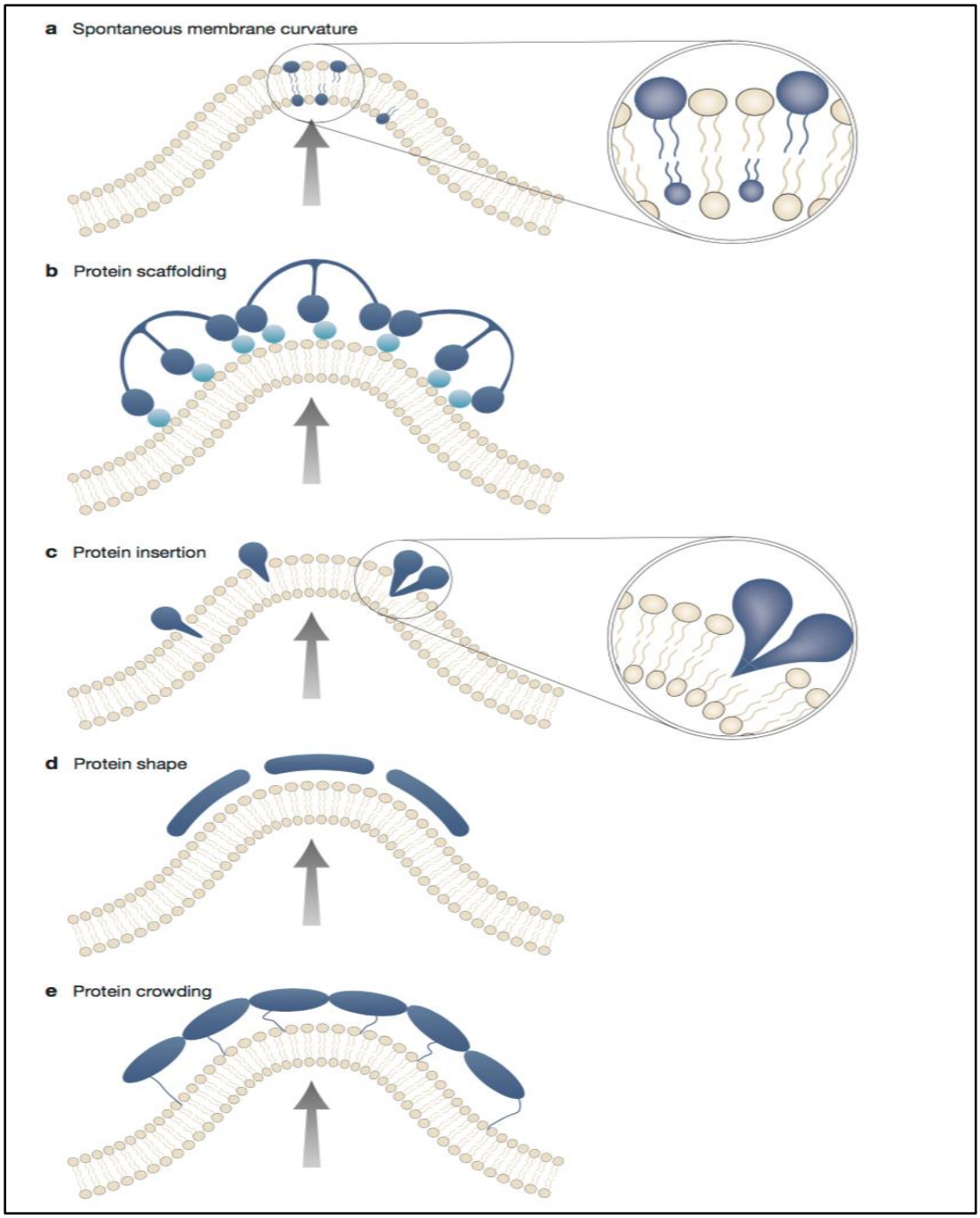

Figure 1.7: Mechanisms of generation of membrane curvature.

(a) Lipids create local spontaneous membrane bending. Positive curvature can be generated by lipids with a greater area proportion of polar head groups to acyl chains; negative curvature may be created by lipids with the reverse ratios. (b) Illustrates the intracellular membrane curvature created by a protein scaffold as is commonly the case in the generation of intracellular carriers associated with COPII and COPI coat protein complexes or clathrin. (c) Membrane curvature created by asymmetrically inserted of hydrophobic or amphipathic protein domains into the lipid bilayer. (d) Membrane curvature resulting from curve shaped protein domains attached to the lipid bilayer. (e) Protein crowding mechanism. Figure adapted from (Kirchhausen 2012).

1.8. Virus egress

During assembly, all enveloped viruses face the challenge of combining capsids proteins and genome produced in the cytosol with glycoproteins that are predominantly in another cellular compartment, the luminal side of the ER. A cell membrane separates these components and must be breached or used in the assembly of the complete virion and this is achieved in three stages. Firstly, the virus proteins coalesce on the membrane, capsid proteins grouping together underneath the patch of membrane where viral glycoproteins are embedded. Secondly, the membrane bulges outward to form a bud decorated by the viral transmembrane proteins and enclosing the capsid proteins and genome. Finally, the bud splits from the rest of the membrane by scission, a pinching off at the base which releases the virion either into an intracellular vesicle, as is the case for coronaviruses or directly out of the cell (Masters, 2006). For many enveloped viruses, these processes are effected by viral protein interaction with host proteins of the ESCRT machinery (Welsch et al 2007). Surprisingly however, perhaps because of incompatibility with the extensive membrane rearrangements induced in infected cells, coronaviruses appear not to use ESCRT proteins for egress (Chen et al 2008). Rather, the S protein has a signal for ERGIC retention in its cytoplasmic tail (Trincone and Schwegmann-Weßels, 2015) while the M protein locates to the ERGIC and cis-Golgi via its first TM domain, where it oligomerises to drive the budding process (Weisz, Swift and Machamer, 1993; Ujike and Taguchi, 2015). M-N interactions ensure that the viral RNPs also occur at these budding sites allowing the budding virus to incorporate a copy of the new genome (Tseng et al 2010). The E protein, as a viroporin, is implicated in membrane scission as although E is present in virus particles its level is very low and most is associated with the ERGIC and *cis* Golgi,

consistent with its predominant role as a mediator of virus assembly and release at this location (Venkatagopalan et al 2015). The lipid content at these locations may also enhance virus budding (Schmitt and Lamb 2005; Schmitt and Lamb 2004).

1.9. Coronavirus membranes as antiviral targets

As coronaviruses cause such extensive membrane perturbation and there is an acknowledged lack of available antiviral compounds to combat disease it is not surprising that membrane rearrangement has been considered as a target for the development of inhibitors that could act as antivirals, along with the more classical targets of the polymerase and proteases (Dyall et al 2017). Peptide therapeutics are promising antagonists in this regard as they compete directly for membrane binding or inhibit the conformational mechanisms involved. Several peptides have been used to target various steps in the coronavirus replication cycle. A HR2 competitive peptide blocked the fusion mechanism of MERS-CoV and prevented virus entry when measured using a pseudotype assay (Gao et al 2013) and a more complex 5 helix bundle, designed as a mimic of the final S fusion intermediate, was also active when measured similarly (Sun et al 2017). SARS-CoV has been similarly inhibited (Sainz, et al 2005; Sainz et al 2006). As membrane microdomains are implicated in coronavirus membrane interaction, drugs that alter microdomain composition, particularly the level of cholesterol present, have been shown to have an effect on some coronaviruses (Yin et al 2010; Jeon and Lee, 2017). More general still is the use of drugs which alter intracellular vesicle pH and so inhibit the entry or exit of many enveloped viruses, including coronaviruses (Dyall et al 2014; de Wilde et al 2014). Vaccines and passive immunotherapy options have also targeted crucial coronavirus-membrane interactions. The predominant antibody response to S is to the S1 domain which has been shown to be a successful vaccine candidate (Jiaming

et al 2017; Wirblich et al 2017) but the binding of antibodies targeting S1 is subject to antigenic drift and may not be effective for all serotypes. The S2 domain by contrast is generally immunologically silent. Rare antibodies that do target S2, the stem of S, inhibit the fusion mechanism and can be broadly reactive and so relatively impervious to serotype changes (Elshabrawy et al 2012). The use of such broadly reactive monoclonal antibodies as therapies may be particularly suitable for the treatment of serious but sporadic coronavirus infections where general vaccination of the target population is not warranted or is impractical.

Coronaviruses stimulate membrane remodeling on a significant scale and require the membranous structures produced at several stages of their replication cycle. In addition, existing cellular membranes are encountered at both virus entry into and exit from the cell. Further understanding of the role of virus proteins in this remodeling, directly and via interaction with host factors, will likely increase the therapeutic options of the future.

1.10. Middle East respiratory syndrome coronavirus (MERS-CoV).

MERS-CoV is one of the newly emerged viruses and was first recognized in Saudi Arabia in 2012 (Zaki et al 2012). Since then 2374 laboratory confirmed cases of MERS-CoV infection, leading to 823 related deaths (34.6% case fatality rate) have been reported to the WHO (as of the end of February 2019) (www.emro.who.int./health-topics/mers-cov/mers-outbreaks.html).

The predominance of these cases is in Saudi Arabia. MERS-CoV can cause severe lower respiratory tract infection and renal failure (Zaki et al 2012). It is the sixth coronavirus recognized to infect humans (Zaki et al 2012; Xia et al 2014). According to phylogenetic studies, MERS-CoV is most closely related to the bat coronavirus as HKU4 and HKU5 and many studies have considered the bat as the most likely

potential reservoir of MERS-CoV. Two mutations are seen to play an essential role in the ultimate bat to human transmission (Boheemen et al 2012; Lau et al 2013; Woo et al 2014; Yang et al 2015; Yang et al 2014). Dromedary camels are assumed to be the main vector host of MERS-CoV as they have a high level of seropositivity to virus structural proteins and in a number of cases, though not all, they seem to be a credible animal source for human infection (Mohd, Al-Tawfiq and Memish, 2016). MERS-CoV is a lineage c coronavirus, has a genome of ~30kb nucleotides and encodes all the canonical coronavirus proteins, nonstructural replicase polyproteins as well as structural proteins S, E, M and N, all encoded by 10 or more open reading frames (Boheemen et al 2012; Zaki et al 2012).

MERS-CoV cell entry is usually via two pathways, either directly at the plasma membrane or endocytosis via a cathepsin L dependent pathway (Qian, Dominguez and Holmes, 2013; Shirato, Kawase and Matsuyama, 2013). In the direct fusion, pH-independent, pathway the virus is capable of fusing at the cell surface after S protein binding receptors in association with cellular proteases such as type II trans-membrane serine protease subfamily (TMPRSS2). The protease ensures S is efficiently cleaved into S1 and S2 and this pathway is considered more effective than pH-dependent endocytosis by 100-1000 fold (Matsuyama et al 2005; Belouzard et al 2012; Shirato, Kawase and Matsuyama, 2013). It seems likely that this pathway is the most utilized by MERS-CoV, at least in infected cell lines, as the virus forms multinuclear syncytia in cells such as liver (Huh-7) and lower airway epithelial cells (Calu-3) (Lu et al 2014; Chan et al 2013). Alternatively, a pH-dependent endocytosis mechanism can operate after receptor binding resulting in fusion occurring in the acidic environment of an endosomal vesicle (Belouzard et al 2012).

The MERS-CoV spike protein comprises 1353 amino acids, with two subunits S1 and S2 as described for coronavirus in general. The roles are typical, S1 binds to cellular receptors (DPP4), while S2 is responsible for membrane fusion (Lu et al 2014; Raj et al 2013; Mou et al 2013). S1 is located between residues 14-751 in the amino terminal half of S and contains the receptor binding domain (RBD) at residues 367-606. The RBD has been characterized structurally and consists of five strands antiparallel β-strands with a number of short α helices (Chen et al 2013; Lu et al 2013; Wang et al 2013; Yuan et al 2017; Gui et al 2017; Walls et al 2016b). Many studies have showed that the RBD can stimulate a considerable neutralizing antibody response during infection, making it an obvious target for the development of subunit vaccines for MERS-CoV infection (Ma et al 2014; Ying et al 2014; Du et al 2017). After aligning MERS-CoV S protein with SARS-S protein, Xia and his colleagues suggested that the S2 subunit of MERS-CoV contains a fusion peptide located at residues 943-982, heptad repeat 1 at residues 984-1104, and heptad repeat 2 at residues 1246-1295. The transmembrane domain is located at residues 1246-1317 followed by the intracellular domain at residues 1318-1353 residues. After binding of S1 to DPP4 a conformational change occurs resulting in exposure of the S2 subunit and insertion of the fusion peptide into the cell membrane. HR1 sequences locate to hydrophobic grooves on the surface of the homotrimer and subsequently, as part of the conformation change initiated by membrane binding, the HR2 sequences fold onto HR1 to form a six-helix bundle (6HB) structure common to many conventional type I membrane fusion proteins. This collapse of the trimer draws the viral and cellular membranes together leading to formal fusion (Xia et al 2014; Harrison, 2015). Although the model is conventional and strongly supported by previous studies on other coronaviruses, notably SARS-CoV, at the time of the

studies described in this thesis the fusion peptide of MERS-CoV had not been formally identified.

1.11. Mouse Hepatitis Virus (MHV)

MHV is a betacoronavirus that causes different diseases including hepatitis, enteric and respiratory infections and acute and chronic demyelination of the central nervous system (Weiss and Navas-martin, 2005; Belouzard et al 2012). Several strains of murine hepatitis virus are used as laboratory models because of the wide range of diseases caused (Weiss and Navas-martin, 2005). Many strains of MHV are known to cause neurological diseases such as severe virulent JHM.SD (MHV4) and a neuroattenuated strain MHV-A59 is hepatotropic (Dalziel et al 1986; Bender et al 2010). As discussed, MHV-A59 has five structural proteins HE, S, E, N and M (**Figure 1.3**). HE is a non-essential glycoprotein ranging from 60-70 kDa in size, its non essential for viral entry and replication (Gagneten et al 1995; Popova and Zhang, 2002; Smits et al 2005) but it has an influence on acute and chronic disease either as a factor of tissue tropism or in the spread of the virus infection (Yokomori et al 1993; Kienzle et al 1990). MHV-A59 S protein is a homotrimer of 180kDa with typical S1 and S2 domains (de Haan et al 2004). Previously, for MHV, it was thought that the S maturation cleavage to S1 and S2 was not required for virus fusion (Bos et al 1997; Hingley et al 2002). However, subsequent studies have demonstrated that cleavage of S in an endosomal compartment of infected cells is crucial for fusion (Simmons et al 2005; Qiu et al 2006). The entry mechanism is typical, that is a conformational change occurs in S protein after binding receptor, a member of the carcinoembryonic antigen (CEA) family (Dveksler et al 1991; Taguchi and Hirai-Yuki, 2012) or by artificial exposure to low pH or temperature, leading to membrane fusion (Sturman, Ricard and Holmes, 1990; Gallagher, 1997; Holmes et al 2001). Despite

its widespread use as a model coronavirus a genome wide screen for amino acid sequences involved in membrane binding has not been reported. Many should be present as so many MHV proteins are located within the ROs but demonstration of their ability to act directly on membranes is lacking.

1.12 Roles of lipids in viral infections

The first barrier viruses need to overcome in the infection process is crossing the cellular lipid rich membranes. Some non-enveloped viruses utilize lipids as a receptor (Taube, Jiang and Wobus, 2010) as in poliovirus binding to glycosphingolipids (Tsai et al 2003; Qian et al 2009). And some enveloped viruses, e.g. hepatitis C virus (HCV) bind to lipid droplets and then to low density lipoprotein (LDL-R) receptor to enter cells (Agnello et al 1999; Molina et al 2007).

In addition, viral processes may need particular lipid compositions in different compartments for proper onward function. For example, the lipid microenvironments affects the viral entry of some viruses, often by influencing the aggregation of receptors in cholesterol rich microdomains, as shown for HIV-1 (Liao et al 2001), Pseudorabies virus (Desplanques et al 2008) and Human Herpes Virus 6 (Huang et al 2006). Viral entry failed or was disrupted for these viruses when cholesterol was depleted. Similarly, in the coronaviruses, cell membrane fusion process and plaque development were hindered by cholesterol depletion during MHV infection (Thorp and Gallagher, 2004).

Many studies have shown that host genes participating in phosphatidylinositol (PI) signaling affect virus replication, e.g. for HCV and enterovirus replication (Berger et al 2009; Hsu et al 2010). These lipid signaling molecules guide cellular membrane trafficking and, with key viral proteins, form the replication complexes (RCs) (Diaz,

Wang and Ahlquist, 2010; Heaton and Randall, 2011).

Lipids also play a key role in viral budding at the plasma membrane. Some viruses such as HIV bud from lipid rafts enriched in cholesterol and sphingolipids (Nguyen and Hildreth, 2000) and these lipid rafts may be induced by virus infection as in HIV infection, which stimulates cholesterol synthesis in infected cells and transfers it to lipid rafts (Zheng et al 2003). The lipid signaling assists in the organization of HIV budding sites by recruiting the Gag (capsid precursor) protein (Saad et al 2006). In another example, lipid can be vigorously synthesized to supply membranes for viral envelope formation, as has been reported for cytomegalovirus (CMV), where the enhanced biosynthesis of fatty acids during CMV infection is a factor in viral budding (Munger et al 2008). In short, lipids form an integral component of many virus life cycles and viruses have come to depend on them for certain stages of their replication. It follows that membrane binding by viral proteins is essential and in turn the sequences within proteins that enable membrane binding are of importance. This fact was the guide for the work described in this thesis, focusing particularly on the proteins of MHV and MERS-CoV.

1.13 Aims of this study

The aim of the research described here was to characterize the membrane binding proteins of MHV and MERS-CoV using a variety of bioinformatics tools and to obtain candidate sequences as peptides for biochemical tests. To provide membranes akin to biological membranes for these studies, giant unilamellar vesicles, GUVs, were formed and the ability of selected peptides to change their shape and size was determined experimentally. Data with wild-type peptides was supported by the use of modified peptides to test the effects of single residues on the membrane binding properties. For selected amino acid sequences the relevance of the peptide data was tested *in vivo* by expression of the complete protein and assessment of membrane binding in a biologically relevant model.

Specifically, the initial aim was to characterize the domains in both structural and nonstructural proteins of coronavirus encoded membrane active regions using sequence alignment and local amphipathy prediction programs. The second aim was to reconstitute the identified conserved, amphipathic peptides into giant unilamellar vesicles (GUVs) in different concentrations and to test their effect on the shape and the size of the electroformed GUVs. A third aim was to modify wild-type peptides to test the effects of point mutations in regions suggested to be the membrane interacting. In the fourth aim selected proteins, containing previously mapped membrane active peptides, were expressing in eukaryotic cells and their membrane binding, or membrane altering properties, were assessed, for example the syncytium formation (fusion) and cellular localization. In the context of the complete proteins with demonstrable biological activity, mutations mapped as affecting activity in the peptide context were re-assessed by constructs that introduced the same mutations into the full length protein. Using transfection of mammalian cells (HEK-293T cells)

the role of peptide bioactive sequences was tested in syncytium formation and cellular distribution, largely confirming the role suggested by the isolated peptides. In all membrane bioactive sequences were identified and validated to add to the knowledge base of coronavirus proteins that interact with cellular membranes.

2. Materials and Methods

2.1. Peptide synthesis used for *in vitro* analysis.

Wildtype and mutated peptides used for the *in vitro* analysis were derived from S, M, E, nsp3, nsp4 and nsp6 proteins of MERS and MHV coronavirus proteins and were synthesized using the PepArray method and supplied as crude lyophilized product with a mean purity of ≥ 70% (Cambridge Research Biochemicals, UK) **Table 2.1,2.2, 2.3 and 2.4**. MERS-S2 and MHV-S2 subunit derived peptides and sequences were designed from the database files (AHX00731.1) and (NP_045300.1) respectively while MERS-M and MHV-M derived peptides and sequences were from (YP_009047210.1) and (NP_045301.1) respectively. E protein derived peptides and sequences for MERS-CoV and MHV-CoV were from (YP_009047209.1) and (NP_068673.1) respectively while MERS-CoV and MHV-CoV-nsp3, nsp4 and nsp6 derived peptides were from (K9N7C7.1) and (NP_068668.2) respectively. As a positive control peptide and to validate the Giant Unilamellar Vesicles (GUVs) assay, the M2-influenza peptide was chosen as a well characterized highly conserved amphipathic helix sufficient for budding into GUVs and the formation of large luminal vesicles (LUVs) (Rossman et al 2010). A buffer only, without the addition of peptide, was used as a negative control.

Table 2.1: Wild type MERS-CoV and MHV-CoV S, M and E peptides used for in vitro analysis.

No.	Name of the peptide	Residues	Residues sequence
1	MERS S-FP	884-898	RSARSAIEDLLFDKV
2	MERS S- HR1	992-1006	ENQKLIANKFNQALG
3	MERS S-Highly conserved region	1098-1111	AKDKVNECVKAQS
4	MERS S- HR2	1252-1266	LTQINTTLLDLTYEMN
5	MERS S Pre-TM	1290-1304	TYYNKWPWYIWLGFI
6	MERS S-cysteine rich motif	1320-1337	CTGCGTNCMGK2LKCNRCC
7	MERS M- PTM3	92-105	ISYFVQSIRLFMRT
8	MERS M-Proline region	107-120	SWWSFNPETNCLLN
9	MERS E-Post TM	49-63	TLLVQPALYLYNTGR
10	MHV S-FP	866-880	IRGRSAIEDLLFDKV
11	MHV S-HR1	968-982	ENQKMIASAFNNALG
12	MHV S-highly conserved region	1074-1088	QAIEKVNECVKSQTT
13	MHV S-HR2	1222-1235	EKLNVTLLDLTYEM
14	MHV S-PreTM	1259-1273	EMYVKWPWYVWLLIG
15	MHV S-cysteine rich motif	1289-1304	CTGCGSCCFKKCGNCC
16	MHV M-TM3	82-95	VYLGFSIVFTIVSI
17	MHV M-PTM3	99-112	IMYFVNSIRLFIR
18	MHV M-Proline region	114-127	SWWSFNPETNNLMC
19	MHV E-TM	16-30	IIFIFAVCLMVTIIV
20	MHV E-Post TM	50-64	LVLSPSIYLYDRSKQ
21	M2-Infleunza	44-62	RLFFKCIYRFFEHGLKRG

Table legend. MERS S-FP-MERS-CoV spike-Fusion Peptide; MERS S-HR1-MERS-CoV spike heptad repeat 1; MERS S-highly conserved region-MERS Spike-Highly Conserved Region (SHCR); MERS S-HR2-MERS-CoV spike heptad repeat 2; MERS S PreTM-MERS-CoV spike Pre-transmembrane region; MERS S-cysteine rich motif-MERS Spike-cysteine rich motif (MERS-SC); MERS M-PTM3-MERS-CoV membrane protein post-transmembrane region3; MERS M-Proline region-MERS-CoV membrane protein Proline region; MERS E-PostTM-MERS-CoV envelope protein Post-transmembrane region; MHV S-FP-MHV spike-fusion peptide; MHV S-HR1-MHV spike-heptad repeat 1; MHV S PreTM-MHV-CoV spike Pre- transmembrane region; MHV S-highly conserved region - MHV Spike-Highly Conserved Region (MHV-SHCR); MHV S-HR2-MHV spike-heptad repeat 2; MHV S-cysteine rich motif - MHV Spike-cysteine rich motif (MHV-SC); MHV M-TM3-MHV membrane protein-transmembrane domain3; MHV M-PTM3-MHV membrane post-transmembrane 3; MHV M-proline region-MHV membrane protein Proline region; MHV E-TM-MHV envelope protein

transmembrane region; MHV E-PostTM- MHV envelope protein Post-transmembrane region.

Table 2.2: Mutant MERS-CoV fusion peptides used for *in vitro* analysis.

No.	Designation	Residues	Sequence
1	Peptide 1 (WT)	884-898	RSARSAIEDLLFDKV
2	Peptide 2	I890A	RSARSAAEDLLFDKV
3	Peptide 3	L893A	RSARSAIEDALFDKV
4	Peptide 4	L894A	RSARSAIEDLAFDKV
5	Peptide 5	F895A	RSARSAIEDLLADKV
6	Peptide 6	V898A	RSARSAIEDLLFDKA

Residues mutated into alanine are in red. WT; Wildtype.

Table 2.3: Wild type MERS-CoV and MHV-CoV nsp3, nsp4 and nsp6 peptides used for *in vitro* analysis.

No.	Name of the peptide	Residues	Residues sequence
1	MERS-nsp 3-1	1584-1600	VANDLTTALRRPINAT
2	MERS-nsp 3-3	1843-1856	SDALKRQIRIACRK
3	MERS-nsp 4-1	267-283	FIDIVRRLAVSLFQPIT
4	MERS-nsp 4-2	402-415	AYFSKKHVEVFTDG
5	MERS-nsp 4-3	444-459	TNDAYSRFLGLFNKYK
6	MERS-nsp 6-1	234-251	NLKLRAPMGVYDFKVSTQ
7	MERS-nsp 6-2	260-276	NLTAPRNSWEAMALNFK
8	MHV-nsp 3-1	1712-1726	AAADLSKELKRPVNP
9	MHV-nsp 3-2	1849-1862	SLTSFVNAAHNSLK
10	MHV-nsp 3-3	1957-1970	VDAFNQLSADLQHR
11	MHV-nsp 4-1	259-275	AFDLIHQVLGGLVRPID
12	MHV-nsp 4-2	394-410	SYCRKIGTEVRSDGTFE
13	MHV-nsp 4-3	432-445	SDVAFNRYLSLYNK
14	MHV-nsp 6-1	225-241	LSLLNSIFRMPLGVYNY
15	MHV-nsp 6-2	255-271	GLRPPRNSFEALMLNFK

Table 2.4: Wild type and mutant MERS-CoV nsp4-1 peptides used for *in vitro* analysis.

No.	Designation	Residues	Sequence
1	MERS 4-1(WT)	267-283	FIDIVRRLAVSLFQPIT
2	M1	F267A	AIDIVRRLAVSLFQPIT
3	M2	I268A	FADIVRRLAVSLFQPIT
4	M3	I270A	FIDAVRRLAVSLFQPIT
5	M4	V271A	FIDIARRLAVSLFQPIT
6	M5	L274A	FIDIVRRAAVSLFQPIT
7	M6	V276A	FIDIVRRLAASLFQPIT
8	M7	L278A	FIDIVRRLAVSAFQPIT
9	M8	F279A	FIDIVRRLAVSLAQPIT
10	M9	I282A	FIDIVRRLAVSLFQPAT
11	M10	F267A + I268A + I270A + V271A + L274A + V276A + L278A + F279A + I282A	AADAARRAAASAAQPAT

Residues mutated into alanine are in red. WT-Wildtype; M1-M10-mutations 1-10.

2.2. Lipids and chemical materials

Table 2.5: Lipids and chemicals used in in vitro analysis throughout this study.

Lipid	Description	Source
DPPC	The phospholipids 1,2-dipalmitoyl-*sn*-glycero-3-phosphocholine	Avanti Polar Lipids, Inc.
EggSM	Sphingomyelin (Egg, Chicken)	Avanti Polar Lipids, Inc.
Cholesterol	Cholesterol (ovine wool)	Avanti Polar Lipids, Inc.
Naphtho [2,3-a] pyrene	Naphtho [2,3-a] pyrene	Tokyo chemical industry UK Ltd
DTT	Dithiothreitol	Fisher
Sucrose	D-sucrose	Fisher
Glucose	D-Glucose	Fisher

2.3. Cell lines and bacterial strains

Table 2.6: Cells used throughout this study.

Strain	Description	Source
Sf9 insect cells	Insect cell line used for the production of recombinant baculoviruses and protein expression	Invitrogen
Lenti-X 293T cells (HEK-293T cells)	Mammalian cell line used for transfection of MERS-S and MHV-E proteins	Clontech
E.coli HST08 (Stellar™ Competent cells)	Bacterial strain used in transformation of *E.coli* for plasmid DNA amplification	Clontech

2.4. Antibodies

Table 2.7: Antibodies used throughout this study.

Antibody	Description	Source
Anti-MERS-CoV Spike (D12)	Monoclonal anti-MERS S antibody	Absolute Antibody, UK-Ab00696
Anti-CD26	Monoclonal anti-DPP4	Abcam-119346
Anti-mouse Alexa Fluor 488 goat antibody	Monoclonal anti-mouse antibody conjugated to Fluor 488	Life technologies-011033
Anti-6X His tag conjugate antibody	Mouse monoclonal anti-mouse 6X His tag conjugated to Alexa Flour 488	ThermoFisher (4E3D10H2/E3)
Anti-6X His tag (HRP) antibody	Rabbit polyclonal to 6X His tag horseradish peroxidase (HRP)	Abcam-1187
Horseradish peroxidase-conjugated goat anti-rabbit Antibody (HRP)	Anti-rabbit antibody HRP conjugate	Dako
Anti- gp64 antibody	Monoclonal anti baculovirus gp64	(Lu et al 2002)
Anti-mouse Immunoglobulin HRP	Goat Anti-Mouse Immunoglobulin HRP conjugated	Dako-P0447

2.5. Buffers and culture media

Table 2.8: Buffers and cultures used throughout this study.

Name	Details	Application
4x LDS loading buffer	106 mM Tris HCl pH 8.5 141 mM Tris Base 2% Lithium dodecyl sulfate 10% Glycerol 0.51 mM EDTA 0.22 mM SERVA Blue G250 0.175 mM Phenol Red	SDS-PAGE
MES running buffer	50mM MES, 50mM Tris pH 7.25, 0.1% SDS, 1% EDTA	SDS-PAGE Running buffer
Tris-Glycine Transfer Buffer	0.025M Tris pH~8.3, 0.192M Glycine, 20% methanol	Protein transfer buffer for western blot
Tris buffered saline-Tween 20 (TBST)	1X diluted with high purity water for a solution	Different application including dilution

	composing from 25Mm Tris, pH 7.4, 0.0027M mM KCl and 0.13M NaCl with 0.2% Tween 20	antibodies and rinse of membranes
Western blot blocking buffer	1X TBST 5% skimmed milk powder	Blocking membrane during western blot
Western blot wash buffer	1X TBST	Washing membrane during western blot
Tris-acetate-EDTA (TAE) buffer	400nM Tris-acetate pH8.0 1mM EDTA	DNA electrophoresis
Stripping buffer	100 mM ß-mercaptoethanol, 2% SDS, 62.5 mM Tris-Hcl pH 6.5	To strip antibodies from a PVDF membrane for re-probing
6x DNA loading buffer	0.25% bromophenol blue 0.25% xylene cyanol FF 15% Ficoll type 400 in water	DNA electrophoresis
5x Orange G DNA loading buffer	5X TAE buffer 15% Ficoll 0.25 EDTA 0.0125% Orange G	DNA electrophoresis
Luria Bertani (LB) broth	1% tryptone 0.5% yeast extract 0.5% NaCl 0.1% glucose	For bacteria growth in suspension culture
Luria Bertani (LB) agar	1% tryptone 0.5% yeast extract 0.5% NaCl 0.1% glucose 1% Difco agar	For bacteria growth on agar plates
EX-CELL® 420 Serum-Free Medium for Insect Cells with L-glutamine	Sigma Cat.No. SLBT0875	Growth of Sf9 insect cells.

Dulbecco's Modified Eagle medium (DMEM)-high glucose	Sigma, Cat.No. RNBG6864	Growth of HEK-293T mammalian cells
Fetal Bovine Serum Gold (FBS)	GE Healthcare Cat.No. A15-151	Supplement for growing insect and mammalian cells
Penicillin-Streptomycin (100x)	GIBCO Cat.No. 15140-122	Antibiotics for growing insect and mammalian cells
Trypsin/EDTA solution 1X	GIBCO Cat.No. R-001-100	Spliting 239T cells
Lipofectine® transfection reagent	Invitrogen Cat.No.	Transfection of Sf9 insect cells to produce recombinant baculoviruses.
Lipofectamine 3000 transfection reagent	Invitrogen Cat.No. L3000015	Transfection of HEK-293T mammalian cells.
Slow Gold Antifade DAPI	ThermoFisher Cat.No. S36942	Anti-fade mount used for fluorescence microscopy

2.6. Vesicle Prep Pro station (Nanion Technologies GmbH, Munich, Germany).

This device was used for GUVs electroformation. It consists of two major components, the Vesicle Prep Pro station and the Vesicle Prep Pro chamber **Figure 2.1** supplied with 1 pair of transparent Indium Tin oxide (ITO) coated glass slides (52x29 mm), typical ohmic resistance ≤ 10 Ω. The Vesicle Prep Pro chamber includes the slide holders (top and bottom), in which the ITO slides are placed with the conductive sides facing each other. A rubber O-ring between the two slides is used as a separator and forms the chamber in which the GUVs are made **Figure 2.1**. The station produces potentials which are applied between the two ITO slides that are placed in the chamber. Voltage signals in the shape of sine waves are delivered by the station at specified amplitudes and frequencies.

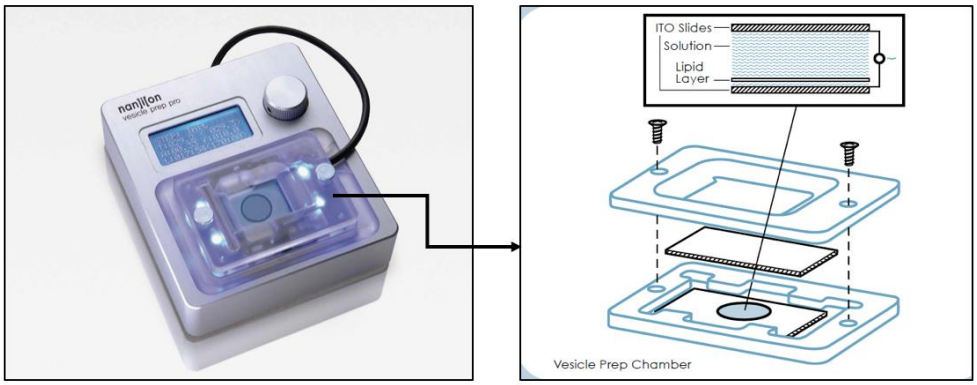

Figure 2.1: Vesicle Prep Pro station with the components of the chamber.

2.7. Preparation of Giant unilamellar vesicles (electroformation).

Giant unilamellar vesicles were generated by electroformation using a Vesicle Prep Pro (Nanion Technologies GmbH, Germany) using a mixture of 5 mM 1,2-dipalmitoyl-sn-glycero-3-phosphocholine (DPPC), 4 mM egg sphingomyelin (eggSM) and 0.5 molar % cholesterol, which was dissolved in chloroform. To visualize the GUVs 0.5 mol% of Naphtho [2,3-a] pyrene (Tokyo Chemical Industry UK Ltd.) was included to allow observation by fluorescence microscope. Lipids were mixed in an amber vial to a final total lipid concentration of 9 mM before preparation by electroformation. Production of GUVs representing a more physiologically relevant lipid mixture, based on what is known of the ER/ Golgi membranes, including ~ 50% PC, ~ 25% PE, ~ 15% PI, ~ 5% PS, ~ 5% SM and ~ 15% cholesterol, was not possible due to the complexity of GUV membrane produced (van Meer, 2008). Briefly, 20µl of lipid stock was spread on the conductive side of an indium tin oxide slide (ITO-slide). After evaporation of the solvent the slide was put into a vacuum desiccator for 1 hr to remove any remaining trace of the solvent. A 28 mm O-ring was coated on one side with silicon grease and placed around the dried lipid film to prevent leakage of the rehydration solution into the chamber. The lipid film was hydrated with 750 µl of 0.1 mM sucrose solution in deionized water, the presence of the sucrose increases the spacing between the lipid bilayers during electroformation process because of water movement toward the interlamellar space as a consequence of osmotic pressure differences (Akashi et al 1996). Then the second ITO slide was placed on top of the O-ring with the conductive sides facing. A tension of 3 volts (V) peak to peak and a frequency of 5 Hertz (Hz) was applied to the ITO slides over a period of 2 hr at 50 °C (Koynova and Caffrey, 1998). GUVs were imaged using an EVOS-FL digital fluorescence microscope (EVOS, USA).

2.8. Preparation of peptide stock solution

Peptides as a stock solution were dissolved using a buffer that consisted of (0.1mM sucrose, 0.1 mM glucose, 10 mM DTT, variable DMSO) and stored at -20 °C. Sucrose and glucose help in GUVs sediment to the bottom of the chamber due to density differences and additionally it has been shown that the refractive differences between the sugars leads to better imaging (Diguet et al 2012).

2.9. GUVs incubation with the peptides

Following electroformation the chamber was disassembled and the sucrose solution removed to leave the GUVs attached to one ITO slide (Kralj-Iglič et al 2001). The diluted peptide was added immediately onto the preformed GUVs and the field imaged in a time-series of 0 min, 1 min, 2 min and 5 min. As the GUV/peptide assay showed rapid changes in GUV morphology during the first minute, a 5-minute time-point was selected as a maximum for the analysis. Longer times were, in fact, tested but they generated poor images due to dryness of the field and deterioration of the GUV's making them invalid for subsequent analysis. ImageJ was used to measure the shape and the relative size of the GUVs. Experiments were performed in triplicate and the average and standard deviation calculated. Buffer only control experiments were conducted in the same way but without the addition of the peptide. All GUVs-peptide incubation experiments were performed at room temperature.

2.10. Measurement of the size and shape of the GUVs.

ImageJ was used to measure shape and size of GUVs. For shape, the longest and shortest diameters (d_{MAX} / d_{MIN}) of each vesicle were measured. Then the ratio was calculated. GUV size was determined as an effective diameter for a spherical

vesicle, the perimeter is estimated by Ramanujan's first approximation of an ellipse

$$p \approx \pi \left[3(a+b) - \sqrt{(3a+b)(a+3b)} \right]$$

The effective diameter is the perimeter divided by π.

2.11. Statistical analysis

Statistical significance was calculated using SPSS software 22 version, using a Linear Mixed Model (LMM) (p • 0.05). Results were expressed as mean ± SEM. Figures were generated using GraphPad Prism 7.0b software.

2.12. Plasmid construction and cloning of desired DNA fragments

2.12.1 Primers

The oligonucleotides used in this study are listed in **Table 2.10 and 2.11**, while the oligonucleotides used for sequencing pTriEx1.1 constructs are detailed in **Table 2.14**. All these oligonucleotide primers were ordered from Integrated DNA Technology (IDT).

Table 2.9: The oligonucleotides used for cloning of MHV-E in pTriEx1.1 vector.

Name	Primer	bp	Tm	%GC
HSV-E-FW	5'-GCGCCATGGCACAGCCAGAACTCGCCCCGGAAG ACCCCGAGGATTTTAATTTATTCCTTACAGACACAGTA TGGTATGTGGGG-3'	83	72.6	53
HSV-E-RV	5'-GCGCTCGAGGATATCATCCACCTCTAATAGGGG-3'	33	64.5	54.5

Table 2.10: Oligonucleotide sequences used for the construction of mutations in MHV-E. Red nucleotides color indicates mutated sequence.

Name	**Oligonucleotide sequences**	bp
L50A	GCGCCATGGCATTTAATTTATTCCTTACAGACACAGTATGGTAT GTGGGGCAGATTATTTTTATATTCGCAGTGTGTTTGATGGTCA CCATAATTGTGGTTGCCTTCCTTGCGTCTATCAAACTTTGTATT CAACTTTGCGGTTTATGTAATACTGCTGTGCTGTCCCCTTCTAT TTATTTGTATGATAGGAGTAAGCAGCTTTATAAGTATTATAATG AAGAAATGAGACTGCCCCTATTAGAGGTGGATGATATCCTCGA GGCG	266
V51A	GCGCCATGGCATTTAATTTATTCCTTACAGACACAGTATGGTAT GTGGGGCAGATTATTTTTATATTCGCAGTGTGTTTGATGGTCA CCATAATTGTGGTTGCCTTCCTTGCGTCTATCAAACTTTGTATT CAACTTTGCGGTTTATGTAATACTTTGGCGCTGTCCCCTTCTAT TTATTTGTATGATAGGAGTAAGCAGCTTTATAAGTATTATAATG AAGAAATGAGACTGCCCCTATTAGAGGTGGATGATATCCTCGA GGCG	266
L52A	GCGCCATGGCATTTAATTTATTCCTTACAGACACAGTATGGTAT GTGGGGCAGATTATTTTTATATTCGCAGTGTGTTTGATGGTCA CCATAATTGTGGTTGCCTTCCTTGCGTCTATCAAACTTTGTATT CAACTTTGCGGTTTATGTAATACTTTGGTGGCGTCCCCTTCTAT TTATTTGTATGATAGGAGTAAGCAGCTTTATAAGTATTATAATG AAGAAATGAGACTGCCCCTATTAGAGGTGGATGATATCCTCGA GGCG	266
P54A	GCGCCATGGCATTTAATTTATTCCTTACAGACACAGTATGGTAT GTGGGGCAGATTATTTTTATATTCGCAGTGTGTTTGATGGTCA CCATAATTGTGGTTGCCTTCCTTGCGTCTATCAAACTTTGTATT CAACTTTGCGGTTTATGTAATACTTTGGTGCTGTCCGCGTCTA TTTATTTGTATGATAGGAGTAAGCAGCTTTATAAGTATTATAAT GAAGAAATGAGACTGCCCCTATTAGAGGTGGATGATATCCTCG AGGCG	266
Y57A	GCGCCATGGCATTTAATTTATTCCTTACAGACACAGTATGGTAT GTGGGGCAGATTATTTTTATATTCGCAGTGTGTTTGATGGTCA	266

	CCATAATTGTGGTTGCCTTCCTTGCGTCTATCAAACTTTGTATT CAACTTTGCGGTTTATGTAATACTTTGGTGCTGTCCCCTTCTAT TGCGTTGTATGATAGGAGTAAGCAGCTTTATAAGTATTATAATG AAGAAATGAGACTGCCCCTATTAGAGGTGGATGATATCCTCGA GGCG	
Y59A	GCGCCATGGCATTTAATTTATTCCTTACAGACACAGTATGGTAT GTGGGGCAGATTATTTTTATATTCGCAGTGTGTTTGATGGTCA CCATAATTGTGGTTGCCTTCCTTGCGTCTATCAAACTTTGTATT CAACTTTGCGGTTTATGTAATACTTTGGTGCTGTCCCCTTCTAT TTATTTGGCGGATAGGAGTAAGCAGCTTTATAAGTATTATAATG AAGAAATGAGACTGCCCCTATTAGAGGTGGATGATATCCTCGA GGCG	266
All EPTM	GCGCCATGGCATTTAATTTATTCCTTACAGACACAGTATGGTAT GTGGGGCAGATTATTTTTATATTCGCAGTGTGTTTGATGGTCA CCATAATTGTGGTTGCCTTCCTTGCGTCTATCAAACTTTGTATT CAACTTTGCGGTTTATGTAATACTGCGGCGGCGTCCGCGTCTA TTGCGTTGGCGGATAGGAGTAAGCAGCTTTATAAGTATTATAA TGAAGAAATGAGACTGCCCCTATTAGAGGTGGATGATATCCTC GAGGCG	266
DeletedEPTM	GCGCCATGGCATTTAATTTATTCCTTACAGACACAGTATGGTAT GTGGGGCAGATTATTTTTATATTCGCAGTGTGTTTGATGGTCA CCATAATTGTGGTTGCCTTCCTTGCGTCTATCAAACTTTGTATT CAACTTTGCGGTTTATGTAATACTCTTTATAAGTATTATAATGAA GAAATGAGACTGCCCCTATTAGAGGTGGATGATATCCTCGAG GCG	221

Table 2.11: Amino acid sequences of the sequences of MHV-E shown in Table 2.10. Red amino acid color indicates mutated residue.

No.	Designation	Residues	Sequence
1	EPTM (WT)	50-64	LVLSPSIYLYDRSKQ
2	L50A	L50A	AVLSPSIYLYDRSKQ
3	V51A	V51A	LALSPSIYLYDRSKQ
4	L52A	L52A	LVASPSIYLYDRSKQ
5	P54A	P54A	LVLSASIYLYDRSKQ

6	Y57A	Y57A	LVLSPSIALYDRSKQ
7	Y59A	Y59A	LVLSPSIYLADRSKQ
8	L50A+V51A+L52A+P54A+Y57A+Y59A	L50A+V51A+ L52A+P54A+Y57A+ Y59A	AAASASIALADRSKQ
9	Deleted EPTM	Deleted residues from L50-Q64	

Residues mutated into alanine are in red. WT; Wildtype.

Table 2.12: Mutant MERS-CoV putative fusion peptides used for *in vivo* fusion analysis.

No.	Designation	Residues	Sequence
1	Peptide 1 (WT)	884-898	RSARSAIEDLLFDKV
2	Peptide 2	I890A	RSARSAAEDLLFDKV
3	Peptide 3	L893A	RSARSAIEDALFDKV
4	Peptide 4	L894A	RSARSAIEDLAFDKV
5	Peptide 5	F895A	RSARSAIEDLLADKV
6	Peptide 6	I890A+ L893A+ F895A	RSARSAAEDALADKV

Residues mutated into alanine are in red. WT; Wildtype.

Table 2.13: Sequencing primers

Oligo	Sequence	bp
T7 Forward 2	5'-TTAATACGACTCACTATAGGGG-3'	22
TriEXUP	5'-GGTTATTGTGCTGTCTCATCA-3'	21
TriEXDOWN 2	5'-TCGATCTCAGTGGTATTTGTGAGC-3'	24
MERSSF1	5'-TCGTCCCAAGTACCGTTTG-3'	19
MERSR1	5'-CGCAAATTAGCGCCGTG-3'	17
MERSSF2	5'-AGTACCGTTTGGGAGGACG-3'	19
MERSR2	5'-TAGCGCCGTGCAAAGCTTG-3'	19

2.13. pTriEx1.1 map.

The pTriEx1.1 vector (5301 bp) (Novagen) was a gift from Prof. Ian Jones lab. It has been designed to contain different types of promoters including the T7 promotor, p10 promotor and chicken β-actin promotor allowing it to be used to express genes in different expression systems such as *E. coli*, insect cells and vertebrate cells respectively. It also contains HSV tag sequences upstream of the cloning site and His tags sequences downstream the cloning site to permit construction of N-terminal HSV /or C-terminal His tagged proteins if required. Furthermore, it includes an ampicillin resistance gene allowing for positive colony selection **Figure 2.2**.

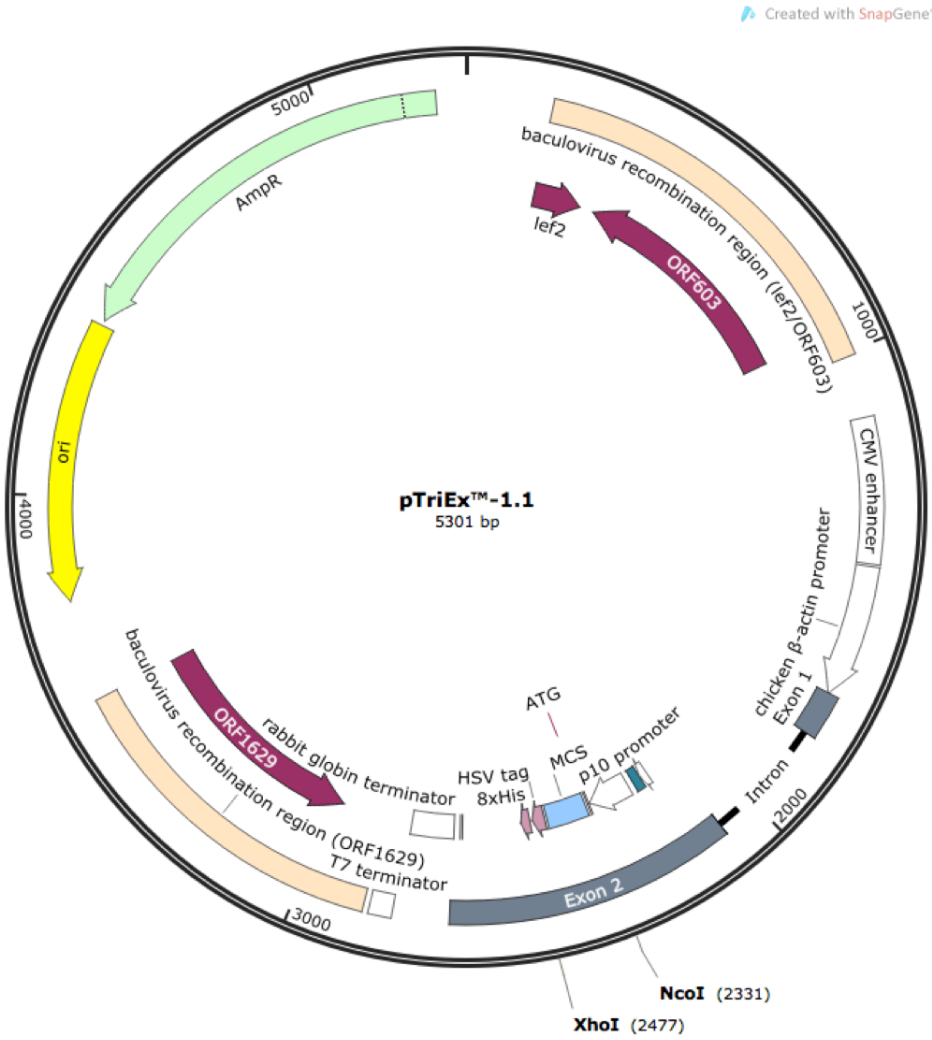

Figure 2.2: pTriEx1.1 vector demonstrating the cloning sites.

2.14. pTriEx1.1 recombinant proteins

In the original design, wildtype MHV-E was cloned so that it would be expressed as an N-terminal HSV tag and C-terminal His tagged fusion protein following insertion between *Nco*I and *Xho*I restriction sites**.** Both sites were included as tags as it was unclear which would be most suitable for the detection of the tagged E protein following expression in eukaryotic cells. On subsequent analysis, it was being found that the HSV tag did not work well i.e. it could not be detected routinely by western blot analysis and later constructs used only the His tag. The HSV and His tags are already present in the pTriEx1.1 vector, part of the design to allow detection of any expressed proteins using SDS-PAGE analysis and western blot with HSV and His tag specific antibodies **Figure 2.3.**

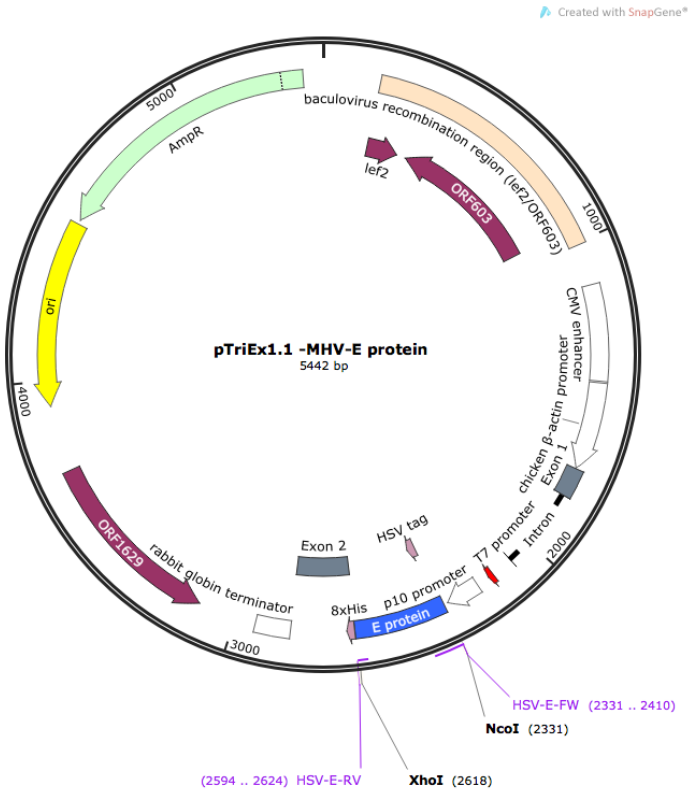

Figure 2.3: pTriEx1.1 vector map showing the site for insertion.

2.15. PCR Amplification of DNA fragments

The coding sequence of E protein of Murine Hepatitis Virus (GenBank accession No. AY700211.1) was amplified by Polymerase Chain Reaction (PCR) from cDNA kindly supplied by Dr. Volker Thiel using the primers listed in **Table 2.10**. The amplification reaction included the following components following the manufacture's protocol: CloneAmp 2x HiFi PCR Premix (25µl), 250ng DNA template, and 3µl of each primer (0.3µM) in a final volume of 50µl using dH_2O. The reaction was incubated in a thermal cycler according to the following thermal cycling conditions:

Step	Temperature	Time	Number of cycles
Initial denaturation	98 C˚	3:00 min	1X
Denaturation	95 C˚	0:10 sec	30X
Annealing	64 C˚	0:10 sec	30X
Extension	72 C˚	0:30 sec	30X
Final extension	72 C˚	5:00	1X

Purification of the amplified product was done for PCR products using a GeneJET PCR purification kit (ThermoFisher) following the manufacture's protocol. PCR products were eluted using ultra-pure water and the concentration of the recovered DNA measured by a Nanodrop spectrophotometer (ND-1000) and stored at -20 C˚.

2.16. Double digest and gel extraction of pTriEX1.1 vector and DNA fragments

In separate tubes pTriEX1.1 vector and the DNA fragment from section 2.15 were linearized using both restriction enzymes *Nco*I and *Xho*I (Thermo Fisher

Scientific) following the manufacturer protocol: 5µl of 10x Green buffer, template (up to 1µg), 1µl *NcoI*, 1 µl *XhoI* restriction enzymes and the volume completed to 50µl by ultra-pure water. The reaction was incubated for 30 minutes at 37 ˚C using a PCR T100^{TM} thermal cycler. 50 µl was subjected to agarose electrophoresis to confirm the digestion. Following visualization by agarose gel electrophoresis, DNA gel extraction and purification were done following the manufacture instructions, the concentration measured by NanoDrop ND_1000 and the eluted DNA stored at -20.

2.17. Agarose gel electrophoresis

A 0.7% agarose gel was used to visualize and estimate the size of the DNA. The gel contained 0.5µg gel red per ml of agarose gel (Cambridge Bioscience) was added to visualize the agarose gel and a Hyperladder 1 kb from Bioline was used to provide DNA markers. Samples were mixed with DNA loading buffer (Bioline) in a 5:1 ratio and loaded to the gel. Electrophoresis was for 1 hr at 120 V in 1x TAE buffer (Thermo Fisher Scientific). DNA bands were visualized and photographed using a SYGENE G: box ChemiXL box.

2.18. T4 ligation

The T4 ligation method was used to ligate the wildtype and mutants of MHV-E proteins and the mutants of MERS-S protein into the pTriEx1.1 vector. Ligation reactions were assembled using an estimated 3:1 molar ratio of the insert to vector as calculated by the Thermo Fisher Scientific online tool. The reactions were 1µl (5 U/ µl) of T4 DNA ligase enzyme (Thermo Fisher Scientific), linearized vector (10-100 ng), linearized DNA (10-100ng), 5X rapid ligation buffer and the volume completed to 20µl with ultra-pure water. The ligation mixture was incubated for 30 minutes at 22 ˚C and then the enzyme was heat inactivated by incubation at 70 ˚C for 5 min.

2.19. In-Fusion cloning

The In-Fusion cloning method was used to ligate the two synthesized MERS-S gene fragments. Each DNA fragment product was mixed with linearized pTriEx1.1 vector double digested with *Nco*I and *Xho*I restriction enzymes in an In-Fusion reaction mix following the manufacturer instructions containing a 3:1 ration of insert to vector as calculated by the Clontech online tool. The cloning reaction included 2µl of 5X In-Fusion HD Enzyme Premix, Xµl of Linearized Vector, Yµl of Insert and 8-(X+Y) µl of ultra-pure water to reach the final volume of 10µl. The reaction mixture was then mixed well and incubated for 15 min at 50 °C using a water bath, then placed on ice for 30 min.

2.20. Transformation

Stellar cells (*E. coli* HST08 strain) (Clontech) were transformed following the manufacture's protocol. Briefly, competent cells were thawed on ice and 50 µl of cells gently mixed with 5 µl of the infusion reaction or T4 ligation mixture. The samples were incubated for 30 minutes on ice then exposed to a heat shock at 42 ˚C for 45 seconds using a water bath. The samples were placed on ice for a further 2 minutes and then 125µl of pre-warmed SOC medium was added to the mixture, followed by incubation for 1 hr at 37 ˚C in a shaker. 100 µl of this mixture was plated onto Luria-Bertani agar (LB agar) contained 100 µg/ml ampicillin for overnight incubation at 37 ˚C. Next day, random colonies were chosen for screening by colony PCR.

2.21. Colony PCR screening for transformants

Colony PCR was chosen to confirm the cloning of the target DNA into vector, using a sterile tip, one random bacterial colony was taken from LB/Ampicillin agar plate and added to 20µl of water in a PCR tube and boiled for 2 minutes at 100 ˚C. The sample was then centrifuged at 13000 rpm for 2 minutes and the supernatant used for PCR reaction composed of: 12.5 µl CloneAmp HiFi premix, 1 µl Forward and Revers primers (0.3 µM), 2 µl of the supernatant as DNA template in a total volume of 50 µl. The PCR protocol was as follow:

Step	Temperature	Time	Number of cycle
Initial denaturation	98 °C	3 min	1 cycle
Denaturation	95 °C	10 sec	30 cycles
Annealing	64 °C	30 sec	
Extension	72 °C	27 min	
Final extension	72 °C	5 min	1 cycle

2.22. Plasmid DNA purification and sequencing

Bacterial colonies containing the expected insert size were chosen and grown in LB broth supplemented with 100µg/ml ampicillin at 37 ˚C overnight with shaking. A Miniprep kit (Thermo Fisher Scientific) was used to purify the plasmid DNA from the cell culture pellet following the manufacture instructions. Sample concentrations were measured using NanoDrop ND_1000. Purified DNA samples were sent for sequencing at Source BioScience.

2.23. Cell culture

2.23.1. Human embryonic kidney cell line (HEK-293T) cells (Lenti-X 293T).

The Lenti-X 293T cell line is a sub clone of the transformed human embryonic kidney cell line (HEK-293) and was used to express the MERS-S and MHV-E proteins as these cells are well known to be easily transfected and to produce high-level expression of proteins (Pear *et al*, 1993).

2.23.2. Transfection of HEK-293T cells

HEK-293T cells were cultured and maintained in Dulbecco's modified Eagle medium (DMEM) (Sigma Aldrich) supplemented with 10% fetal bovine serum (FBS) (GE Healthcare) and antibiotics penicillin/streptomycin (penicillin 100 U/ml, streptomycin 0.1 mg/ml; Gibco/Invitrogen) on glass coverslips in a 12 well plate. The cells were transfected with plasmid DNA to express Wildtype or mutant genes using the Lipofectamine3000 transfection reagent (Invitrogen) following the manufacturer's protocol. After incubation for 24 hr, cells were washed twice with cold PBS and fixed and permeabilized for immunofluorescent. A control vector pTriEx1.1-GFP, which carries the Green Fluorescent Protein (GFP) gene, was used to visualize the efficiency of transfection.

2.23.3. Immunofluorescent staining of HEK-293T cells.

One day before transfection, a total of 1.25 x 10^5 HEK-293Tcells were seeded on a glass coverslip in a 12 well plate and incubated for 24 hr at 37 ˚C / 5% CO_2. Next day, the cells were transfected with plasmid DNA using Lipofectamine 3000

transfection reagent (Invitrogen) following the manufacturer's instruction protocol and incubated for 24hr at 37 ˚C / 5% CO_2. A control vector pTriEx1.1-GFP-His (a gift from B. Abdulsattar) which carried the Green Fluorescent Protein (GFP) gene was also transfected into cells and used to visualize the efficiency. Twenty hours after transfection, the media was removed and the cells washed twice with cold PBS for 5 minutes, then the cells were fixed in fixation buffer (eBioscience™) for 1 hr at room temperature. Cells were permeabilized by permeabilization buffer (eBioscience™) for 5 min at room temperature in dark following manufacturer protocol. Then the cells were incubated with the diluted primary Ab for 1 hr at room temperature followed by being washed twice with wash buffer and incubated with diluted secondary Ab for 1 hr at room temperature. The cells were washed twice with wash buffer for 15 min at room temperature in the dark, counterstained with DAPI and subjected to imaging by fluorescence microscope. Cells were mounted by placing the cover slip upside down on a clean glass slide with a drop of Slowfade™ Gold antifade reagent before being imaged by an EVOS-FL digital fluorescent microscope. Typically, images were captured at 20X magnification power and further manipulated, if required, using ImageJ software.

2.23.4. MERS-CoV S Syncytium formation.

A total of 1.25 x 10^5 HEK-239T cells were seeded on a glass coverslip in a 12 well plate and incubated for 24h at 37 °C. Cells were transfected with 1µg of plasmid DNA using Lipofectamine 3000 (Invitrogen) for 24h at 37 °C. Prior to the assay S cleavage was ensured by treatment with 2 µg/ml of trypsin in Opti-MEM (Sigma Aldrich) for 30min at 37 °C as previously described (Madu et al 2009). The medium was removed and the cells rinsed once with PBS adjusted to pH 5.0 (with citric acid)

followed by incubation for 5 min in the same buffer at 22 °C. The PBS was replaced with complete DMEM for 1h at 37 °C and the monolayer then fixed and processed as described for immunofluorescent staining. Permeabilized cells were incubated with primary antibody anti-MERS-CoV Spike (D12) monoclonal antibody (Ab00696, Absolute Antibody, UK) at 1:500 dilution for 1h then the monolayers washed and incubated with the secondary Ab conjugate AIexa Fluor 488 goat anti-mouse antibody (Life technologies) for 1h at 1:500 dilution. Following final washing the stained cells were counterstained with Slowfade™ Gold antifade reagent with DAPI (Invitrogen) and visualized using an EVOS-FL digital fluorescence microscope (EVOS, USA).

2.23.5. Baculovirus expression system.

To examine MHV-E expression levels in a cellular environment, the baculovirus *Autographa californica* multiple nuclear polyhedrosis virus (AcMNPV) expression system was utilized with vectors encoding the full sequence of MHV-E proteins and mutations C-terminally His tagged.

2.23.6. Sf9 cells

Spodoptera frugiperda was used as a source for insect cell line *Spodoptera frugiperda* 9 (Sf9) (Invitrogen USA). This cell line was used for baculovirus amplification and protein expression. Sf9 cells were seeded as a monolayer or suspension and maintained at a cell density of between 2.5 × 10^5 /ml and 1x10^6 by passage in Ex-cell serum free medium supplemented with 2% foetal calf serum (FCS), 1% penicillin/streptomycin, at 27 ˚C with shaking typically for 3-5 days.

2.23.7. Transfection of Sf9 cells and production of recombinant baculovirus.

The recombinant baculovirus expression system is extensively utilized to express proteins in insect cells (Kitts et al 1990; Kitts 1993). The system offers high level of protein expression and is easy to scale up allowing for production of proteins at large scale if required (Smith, Summers and Fraser, 1983; Hasemann and Capra, 1990).

The flashBAC™ GOLD (FBG) baculovirus Expression System (Mirus Bio) was used to produce recombinant baculoviruses. The pTriEx 1.1 based plasmids described were transfected with linearised viral DNA to produce recombinant baculovirus stocks. 1 x 10^6 Sf9 insect cells were seeded into 6 well tissue culture plates and left to settle for 1 hr at room temperature, cells then washed twice with new 2ml fresh media. A transfection mix was prepared according to the manufacture protocol by combining (500ng/µl) of the recombinant plasmid with 2µl of the FBG and 8µl of nuclease free water in one sterile eppendorf tube, and in a second sterile eppendorf tube 8µl of Lipofectine transfection reagent (Invitrogen) were mixed with 4µl of nuclease free water. Then the two tubes were mixed and incubated for 15 min at room temperature. After incubation, the transfection mixture was added gently to the cells. Cells were incubated at 27 ˚C for 5-6 days. After incubation cells were examined under microscope to visualize the cytopathic effect caused by the recombinant virus. Cells then harvested by displacing and spun down at 4000 rpm/ 10 min then the supernatant was collected as passage 0 (P0) and stored at 4 ˚C. A control vector pTriEx1.1-GFP, which carries the Green Fluorescent Protein (GFP) gene, was used to visualize the efficiency of transfection. Subsequent passage of the

P0 stock produced P1 and P2 stocks with increasing CPE, which were stored at 4 ˚C priors to use for expression tests.

2.23.8. Small scale protein expression using recombinant baculovirus system.

The small-scale protein expression was performed by infection of a 6-well plate seeded with 1 x 10^6 Sf9 cells per well and incubated at room temperature for 1 hr to allow the cells to attach. The cells were washed two times with a fresh 1ml of insect cells media (Sigma) then replaced with 2ml of Insect EX-cell serum free media with L-glutamine (Sigma) supplemented with 2% of foetal calf serum (FCS). Then 200µl of a high titer stock of the recombinant baculovirus, typically passage 2, was added to the well and incubated for 5 days at 27 °C. After incubation, all the cells and culture media were harvested and centrifuged at 4000 rpm for 10 min. The cell pellets were either used for western blot or fluorescence microscope.

2.23.9. Baculovirus amplification

Large scale recombinant baculovirus amplification was carried out by infection of monolayers of Sf9 insect cells. T300 flasks were seeded with 30x10^6 cells in a total volume of 50 mL of 2% FCS Insect media and left for 1hr at room temperature, allowing the cells to adhere to the flask. The cells were inoculated with 500µl of the high titer (P2) stock of the recombinant baculovirus and incubated for up to 96 hr at 27 ˚C. Then cells were harvested and centrifuged 4000 rpm / 20 minutes at 4 ˚C. The supernatants were removed and stored at 4 ˚C.

2.24. SDS-PAGE

Proteins were separated using Sodium dodecyl sulphate polyacrylamide gel electrophoresis (SDS-PAGE) using precast gels (Invitrogen). The protein samples were mixed with half of the volume of 4 x LDS loading buffer and 2% ß-mercaptoethanol and boiled at 100 ˚C for 10 minutes. Then samples were loaded on gradient 4-12% Tris-Glycine SDS polyacrylamide gels (Invitrogen) and electrophoresis was done using MES running buffer for 30 minutes at 170 V. After electrophoresis, gels were transferred to PVDF membranes for Western blot analysis.

2.25. Western blot

For confirmation of protein expression, western blotting was done to detect the expressed proteins. SDS-PAGE gels were transferred to PVDF membranes (Whatman) that had been pre-soaked in 100 % methanol (Fisher) for 5 min then transferred into 1X transfer buffer (25 mM Tris, 192 mM Glycine pH~8.3) with 20% methanol and electroblotted for 1 hr 20 min at 35 V and 150 mA using a semi-dry western blotting apparatus. The membrane was then incubated in blocking buffer consisting of (5% of skimmed milk powder, 0.2% Tween-20, 1x TBS) for 1 hr, then the membrane washed 3x for 5 minutes each and incubated with the primary antibody e.g Rabbit polyclonal 6x His tag HRP Ab at 1: 10,000 in 1x TBST buffer for 1 hr followed by 3x washes for 5 minutes each with TBST buffer on a platform rocker. The membrane was then incubated with secondary antibody horseradish-peroxidase (HRP) conjugated goat anti-rabbit antibody (Dako) diluted 1:10,000 in 1x TBST for 1 hr followed by 3x washes for 5 minutes each with TBST buffer on a platform rocker. To visualize the protein signal, a chemiluminescent reagent

(CYANAGEN) was utilized following manufacturer protocol and the membrane imaged using a Syngene G: BOX.

2.26. Stripping membrane

To allow re-probing of a PVDF membrane with a different antibody, the membrane was stripped following the manufacturer instructions using a stripping buffer (100 mM ß-mercaptoethanol, 2% SDS, 62.5 mM Tris-Hcl pH 6.7) for 30 minutes at 50 ˚C. Then the membrane was washed 3x with TBST buffer for 10 minutes to remove any trace of the stripping buffer an then re-blocked with blocking buffer (5% skimmed milk powder, 0.2% Tween-20, 1x TBS) for 1 hr at room temperature on a rocking platform. The membrane was then processed for western blot as before.

2.27. Differential centrifugation experiment for wildtype and mutant MHV-E C-terminal His tagged proteins.

A total of $2.5x10^6$ Sf9 cells were seeded in T25 flasks as monolayers and incubated for 1 hr to allow the cells to adhere to the flasks at room temperature. Then cells were infected with recombinant baculoviruses at high MOI and incubated for 72 hr at 27 C˚. The infected cells were harvested by loosening the monolayer into the media and collected by centrifugation at 4000 rpm / 20 minutes/ 4 ˚C. The cell pellets were resuspended with 500µl cold PBS and lysed by sonication for 10 min at 20 seconds' intervals with an 80% amplitude (Sonics, Vibra cell™). No detergent was used in these preparations. The cell lysates were centrifuged at low speed 10,000 rpm / 15 min / 4 ˚C using a bench top centrifuge to remove unbroken cells and large debris and the pelleted material kept as low speed (LS) pellets. The supernatants

were collected and centrifuged at high speed, 50,000 rpm/ 90 minutes/ 4 ˚C, using the Beckman TL-100 ultracentrifuge, and the supernatants and pellets were collected as high speed supernatants and pellets (HSP) respectively. Low speed pellet and high speed pellet were tested for the presence of MHV E by western blot as before.

Chapter 3 Bioinformatics analysis of S, M, E, nsp3, nsp4 and nsp6 proteins of MERS-CoV and MHV-CoV

3.1. Bioinformatics analysis of S, M, and E proteins of MERS-CoV and MHV-CoV

3.1.1 Introduction

Many proteins including viral proteins use an amphipathic helix for modulating membrane curvature, such as the M2 amphipathic helix in influenza virus and the alpha helix of Hepatitis C virus nonstructural protein 4B (Gouttenoire et al 2009; Antonny 2006; Rossman et al 2010). In this chapter bioinformatics analysis was carried out to investigate the presence of similar highly conserved regions in select coronavirus proteins to address their roles in modifying membrane curvature during viral fusion and fission processes. The AmphipaSeek program (Sapay, Guermeur and Deléage, 2006) was used to assess local amphipathy in the coronavirus membrane binding proteins S, M and E. The criteria used for identifying putative membrane-binding regions for further testing were that regions that earned high scores for amphipathicity were also highly conserved. This selection was performed on the basis that a functionally important region involved in membrane fusion is likely to show greater amino acid conservation than other regions, for example surface loops. The amino-acid sequences of 17 CoVs representing a phylogenetically diverse set of S, M, and E proteins were downloaded from NCBI GenBank. The multiple sequence alignment program Jalview V 2.9.0b2 (Waterhouse et al 2009), was utilized to align the 17 S, M and E proteins which together were derived from four genera, α, β, γ and δ coronaviruses. The proteins chosen showed less than 90% overall identity at the amino acid level. The initial protein dataset was also interrogated using NCBI Protein BLAST and Clustal Omega (Wheeler et al 2005;

Sievers et al 2011; McWilliam et al 2013; Li et al 2015) to minimize the chance of biasing the alignment toward well-chosen groups. After the initial automated alignment, the alignment of conserved regions was adjusted manually based on the locations of the homologous features that had already been proposed or demonstrated in the literature. The program TMHMM2.0 was used to predict transmembrane helices in the proteins (Krogh et al 2001). AmphipaSeek results were averaged across the alignments to better identify regions that might show high amphipathicity despite some variation at the amino acid level. In this way, AmphipaSeek was used to predict the amphipathic helices in the proteins (Sapay, Guermeur and Deléage, 2006) with amphipathy values ranging from 0= low to 5= high. A cutoff of >3 in the overall amphipathy average value was taken in addition to their high conservation. The total hydrophobicity for each of the identified peptides was also calculated using Kyte-Doolittle amino acid hydrophobicity values for individual amino acids (Kyte and Doolittle, 1982).

3.2. Alignment of spike proteins (S)

3.2.1. Results.

3.2.1.1. Fusion peptide

Fusion peptides have been described generally as sequences of 15-25 apolar amino acids. These regions interplay with membranes and initiate the fusion process between viral and cellular membranes (Earp et al 2005). They are classified into two types based on their location in the target protein; the first type is N-terminal and the second is internal (Lai et al 2005). It has been shown that within the same virus family there is a high level of conservation of such sequences, which is considered one of the characteristic properties of viral fusion peptides (Martin and Ruysschaert, 2000). In terms of precise sequence and location, fusion peptides (FP) have yet to

be defined for all coronaviruses, as recognition of the FP motif within the large spike protein can be difficult. However, bioinformatics analysis suggests that at least part of the fusion peptide is located near the N-terminus of S2 where a conserved motif with properties consistent with those expected of an FP occurs across the coronavirus family (Bosch and Rottier 2008). This is in keeping with the consensus view that the S fusion peptide should lie in the S2 domain, downstream of the S1/S2 boundary (Bosch, Bartelink and Rottier, 2008). For SARS CoV S, mutagenesis, structural and lipid mixing studies have suggested a motif SFIEDLLFNKVTLADAGF which is conserved across the coronavirus family and within which the core sequence IEDLLF demonstrates only infrequent and conservative replacements (Belouzard et al 2012; Madu et al 2009). The motif is not located at the N-terminus of HR1 as suggested in some S protein cleavage maps (e.g. (Du et al 2017) but immediately follows the second, S2' cleavage site originally mapped in SARS-CoV S and later in MERS CoV S (Belouzard, Chu and Whittaker, 2009; Millet et al 2016). A sequence which includes this motif has been shown directly for SARS-CoV to act as a fusion peptide when tested in an *in vitro* binding assay with multilamellar vesicles (MLVs) where it reorders membranes in a calcium dependent manner (Lai et al 2017). In contrast with other fusion peptides of other viruses such as Avian Leucosis Virus and Ebola virus, this proposed fusion peptide could be considered as an "internal" fusion peptide in the context of the complete S because it is only exposed following proteolytic cleavage of S (Bale et al 2011; Lai et al 2005; White et al 2008).

When the S2 subunit of S proteins was aligned for the 17 representatives of coronaviridae using JalviewV 2.9.0b2 (Waterhouse et al 2009) the results showed high conservation of different domains as shown in **Figure 3.1**. Highly conserved areas as well as high Amphipathic averages were chosen from the S2 subunit of

MERS-CoV and MHV-A59 as models to test their roles in fusion and membrane binding in this study. Other conserved regions were the heptad repeats of SARS-CoV (Xu et al 2004a; Xu et al 2004b; Zhu et al 2004) and MERS-CoV (Gao et al 2013) and acted as landmarks for the 17 CoV representatives and also showed a conservation at the amino acid level as shown in the **Figure 3.1**.

In addition, conserved regions were found at the C-terminus of the S2 subunit, comprising eight aromatic hydrophobic amino acids beginning at the transmembrane region and extending into the hydrophilic endodomain represented by KWPWWVWL **Figure 3. 1.** This region has been studied by Sainz et al, 2005 (Sainz, et al 2005) who, based on lipid vesicle binding, showed that it, along with the putative fusion peptide and the transmembrane anchors may provide a continuous hydrophobic surface in coronaviruses S that assists in viral fusion and entry. Sainz et al, 2005 also concluded that the result of this study was similar in principle to that for studies of Ebola GP2 and HIV gp41(Salzwedel, West and Hunter, 1999; Suarez et al 2000). These two domains have also been shown in many studies to be required for the recruitment of S protein by M protein during viral assembly, another function for which conservation would be expected (de Haan et al 1999; Godeke et al 2000; de Haan et al 2000).

The endodomain of S2 can been subdivided into two regions, a cysteine-rich region at the N-terminus and a carboxy-terminal region rich in charged residues (Bos et al, 1995; Chang, Sheng and Gombold, 2000; Kuo et al, 2000). It has been shown that clusters of cysteine residues are important for the palmitoylation of S (Yao, Masters and Ye, 2013). No particular cysteine residue is critical but in a study of fusion competence and replication in MHV coronavirus a total of at least 3 cysteine residues was required (Yang et al 2012) and other studies have confirmed that the

cysteine-rich region is necessary for syncytium formation during viral infection (Bos et al 1995; Bosch et al 2005; Chang et al 2000; Thorp and Gallagher 2004; Thorp et al 2006; Ye et al 2004). While membrane binding and deformation is clearly a property of the FP sequence, propelled into the membrane by the conformational changes in S, palmitoylation of S may serve to stabilize the protein during its interactions with lipid rafts in the target membranes to allow time for fusion to occur.

Figure 3.1: Multiple sequence alignment of coronavirus S2 subunit of spike protein. Jalview alignment of the amino acid sequences of 17 representative coronaviruses. Four genera of coronavirus are representing as follows: **α-CoV** is represented by HCOV-229E, Human coronavirus 229E (ABB90529.1); HCoV-NL63, Human coronavirus NL63 (YP_003767.1); TGEV-Purdue, transmissible gastroenteritis virus-Purdue

(ABG89335.1); FCoV, Feline coronavirus (AFH58021.1) M-BatCoV-HKU8, Miniopterus bat coronavirus Hong Kong University 8 (YP_001718612.1); PEDV, Porcine epidemic diarrhea virus, (NP_598310.1); **β-CoV** include, HCoV- HKU1, Human coronavirus Hong Kong University 1(ADN03339.1); Murine hepatitis virus-A59, MHV-A59 (NP_045300.1); Bat-CoV-HKU9, Bat coronavirus Hong Kong University 9 (YP_001039971.1); SARS-CoV, Severe acute respiratory syndrome coronavirus (NP_828851.1); MERS-CoV, Middle East respiratory syndrome coronavirus (AHX00731.1); **γ-CoV** include IBV, Infectious bronchitis virus (ADP06471.2); SW1, Sperm Whale coronavirus1 (YP_001876437.1); BdCoV-HKU22, Bottlenose dolphin coronavirus Hong Kong University 22 (AHB63508.1) **δ-CoV** consists of NHCoV-HKU19, Night-heron-coronavirus- Hong Kong University 19 (AFD29226.1); PorCoV-HKU15, Porcine coronavirus Hong Kong University 15 (AFD29187.1); MCoV-HKU13, Munia coronavirus Hong Kong University 13-3514, (YP_002308506.1). FP: Fusion peptide; HR1: Heptad repeat 1; HR2: Heptad repeat 2; PreTM: Pre-transmembrane region; TM: transmembrane domain. Blue colour represents hydrophobic amino acids (A, I, L, M, F, W, V); Red colour represents positive charge amino acids (K, R); Magenta colour represents negative charge amino acids (E, D); Green colour represents polar amino acids (N, Q, S, T); Pink colour represents cysteines (C); Orange colour represents glycines (G); Yellow colour represents prolines (P); Cyan color represents aromatic amino acids (H, Y); White colour represents any unconserved/gap.

3.2.1.2. MERS-CoV and MHV-A59 Spike derived peptides

The spike protein of MERS-CoV consist of 1353 amino acids with the S2 subunit starting at V877, while for MHV-A59 the spike protein contains 1324 amino acids and the S2 subunit begins at D859. Based on the bioinformatics analysis (above) several peptides from MERS-CoV and MHV-A59 S2 were chosen **Table 3.1** for future *in vitro* analysis based on their high conservation, by Amphipathy **Figure 3.2 and 3.3** coupled with TMHMM transmembrane region prediction (Krogh et al 2001).

Table 3.1: Selected peptides of MERS-CoV and MHV S2 subunit of spike proteins.

MERS & MHV- S2	Residues sequence	Residues	Amphipathic average	TMHMM.2 average	Total Hydrophobicity (Kyte and Doolittle, 1982)
MERS-FP	RSARSAIEDLLFDKV	884-898	3.3	0	-2.30
MERS S-HR1	ENQKLIANKFNQALG	992-1006	3.3	0	-10.7
MERS S-Highly conserved region	LAKDKVNECVKAQS	1098-1111	2.9	0	-8.2
MERS S-HR2	LTQINTTLLDLTYEM	1252-1266	2.7	0	3.5
MERS S Pre-TM	TYYNKWPWYIWLGFI	1290-1304	1.7	0.5	-5.6
MERS S-TM	AGLVALALCVFFILC	1305-1319	1.3	0.96	43.7
MERS S-cysteine rich motif	CTGCGTNCMGKLKCNRCC	1320-1337	2.1	0	-1.2
MHV S-FP	IRGRSAIEDLLFDKV	866-880	2.5	0	0.8

MHV S-HR1	ENQKMIASAFNNALG	968-982	3.7	0	-4.2
MHV S-highly conserved region	QAIEKVNECVKSQTT	1074-1088	3.7	0	-10.3
MHV S-HR2	EKLNVTLLDLTYEM	1222-1235	2.8	0	3.5
MHV S Pre-TM	EMYVKWPWYVWLLIG	1259-1273	1.8	0.5	7.7
MHV S-TM	LAGVAVCVLLFFICC	1274-1288	1.1	0.96	44.8
MHV S-cysteine rich motif	CTGCGSCCFKKCGNCC	1289-1304	2.9	0	6.3
M2-Infleunza (Positive control)	RLFFKCIYRFFEHGLKRG	44-62	2.5	0	-4.3
MERS S-Scrambled (Negative control)	AISLKFSAEVRDRDL		2.5	N/A	-2.3

Amphipathic average, TMHMM.2 average and total hydrophobicity for each peptide selected for further study. MERS S-FP: MERS-CoV spike -Fusion peptide; MERS S-HR1: MERS-CoV spike heptad repeat 1; MERS S-HR2: MERS-CoV spike heptad repeat 2; MERS S PreTM: MERS-CoV spike Pre- transmembrane region; MERS S-TM: MERS-CoV spike-transmembrane region. MHV S-FP: MHV spike-fusion peptide; MHV S-HR1: MHV spike -heptad repeat 1; MHV S-HR2: MHV spike-heptad repeat 2; MHV S PreTM: MHV spike Pre-transmembrane region.

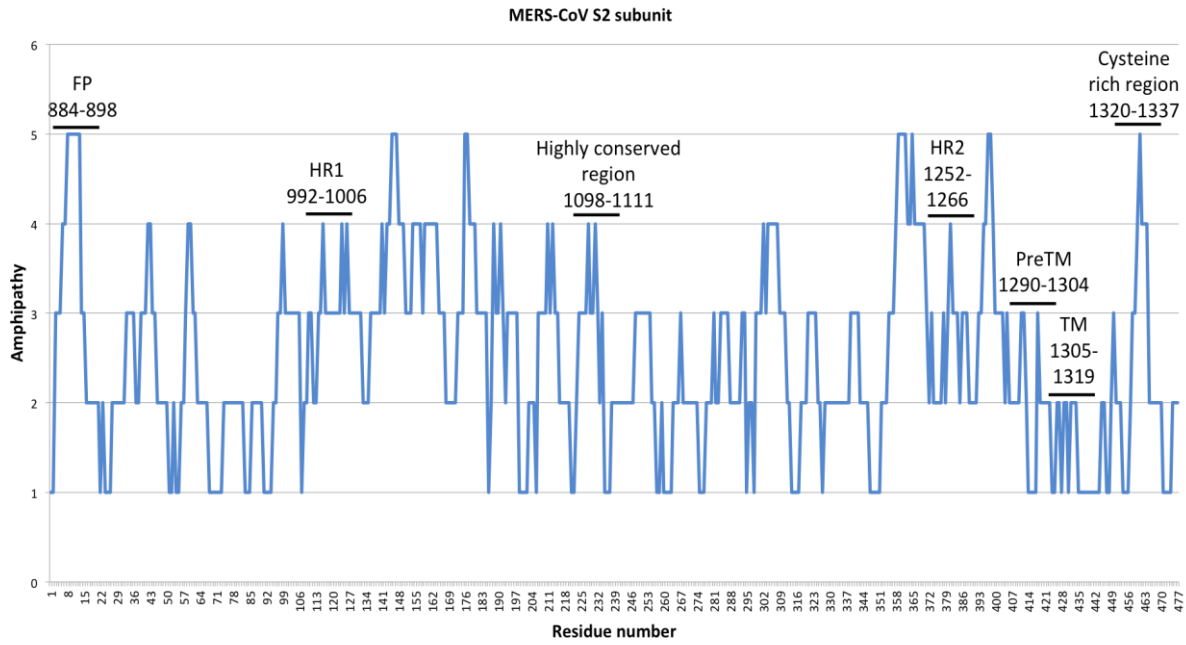

Figure 3.2: Amphipathic values of S2 subunit of MERS-CoV S protein. S2 subunit of MERS-CoV spike protein starts (877-1353 residues). The positions of the selected peptides are shown by the black bars. FP: Fusion peptide; HR1: Heptad repeat 1; HR2: Heptad repeat 2; PreTM: Pre-transmembrane region; TM: transmembrane region.

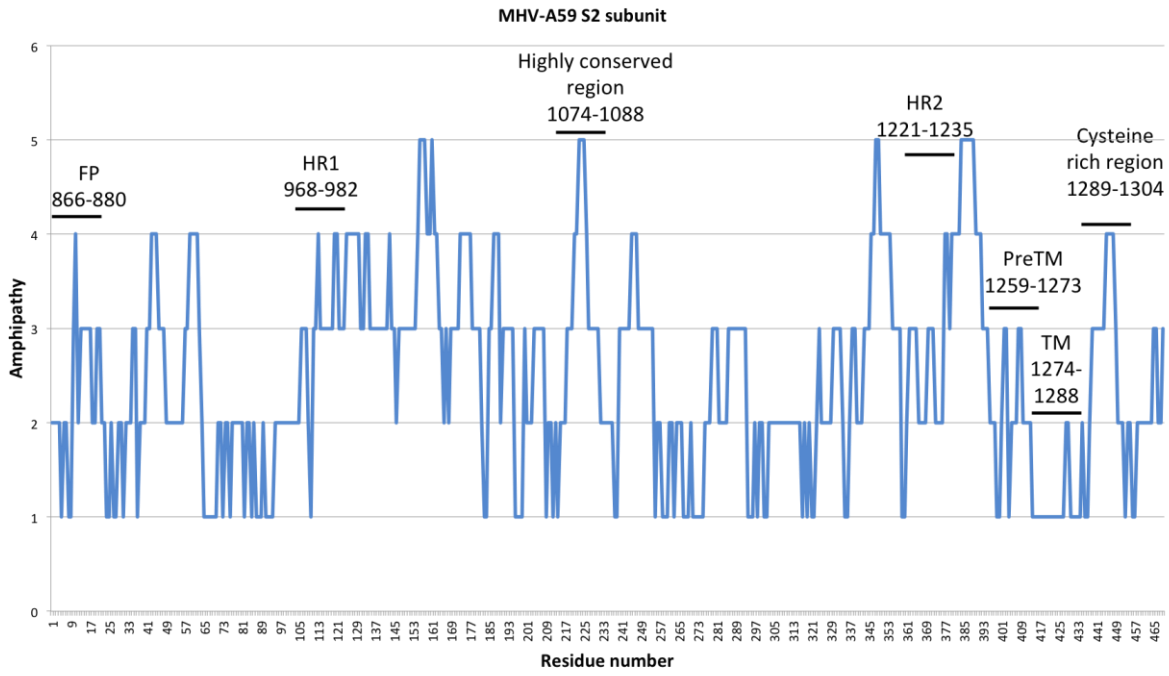

Figure 3.3: Amphipathic values of S2 subunit of MHV-A59 S protein. S2 subunit of MHV-A59 spike protein starts 859- 1324 residues. Positions of selected peptides are shown by the black bars. FP: Fusion peptide; HR1: Heptad repeat 1; HR2: Heptad repeat 2; PreTM: Pre-transmembrane region; TM: transmembrane domain.

3.3. Alignment of Membrane protein (M)

3.3.1. Results.

3.3.1.1. M proteins

The M protein structure is composed of an ectodomain, three transmembrane regions and a carboxy terminal domain leading to a topology of a N-terminal ecto- and *C*-terminal endo protein (Armstrong et al 1984; Voß et al 2009). An exception is transmissible gastroenteritis virus (TGEV) which has been reported to have two topologies, N-terminal exo and C-terminal endo or more uncommonly an N-terminal exo C-terminal exo orientation (Risco et al 1995; Escors et al 2002). Bioinformatics analysis shows that there is a highly conserved amphipathic region at the end of third transmembrane region of M protein in almost all the 17 CoV representatives **Figure 3.4**. It consists of 13 amino acids located at amino acids 114-126 (SWWSFNPETNNLM) in MHV-A59. The aligned sequence in MERS-CoV is (SWWSFNPETNCLL) and is situated at position 107-119. It has been reported that this conserved region is required for mediate M-M interactions and thus it assists in viral envelope formation (Arndt, Larson and Hogue, 2010).

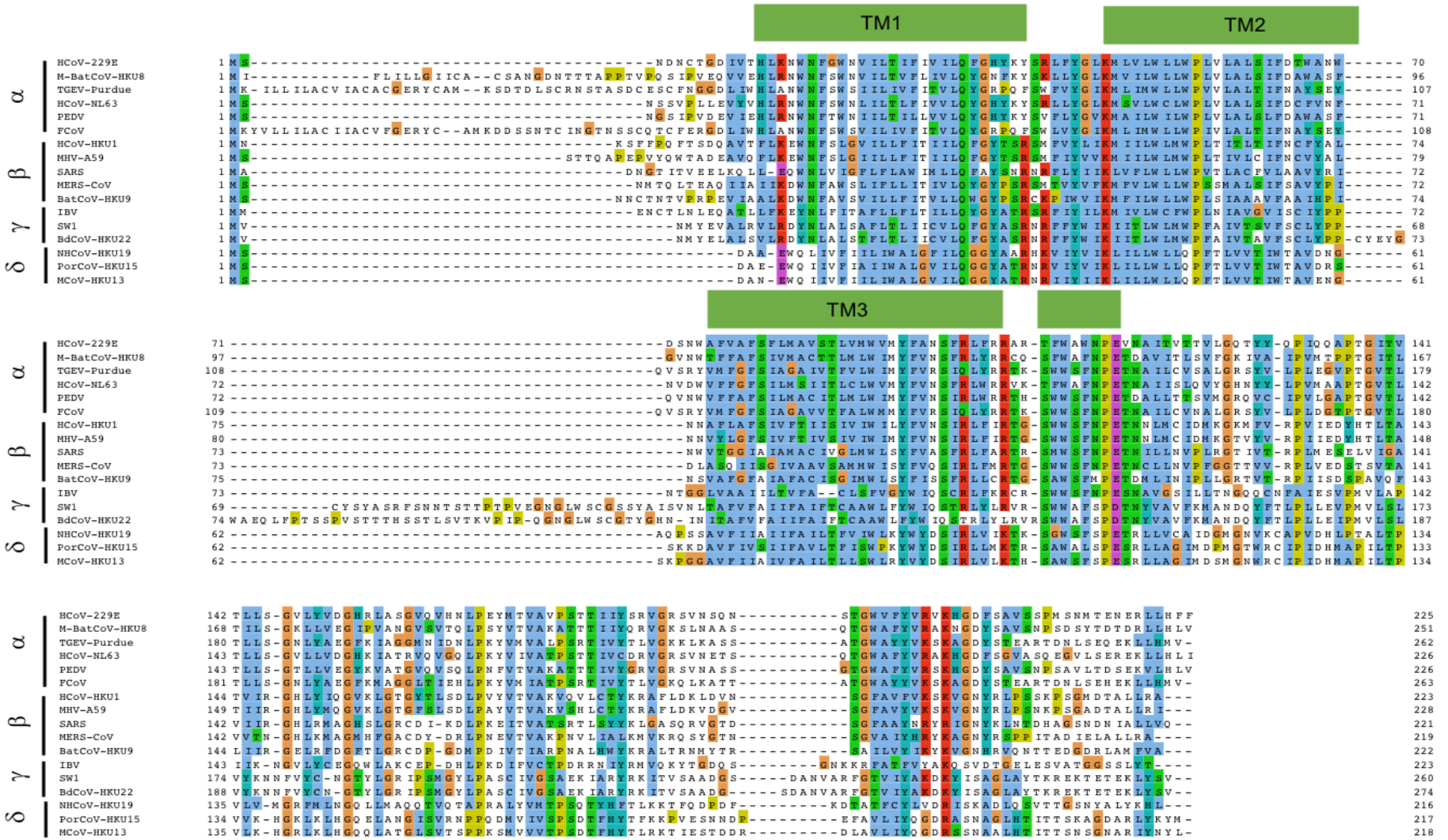
TM1
TM2
TM3
α
β
γ
δ
HCoV-229E
M-BatCoV-HKU8
TGEV-Purdue
HCoV-NL63
PEDV
FCoV
HCoV-HKU1
MHV-A59
SARS
MERS-CoV
BatCoV-HKU9
IBV
SW1
BdCoV-HKU22
NHCoV-HKU19
PorCoV-HKU15
MCoV-HKU13

Figure 3.4: Multiple sequence alignment of coronavirus M protein. Amino acid sequence alignment by Jalview 2.9.0b2 for the 17 representative coronaviruses. Four genera of coronavirus are representing as follows: **α-CoV** is represented by HCOV-229E, Human coronavirus 229E (AGW80952.1); M-BatCoV-HKU8, Miniopterus bat coronavirus Hong Kong University 8 (YP_001718615.1); TGEV-Purdue, transmissible gastroenteritis virus- Purdue (ABG89329.1); HCoV-NL63, Human coronavirus NL63 (YP_003770.1); PEDV, Porcine epidemic diarrhea virus (NP_598313.1); FCoV, Feline coronavirus (BAC01158.1); **β-CoV** include HCoV-HKU1, Human coronavirus Hong Kong University 1 (ADN03342.1); MHV-A59, Murine hepatitis virus-A59 (NP_045301.1); SARS, Severe acute respiratory syndrome (NP_828855.1); MERS-CoV, Middle East respiratory syndrome coronavirus (YP_009047210.1); BatCoV-HKU9, Bat coronavirus Hong Kong University 9 (YP_001039974.1); **γ-CoV** include IBV, Infectious bronchitis virus (ADP06463.2); SW1, Sperm Whale coronavirus (YP_001876439.1); BdCoV-HKU22, Bottlenose dolphin coronavirus Hong Kong University 22 (AHB63510.1) **δ-CoV** consists of NHCoV-HKU19, Night-heron-coronavirus-Hong Kong University 19, (AFD29228.1); PorCoV-HKU15, Porcine coronavirus Hong Kong University 15 (AFD29196.1); MCoV-HKU13, Munia coronavirus Hong Kong University13-3514 (YP_002308508.1). TM: transmembrane domain; green box indicates the conserved residues of amphipathic domain at the end of third transmembrane domain.

3.3.1.2. MERS-CoV and MHV-A59 M derived peptides

The MERS-CoV M protein contains 219 amino acids, while MHV-A59 M protein contains 228 amino acids. Both consist of a short ectodomain, three transmembrane domains and a long endodomain extending to the carboxy terminus. As described for the S protein, several peptides that could act as membrane modulators in the virus life cycle were selected from the MERS-CoV and MHV-A59 M protein sequences **Table 3.2** based on high conservation by Amphipathy (Sapay, Guermeur and Deléage, 2006) **Figures 3.5 and 3.6** and on the output of TMHMM transmembrane prediction (Krogh et al 2001).

Table 3.2: Selected peptides of MERS-CoV and MHV M proteins.

MERS & MHV- M	Residues sequence	Residues	Amphipathic average	TMHMM.2 average	Total hydrophobicity (Kyte and Doolittle, 1982)
MERS M-TM3	ASQIISGIVAAVSA	75-88	2.9	0.8	22.8
MERS M-Post TM3	ISYFVQSIRLFMRT	92-105	4.3	0.4	8.4
MERS M-Proline region	SWWSFNPETNCLLN	107-120	1.9	0	-6.8
MHV M-TM3	VYLGFSIVFTIVSI	82-95	2.4	0.9	31.5
MHV M-Post TM3	IMYFVNSIRLFIRT	99-112	4.2	0.4	13.7
MHV M-Proline region	SWWSFNPETNNLMC	114-127	1.9	0	-8.7

Amphipathic average, TMHMM.2 average and total hydrophobicity for each peptide. MERS M-TM3: MERS-CoV membrane protein transmembrane domain3; MERS M-Post TM 3: MERS-CoV membrane protein post-transmembrane region3; MERS M-Proline region: MERS-CoV membrane protein Proline region. MHV M-TM 3: MHV membrane -transmembrane domain; MHV M-Post-transmembrane region 3: MHV membrane post-transmembrane 3.

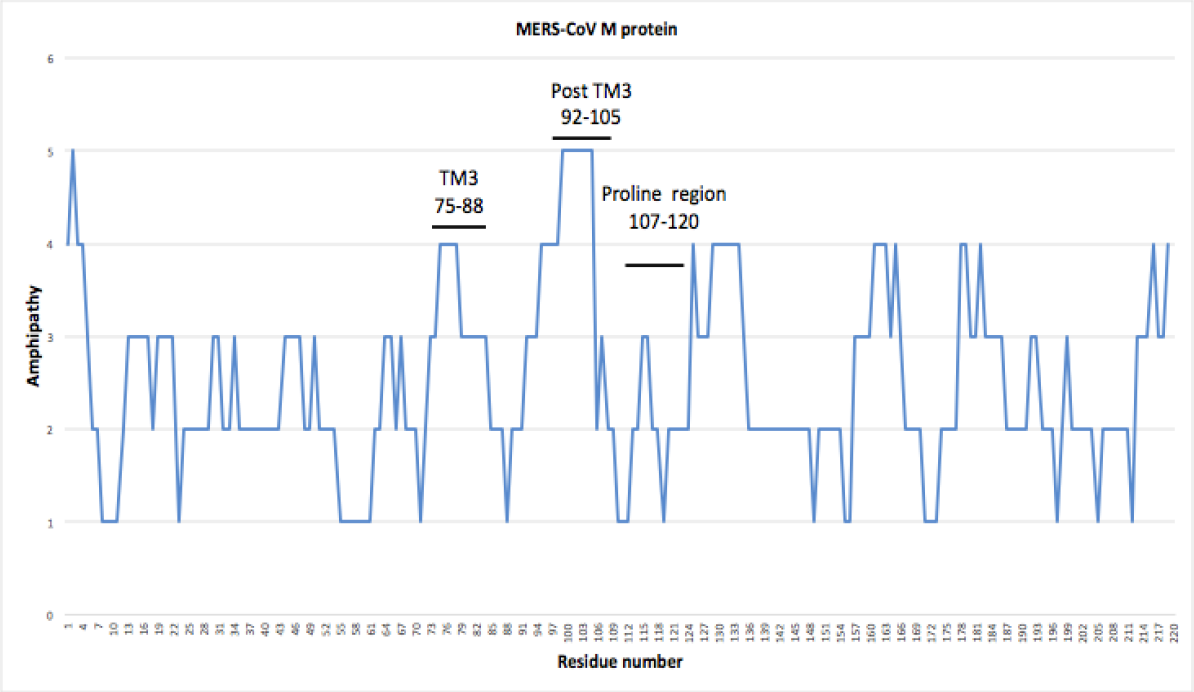

Figure 3.5: Amphipathic values of MERS-CoV M protein. Positions of selected peptides are indicated by the black bars. TM3: transmembrane domain 3; Post TM3: Post transmembrane region 3.

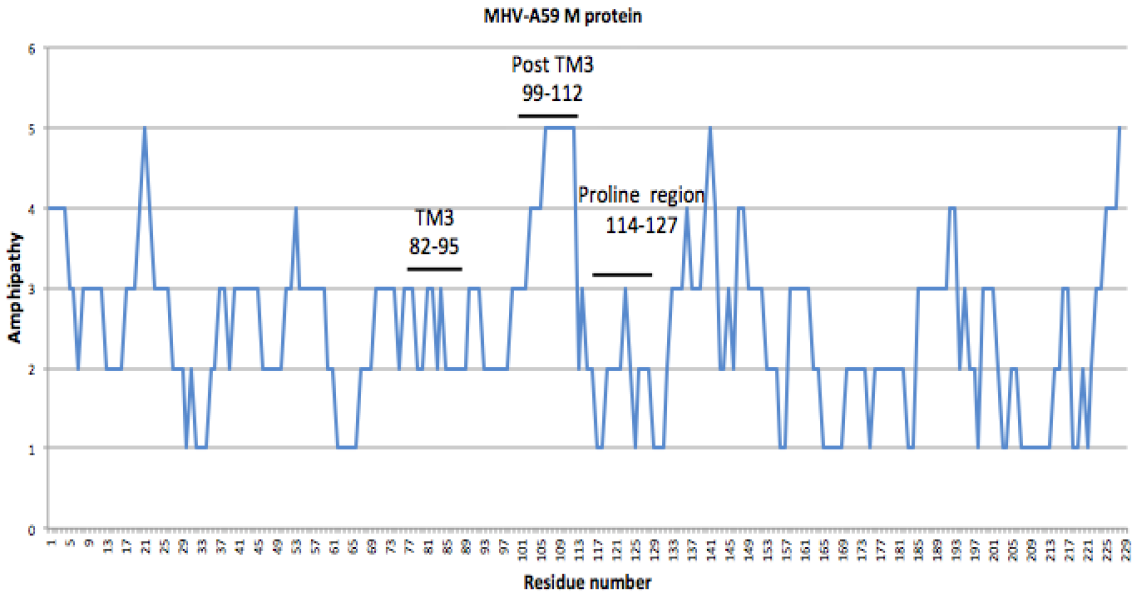

Figure 3.6: Amphipathic values for MHV-A59 M protein. Positions of selected peptides are indicated by the black bars. TM3: transmembrane domain3; PostTM 3: Post transmembrane region 3.

3.4. Alignment of Envelope protein (E)

3.4.1. Results.

3.4.1.1. E protein

Structurally the E proteins of coronaviruses are composed of a short N-terminal domain, long hydrophobic transmembrane domain and a carboxy terminal domain. Despite this there is a little homology among coronaviruses E proteins. Cysteine residues at the end of predicted transmembrane region seem to be the most conserved feature in all of the *Coronaviridae* (Torres et al 2007) **Figure 3.7**. It has been reported that these cysteines are palmitoylated intracellularly (Parthasarathy et al 2012; Lopez et al 2008) and that palmitoylation aids the contact between the lipid bilayer and E protein in ERGIC/ Golgi compartment (Joseph and Nagaraj, 1995). Conformational flexibility could also be important for interactions between E-E or between E and other proteins. In addition, palmitoylation might lead to aggregation of E protein on specific lipid microdomains and this could be significant during vesicle formation or virus assembly, specifically during transport of the mature virus to the cell boundaries. There are also conserved proline residues in the carboxy tail of the protein (Lopez et al 2008). These residues are predicted to form a beta-stand hairpin and are significant as a Golgi complex targeting signal (Cohen, Lin and Machamer, 2011).

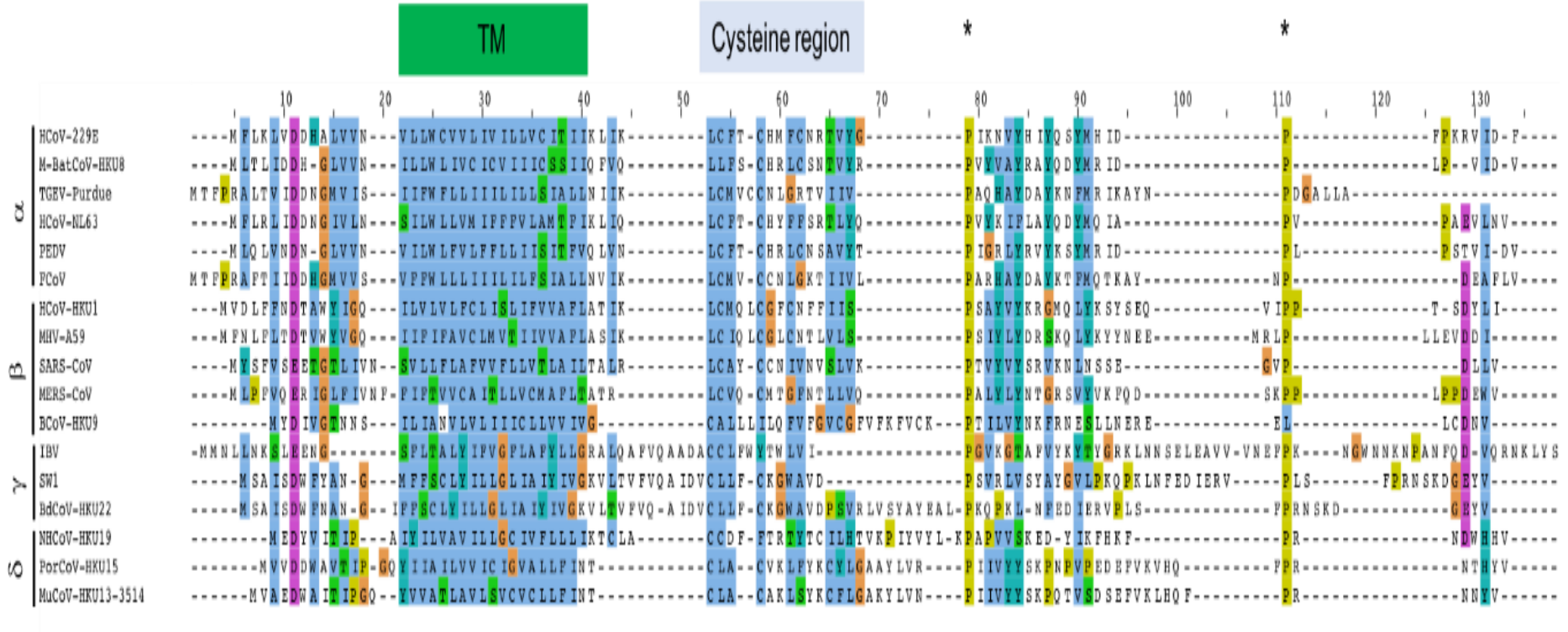
TM
Cysteine region
*
*
α
β
γ
δ
HCoV-229E
M-BatCoV-HKU8
TGEV-Purdue
HCoV-NL63
PEDV
PCoV
HCoV-HKU1
MHV-A59
SARS-CoV
MERS-CoV
BCoV-HKU9
IBV
SW1
BdCoV-HKU22
NHCoV-HKU19
PorCoV-HKU15
MuCoV-HKU13-3514

Figure 3.7: Multiple sequence alignment of coronavirus E proteins.

Alignment was done using Jalview software 2.9.0b2. Four genera of coronavirus are representing as follows: **α-CoV** is represented by HCOV-229E, Human coronavirus 229E (NP_073554.1); M-BatCoV-HKU8, Miniopterus bat coronavirus Hong Kong University 8 (YP_001718614.1); TGEV-Purdue, transmissible gastroenteritis virus- Purdue (ABG89336.1); HCoV-NL63, Human coronavirus NL63 (YP_003769.1); PEDV, Porcine epidemic diarrhea virus (NP_598312.1); FCoV, Feline coronavirus (YP_004070197.1); **β-CoV** include HCoV-HKU1, Human coronavirus Hong Kong University 1(YP_173240.1); MHV-A59, Murine hepatitis virus-A59 (NP_068673.1); SARS-CoV, Severe acute respiratory syndrome coronavirus (NP_828854.1); MERS-CoV, Middle East respiratory syndrome coronavirus (YP_009047209.1); BCoV-HKU9, Bat coronavirus Hong Kong University 9 (YP_001039973.1); **γ-CoV** include IBV, Infectious bronchitis virus (ADP06512.1); SW1, sperm Whale coronavirus 1(YP_001876438.1); BdCoV-HKU22, Bottlenose dolphin coronavirus Hong Kong University 22 (AHB63482.1); **δ-CoV** consists of NHCoV-HKU19, Night-heron-coronavirus- Hong Kong University 19 (AFD29227.1); PorCoV-HKU15, Porcine coronavirus Hong Kong University 15(YP_005352832.1); MCoV-HKU13, Munia coronavirus Hong Kong University 13-3514(YP_002308507.1). TM: transmembrane domain; highly conserved cysteine residues indicated; conserved proline indicated by stars.

3.4.1.2. MERS-CoV and MHV-A59 E derived peptides

The amino acid sequence of MERS-CoV E protein is 82 amino acids long while that of MHV-A59 contains 83 amino acids. MERS-CoV E protein has four cysteine residues, the first being situated at position of 23 in the hydrophobic domain and the rest are located at positions 30, 40, and 43. The conserved cysteine residues in MHV-A59 E protein are located at 23, 40, 44 and 47. Several peptides for further study from MERS-CoV and MHV-A59 E were selected **Table 3.3** based on their high level of conservation following bioinformatics analysis as well as the outputs of Amphipathy (Sapay, Guermeur and Deléage, 2006) **Figures 3.8 and 3.9** and TMHMM transmembrane region prediction (Krogh et al 2001).

Table 3.3: Selected peptides of MERS-CoV and MHV E proteins.

MERS & MHV-E	Residues sequence	Residues	Amphipathic average	TMHMM.2 average	Total hydrophobicity (Kyte and Doolittle, 1982)
MERS E-TM	FIFTVVCAITLLVCM	17-31	1.7	0.99	42.1
MERS E-Post TM	TLLVQPALYLYNTGR	49-63	2.9	0.2	3.7
MHV E-TM	IIFIFAVCLMVTIIV	16-30	1.6	0.99	50
MHV E-Post TM	LVLSPSIYLYDRSKQ	50-64	2.5	0.4	-1.9

Amphipathic average, TMHMM.2 average and total hydrophobicity for each peptide selected. MERS E-TM: MERS-CoV envelope protein transmembrane region. MERS E-PostTM: MERS-CoV envelope protein Post-transmembrane region. MHV E-TM: MHV-A59 envelope protein transmembrane domain; MHV E-PostTM: MHV-A59 envelope protein Post-transmembrane region.

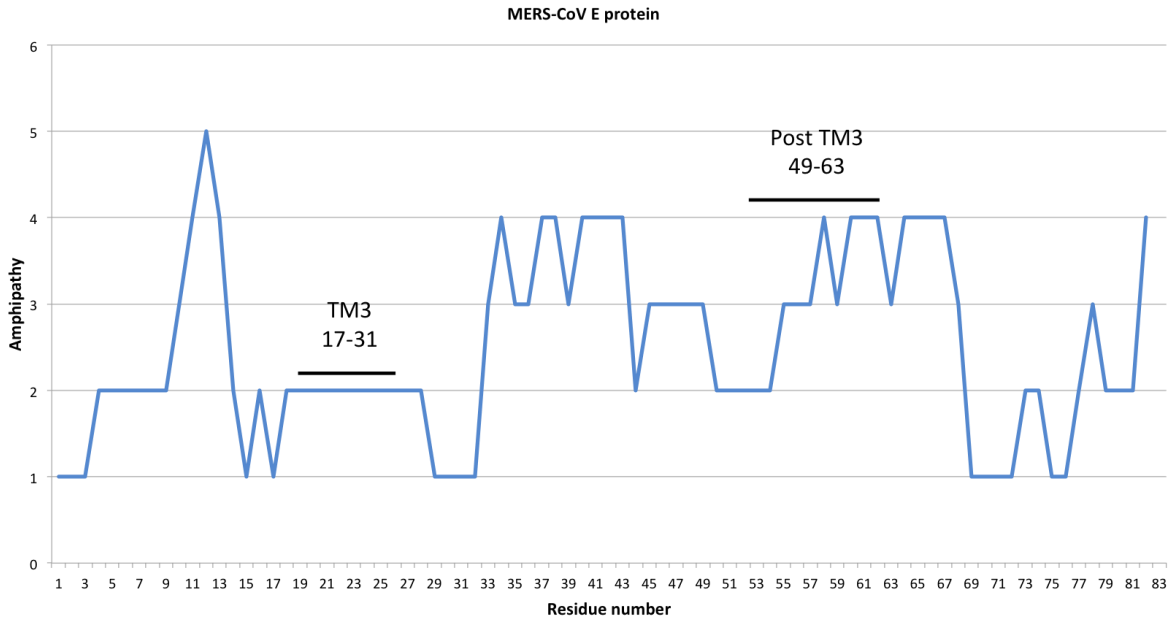

Figure 3.8: Amphipathic values of MERS-CoV E protein. Positions of selected peptides are indicated by black bars. TM: transmembrane domain; Post TM: Post-transmembrane domain.

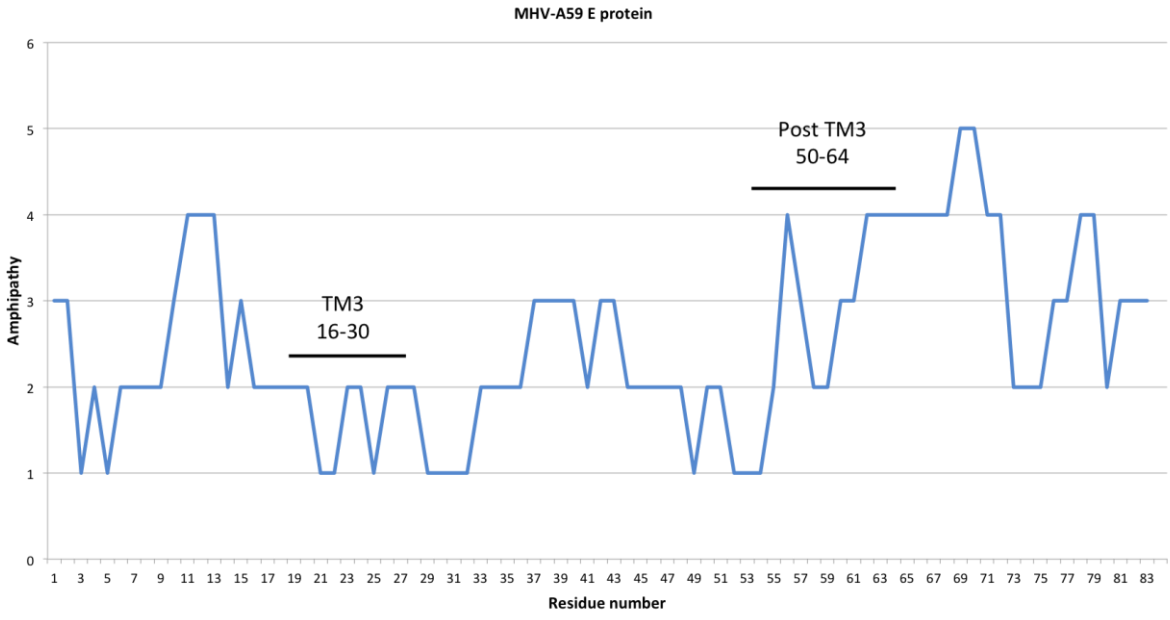

22

Figure 3.9: Amphipathic values of MHVA59- E protein. Positions of selected peptides are indicated by black bars. TM: transmembrane domain; PostTM: Post-transmembrane domain.

3.5 Bioinformatics analysis of nsp 3, 4, and 6 proteins of MERS-CoV and MHV-CoV

3.5.1 Introduction

The coronavirus nsp 3, 4, and 6 proteins have fundamental functions in the rearrangement of the membranes that are essential for the creation of replicative structures and in establishment of the viral replication-transcription complexes (RTCs) (Hagemeijer et al 2011). All have transmembrane regions that are probably significant for virus-induced membrane modifications (Baliji et al 2009; Kanjanahaluethai et al 2007; Lee et al 1991). In addition, forming the double-membrane vesicles has been shown following expression of only nsp3, nsp4 and nsp6 (Neuman et al 2014). Bioinformatics analyses of these nsp proteins were carried out as before to investigate highly conserved regions that could modify membranes during viral replication. The amino-acid sequences nsp3, nsp4, and nsp6 proteins of 30, 32, and 33 CoVs respectively representing four genera of coronaviruses were downloaded from NCBI GenBank and aligned using Jalview V 2.9.0b2 (Waterhouse et al 2009). A cutoff of less than 90% overall identity at the amino acid level was taken, again using NCBI Protein BLAST and Clustal Omega (Wheeler et al 2005; Sievers et al 2011; McWilliam et al 2013), to reduce the chance of biasing the alignment toward well-chosen species. The alignment was trimmed manually and TMHMM2.0 was used to predict the transmembrane helices in the proteins (Krogh et al 2001). As before AmphipaSeek was used to predict the amphipathic helices in the proteins (Sapay, Guermeur and Deléage, 2006) .

3.5.2 Alignment of nonstructural protein 3 (nsp3)

3.5.2.1 Results.

3.5.2.2. Nsp3

It has been shown that the nonstructural protein 3 (nsp3) of CoVs is an integral membrane protein that is co-translationally inserted into the endoplasmic reticulum (Kanjanahaluethai et al 2007). Nsp3 has two transmembrane helices (Ziebuhr, Thiel and Gorbalenya, 2001). It is the largest multi domain nsp with a molecular mass of about 200 kDa. It is characterized by distinct domain organization in different CoV genera (Neuman, 2016) and has many functions ascribed to it. Scaffolding is one of nsp3s' functions, it interacts with itself and other viral non-structural proteins and host proteins, e.g. antagonizing antiviral proteins such as p53 in SARS infected cells (von Brunn et al 2007; Pan et al 2008; Imbert et al 2007; Pfefferle et al 2011; Ma-Lauer et al 2016). In addition, nsp3 is crucial for RTC development (van Hemert et al 2008; Angelini and Akhlaghpour 2013).

Bioinformatics analysis of the 30 coronaviruses showed that the membrane spanning features of nsp3-TM were conserved in all viruses. MHV-A59 nsp3 comprises 2005 amino acids (Coley et al, 2005) while MERS nsp3 contains 1887 residues and several peptides from nsp3 of MERS-CoV and MHV-A59 were selected as model to test their membrane binding function with GUVs later in this study **Figure 3.10, Table 3.4**.

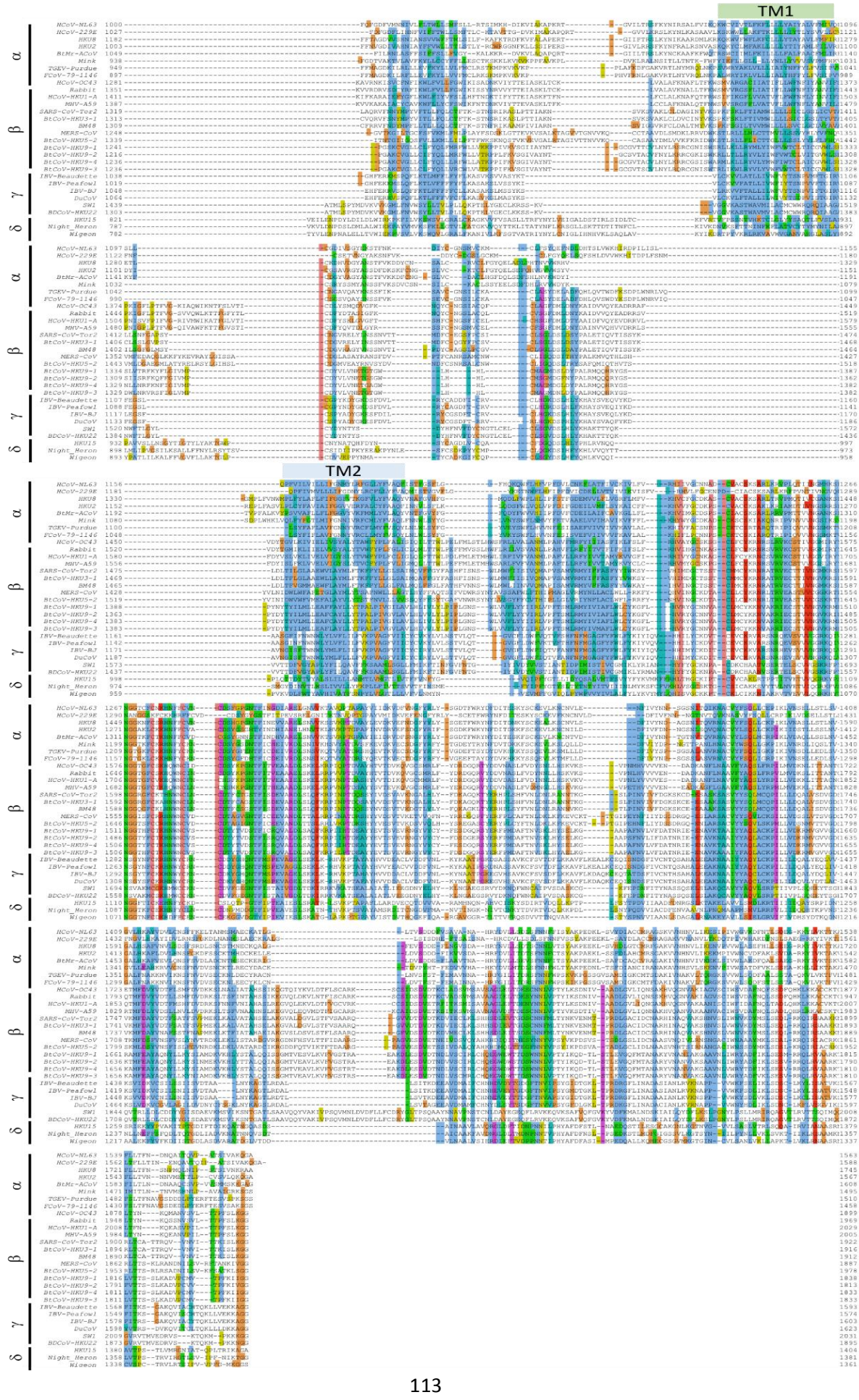
TM1
TM2
α
β
γ
δ

Figure 3.10: Multiple sequence alignment of coronavirus nsp3 proteins spanning the TM region. Amino acid sequence alignment was generated by Jalview 2.9.0b2 for the 30 representatives of coronaviruses. Four genera of coronavirus are representing as follows: **α-CoV** is represented by HCoV-NL63, Human coronavirus NL63 (GenBank accession number YP_003766.2); HCOV-229E, Human coronavirus 229E (NP_073549.1); HKU8, Hong Kong University 8 (YP_001718610.1); HKU2, Hong Kong University 2 (ABQ57238.1); BtMr-ACoV, BtMr-Alpha coronavirus (YP_009199608.1); Mink, Mink coronavirus strain WD1133 (ADI80522); TGEV virulent Purdue, transmissible gastroenteritis virus-Purdue (ND_058422.1); FCoV, Feline coronavirus (YP_239353) ; **β-CoV** include HCoV-OC43, Human coronavirus OC43 (NP_937947); Rabbit-HKU14, Rabbit-Hong Kong University 14 (AFE48811.1); HCoV-HKU1, Human coronavirus Hong Kong University 1-A (YP_173236.1); MHV-A59, Murine hepatitis virus-A59 (NP_068668.2); SARS-CoV-Tor2, Severe acute respiratory syndrome strain Tor2 (AAP41036); BtCoV-HKU3-1,Bat coronavirus Hong Kong University 3-1(P0C6F8.1); BM48, Bat coronavirus BM48 (YP_003858583); MERS-CoV, Middle East respiratory syndrome coronavirus (K9N7C7.1); BtCoV-HKU5-2, Bat coronavirus Hong Kong University 5-2 (ABN108831.1); BtCoV-HKU9-1, Bat coronavirus Hong Kong University 9-1 (YP_001039970.1); BtCoV-HKU9-2, Bat coronavirus Hong Kong University 9-2 (ABN10918.1); BtCoV-HKU9-4, Bat coronavirus Hong Kong University 9-4 (ABN10934.1); BtCoV-HKU9-3, Bat coronavirus Hong Kong University 9-3 (ABN10926.1); **γ-CoV** include IBV-Beaudette, Infectious bronchitis virus-Beaudette strain (NP_066134.1); IBV-Peafowl, Infectious bronchitis virus-Peafowl strain (AAT70073.1); IBV-BJ, Infectious bronchitis virus-BJ strain (AAP92673.1); DuCoV, Duck coronavirus (AKF17723.1); SW1, Sperm Whale coronavirus SW1 (YP_001876436.1); BdCoV-HKU22, Bottlenose dolphin coronavirus Hong Kong University 22 (AHB63507.1) **δ-CoV** consists of HKU15, Porcine coronavirus Hong Kong University 15 (YP_005352830); Night-Heron , Night-heron coronavirus-Hong Kong University 19 (YP_005352862); Wigeon, Wigeon coronavirus Hong Kong University 20 (YP_005352870.1). TM: transmembrane domain.

Table 3.4: Selected peptides of MERS-CoV and MHV of nsp3 protein.

MERS & MHV nsp3	Residues sequence	Residues	Amphipathic average	TMHMM average	Total hydrophobicity (Kyte and Doolittle, 1982)
MERS-nsp 3-1	VANDLTTALRRPINAT	1584-1600	4.3	0	-1.5
MERS-nsp 3-2	MFDSFVNSFVSLYN	1710-1723	3.7	0	8.3
MERS-nsp 3-3	SDALKRQIRIACRK	1843-1856	4.7	0	-10.2
MHV-nsp 3-1	AAADLSKELKRPVNP	1712-1726	4.3	0	-8.8
MHV-nsp 3-2	SLTSFVNAAHNSLK	1849-1862	3.7	0	1
MHV-nsp 3-3	VDAFNQLSADLQHR	1957-1970	3.1	0	-7.8

Amphipathic average, TMHMM.2 average and total hydrophobicity for each peptide are shown.

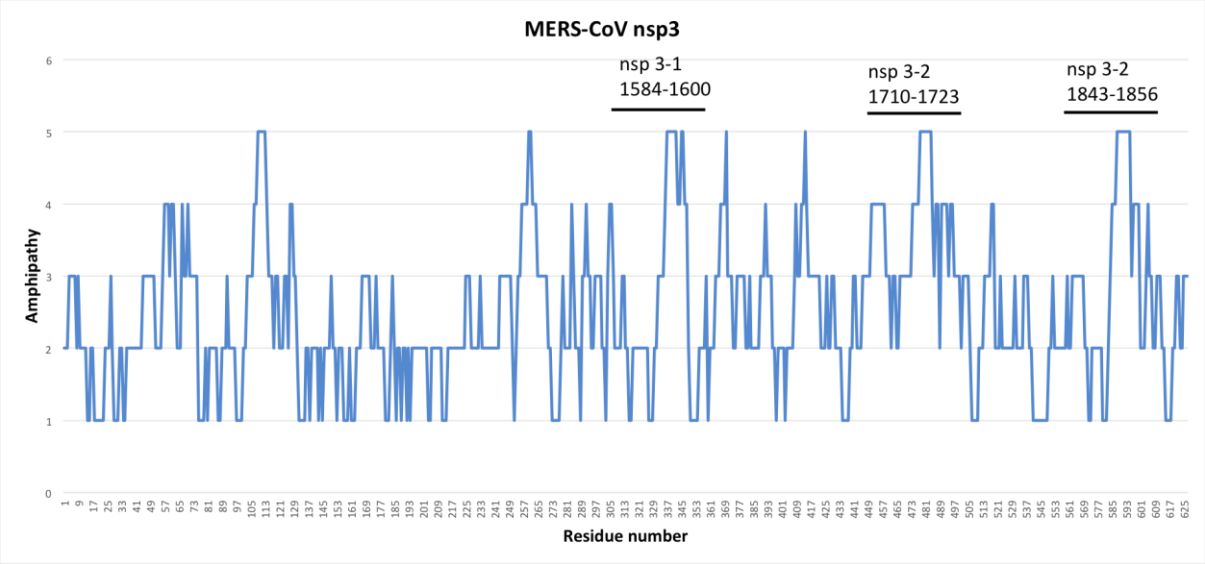

Figure 3.11: Amphipathic values of MERS-CoV nsp3 protein. Positions of selected peptides has been indicated by bar.

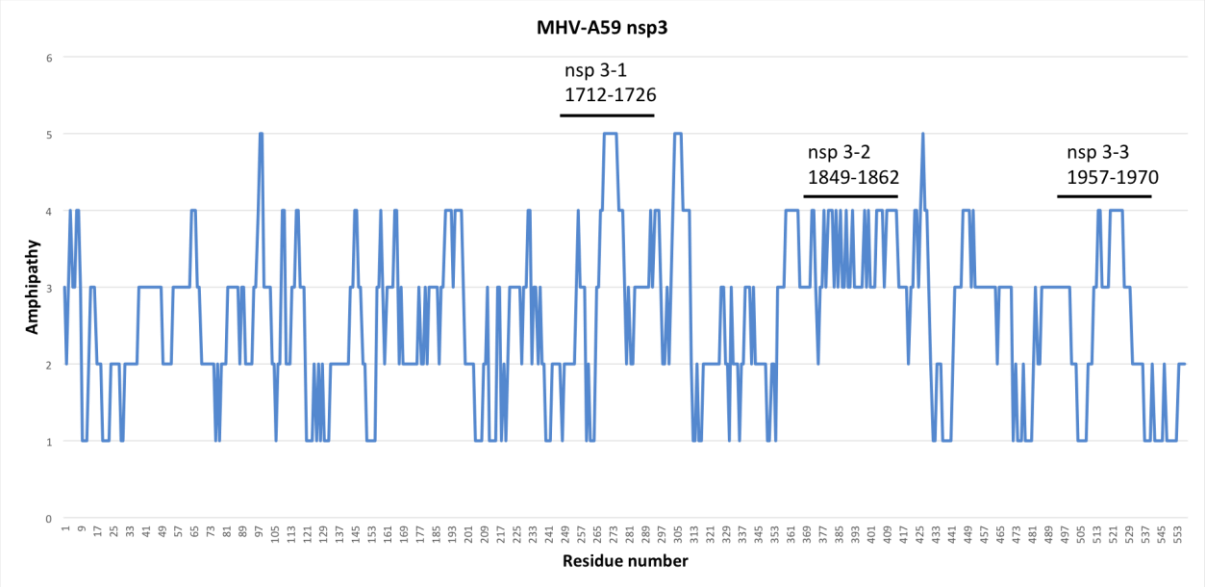

Figure 3.12: Amphipathic values of MHVA59- nsp3 protein. Positions of selected peptides has been indicated by bar.

3.5.3 Alignment of nonstructural protein 4 (nsp4)

3.5.3.1 Results.

3.5.3.2 Nsp4

CoV nsp4 is considered a transmembrane protein having four transmembrane regions and an internal C-terminal domain (Oostra et al 2007)**.** It has been shown that nsp4 is indispensable for double-membrane vesicle formation (Angelini et al 2013). The nsp4 domain of coronavirus is about 500 amino acids with MHV-A59 and MERS-nsp4 being 496 and 507 amino acids respectively.

Multiple sequence alignment of the 32 coronaviruses showed a similar membrane topology for nsp4 in most viruses. In addition, there is high conservation at the C-terminal in almost all viruses **Figure 3.13** as previously shown in (Xu *et al*, 2009). Several peptides from nsp4 of MERS-CoV and MHV-A59 were selected based on the same criteria as previously **Figures 3.14 and 3.15, Table 3.5**.


TM1
TM2
TM3
TM4
α
β
γ
δ

Figure 3.13: Multiple sequence alignment of coronaviruses nsp4 protein. Amino acid sequence alignment was performed by Jalview 2.9.0b2 for the 32 representatives of coronaviruses. Four genera of coronavirus are representing as follows: **α-CoV** is represented by HCoV-NL63, Human coronavirus NL63 (GenBank accession number YP_003766.2); HCOV-229E, Human coronavirus 229E (NP_073549.1); HKU2, Rhinolophus bat coronavirus Hong Kong University 2 (ABQ57238.1); BtMr-ACoV, BtMr-AlphaCoV (YP_009199608.1); HKU8, Miniopterus bat coronavirus Hong Kong University 8 (YP_001718610.1); Mink, Mink coronavirus strain WD1133 (ADI80522); TGEV-Purdue, transmissible gastroenteritis virus- Purdue (ND_058422.1) ; FCoV, Feline coronavirus (YP_239353); **β-CoV** include HCoV-OC43, Human coronavirus OC43 (NP_937947); MHV-A59, Murine hepatitis virus-A59(NP_068668.2); HCoV-HKU1, Human coronavirus Hong Kong University 1 (YP_173236.1); Rabbit-HKU14, Rabbit coronavirus Hong Kong University 14 (AFE48811.1); SARS-CoV-Tor2, Severe acute respiratory syndrome strain Tor2(AAP41036); BtCoV-HKU3-1,Bat coronavirus Hong Kong University 3-1 (P0C6F8.1); BM48, Bat coronavirus BM48-31 (YP_003858583); MERS-CoV, Middle East respiratory syndrome coronavirus (K9N7C7.1); BtCoV-HKU5-2, Bat coronavirus Hong Kong University 5-2(ABN108831.1); Erinaceus (YP_008719931.1) BtCoV-HKU9-1, Bat coronavirus Hong Kong University 9-1 (YP_001039970.1); BtCoV-HKU9-2, Bat coronavirus Hong Kong University 9-2 (ABN10918.1); BtCoV-HKU9-3, Bat coronavirus Hong Kong University 9-3 (ABN10926.1); BtCoV-HKU9-4, Bat coronavirus Hong Kong University 9-4 (ABN10934.1); **γ-CoV** include IBV-Beaudette, Infectious bronchitis virus (NP_066134.1); IBV-Peafowl, Infectious bronchitis virus (AAT70073.1); IBV-BJ, Infectious bronchitis virus (AAP92673.1); DuCoV, Duck coronavirus (AKF17723.1); SW1, Sperm Whale coronavirus SW1 (YP_001876436.1); BdCoV-HKU22, Bottlenose dolphin coronavirus Hong Kong University 22 (AHB63507.1); **δ-CoV** consists of Munia coronavirus Hong Kong University 13-3514 (YP_002308505); HKU15, Hong Kong University 15 (YP_005352830); Night-heron-coronavirus- Hong Kong University 19 (YP_005352862); Wigeon, Wigeon coronavirus Hong Kong University 20 (YP_005352870.1). TM: transmembrane domain.

Table 3.5: Selected peptides of MERS-CoV and MHV of nsp4 protein.

MERS & MHV nsp4	Residues sequence	Residues	Amphipathic average	TMHMM average	Total hydrophobicity (Kyte and Doolittle, 1982)
MERS-nsp 4-1	FIDIVRRLAVSLFQPIT	267-283	3	0	17.8
MERS-nsp 4-2	AYFSKKHVEVFTDG	402-415	2.7	0	-5.4
MERS-nsp 4-3	TNDAYSRFLGLFNKYK	444-459	3	0	-12.3
MHV-nsp 4-1	AFDLIHQVLGGLVRPID	259-275	4.4	0	12.8
MHV-nsp 4-2	SYCRKIGTEVRSDGTFE	394-410	3.2	0	-14.5
MHV-nsp 4-3	SDVAFNRYLSLYNK	432-445	2.7	0	-6.7

Amphipathic average, TMHMM.2 average and total hydrophobicity for each peptide has been calculated.

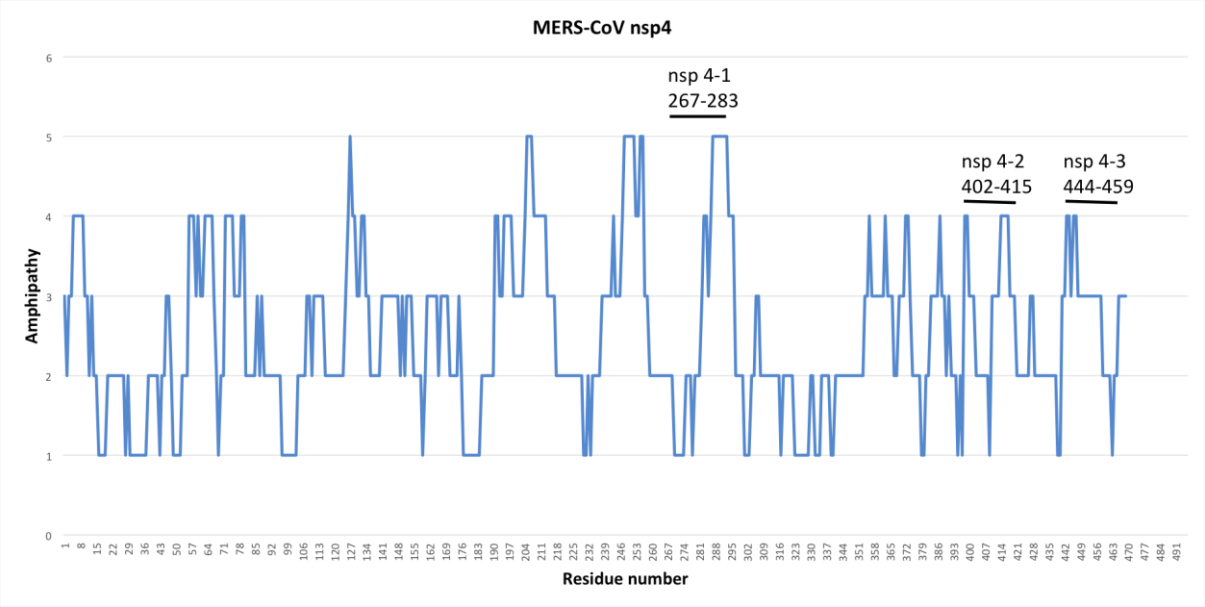

Figure 3.14: Amphipathic values of MERS-CoV nsp4 protein. Positions of selected peptides has been indicated by bar.

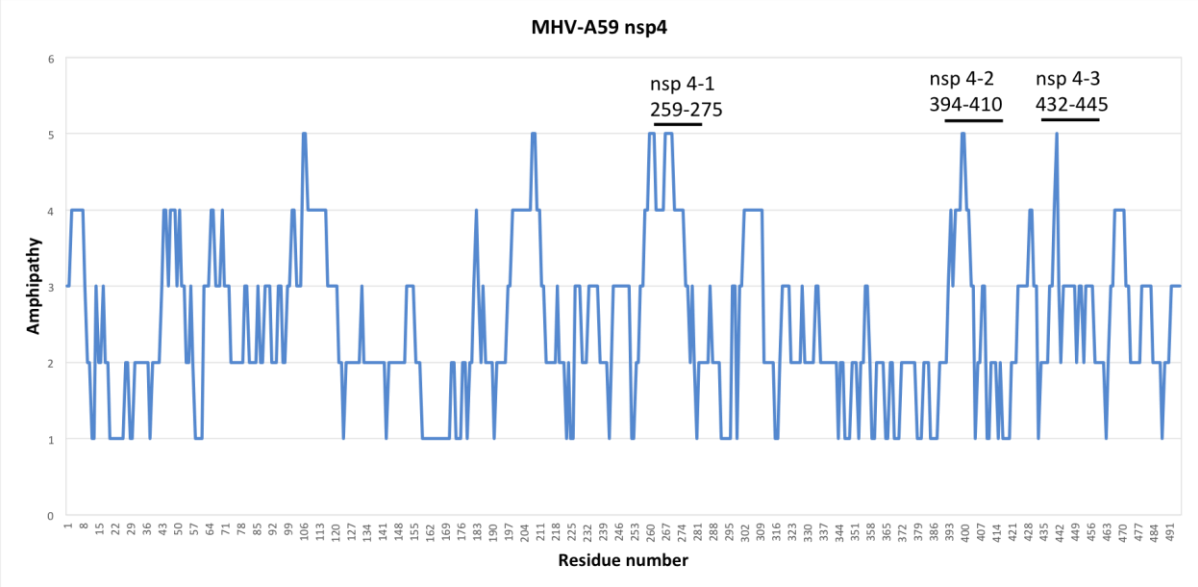

Figure 3.15: Amphipathic values of MHV-A59 nsp4 protein. Positions of selected peptides has been indicated by bar.

3.5.4 Alignment of nonstructural protein 6 (nsp6)

3.5.4.1 Results.

3.5.4.2. Nsp6

Coronavirus nsp6 has six transmembrane helices (Baliji et al 2009)**.** Bioinformatics analysis showed a similar membrane topology of nsp6 in almost all cases. In addition, there is high conservation at the C-terminal in almost all viruses **Figure 3.16** and as previously described by (Baliji et al 2009) suggested an important function for these domains in the viral life cycle. The sizes of nsp6 are around 300 amino acids with MHV-A59 and MERS nsp6 being 287 and 292 amino acids respectively. Baliji and his colleagues hypothesized that the conserved hydrophobic domain of nsp6 perhaps modified by palmitoylation, may have an essential function in the creation of protein-membrane or protein–protein interactions. Several peptides from nsp6 of MERS-CoV and MHV-A59 were selected as before **Table 3.6**. **Figures 3.17 and 3.18**.

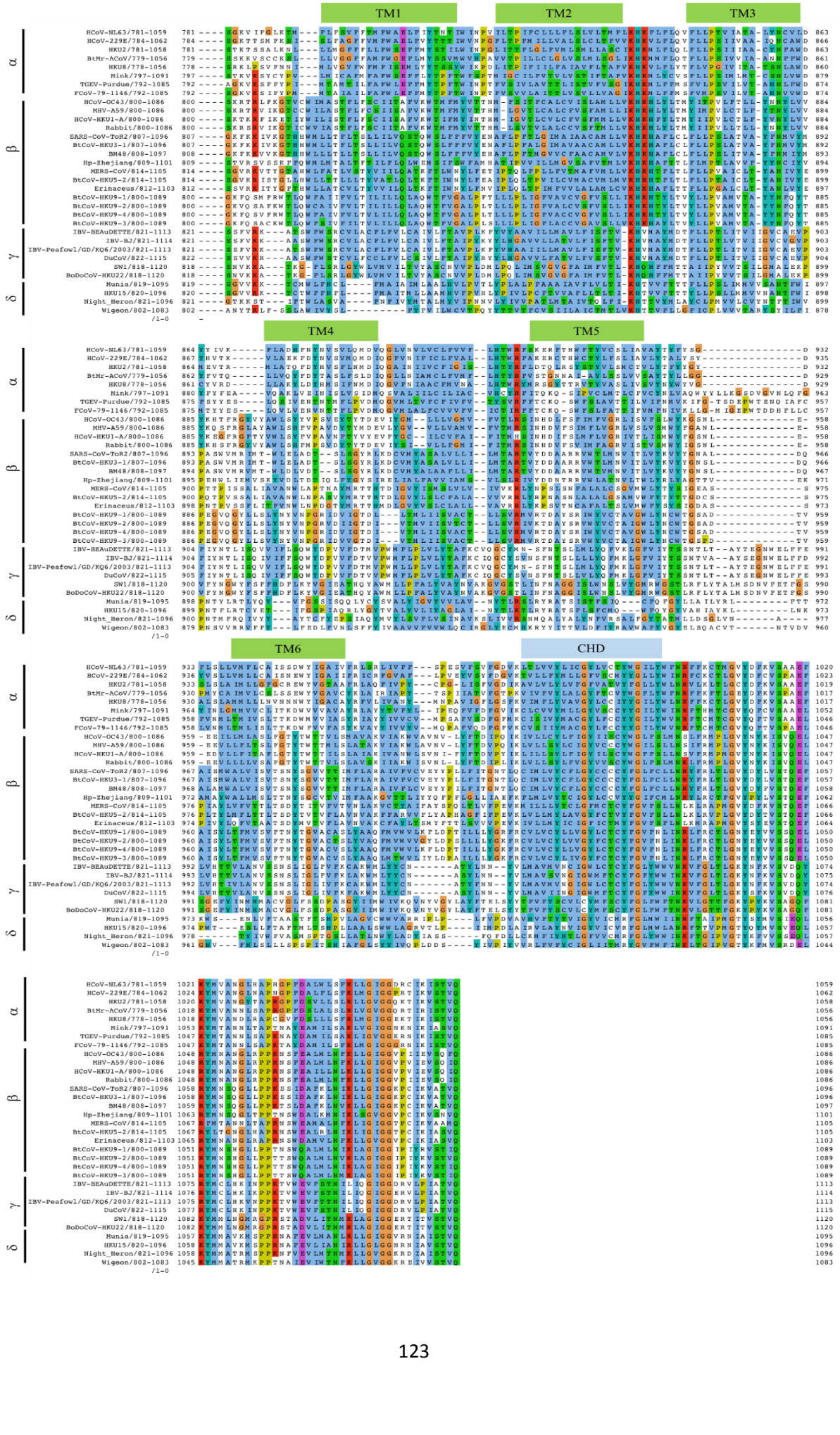
TM1
TM2
TM3
TM4
TM5
TM6
CHD
α
β
γ
δ

Figure 3.16: Multiple sequence alignment of coronaviruses nsp6 protein. Amino acid sequence alignment was performed by Jalview 2.9.0b2 for the 33 representatives of coronaviruses. Four genera of coronavirus are representing as follows: **α-CoV** is represented by HCoV-NL63, Human coronavirus NL63 (GenBank accession number YP_003766.2); HCOV-229E, Human coronavirus 229E (NP_073549.1); HKU2, Hong University coronavirus 2 (ABQ57238.1); BtMr-ACoV, BtMr-AlphaCoV (YP_009199608.1); HKU8, Hong University coronavirus 8 (YP_001718610.1); Mink, Mink coronavirus strain WD1133 (ADI80522); TGEV-Purdue, transmissible gastroenteritis virus-Purdue (ND_058422.1); FCoV, Feline coronavirus (YP_239353); **β-CoV** include HCoV-OC43, Human coronavirus OC43 (NP_937947); MHV-A59, Murine hepatitis virus-A59(NP_068668.2); HCoV-HKU1, Human coronavirus Hong Kong University 1 (YP_173236.1); Rabbit-HKU14, Rabbit coronavirus Hong Kong University 14 (AFE48811.1); SARS-CoV-Tor2, Severe acute respiratory syndrome strain Tor2 (AAP41036); BtCoV-HKU3-1,Bat coronavirus Hong Kong University 3-1(P0C6F8.1); BM48, Bat coronavirus BM48-31 (YP_003858583); MERS-CoV, Middle East respiratory syndrome coronavirus (K9N7C7.1); BtCoV-HKU5-2, Bat coronavirus Hong Kong University 5-2 (ABN108831.1); BtCoV-HKU9-1, Bat coronavirus Hong Kong University 9-1 (YP_001039970.1); BtCoV-HKU9-2, Bat coronavirus Hong Kong University 9-2 (ABN10918.1); BtCoV-HKU9-4, Bat coronavirus Hong Kong University 9-4 (ABN10934.1); BtCoV-HKU9-3, Bat coronavirus Hong Kong University 9-3 (ABN10926.1); **γ-CoV** include IBV-Beaudette, Infectious bronchitis virus (NP_066134.1); IBV-Peafowl, Infectious bronchitis virus (AAT70073.1); IBV-BJ, Infectious bronchitis virus (AAP92673.1); DuCoV, Duck coronavirus (AKF17723.1); SW1, Sperm Whale coronavirus SW1 (YP_001876436.1); BdCoV-HKU22, Bottlenose dolphin coronavirus Hong Kong University 22 (AHB63507.1); **δ-CoV** consists of Munia, Munia coronavirus Hong Kong University 13-3514 (YP_002308505); HKU15, Hong Kong University 15 (YP_005352830); Night-heron-coronavirus- Hong Kong University 19(YP_005352862); Wigeon, Wigeon coronavirus Hong Kong University 20 (YP_005352870.1). TM: transmembrane domain; CHD: conserved hydrophobic domain.

Table 3.6: Selected peptides of MERS-CoV and MHV of nsp6 protein.

MERS & MHV nsp6	Residues sequence	Residues	Amphipathic average	TMHMM average	Total hydrophobicity (Kyte and Doolittle, 1982)
MERS-nsp 6-1	NLKLRAPMGVYDFKVSTQ	234-251	2.3	0.03	-5.1
MERS-nsp 6-2	NLTAPRNSWEAMALNFK	260-276	2.5	0.04	-8.7
MHV-nsp 6-1	LSLLNSIFRMPLGVYNY	225-241	2.7	0.02	10.9
MHV-nsp 6-2	GLRPPRNSFEALMLNFK	255-271	2.6	0.05	-7.1

Amphipathic average, TMHMM.2 average and total hydrophobicity for each peptide has been calculated.

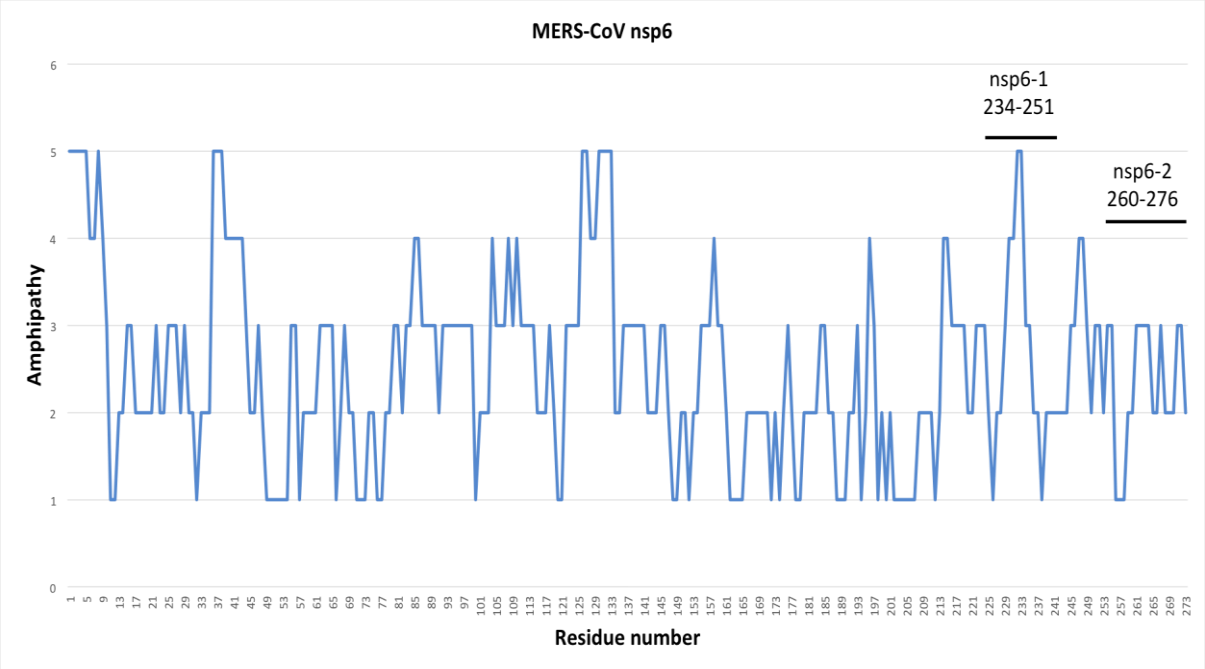

Figure 3.17: Amphipathic values of MERS-CoV nsp6 protein. Positions of selected peptides has been indicated by a bar.

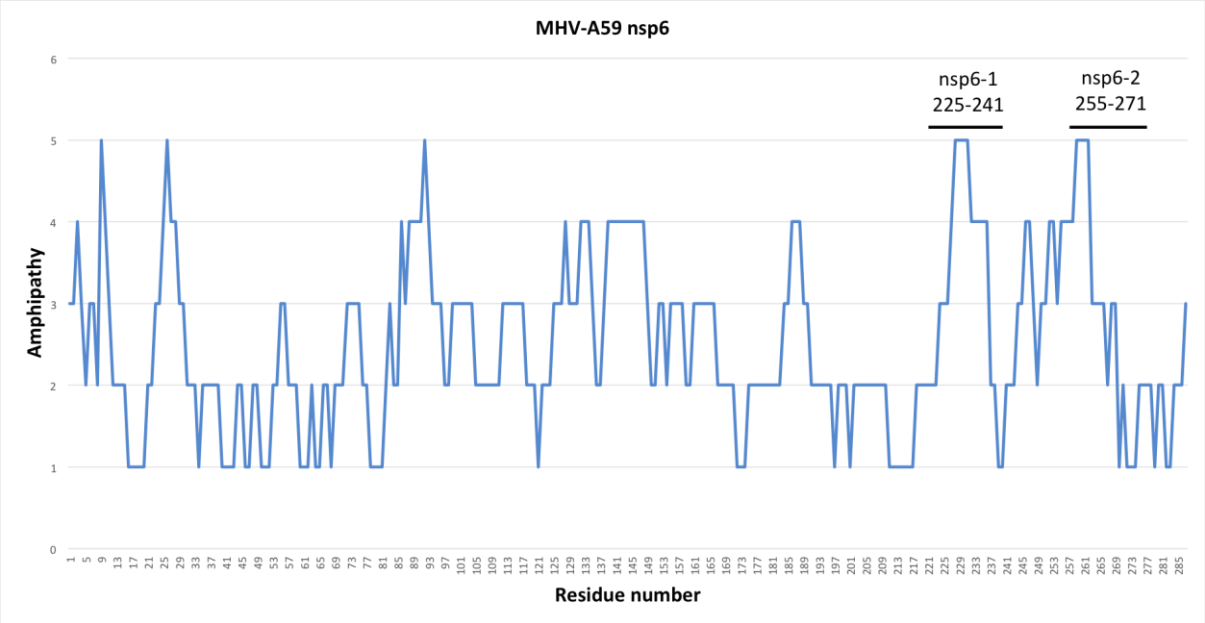

Figure 3.18: Amphipathic values of MHV-A59 nsp6 protein. Positions of selected peptides have been indicated by a bar.

4 Effect of structural and nonstructural MERS-CoV and MHV derived peptides on size and shape of GUVs.

4.1. Introduction

As outlined in chapters 1 and 3 mature coronavirus particle assembly requires protein-protein and protein-RNA interactions (Bos et al 1996; Vennema et al 1996; Godeke et al 2000) and during coronavirus infection all CoV structural proteins must interact with host cell membranes, specially during replication and assembly; ER membranes, the ERGIC compartment (Klumperman et al 1994; Hurst et al 2005) and eventually the secretory pathway where budding of the mature virions occurs (de Haan et al 2004; Perlman and Netland 2009). In addition, all coronaviruses modulate host cytoplasmic membranes for viral replication complex, or replication organelles (ROs) formation (Snijder et al 2006; Maier et al 2013; Zhou et al 2017). The membrane-interacting regions and mechanisms of membrane modification are therefore crucial for both understanding viral replication and for antiviral development. Some CoV proteins, nsp3, nsp4 and nsp6, are clearly characterized by membrane spanning regions and are considered the main drivers for directing the ROs (Angelini, Neuman and Buchmeier, 2014; Neuman, 2016).

Based on the bioinformatics analysis in chapter 3 several peptides from MERS-CoV and MHV-A59 were chosen for *in vitro* analysis based on their high conservation by Amphipathy coupled with TMHMM transmembrane region prediction. The peptides represent conserved and predicted amphipathic helices of MERS-CoV and MHV proteins S2, M, E, nsp3, nsp4, and nsp6. To assess their effect on the morphology and size of reconstituted GUV membranes, GUVs composed of 5 mM DPPC, 4 mM eggSM and 0.5 molar % cholesterol with 0.5% naphthopyrene were generated using the electroformation method as described in

chapter 2 section 2.7, reconstituted with the chosen peptide and imaged in a time-series of 0 min, 1 min, 2 min and 5 min using an EVOS-FL digital fluorescence microscope (EVOS, USA). The relative size and shape of the GUVs were measured as described before section 2.10.

4.1.1. Giant Unilamellar Vesicles (GUV)

Methods for comprehending interactions between proteins and lipids are fundamental to study biological structure function relationships. The complex composition of cellular membranes represented by different membrane proteins integrated within different complex lipid bilayers (Alberts and Bray 1994) has led to the design of various systems to study and understand them (Girard et al 2004). These systems depend on the formation of artificial vesicles consisting of stable self-assembled lipid bilayers that can, in some circumstances, be reconstituted with membrane proteins. They are called giant unilamellar vesicles (GUVs) (Rigaud, Pitard and Levy, 1995; De La Serna et al 2004; Girard et al 2004; Bouvrais et al 2008; Aimon et al 2011) and resemble biological cellular membranes both dynamically and structurally (Luisi, Walde and Oberholzer, 1999; Szostak, Bartel and Luisi, 2001). GUVs were originally characterized by Reeves and Dowben (Reeves and Dowben 1969) and later became more widely known. They are easy to visualize under optical microscopy due to their size which ranges from 1-100 μm (Bhatia et al 2015; Israelchvili 2010) and this allows a number of biological phenomena to be studied (Walde et al 2010). Vesicles are usually composed of different types of lipids either as a lipid mixture or a single lipid element from natural cell membranes (Rigaud, Pitard and Levy, 1995; De La Serna et al 2004; Girard et al 2004; Bouvrais et al 2008; Aimon et al 2011). Formation of the vesicles involves several steps

including lipid mixture dissolution in an organic solvent (Bhatia et al 2015), hydration of lipids as well as evaporation of the solvent leading to the formation of giant liposomes (Hishida, Seto and Yoshikawa, 2005; Horger et al 2009). There are several methods to generate GUVs, gentle hydration (spontaneous swelling or natural swelling) (Tsumoto et al 2009), electro swelling or electroformation (Angelova and Dimitrov 1986) and by stabilization of lipids or stabilizing surfactant water/oil emulsions (Pautot, Frisken and Weitz, 2003; Yamada et al 2006). Electroformation has been widely used for studying the interactions between proteins and lipids bilayers (Shimanouchi et al 2007; Carvalho et al 2008; Krishnan et al 2009; Yu et al 2009), understanding virus-like-particle membrane interaction (Ewers *et al*, 2010), studying reconstituted proteins with the membrane vesicles (Bacia et al 2004; Streicher et al 2009; Shaklee et al 2010) and exploring membrane budding and fission (Heuvingh, Pincet and Cribier, 2004; Baumgart et al 2007; Yu et al 2009). Fusion of small vesicles to form giant vesicles is considered another method to form GUVs (Wilschut et al 1980; Ohki and Arnold 2000), with the combination of vesicles with opposite charged lipids (Bailey et al 1997; Caponea et al 2008) after adding small molecules or fusogenic peptides (Pécheur et al 1998; Haluska et al 2006) although this method is complex (Walde et al 2010).

4.1.2. Solubility of the peptides

As the selected peptides in this study were hydrophobic, DMSO was chosen as an organic solvent to dissolve them (Yu and Quinn 1994). Some of these peptides dissolved completely in a buffer containing 0.1 mM sucrose, 0.1 mM glucose, and 0.5% DMSO, including WT MERS-putative FP and its mutants, MERS S-highly conserved region, MERS S-cysteine rich motif, MHV-FP, MHV S-highly conserved

region, MERS-HR2 and MHV E-PTM**.** However, several peptides had to be excluded from the study due to their poor solubility in many hydrophobic solvents including 100% DMSO, Dimethyl formamide (DMF) and ethanol. These peptides included a MERS-S scrambled fusion peptide which was to be used as a control along with MERS S-TM, MERS M-TM3, MERS E-TM, MHV S-TM and MERS nsp3-2. Additionally, others were excluded due to their appearance as a gel upon reconstitution such as MERS M-Post TM3C, which was to use as a control for MERS M-Post TM, see -**Table 4.1**.

Table 4.1: Insoluble peptides of MERS-CoV and MHV-CoV

No.	Name of the peptide	Residues	Residues sequence
1	MERS S-scrambled fusion peptide (control)		AISLKFSAEVRDRDL
2	MERS S- TM	1305-1319	AGLVALALCVFFILC
3	MERS M-TM3	75-88	ASQIISGIVAAVSA
4	MERS M-PTM3C scrambled peptide (control)		FRISIQVSLTFYMR
5	MERS E-TM	17-31	FIFTVVCAITLLVCM
6	MHV S- TM	1274-1288	LAGVAVCVLLFFICC
7	MERS-nsp3-2	1710-1723	MFDSFVNSFVSLYN

MERS S-TM- MERS-CoV spike protein transmembrane; MERS M-TM3- MERS-CoV membrane protein-transmembrane3; MERS M-PTM3C- MERS-CoV membrane protein- post transmembrane3 control; MERS E-TM- MERS-CoV envelope protein- transmembrane.

4.2. Effect of structural MERS-CoV and MHV derived peptides on size and shape of GUVs.

4.2.1. Results.

4.2.1.1 Effects of different DMSO concentration buffers on the size and shape of the GUVs.

As dimethyl sulfoxide (DMSO) was used in different concentration to dissolve the peptides in this study, it was necessary to control for the influence of the various DMSO concentration on the shape and size of GUVs. GUVs were generated by electroformation as described and treated with 10 µl buffer at 0.5%, 1%, 5%, 13%, 14.7%, 15%, 17% and 25.5% DMSO **Figure 4.1 A**. The relative size and shape of the GUVs were measured as described in chapter 2 section 2.10 **Figures 4.1 B and C**.

There was a statistically significant difference between the 0.5% DMSO buffer and 13%, 14.7%, 15%, 17% and 25.5% DMSO buffers on the size of the GUVs at all time points ($P < 0.01$; Linear Mixed Model), (Appendix 1) **Figure 4.1B**. However, there was no statistical difference between 0.5%, 1% and 5% DMSO buffers on the size of the GUV at all time points ($P > 0.05$; Linear Mixed Model), (Appendix 1) **Figure 4.1B**. This indicates that the 0.5%, 1% and 5% DMSO buffers concentration have no effect on the size of the GUV.

When tested for shape deformation, there was a statistically significant difference between 0.5% and 25.5% DMSO buffer on the shape of the GUV at time 1 and 5 min ($P < 0.01$, $P < 0.05$ respectively; Linear Mixed Model) but no significantly different at time 2 min ($P > 0.05$; Linear Mixed Model), (Appendix 2). There was no statistical difference between 0.5% DMSO buffer and 1%, 5%, 13%, 14.7%, 15%,

and 17% DMSO buffers on the shape of the GUVs at any time point ($P > 0.05$; Linear Mixed Model), (Appendix 2). Together the data show that a 5% DMSO concentration had no effect on either shape or size of GUV treated and was a suitable mobile phase for all subsequent peptide tests.

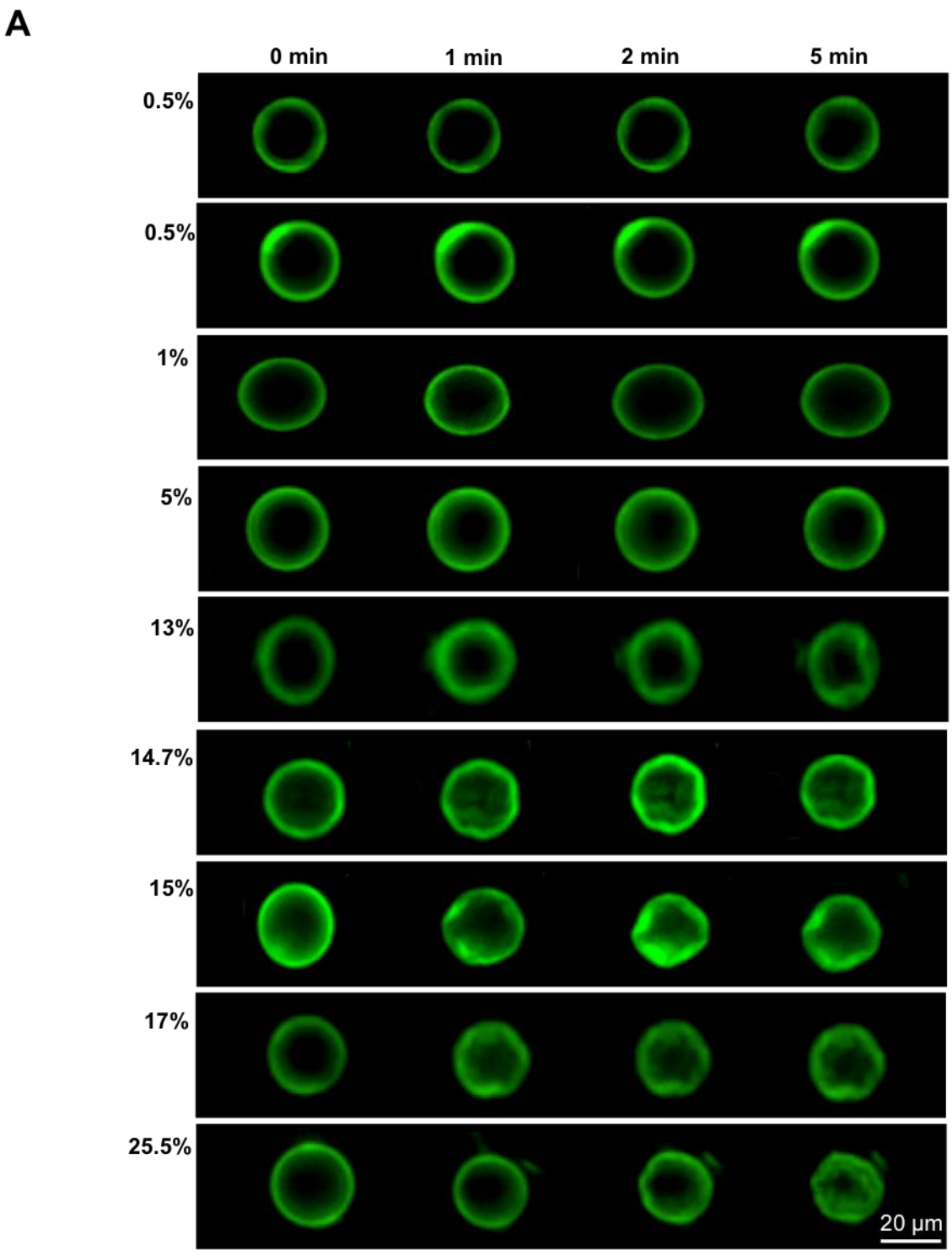
A
0 min
1 min
2 min
5 min
0.5%
0.5%
1%
5%
13%
14.7%
15%
17%
25.5%
20 µm

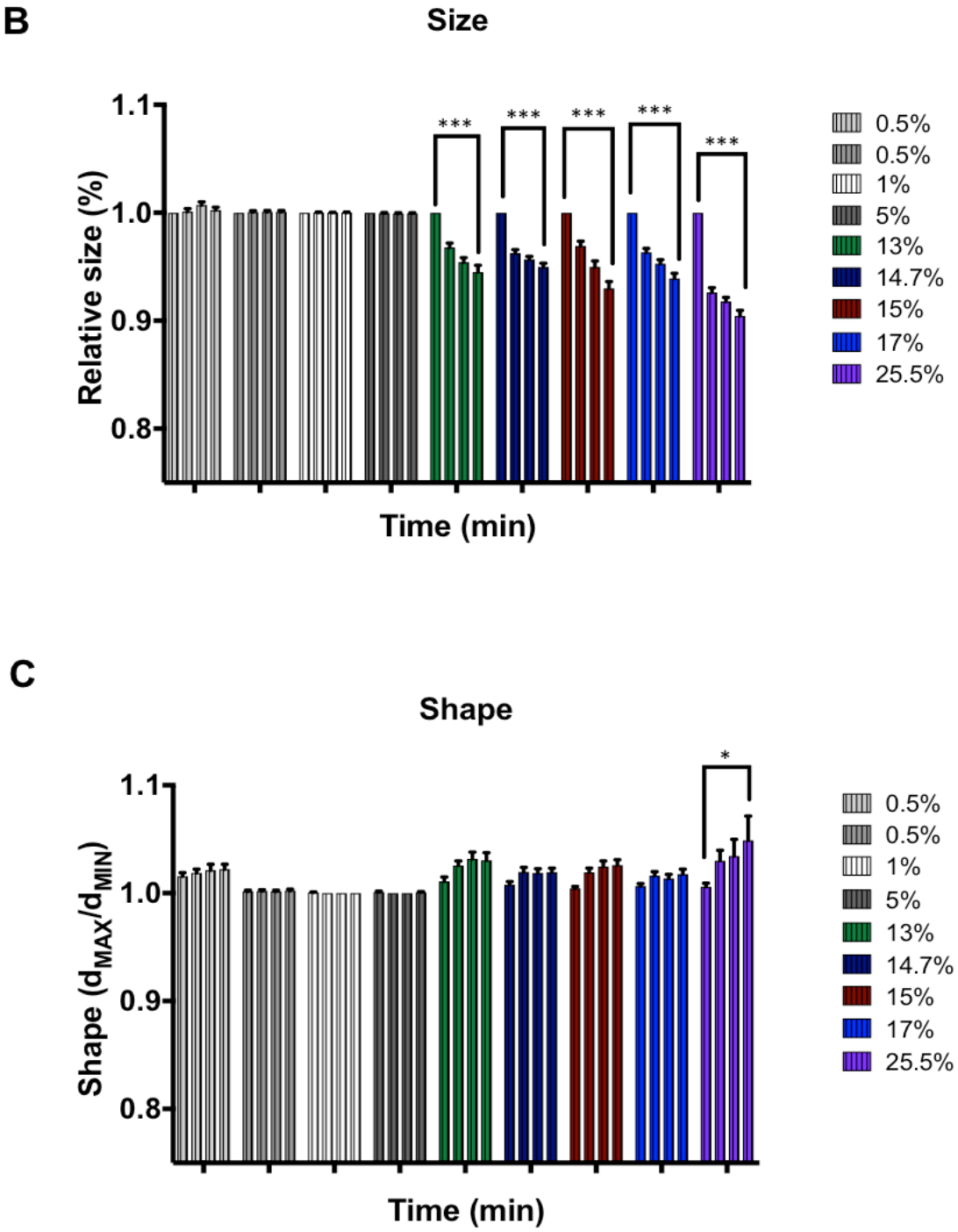

Figure 4.1: Effect of various DMSO concentration buffers on GUVs size and shape.

A- Fluorescent images of electroformed GUVs treated with corresponding DMSO buffer concentrations and imaged at 0 min, 1 min, 2 min and 5 min. **B-** GUV relative size. To measure the relative size of the GUVs, the perimeter is estimated by Ramanujan's first approximation, the effective diameter is the perimeter divided by π, the average standard deviation for both long and short measurements for a vesicle was also measured and averaged for each GUV for three separate experiments for 40 GUVs each. **C-** GUVs shape, to measure the shape of the GUVs, the ratio between longest and shortest radii were

measured and averaged for each GUV for three separate experiments for 40 GUVs each. The scale bar indicates 20µm. Error bars shown are mean ± SEM. * and *** indicate significance (P ≤ 0.05 or 0.001; with respect to the 0.5% DMSO buffer; Linear Mixed). Coloured key features of the tested buffers are marked. Each colored group of four columns represents the data for a single DMSO test at each time point, left to right, 0,1, 2 & 5 min. Some error bars are too small to be observed.

4.2.1.2 Effect of MERS and MHV S2 derived peptides on size and shape of GUVs.

To address the role and effect of predicted amphipathic helices of the chosen S2-derived peptides on the morphology and the size of reconstituted GUVs membrane. GUVs composed from 5 mM DPPC, 4 mM eggSM and 0.5 molar % cholesterol with 0.5% naphthopyrene were generated using the electroformation method as described and reconstituted with 10µM of MERS-FP, MERS-S highly conserved region (MERS-SHCR), MERS-S cysteine region (MERS-SC), MHV-FP, MHV-S highly conserved region (MHV-SHCR) in 0.5% DMSO buffer. In addition 10µM of MERS-HR1 and MERS-SPreTM were added in 5% DMSO buffer, and 10µM of MHV-HR1 in 25.5 % DMSO buffer. Finally, 0.5 µM of MERS-HR2, MHV-HR2, MHV-SPreTM and MHV-SC peptides in 1% DMSO buffer were assessed and all samples imaged by fluorescence microscopy **Figures 4.2 A & B**. Buffer only controls were treated in the same way. As a positive control peptide and to validate the GUVs assay, the M2-influenza peptide was chosen as it is a highly conserved amphipathic helix and is sufficient for budding into GUVs leading to the formation of large luminal vesicles (LUVs) (Rossman et al 2010). The size and the shape of GUVs were measured as before.

There was a statistically significant difference between MERS-FP and MHV-FP peptides and 0.5% DMSO buffer at all time points on the size of the GUV (P <0.01;

Linear Mixed Model) (Appendix 3). Additionally, there was a statistically significant difference between 0.5% DMSO buffer and MERS-SHCR on the size of the GUV at time 2 and 5 min ($P < 0.05$ and $P < 0.01$ respectively; Linear Mixed Model) (Appendix 3). This indicates that MERS-FP, MHV-FP, MERS-SHCR peptides have changed the size of the GUVs **Figures 4.2 A, B, C and E** (Appendix 3) while MERS-SC and MHV-SHCR showed no significant difference in size from the 0.5% DMSO buffer at all time points ($P > 0.05$; Linear Mixed Model) (Appendix 3) **Figures 4.2 A, B, C and E**. In addition, there was a statistically significant difference between 0.5% DMSO buffer and MERS-FP and MHV-FP at all time points on the shape of the GUV ($P < 0.01$; Linear Mixed Model) (Appendix 4) showing that they too deform GUV membranes **Figures 4.2 A, B, D and F**.

In contrast, MERS-SHCR, MERS-SC, MHV-SHCR peptides revealed no significant difference between any peptide and the 0.5% DMSO buffer control at all time points ($P > 0.05$; Linear Mixed Model) (Appendix 4) showing these peptides have no effect on the shape of the GUV **Figures 4.2 A, B, D and F**. M2-influenza peptide at 10µM concentration in 17% cholesterol and 0.5% DMSO buffer led to GUVs budding and forming LUVs, validating the assay.

MERS-HR1 and MERS-SPreTM were also tested at 10µM in 5% DMSO buffer and showed a statistically significant difference between control and MERS-HR1 peptide at all time points on the shape and size of the GUV **Figures 4.2 A, C, and D** ($P < 0.01$; Linear Mixed Model) (Appendix 5 and 6). MERS-SPreTM however showed no significant difference on the shape and size of the GUV ($P > 0.05$; Linear Mixed Model) (Appendix 5 and 6).

MHV-HR1 peptide was only soluble in 25.5% DMSO buffer so 10µM of MHV-HR1 was compared with a 25.5% DMSO buffer control **Figures 4.2 B** but showed no

statistical difference in size of GUVs at any time point (P >0.05; Linear Mixed Model) (Appendix 7). MHV-HR1 peptide thus appears to have no influence on the size of the GUVs, although the requirement for high DMSO concentration must be kept in mind **Figure 4.2 E**. However, there was a statistical significant difference in shape of GUV at time point 2 min (P <0.05; Linear Mixed Model) (Appendix 8) **Figures 4.2 B and F**.

4.2.1.3 Effect of MERS-HR2, MHV-HR2, MHV-SPreTM and MHV-SC peptides on size and shape of GUVs at 0.5 µM in 1% DMSO buffer.

MERS-HR2, MHV-HR2, MHV-SPreTM and MHV-SC peptides were dissolved in 1% DMSO buffer and 0.5µM of these peptides was tested compared with 1% DMSO buffer control.

There was no statistical difference in size of GUVs between MERS-HR2, MHV-HR2, MHV-SPreTM, MHV-SC and 1% DMSO buffer at all time points (P >0.05; Linear Mixed Model) (Appendix 9) **Figures 4.2 A, B, C and E**. This indicates that these peptides have no effect on the size of the GUV. The shape of the GUV was also measured after addition of these peptides. These data also revealed no statistical difference in shape of GUVs between these peptides and 1% DMSO buffer at all time points (P >0.05; Linear Mixed Model) (Appendix 10). However, MHV-SC showed a cup like shape. This indicates that MHV-SC may have the ability to permeabilize GUV's **Figures 4.2 A, B, D and F.**

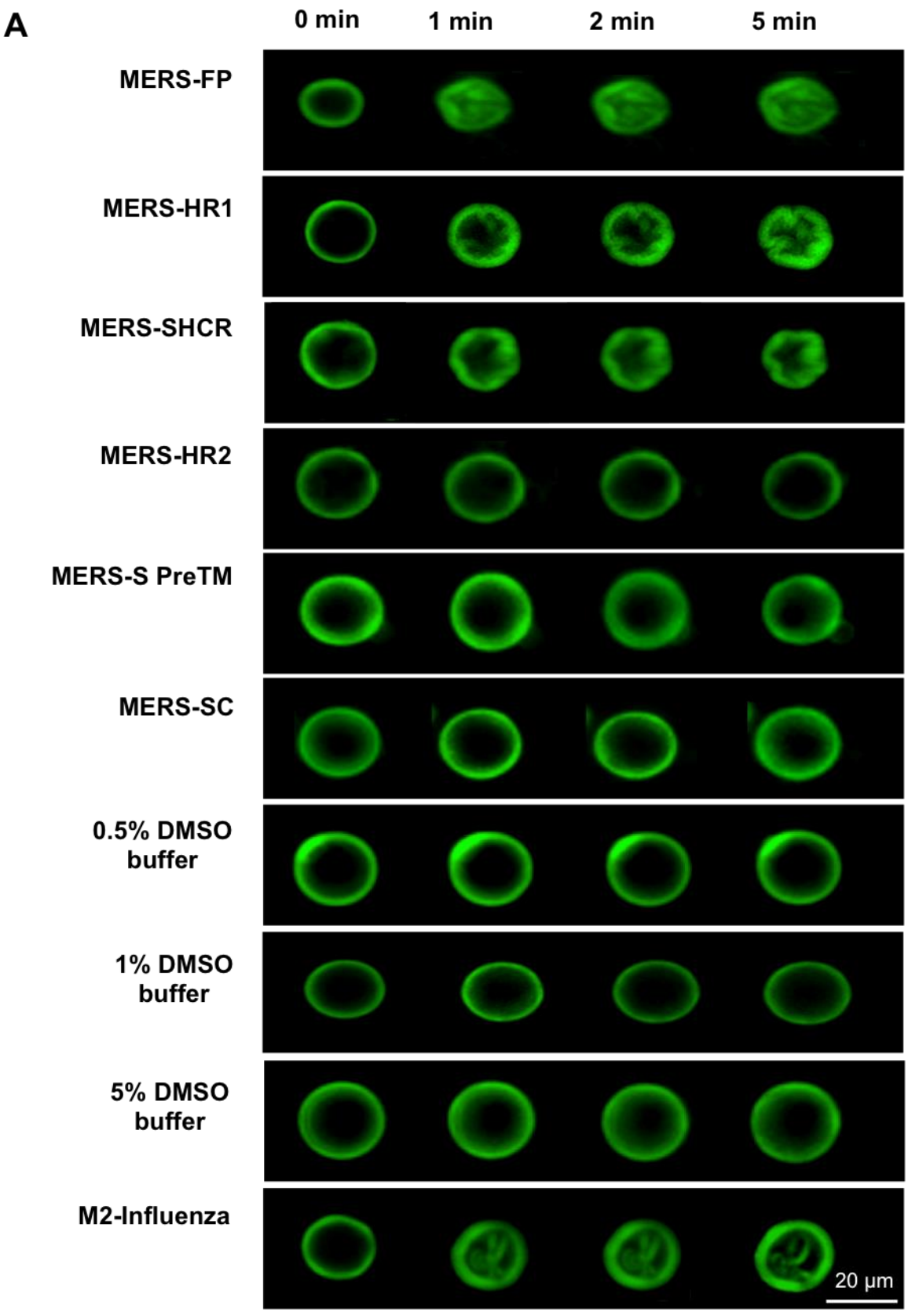
A
0 min
1 min
2 min
5 min
MERS-FP
MERS-HR1
MERS-SHCR
MERS-HR2
MERS-S PreTM
MERS-SC
0.5% DMSO buffer
1% DMSO buffer
5% DMSO buffer
M2-Influenza
20 μm

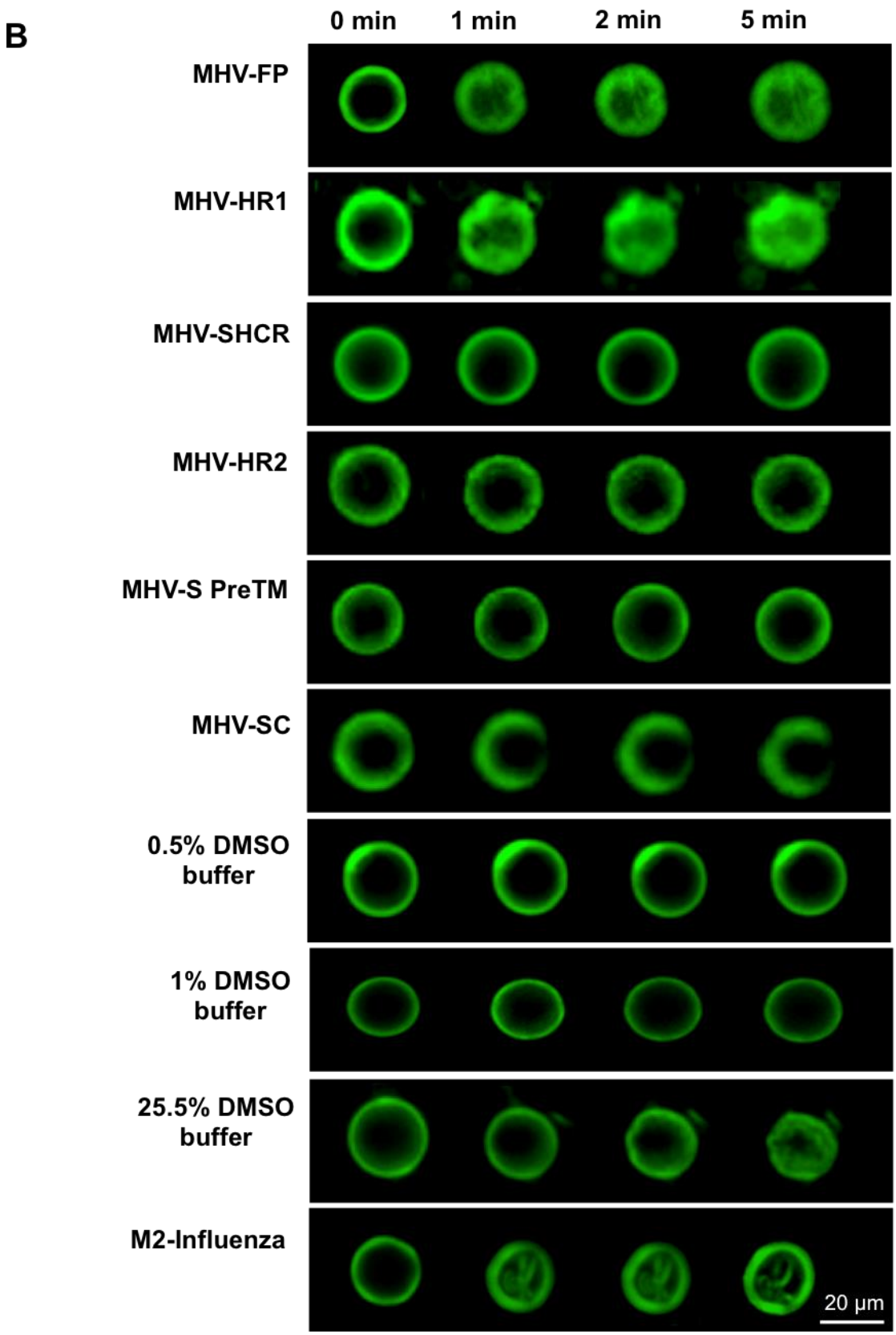
B
0 min
1 min
2 min
5 min
MHV-FP
MHV-HR1
MHV-SHCR
MHV-HR2
MHV-S PreTM
MHV-SC
0.5% DMSO buffer
1% DMSO buffer
25.5% DMSO buffer
M2-Influenza
20 µm

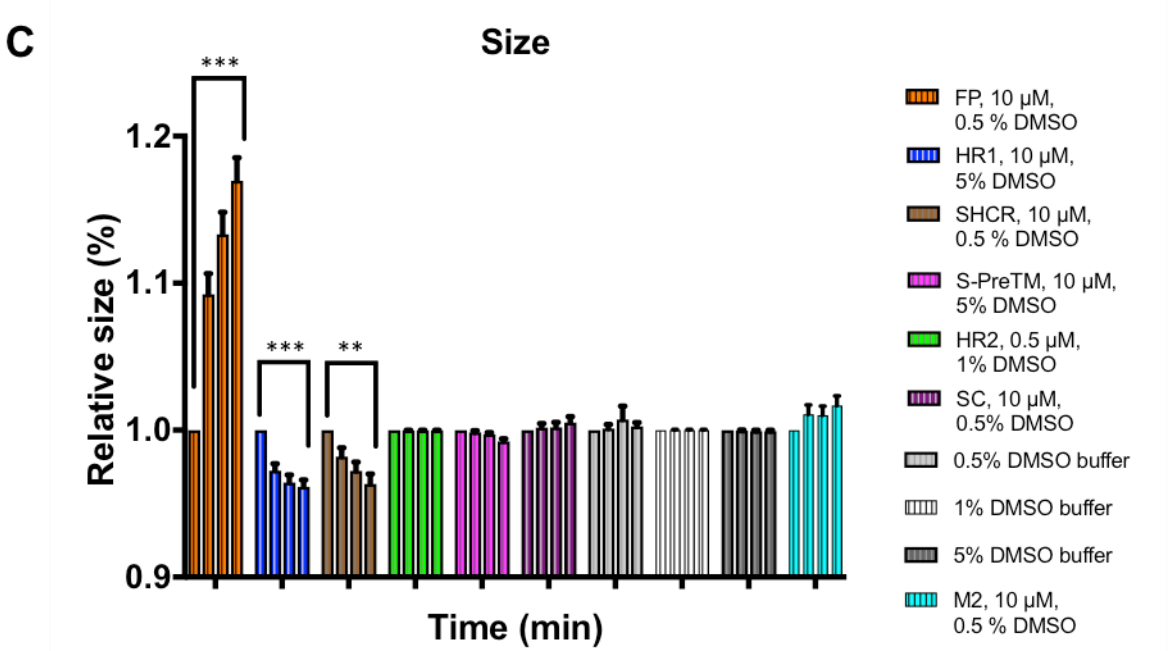
C
Size
***
***
**
1.2
1.1
1.0
0.9
Relative size (%)
Time (min)
FP, 10 µM, 0.5 % DMSO
HR1, 10 µM, 5% DMSO
SHCR, 10 µM, 0.5 % DMSO
S-PreTM, 10 µM, 5% DMSO
HR2, 0.5 µM, 1% DMSO
SC, 10 µM, 0.5% DMSO
0.5% DMSO buffer
1% DMSO buffer
5% DMSO buffer
M2, 10 µM, 0.5 % DMSO

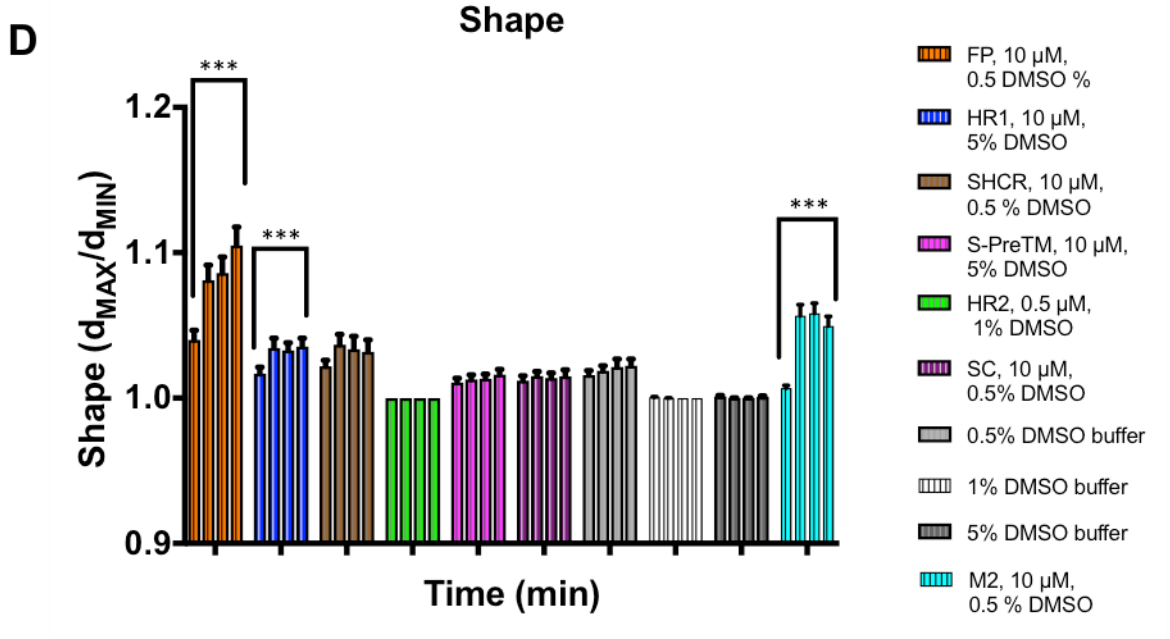
D
Shape
***
***
***
1.2
1.1
1.0
0.9
Shape (d_{MAX}/d_{MIN})
Time (min)
FP, 10 µM, 0.5 DMSO %
HR1, 10 µM, 5% DMSO
SHCR, 10 µM, 0.5 % DMSO
S-PreTM, 10 µM, 5% DMSO
HR2, 0.5 µM, 1% DMSO
SC, 10 µM, 0.5% DMSO
0.5% DMSO buffer
1% DMSO buffer
5% DMSO buffer
M2, 10 µM, 0.5 % DMSO

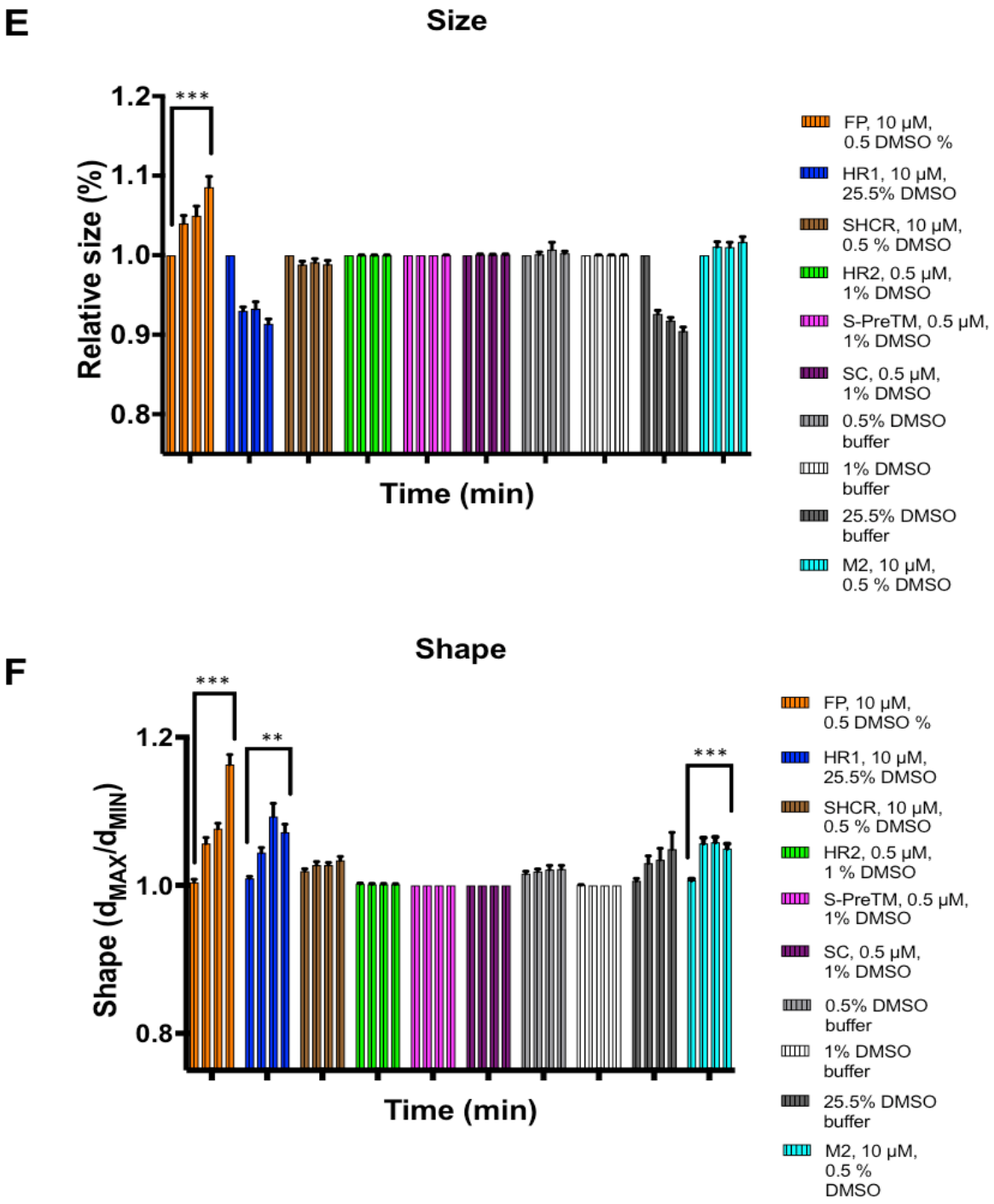

Figure 4.2: Effect of MERS and MHV S2 derived peptides on size and shape of GUVs.

A & B- Fluorescent images of electroformed GUVs treated with 10 µM of or 0.5 µM of corresponding peptides and compared with corresponding DMSO buffer concentration and M2 influenza peptide and imaged at 0 min, 1 min, 2 min and 5 min. **C & E-** GUV relative size for MERS-S2 and MHV-S2 respectively. To measure the relative size of the GUVs, the perimeter is estimated by Ramanujan's first approximation, the effective diameter is perimeter divided by π, the average standard deviation for both long and short

measurements for a vesicle was also measured and averaged for each GUV for three separate experiments for 40 GUVs each. **D & F-** GUVs shape for MERS-S2 and MHV-S2 respectively. To measure the shape of the GUVs, the ratio between longest and shortest radii were measured and averaged for each GUV for three separate experiments for 40 GUVs each. The scale bar indicates 20µm. Error bars shown are mean ± SEM. The stars ** and *** indicate significance (P ≤ 0.01 or 0.001; with respect to the corresponding buffer; Linear Mixed). Coloured key features of the tested peptides are marked. Each colored group of four columns represents the data for a single peptide test at each time point. Left to right, 0,1, 2 & 5 min. Some error bars are too small to be observed.

4.2.1.4 Effect of MERS and MHV putative fusion peptides on GUVs size and shape in different peptide concentration.

To address their potential as fusion peptides the putative FPs of MERS-S and MHV-S were included in the reconstitution of GUVs and the effect on size and morphology measured as described previously. GUVs composed of 5 mM DPPC 4 mM eggSM and 0.5 molar % cholesterol, were reconstituted with the different peptides concentrations at 10µM, 1µM and 0.1µM. All samples also contained 0.5% naphthopyrene to allow observation by fluorescence microscopy and the field was imaged in a time-series of 0 min and 5 min **Figure 4.3 A**. There was no statistical difference in size of GUVs between MERS-FP in 1µM and 0.5% DMSO buffer at all time point (P >0.05; Linear Mixed Model) (Appendix 11) **Figures 4.3 A and B**. This indicates that the effect of the MERS-FP on the GUVs membrane size at 1µM is less than its effect at the higher concentration (10µM) described previously. However, there was a statistical difference of the effects of MERS-FP in 1µM and the 0.5% DMSO buffer on the shape of the giant liposomes leading to extensive deformation (P <0.01; Linear Mixed Model), (Appendix 12) **Figures 4.3 A and C** suggesting that MERS-FP binds to the GUVs membrane and deforms them. Although there was no statistical difference between the effects of MERS-FP at 0.1 µM and the 0.5% DMSO buffer control on the size and the shape of the giant liposomes (P >0.05; Linear

Mixed Model) (Appendix 13 and 14), the putative MERS fusion peptide at 0.1 µM causes membrane permeability due to pore formation observed as a loss of fluorescence leading to a cup like shape described elsewhere (Takahashi et al 2013) **Figures 4.3 A, B and C**.

Similarly, there was no statistical difference in size of GUVs treated with MHV-FP at 1µM and 0.1µM and 0.5% DMSO buffer at all time points ($P > 0.05$; Linear Mixed Model) (Appendix 15) **Figures 4.4 A and B**. There was also no statistical difference between the effects of MHV-FP at 1µM and 0.1µM and the 0.5% DMSO buffer on the shape of the giant liposomes ($P > 0.05$; Linear Mixed Model), (Appendix 16), **Figures 4.4 A and C**. However, the putative fusion peptide of MHV-S at 1 µM causes cup like shape GUVs as reported in MERS-FP but at a lesser concentration (0.1 µM) **Figure 4.4 A**.

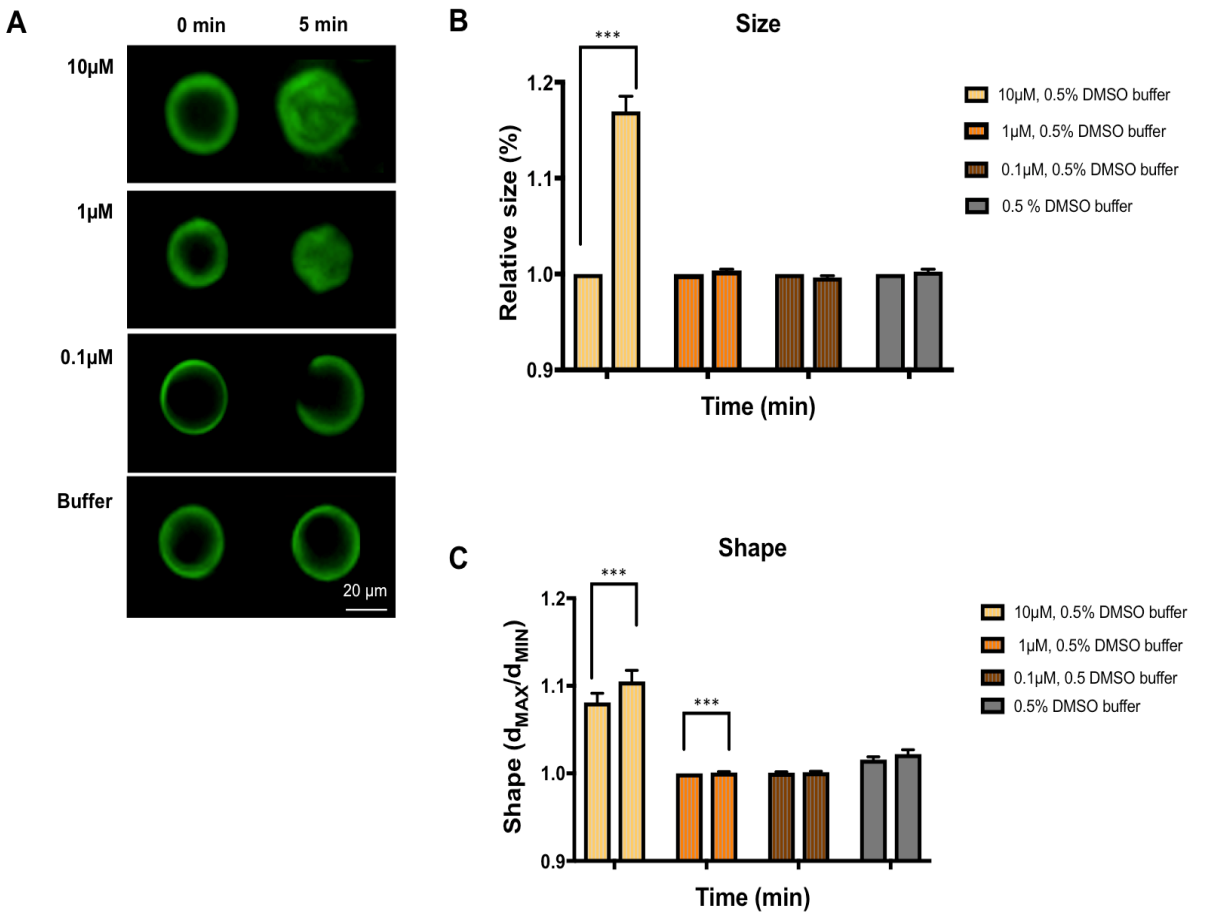

Figure 4.3: Effect of MERS- putative FP in different peptide concentration on shape and size of GUVs.

A- Fluorescent images of electroformed GUVs treated with 10 µM, 1 µM, 0.1 µM peptides concentration and compared with corresponding DMSO buffer concentration and imaged at 0 min and 5 min. **B-** GUV relative size. To measure the relative size of the GUVs, the perimeter is estimated by Ramanujan's first approximation, the effective diameter is perimeter divided by π, the average standard deviation for both long and short measurements for a vesicle was also measured and averaged for each GUV for three separate experiments for 40 GUVs each. **C-** GUVs shape, to measure the shape of the GUVs, the ratio between longest and shortest radii were measured and averaged for each GUV for three separate experiments for 40 GUVs each. The scale bar indicates 20µm. Error bars shown are mean ± SEM. The stars *** indicates significance ($P \leq 0.001$; with respect to the corresponding buffer; Linear Mixed). Coloured key features of the tested peptide concentration are marked. . Each colored group of two columns represents the data for a single peptide test at each time point. Left to right, 0 & 5 min. Some error bars are too small to be observed.

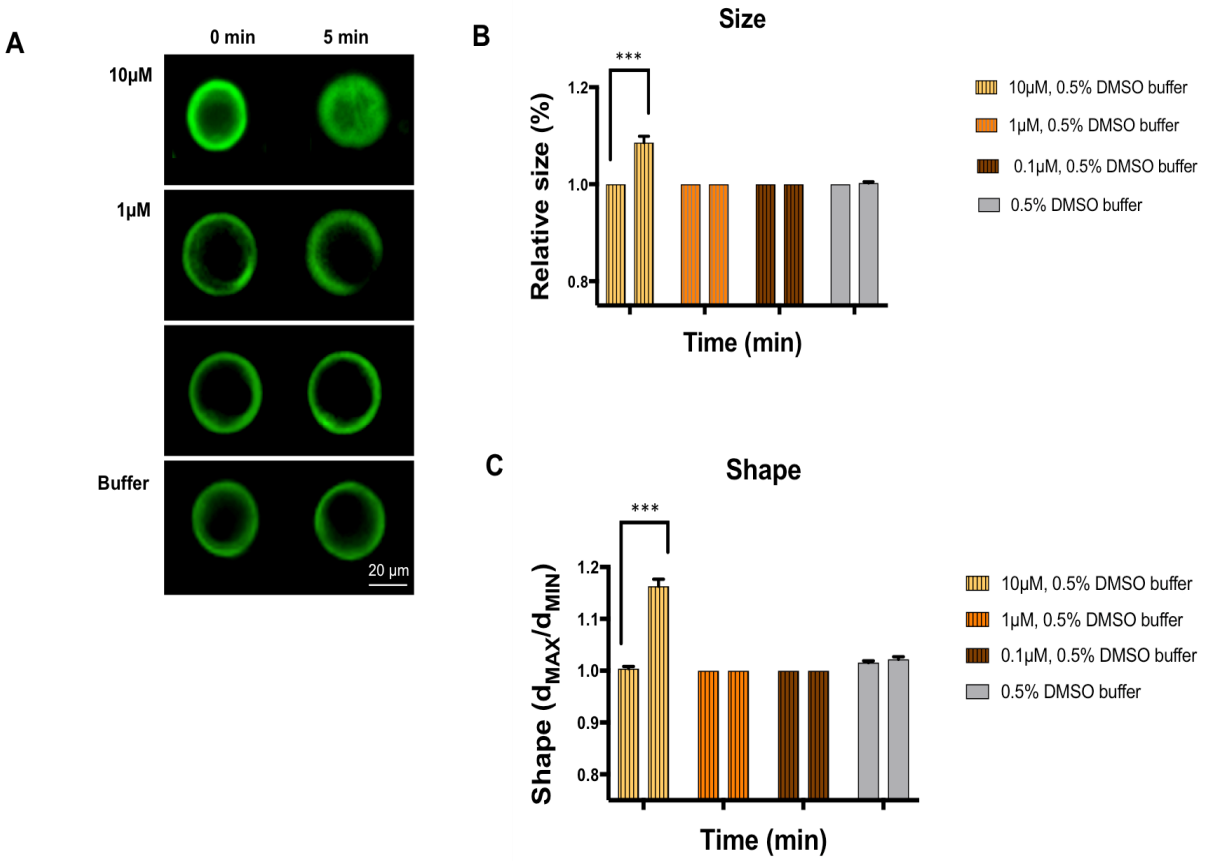

Figure 4.4: Effect of MHV- putative FP in different peptide concentration on size and shape of GUVs.

A- Fluorescent images of electroformed GUVs treated with 10 μM, 1 μM, 0.1 μM peptides concentration and compared with corresponding DMSO buffer concentration and imaged at 0 min and 5 min. **B-** GUV relative size. To measure the relative size of the GUVs, the perimeter is estimated by Ramanujan's first approximation, the effective diameter is perimeter divided by π, the average standard deviation for both long and short measurements for a vesicle was also measured and averaged for each GUV for three separate experiments for 40 GUVs each. **C-** GUVs shape, to measure the shape of the GUVs, the ratio between longest and shortest radii were measured and averaged for each GUV for three separate experiments for 40 GUVs each. The scale bar indicates 20μm. Error bars shown are mean ± SEM. The stars *** indicates significance ($P \leq 0.001$; with respect to the corresponding buffer; Linear Mixed). Coloured key features of the tested peptide concentration are marked. Each colored group of two columns represents the data for a single peptide test at each time point. Left to right, 0 & 5 min. Some error bars are too small to be observed.

4.2.1.5 Effect of MERS-S putative fusion peptide mutations on GUVs size and shape.

To address the key residues within the putative fusion peptide a series of 5 additional peptides (see **Table 2.2)** were included, all at 10µM dissolved in 2% DMSO buffer and compared with 5% DMSO only buffer controls, where the key residues were exchanged for alanine to probe those positions key to activity with the reconstituted GUVs and their size and shape were measured as before.

There was no statistical difference in size and shape of GUVs among MERS-FP peptides 2, 3 and 5 and 5% DMSO buffer at all time points (P >0.05; Linear Mixed Model) (Appendix 19 and 20), **Figures 4.5 A, B and C**. However there was a statistical difference between the effects of MERS-FP peptide 4 and 6 and the 5% DMSO buffer on the size and shape of the giant liposomes leading to a decrease in the size and a deformed shape of the GUVs (P< 0.01; Linear Mixed Model), (Appendix 19 and 20) **Figures 4.5 A, B and C**. The amphipathic value for each mutated peptide has been calculated see- **Table 4.2.**

Table 4.2: Amphipathic average for mutant MERS-CoV putative fusion peptides used for *in vivo* fusion analysis.

No.	Designation	Residues	Sequence	Amphipathic average
1	Peptide 1 (WT)	884-898	RSARSAIEDLLFDKV	3.3
2	Peptide 2	I890A	RSARSAAEDLLFDKV	2.4
3	Peptide 3	L893A	RSARSAIEDALFDKV	2.4
4	Peptide 4	L894A	RSARSAIEDLAFDKV	2.4
5	Peptide 5	F895A	RSARSAIEDLLADKV	2.5
6	Peptide 6	I890A+ L893A+ F895A	RSARSAAEDALADKV	2.4

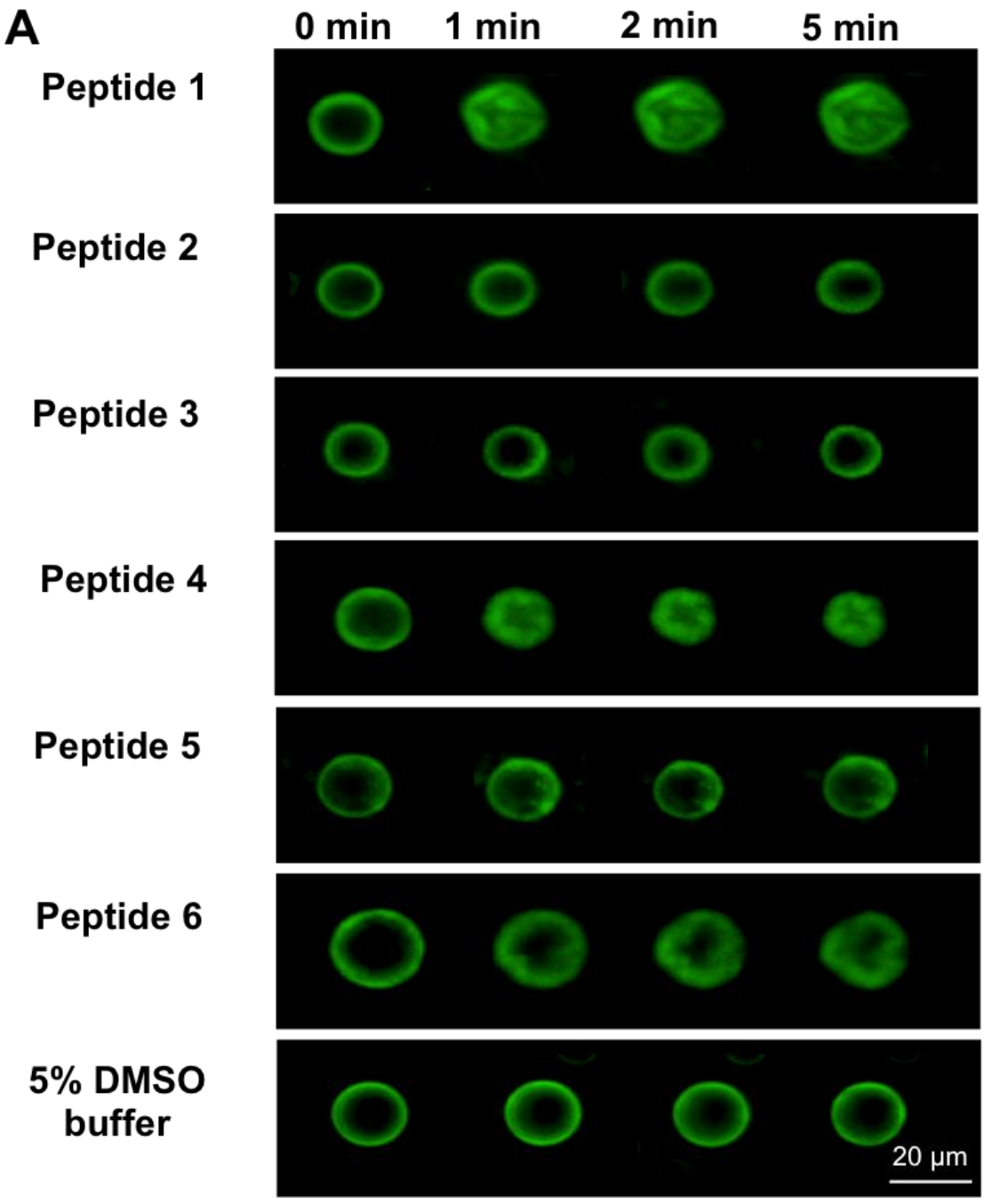
A
0 min
1 min
2 min
5 min
Peptide 1
Peptide 2
Peptide 3
Peptide 4
Peptide 5
Peptide 6
5% DMSO buffer
20 µm

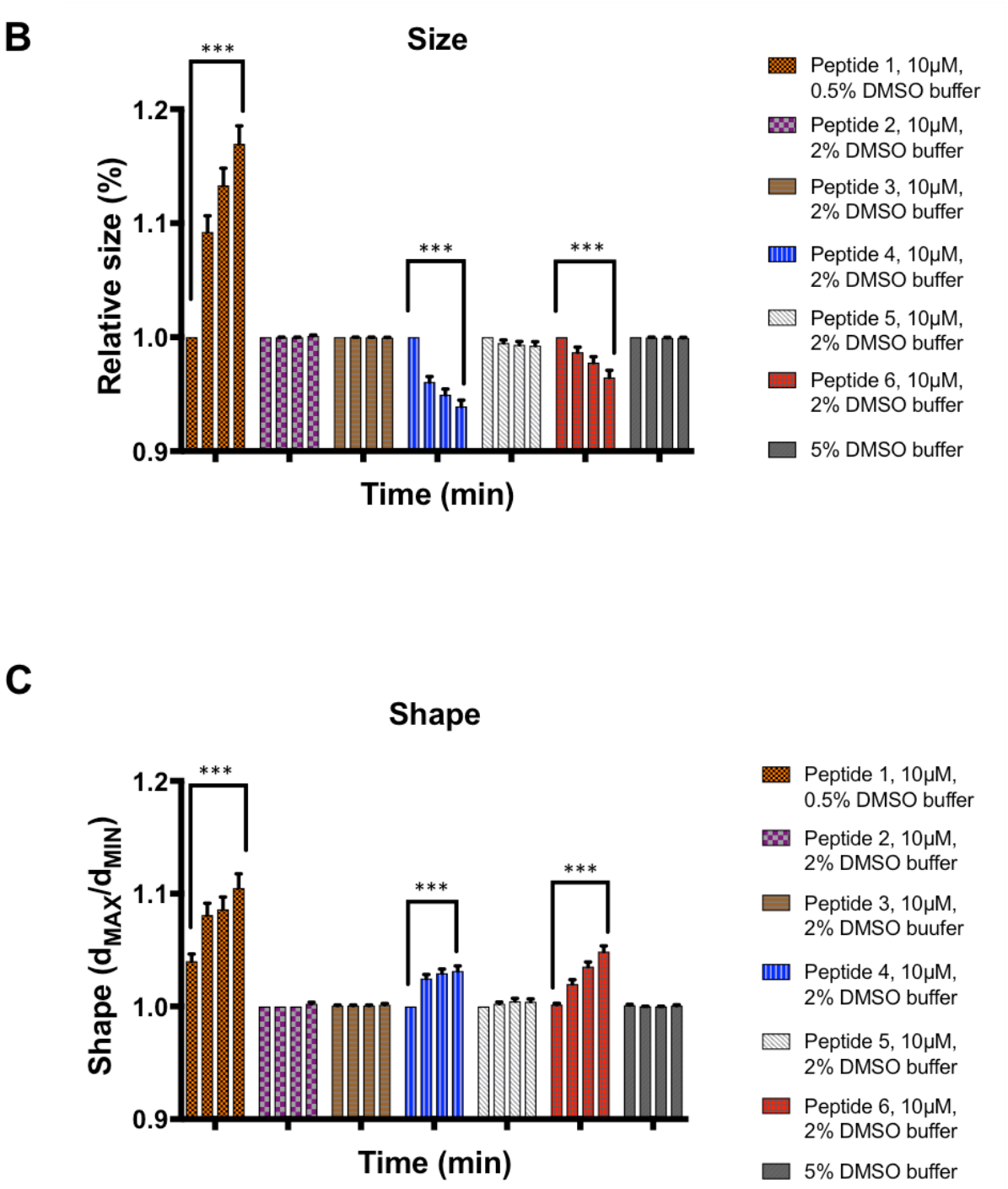

Figure 4.5: Effect of mutated MERS- putative fusion peptide on size and shape of GUVs. A- Fluorescent images of electroformed GUVs treated with 10 μM peptides concentration and compared with corresponding DMSO buffer concentration and imaged at 0 min,1 min, 2 min and 5 min. **B-** GUV relative size. To measure the relative size of the GUVs, the perimeter is estimated by Ramanujan's first approximation, the effective diameter is perimeter divided by π, the average standard deviation for both long and short measurements for a vesicle was also measured and averaged for each GUV for three separate experiments for 40 GUVs each. **C-** GUVs shape, to measure the shape of the GUVs, the ratio between longest and shortest radii were measured and averaged for each GUV for three separate experiments for 40 GUVs each. The scale bar indicates 20μm. Error

bars shown are mean ± SEM. The stars *** indicates significance (P ≤ 0.001; with respect to the corresponding buffer; Linear Mixed). Coloured key features of the tested peptide concentration are marked. Each colored group of four columns represents the data for a single peptide test at each time point. Left to right, 0,1, 2 & 5 min. Some error bars are too small to be observed.

4.2.1.6 Effect of MERS and MHV M protein-derived peptides on size and shape of GUVs.

Several MERS and MHV M-derived peptides including MERS-MPTM3, MERS-M Proline region, MHV-MTM3, MHV-MPTM3 and MHV-M Proline region were tested for their effect on the giant liposomes. These peptides were dissolved in sufficient DMSO to enable solubility and were always tested next to the equivalent DMSO buffer control. Thus, each peptide with its corresponding DMSO buffer was tested to show their effect on the GUVs size and shape **Figure 4.6 A**.

The result revealed that there was no significant effect on GUV size between the MERS-MPTM3 peptide and the 17% DMSO buffer control at time 1 min ($P > 0.05$; Linear Mixed Model). However, at time 2 and 5 min, there was statistically significant difference on GUV size ($P < 0.05$; Linear Mixed Model) (Appendix 21) **Figure 4.7 B**. Thus, MERS-MPTM3 peptide has an effect on the size of the GUV. Despite this there was no statistical difference between the effects of MERS-MPTM3 peptide and the 17% DMSO buffer on the shape of the giant liposomes ($P > 0.05$; Linear Mixed Model), (Appendix 22) **Figure 4.6 C** which indicated that the MERS-MPTM3 peptide had no effect on the morphology of the GUV. In addition, 10 µM of MERS-M Proline region in 14.7% DMSO concentration was reconstituted into GUVs **Figure 4.6 A** resulting in a statistically significant difference between MERS-M Proline treatment and the 14.7% DMSO buffer on the size of the GUV in all time points ($P < 0.01$; Linear Mixed Model), (Appendix 23) **Figure 4.6 B**.

In addition, there was a statistically significant difference between MERS-M Proline treatment and the 14.7% DMSO buffer control on the shape of the GUV in all time points ($P < 0.01$; Linear Mixed Model), (Appendix 24) suggesting that MERS-M Proline peptide deforms the shape of GUVs membranes **Figure 4.6 C**.

MHV-MTM3 and MHV-M Proline region were tested at 0.5 µM in 1% DMSO buffer and reconstituted into GUVs **Figure 4.6**. The result showed that there was no statistical difference in size and shape of GUVs between MHV-MTM3, MHV-M Proline region and 1% DMSO buffer at all time point ($P > 0.05$; Linear Mixed Model) (Appendix 25 and 26) **Figure 4.6 A, B, C**. However, the Proline region of MHV-M causes membrane permeability due to pore formation observed as loss of fluorescence leading to a cup like shape as described before **Figure 4.6 A**.

10 µM of MHV-MPTM3 peptide in 15% DMSO buffer was also tested and reconstituted into GUVs produced as above, **Figure 4.6 A**. The result revealed that there was a statistically significant difference between the MHV-MPTM3 peptide and the 15% DMSO buffer on the size of the GUVs at time 1 min. ($P < 0.01$; Linear Mixed Model), (Appendix 27) **Figure 4.6 B** but not at times 2 and 5 min ($P > 0.05$; Linear Mixed Model) (Appendix 27). This indicated that MHV-MPTM3 had decreased the size of the GUV more than the buffer **Figure 4.6 B**. but there was no statistical difference on the GUV shape between the MHV-MPTM3 peptide and the 15% DMSO buffer ($P > 0.05$; Linear Mixed Model), (Appendix 28) **Figure 4.6 C** and it must be concluded that MHV-MPTM3 has no effect on the morphology of the GUVs.

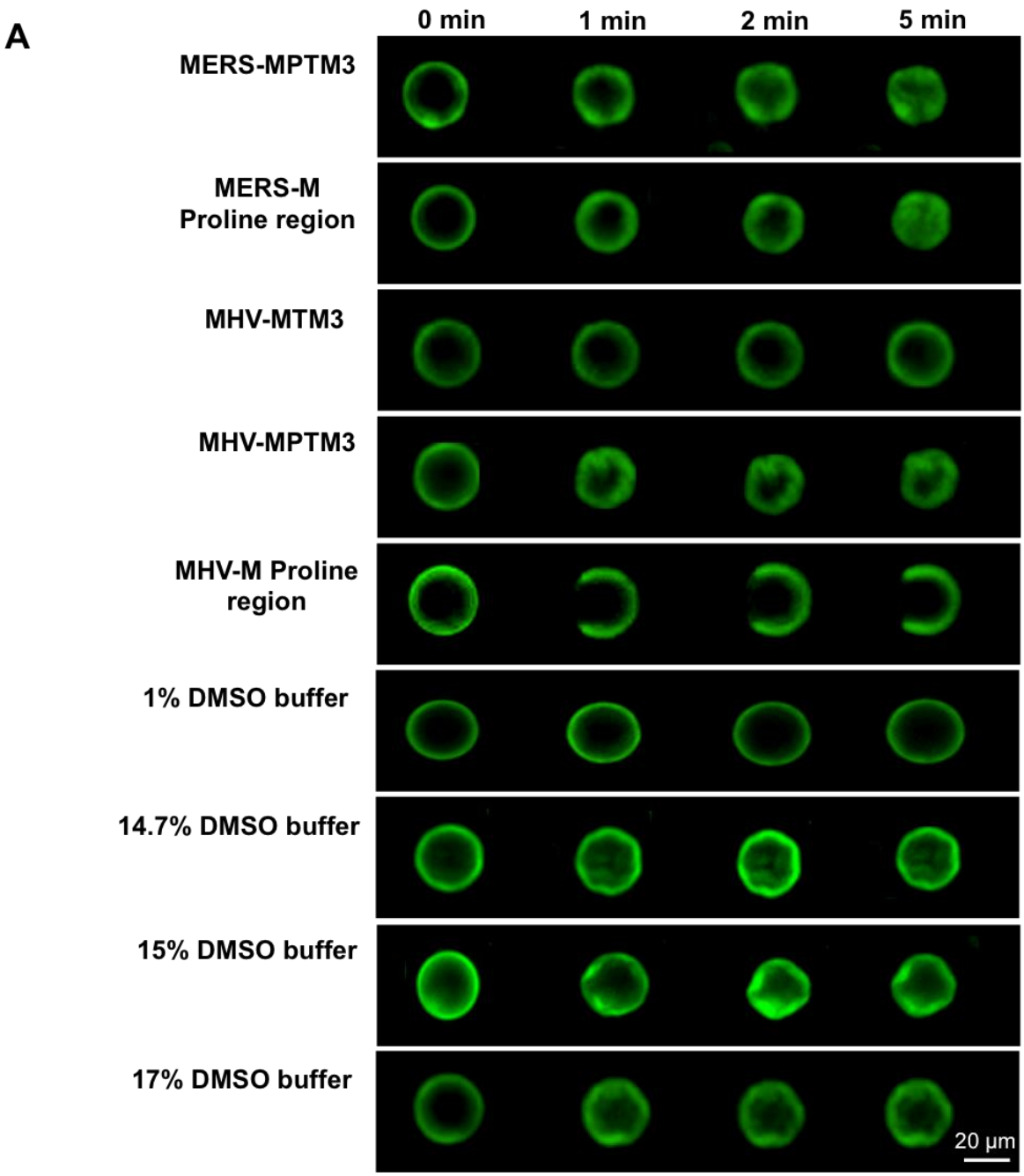
A
0 min
1 min
2 min
5 min
MERS-MPTM3
MERS-M Proline region
MHV-MTM3
MHV-MPTM3
MHV-M Proline region
1% DMSO buffer
14.7% DMSO buffer
15% DMSO buffer
17% DMSO buffer
20 μm

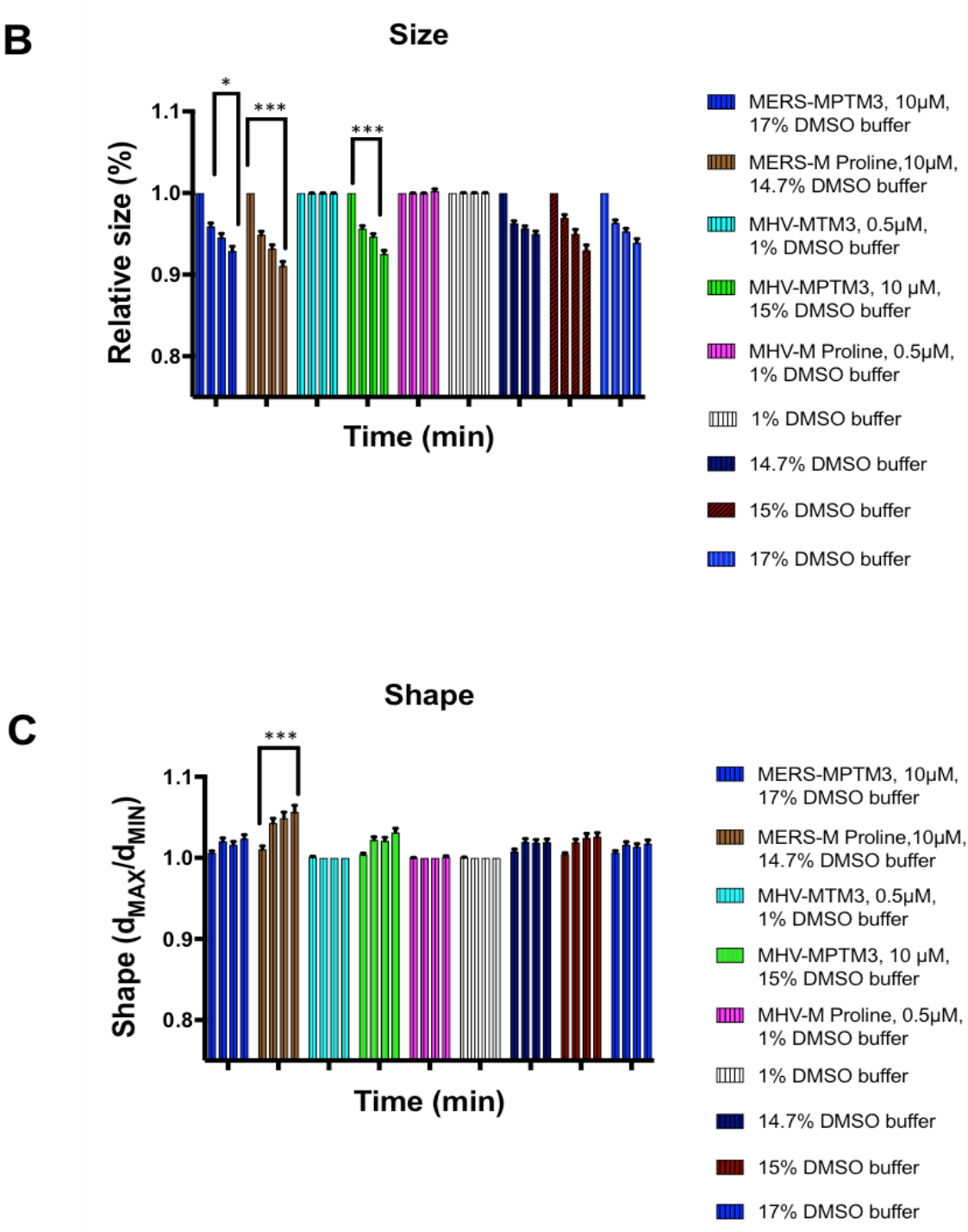

Figure 4.6: Effect of MERS and MHV M protein-derived peptides on size and shape of GUVs. A- Fluorescent images of electroformed GUVs treated with 10 μM peptides concentration of MERS MPTM3, MERS-M Proline region, MHV-M PTM3 and with 0.5 μM peptides concentration of MHV-MTM3 and MHV-M Proline region and compared with the corresponding DMSO buffer concentration and imaged at 0 min, 1 min, 2 min and 5 min. **B-** GUV relative size. To measure the relative size of the GUVs, the perimeter is estimated by Ramanujan's first approximation, the effective diameter is perimeter divided by π, the average standard deviation for both long and short measurements for a vesicle was also measured and averaged for each GUV for three separate experiments for 40 GUVs each. **C-**

GUVs shape, to measure the shape of the GUVs, the ratio between longest and shortest radii were measured and averaged for each GUV for three separate experiments for 40 GUVs each. The scale bar indicates 20µm. Error bars shown are mean ± SEM. The stars * and *** indicate significance (P ≤ 0.05 or 0.001; with respect to the corresponding buffer; Linear Mixed). Coloured key features of the tested peptide concentration are marked. Each colored group of four columns represents the data for a single peptide test at each time point. Left to right, 0,1, 2 & 5 min. Some error bars are too small to be observed.

4.2.1.7 Effect of MERS and MHV E protein-derived peptides on size and shape of GUVs.

E derived peptides, MERS-EPTM, MHV-ETM and MHV-EPTM were tested in their corresponding DMSO buffer concentrations but the data showed that there was no statistical significant difference between MERS-EPTM and 13% DMSO buffer treatment on the GUV size and shape at all time points (P >0.05; Linear Mixed Model), (Appendix 29 and 30). This indicates that, the MERS-EPTM has no effect on the GUV size and shape **Figure 4.7 A, B, C.** Similarly**,** MHV-ETM was tested at 0.5µM concentration in 1% DMSO buffer concentration and, as before, the data showed that there was no statistical significant difference between MHV-ETM and 1% DMSO buffer treatment on the GUV size and shape at all time points (P >0.05; Linear Mixed Model), (Appendix 31 and 32).

At 10 µM of MHV-EPTM peptide in 0.5% DMSO buffer concentration however, there was a statistical significant difference between MHV-EPTM and 0.5% DMSO buffer treatment on the GUV size and shape at all the time points (P <0.01; Linear Mixed Model), (Appendix 33 and 34) Thus, MHV-EPTM reduced the size of the GUV at all time points **Figure 4.7 A, B, C.**

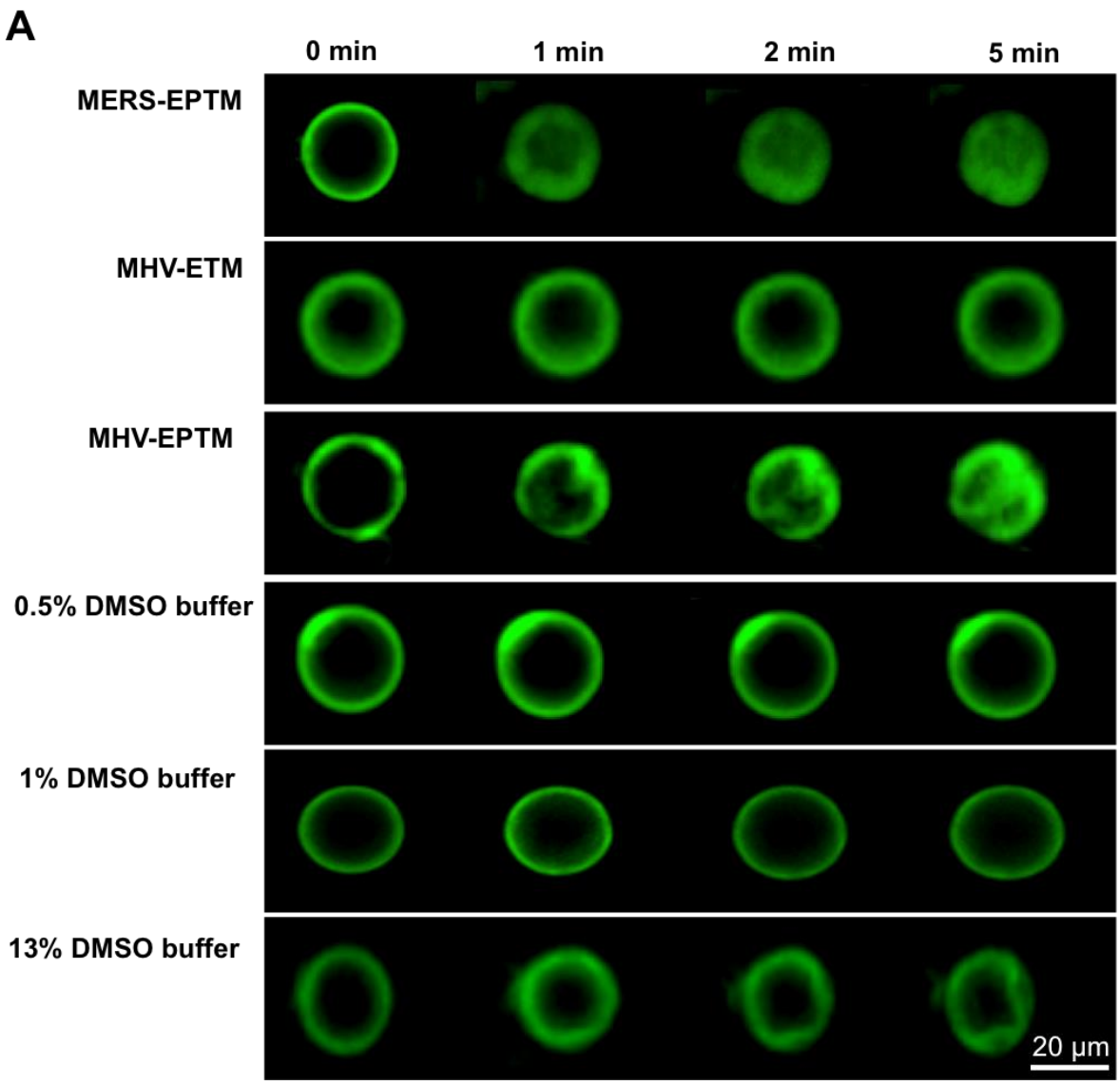
A
0 min
1 min
2 min
5 min
MERS-EPTM
MHV-ETM
MHV-EPTM
0.5% DMSO buffer
1% DMSO buffer
13% DMSO buffer
20 μm

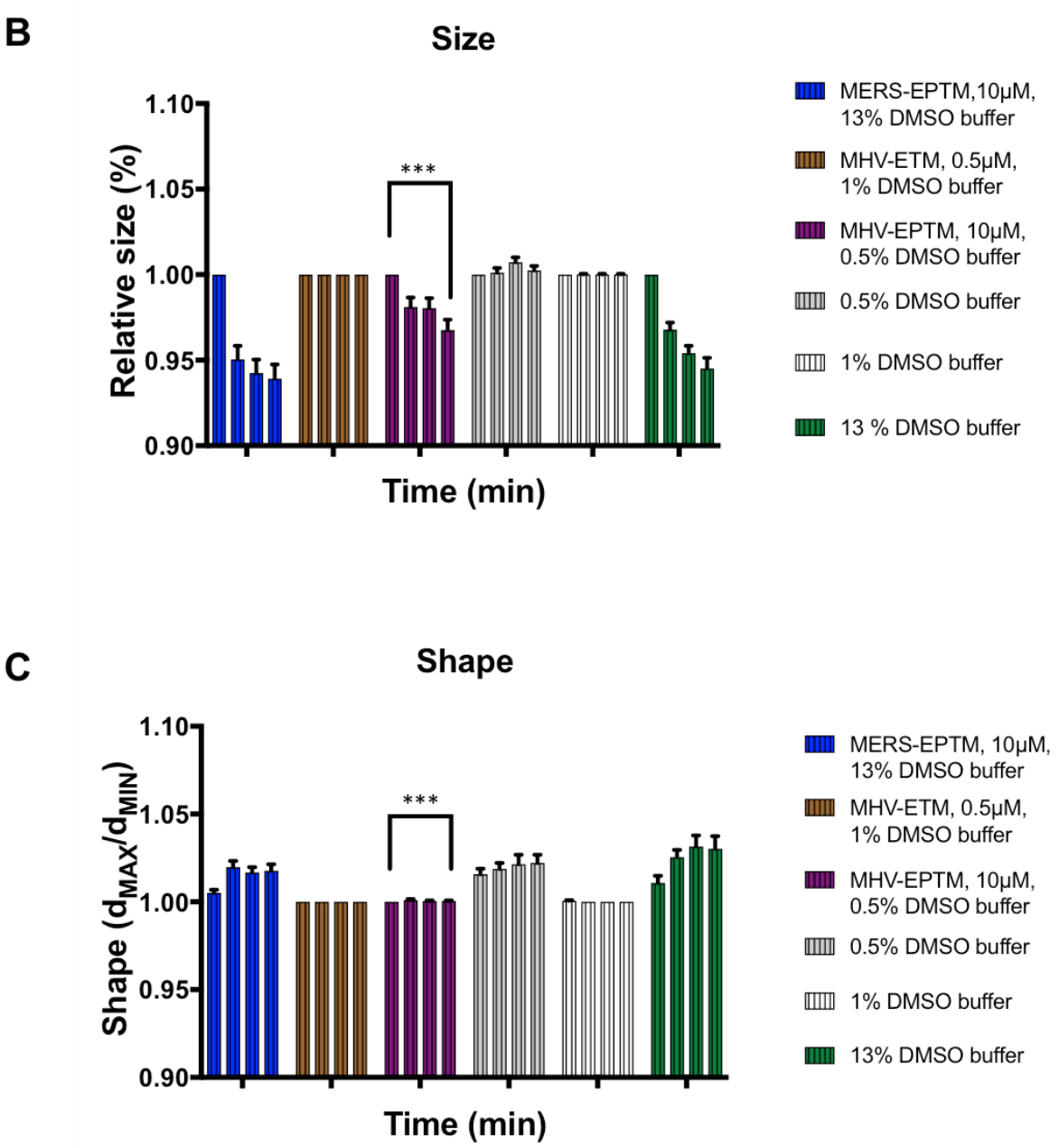

Figure 4.7: Effect of MERS and MHV E protein-derived peptides on size and shape of GUVs. **A-** Fluorescent images of electroformed GUVs treated with 10 μM peptides concentration of MERS- EPTM, MHV-EPTM and with 0.5 μM peptides concentration of MHV-ETM and compared with the corresponding DMSO buffer concentration and imaged at 0 min,1 min, 2 min and 5 min. **B-** GUV relative size. To measure the relative size of the GUVs, the perimeter is estimated by Ramanujan's first approximation, the effective diameter is perimeter divided by π, the average standard deviation for both long and short measurements for a vesicle was also measured and averaged for each GUV for three separate experiments for 40 GUVs each. **C-** GUVs shape, to measure the shape of the GUVs, the ratio between longest and shortest radii were measured and averaged for each GUV for three separate experiments for 40 GUVs each. The scale bar indicates 20μm. Error bars shown are mean ± SEM. The stars *** indicate significance ($P \leq 0.001$; with respect to the corresponding buffer; Linear Mixed). Coloured key features of the tested peptide concentration are marked. Each colored group of four

columns represents the data for a single peptide test at each time point. Left to right, 0,1, 2&5 min. Some error bars are too small to be observed.

4.3 Effect of MERS and MHV nonstructural proteins-derived peptides on size and shape of GUVs.

Nonstructural protein derived peptides of MHV and MERS were also tested on GUV membranes **Table 2.3 and 2.4**. Most of these peptides dissolved completely in a buffer containing 0.1mM sucrose, 0.1mM glucose, and 0.5% DMSO concentration. However, MERS-nsp3-2 was excluded from the study due to its poor solubility in 100% DMSO. Otherwise, the GUVs were reconstituted with 10 µM of selected peptides unless otherwise stated and the shape and relative size of the GUVs were measured as before.

4.3.1 Effect of MERS and MHV nonstructural-derived peptides on size and shape of GUVs at 10 µM and 0.5 µM peptide concentrations.

MERS-nsp 3-1, MERS-nsp 3-3, MERS-nsp 4-3, MERS-nsp 6-1, MERS-nsp 6-2, MHV-nsp 3-1, MHV-nsp 3-2, MHV-nsp 3-3, MHV-nsp 4-1, MHV-nsp 4-2 and MHV-nsp 6-2 at 10 µM in 0.5% DMSO and MERS-nsp 4-1, MERS-nsp 4-2, MHV-nsp 4-3 and MHV-nsp 6-1 were used at 0.5 µM dissolved in 1% DMSO buffer.

The results showed there was a statistically significant difference between MERS-nsp 3-1, MERS-nsp 3-3, MERS-nsp 4-3, MHV-nsp 3-1, MHV-nsp 3-2, MHV-nsp 4-2, MHV-nsp 6-2 and 0.5% DMSO buffer on the size of the GUVs at all time points, however, MHV-nsp 4-2 and MHV-nsp 6-1 showed a significance difference at only time points 2 and 5 min ($P < 0.01$; Linear Mixed Model) (Appendix 35) **Figures 4.8 A, B, C and E.** Thus these peptides have changed the size of the GUVs**.** However, there was no statistical significance difference between MERS-nsp 6-1,

MERS-nsp 6-2, MHV-nsp 3-3, MHV-nsp 4-1 and 0.5% DMSO buffer on the size of GUVs.

There was no statistically significant difference between MERS-nsp 3-1, MERS-nsp 3-3, MERS-nsp 4-3, MERS-nsp 6-2, MHV-nsp 3-1, MHV-nsp 3-2, MHV-nsp 4-1, MHV-nsp 4-2, MHV-nsp 6-2 and 0.5% DMSO buffer on the shape of the GUVs at all time points (P >0.05; Linear Mixed Model) (Appendix 36) although the GUV membrane showed slight deformation that did not reach statistical significance **Figures 4.8 A, B, D and F**. However, there was a statistically significant difference between MERS-nsp 6-1 and 0.5% DMSO buffer at times 2 and 5 min on the shape of the GUVs membrane (P <0.01; Linear Mixed Model) (Appendix 36) **Figures 4.8 A and D** indicating that MERS-nsp 6-1 has changed the GUVs membrane.

Several MERS and MHV nsp-derived peptides including MERS-nsp 4-1, MERS-nsp 4-2, MHV-nsp 4-3 and MHV-nsp 6-1, dissolved in 1% DMSO buffer were tested at 0.5μM peptide concentration. The data showed that there was no statistically significant difference between MERS-nsp 4-1, MHV-nsp 4-3, MHV-nsp 6-1, and 1% DMSO buffer on the size of the GUVs at all time points (P >0.05; Linear Mixed Model) (Appendix 37) **Figures 4.8 A, B, C and E**. However, there was a statistical significance difference between MERS-nsp 4-2 and 1% DMSO buffer at all time points (P <0.01; Linear Mixed Model) (Appendix 37) **Figure 4.8 A and C** indicating this peptide has an influence on the size of the GUVs membranes.

The effect of the same peptides at 0.5 μM concentration showed there was no statistically significant difference between MERS-nsp 4-1, MERS-nsp 4-2, MHV-nsp 4-3, MHV-nsp 6-1, and 1% DMSO buffer on the shape of the GUVs at all time points (P >0.05; Linear Mixed Model) (Appendix 38) **Figures 4.8 A, B, D and F**. However, MERS-nsp 4-1, MHV-nsp 4-3, MHV-nsp 6-1 peptides cause membrane permeability

due to pore formation observed as loss of fluorescence leading to a cup like shape described elsewhere (Takahashi et al, 2013) **Figure 4.8 A**.

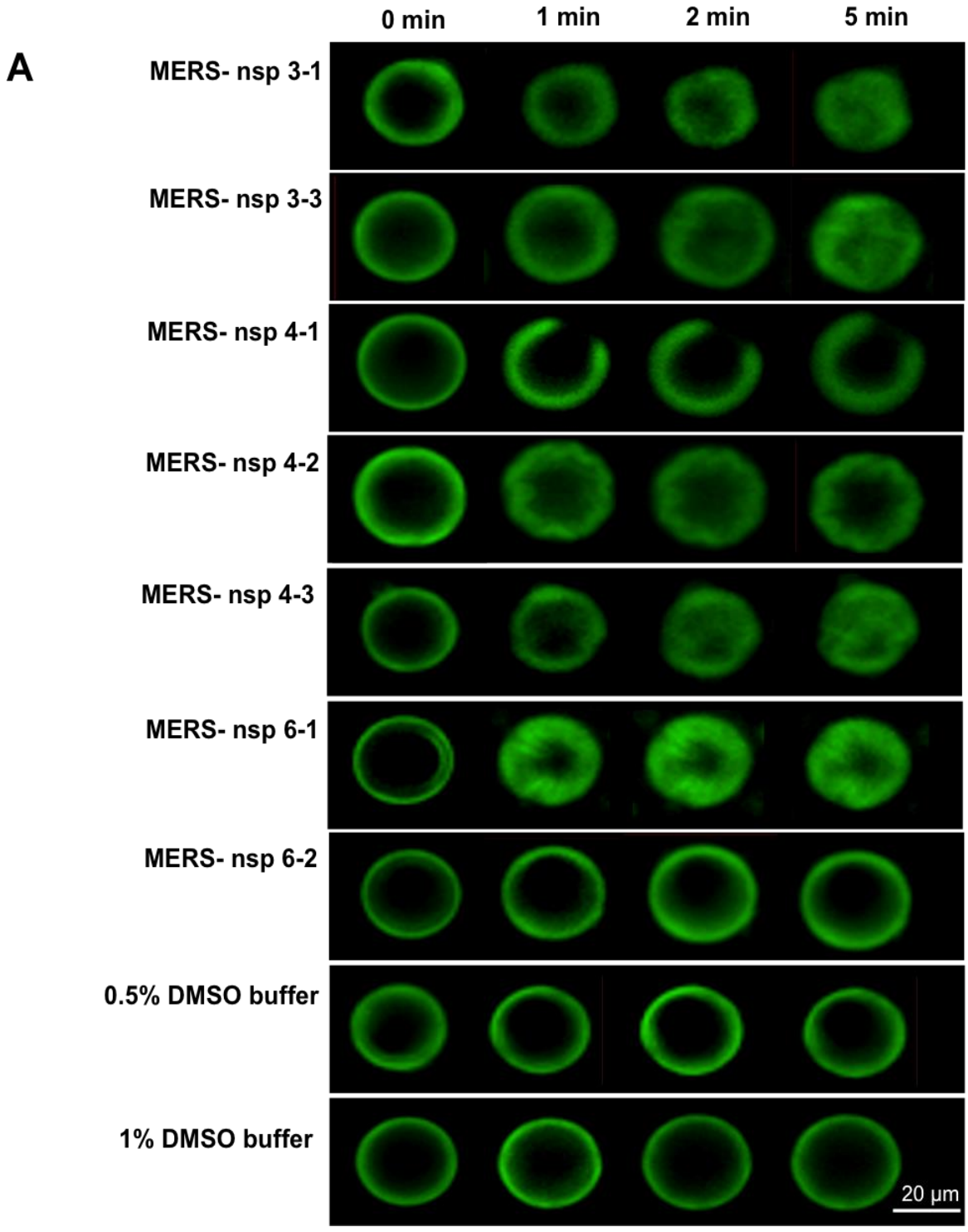

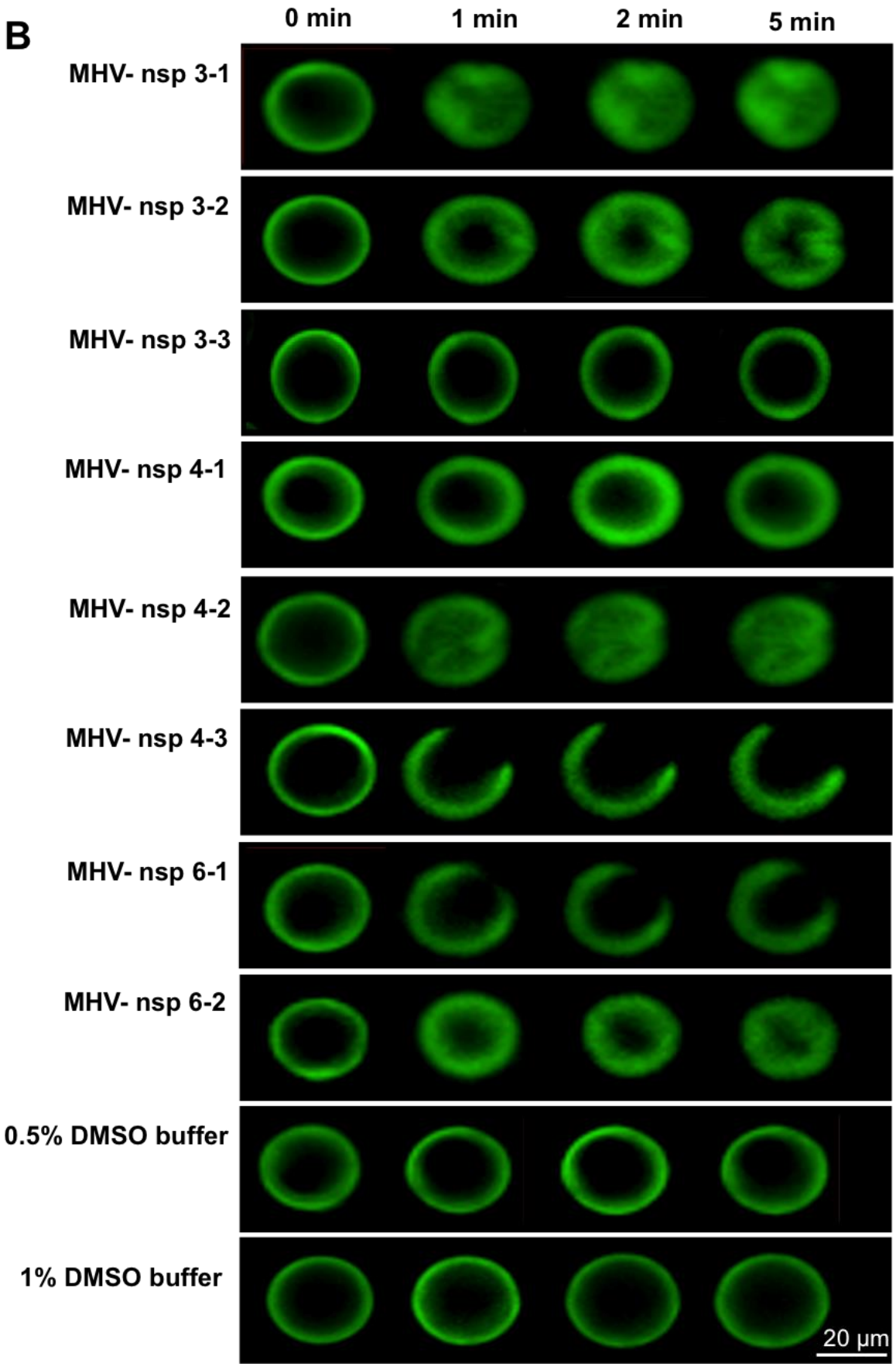
B
0 min
1 min
2 min
5 min
MHV- nsp 3-1
MHV- nsp 3-2
MHV- nsp 3-3
MHV- nsp 4-1
MHV- nsp 4-2
MHV- nsp 4-3
MHV- nsp 6-1
MHV- nsp 6-2
0.5% DMSO buffer
1% DMSO buffer
20 μm

C

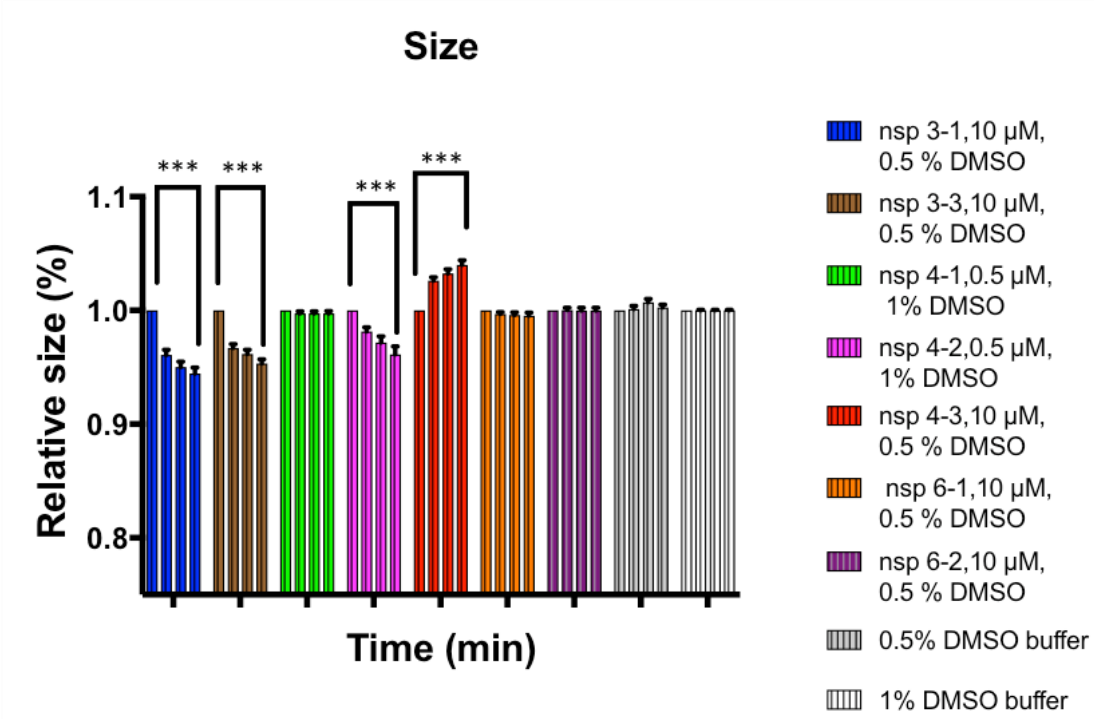
Size
Relative size (%)
1.1
1.0
0.9
0.8
***
***
***
***
Time (min)
nsp 3-1,10 µM, 0.5 % DMSO
nsp 3-3,10 µM, 0.5 % DMSO
nsp 4-1,0.5 µM, 1% DMSO
nsp 4-2,0.5 µM, 1% DMSO
nsp 4-3,10 µM, 0.5 % DMSO
nsp 6-1,10 µM, 0.5 % DMSO
nsp 6-2,10 µM, 0.5 % DMSO
0.5% DMSO buffer
1% DMSO buffer

D

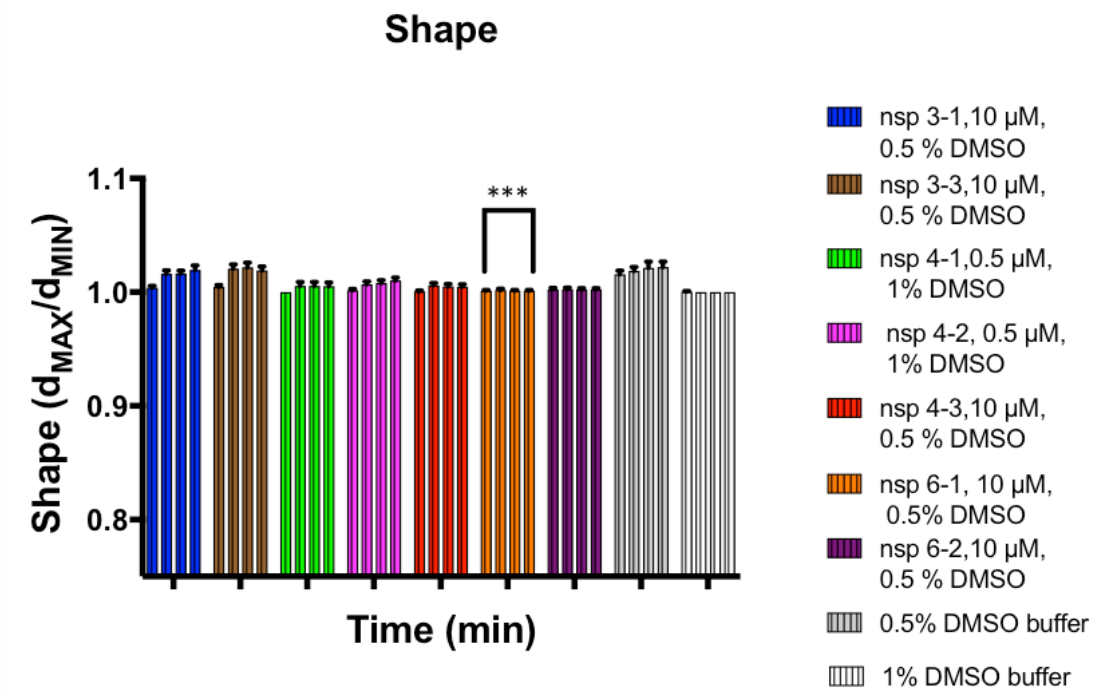
Shape
Shape (d_{MAX}/d_{MIN})
1.1
1.0
0.9
0.8
***
Time (min)
nsp 3-1,10 µM, 0.5 % DMSO
nsp 3-3,10 µM, 0.5 % DMSO
nsp 4-1,0.5 µM, 1% DMSO
nsp 4-2, 0.5 µM, 1% DMSO
nsp 4-3,10 µM, 0.5 % DMSO
nsp 6-1, 10 µM, 0.5% DMSO
nsp 6-2,10 µM, 0.5 % DMSO
0.5% DMSO buffer
1% DMSO buffer

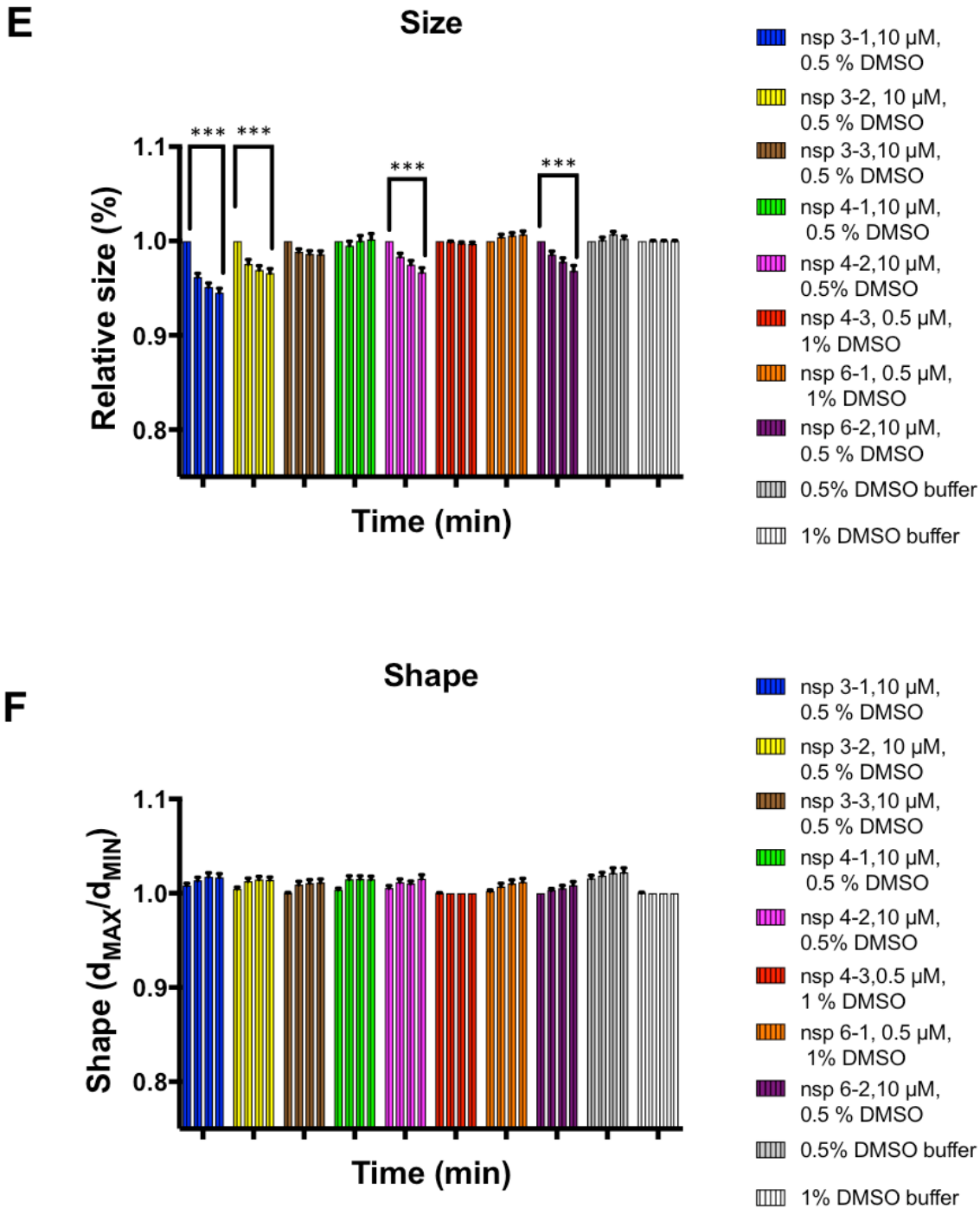

Figure 4.8: Effect of MERS and MHV nsp3, nsp4 and nsp6 derived peptides on size and shape of GUVs. A and B- Fluorescent images of electroformed GUVs treated with 10 µM peptides concentration of MERS-nsp 3-1, MERS-nsp 3-3, MERS-nsp 4-3, MERS-nsp 6-1, MERS-6-2, MHV-nsp 3-1, MHV-nsp 3-2, MHV-nsp 3-3, MHV-nsp 4-1, MHV-nsp 4-2 and MHV-nsp 6-2 and with 0.5 µM peptides concentration of MERS-nsp4-1, MERS-nsp 4-2, MHV-nsp 4-3 and MHV-nsp 6-1 and compared with the corresponding DMSO buffer concentration and imaged at 0 min, 1 min, 2 min and 5 min. **C & E**- GUV relative size for MERS and MHV-nsps respectively. To measure the relative size of the GUVs, the perimeter is estimated by Ramanujan's first approximation, the effective diameter is perimeter divided by π, the average standard deviation for both long and short measurements for a vesicle

was also measured and averaged for each GUV for three separate experiments for 40 GUVs each. **D & F**- GUVs shape for MERS and MHV-nsps respectively, to measure the shape of the GUVs, the ratio between longest and shortest radii were measured and averaged for each GUV for three separate experiments for 40 GUVs each. The scale bar indicates 20µm. Error bars shown are mean ± SEM. The stars *** indicate significance (P ≤ 0.001; with respect to the corresponding buffer; Linear Mixed). Coloured key features of the tested peptide concentration are marked. Each colored group of four columns represents the data for a single peptide test at each time point. Left to right, 0,1, 2 & 5 min. Some error bars are too small to be observed.

4.3.2 Effect of MERS and MHV nsp4, nsp6-derived peptides on size and shape of GUVs at different concentrations.

As the MERS-nsp 4-1, MHV-nsp 4-3 and MHV-nsp 6-1 peptides showed cup like shape effects on GUVs membrane in 0.5µM, they were also tested at different concentrations, 1µM, 0.25µM and 0.125µM, imaged at 0 and 5 min only and measured as described before.

4.3.2.1 Effect of MERS and MHV nsp4, nsp6-derived peptides on shape and size of GUVs in 1µM and 0.25 µM concentrations.

The MERS-nsp 4-1, MHV-nsp 4-3 and MHV-nsp 6-1 peptides were tested at 1µM and 0.25µM concentrations in 5% and 1% DMSO buffers respectively, using GUVs generated by electroformation as before and imaged at 0 and 5 min.

The results showed that there was no statistically significant difference among MERS-nsp 4-1, MHV-nsp 4-3, MHV-nsp 6-1, and 5% and 1% DMSO buffers respectively on the size and shape of the GUVs at all time points in both concentrations (1µM and 0.25µM) (P >0.05; Linear Mixed Model) (Appendix 39,40, 41 and 42) **Figures 4.9 A, B, C, D, E and F.** However, the peptides still cause membrane permeability due to pore formation demonstrated as loss of fluorescence

leading to a cup like shape described elsewhere (Takahashi et al 2013) **Figures 4.9 A and D,** indicating these peptides are *bona fide* membrane active at these concentrations (1µM and 0.25µM).

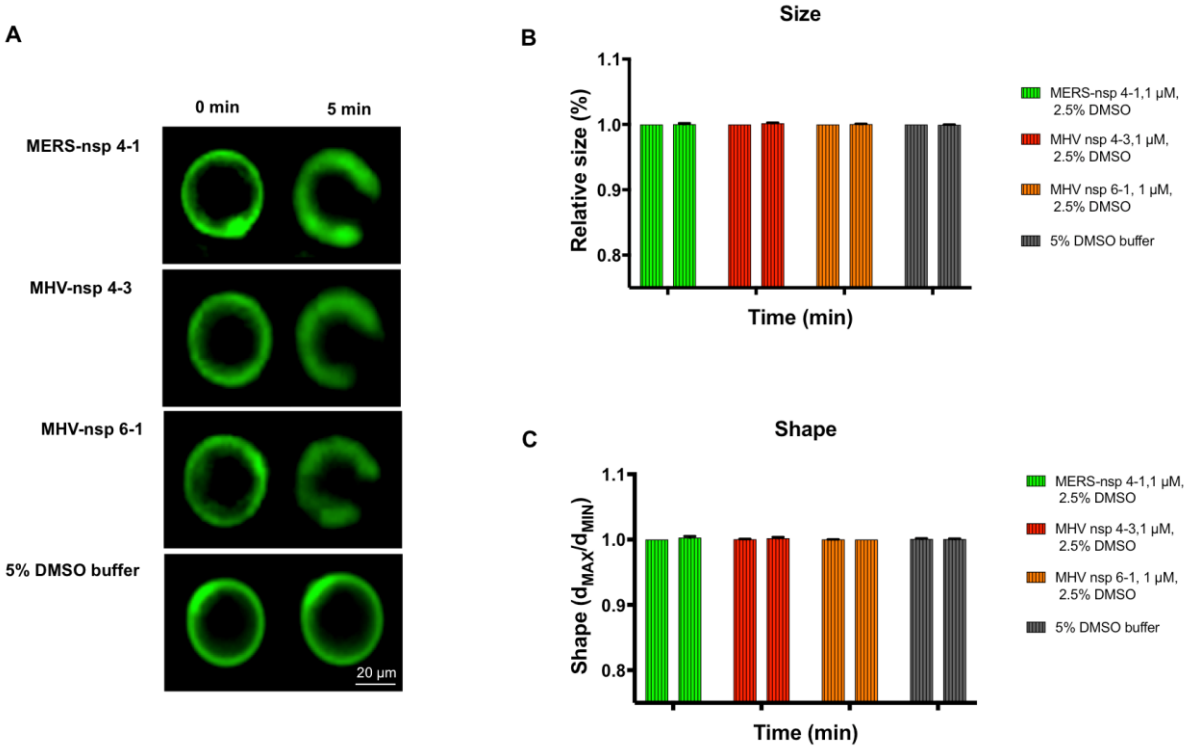

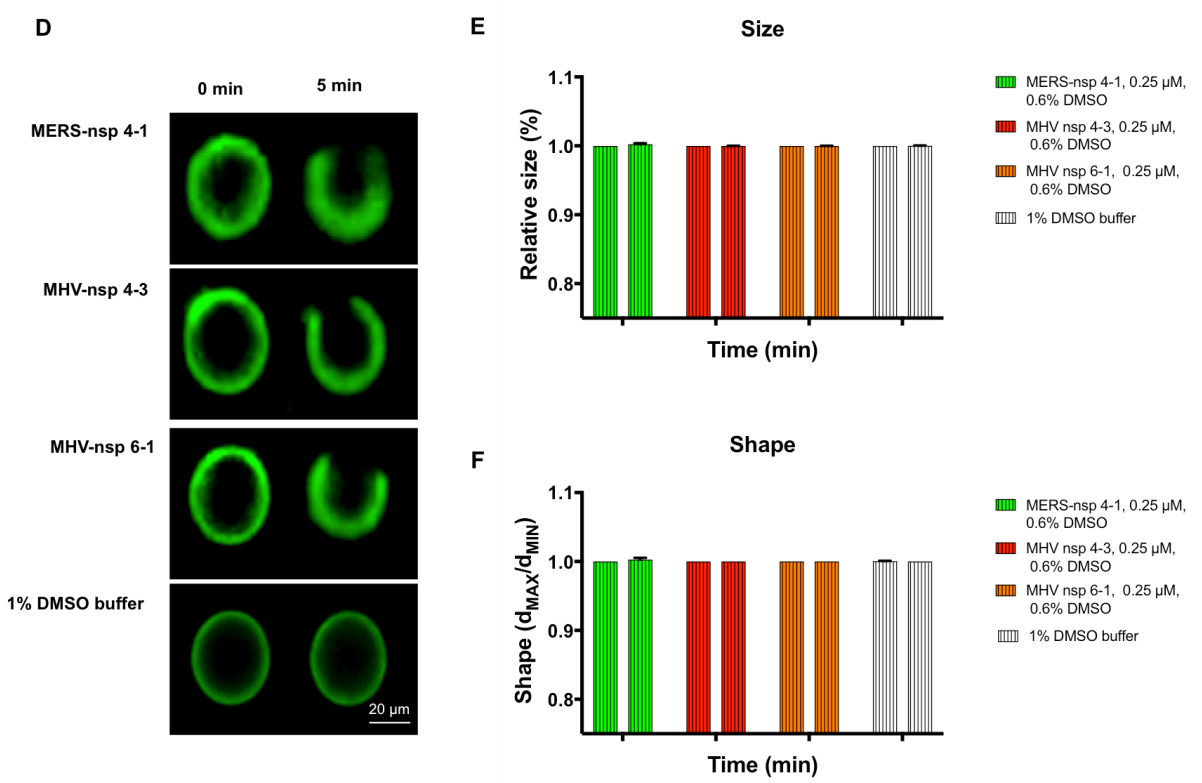

Figure 4.9: Effect of MERS and MHV nsp4 and nsp6-derived peptides on shape and size of GUVs in 1µM (A, B, C) and 0.25 µM (D, E, F). **A & D**- Fluorescent images of electroformed GUVs treated with 1µM & 0.25 µM peptides concentration of MERS-nsp 4-1, MHV-nsp 4-3 and MHV-nsp 6-1 respectively with the corresponding DMSO buffer concentration and imaged at 0 min and 5 min. **B& E**- GUV relative size. To measure the relative size of the GUVs, the perimeter is estimated by Ramanujan's first approximation, the effective diameter is perimeter divided by π, the average standard deviation for both long and short measurements for a vesicle was also measured and averaged for each GUV for three separate experiments for 40 GUVs each. **C& F**- GUVs shape, to measure the shape of the GUVs, the ratio between longest and shortest radii were measured and averaged for each GUV for three separate experiments for 40 GUVs each. The scale bar indicates 20µm. Error bars shown are mean ± SEM. ($P > 0.05$; Linear Mixed). Coloured key features of the tested peptide concentration are marked. Each colored group of two columns represents the data for a single peptide test at each time point. Left to right, 0 & 5 min. Some error bars are too small to be observed.

4.3.2.2 Effect of MERS and MHV nsp4, nsp6-derived peptides on shape and size of GUVs in 0.125μM concentration.

The MERS-nsp 4-1, MHV-nsp 4-3 and MHV-nsp 6-1 peptides were also tested at 0.125μM concentration in 0.5% DMSO buffer but the data showed there was no statistically significant difference between MERS-nsp 4-1, MHV-nsp 4-3, MHV-nsp 6-1, and 0.5% DMSO buffer on the size and shape of the GUVs at all time points ($P > 0.05$; Linear Mixed Model) (Appendix 43 and 44) **Figures 4.10 A, B, and C**. These results suggest that these peptides have no influence on the GUVs size and shape. However, MERS-nsp 4-1 peptide still causes membrane permeability due to pore formation demonstrated as loss of fluorescence leading to a cup like shape described elsewhere (Takahashi et al 2013) **Figure 4.10 A** indicating that MERS-nsp 4-1 peptide is a genuine membrane active peptide while MHV-nsp 4-3, MHV-nsp 6-1 peptides are not membrane active at this concentration **Figure 4.10 A**.

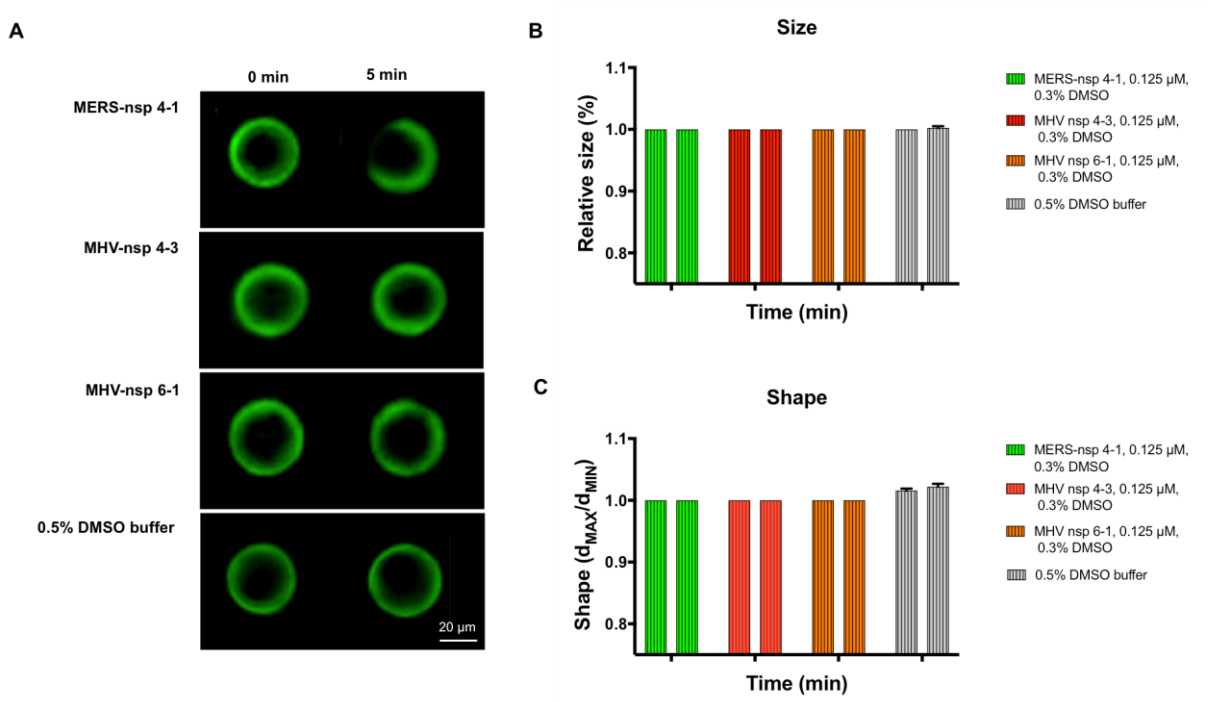

Figure 4.10: Effect of MERS and MHV nsp4 and nsp6-derived peptides on shape and size of GUVs in 0.125µM. A- Fluorescent images of electroformed GUVs treated with 0.125 µM peptides concentration of MERS-nsp 4-1, MHV-nsp 4-3 and MHV-nsp 6-1 r with the corresponding DMSO buffer concentration and imaged at 0 min and 5 min. **B-** GUV relative size. To measure the relative size of the GUVs, the perimeter is estimated by Ramanujan's first approximation, the effective diameter is perimeter divided by π, the average standard deviation for both long and short measurements for a vesicle was also measured and averaged for each GUV for three separate experiments for 40 GUVs each. **C-** GUVs shape, to measure the shape of the GUVs, the ratio between longest and shortest radii were measured and averaged for each GUV for three separate experiments for 40 GUVs each. The scale bar indicates 20µm. Error bars shown are mean ± SEM. ($P > 0.05$; Linear Mixed). Coloured key features of the tested peptide concentration are marked. Each colored group of two columns represents the data for a single peptide test at each time point. Left to right, 0 & 5 min. Some error bars are too small to be observed.

4.3.2.3 Effect of mixing MHV nsp4-3 and nsp6-1 derived peptides on shape and size of GUVs.

To test whether mixing the MHV nsp 4-3 and nsp 6-1 derived peptides together may influence GUV membranes they were used in 1µM concentration and reconstituted with the GUVs as before. The results showed that there was no statistically significant difference on the size and shape of the GUVs at all time points

(P >0.05; Linear Mixed Model) (Appendix 45 and 46) **Figures 4.11 B and C** although as before they still caused membrane permeability due to pore formation (Takahashi et al 2013) **Figure 4.11 A.**

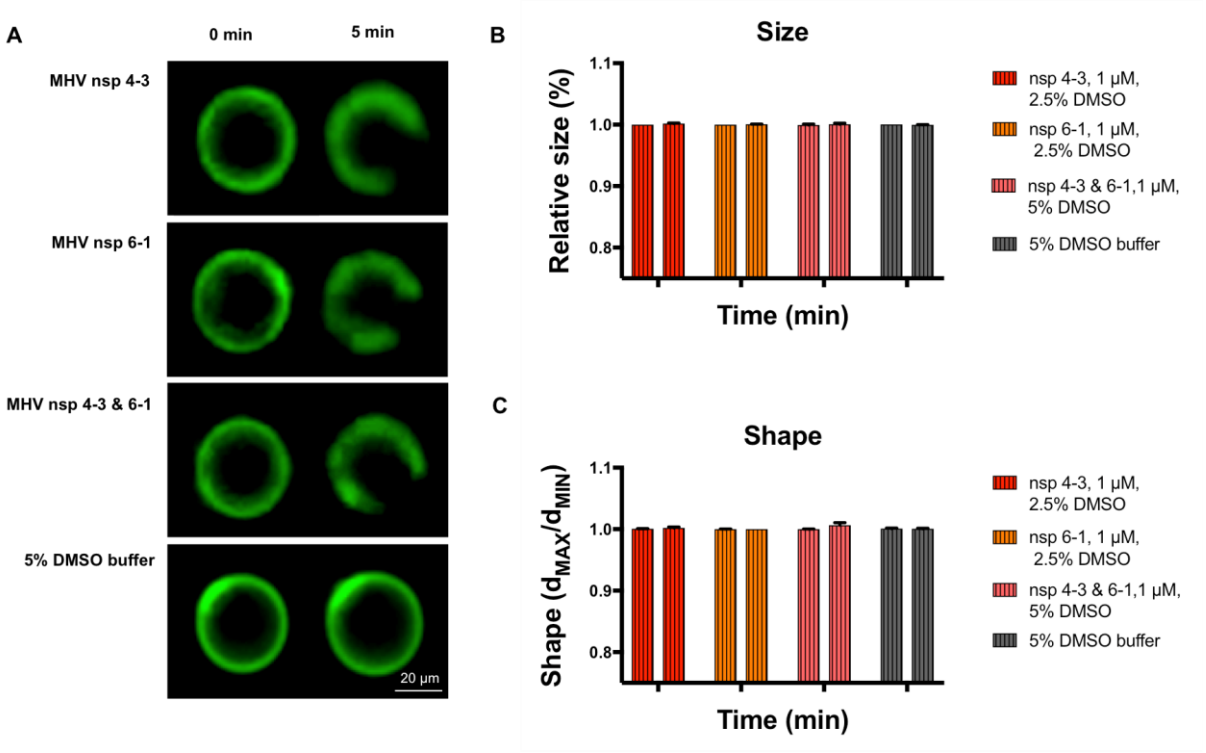

Figure 4.11: Effect of MHV nsp4-3, nsp6-1 and nsp4-3 and nsp6-1 peptides together on shape and size of GUVs. **A-** Fluorescent images of electroformed GUVs treated with 1 µM peptides concentration of MHV-nsp 4-3, MHV-nsp 6-1 and MHV-nsp 4-3 & MHV-nsp 6-1 together with the corresponding DMSO buffer concentration and imaged at 0 min and 5 min. **B-** GUV relative size. To measure the relative size of the GUVs, the perimeter is estimated by Ramanujan's first approximation, the effective diameter is perimeter divided by π, the average standard deviation for both long and short measurements for a vesicle was also measured and averaged for each GUV for three separate experiments for 40 GUVs each. **C-** GUVs shape, to measure the shape of the GUVs, the ratio between longest and shortest radii were measured and averaged for each GUV for three separate experiments for 40 GUVs each. The scale bar indicates 20µm. Error bars shown are mean ± SEM. (P > 0.05; Linear Mixed). Coloured key features of the tested peptide concentration are marked. Each colored group of two columns represents the data for a single peptide test at each time point. Left to right, 0 & 5 min. Some error bars are too small to be observed.

4.3.3. Effect of mutated MERS-nsp4-1 derived peptides on size and shape of GUVs.

As shown earlier, MERS-nsp 4-1, MHV- nsp 4-3 and MHV-nsp 6-1 derived peptide show a cup-like shape in GUV membranes and one of these cup-like forming peptides, MERS-nsp 4-1, was further studied. Key residues within this peptide were mutated in a series of 10 additional peptides synthesized as described in chapter 2 section 2.1 by exchanging the hydrophobic amino acids into an alanine and predicted amphipathic values have been calculated too (see **Table 2.4 and 4.3)**. The results showed there was no statistically significant difference among the MERS-nsp 4-1 mutants (P >0.05; Linear Mixed Model) (Appendix 47 and 48) **Figures 4.12 A, B, and C**, all continued to show the cupping effect with the exception of mutant 6 (V276A) which did not show this change of GUVs shape and resembled the control GUVs treated with buffer only, showing no deformation. Changing individual hydrophobic residues therefore is not sufficient in most cases to affect overall membrane deformation ability. Multiple residue changes were not investigated.

Table 4.3: Amphipathic average for wild type and mutant MERS-CoV nsp4-1 peptides used for *in vitro* analysis.

No.	Designation	Residues	Sequence	Amphipathic average
1	MERS 4-1 (WT)	267-283	FIDIVRRLAVSLFQPIT	3
2	M1	F267A	AIDIVRRLAVSLFQPIT	2.5
3	M2	I268A	FADIVRRLAVSLFQPIT	2.4
4	M3	I270A	FIDAVRRLAVSLFQPIT	2.4
5	M4	V271A	FIDIARRLAVSLFQPIT	2.5
6	M5	L274A	FIDIVRRAAVSLFQPIT	2.5
7	M6	V276A	FIDIVRRLAASLFQPIT	2.4

8	M7	L278A	FIDIVRRLAVSAFQPIT	2.6
9	M8	F279A	FIDIVRRLAVSLAQPIT	2.3
10	M9	I282A	FIDIVRRLAVSLFQPAT	2.5
11	M10	F267A + I268A + I270A + V271A + L274A + V276A + L278A + F279A + I282A	AADAARRAAASAAQPAT	2.4

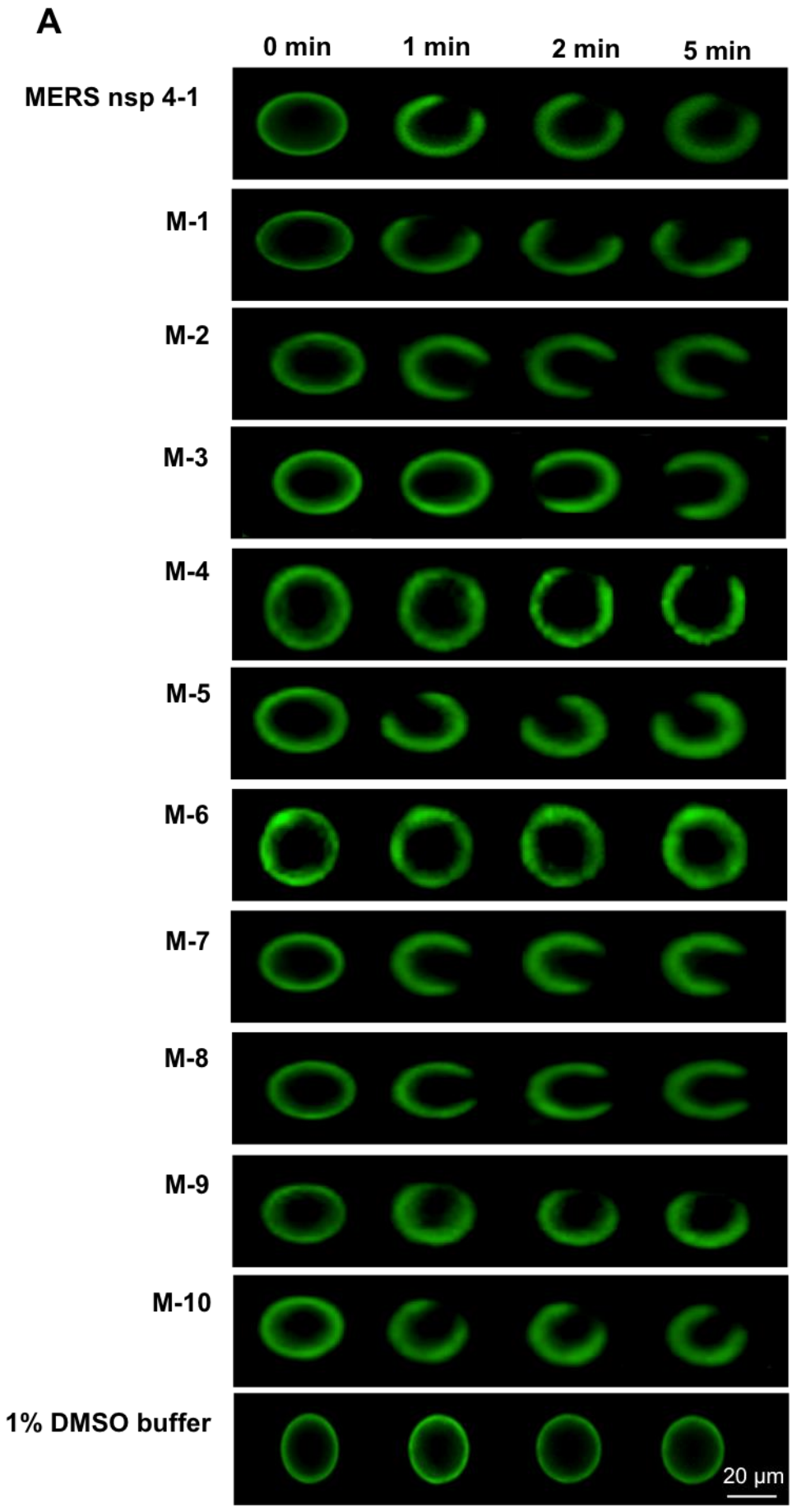
A
0 min
1 min
2 min
5 min
MERS nsp 4-1
M-1
M-2
M-3
M-4
M-5
M-6
M-7
M-8
M-9
M-10
1% DMSO buffer
20 μm

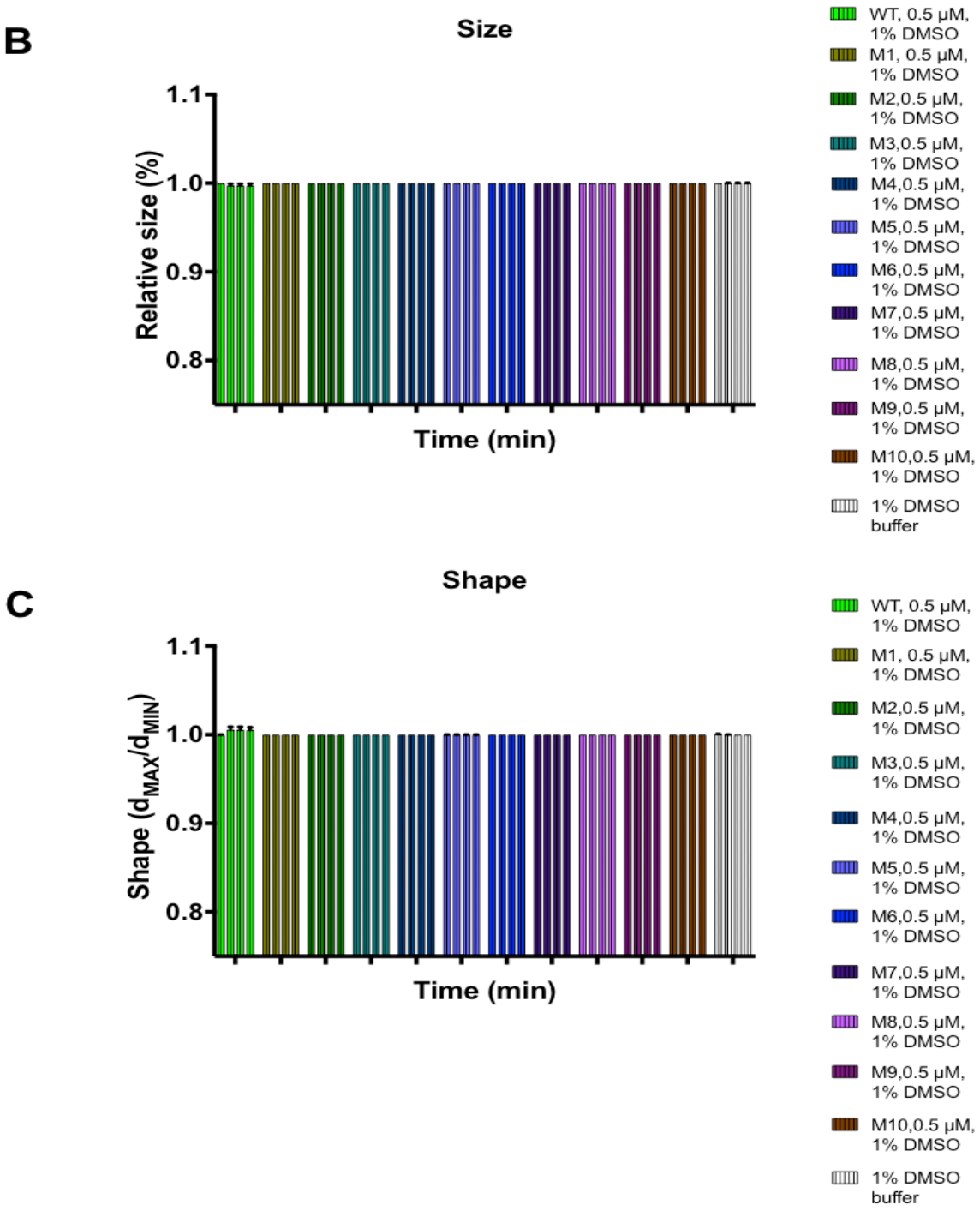

Figure 4.12: Effect of MERS nsp4-1 mutated peptides on shape and size of GUVs. A- Fluorescent images of electroformed GUVs treated with 0.5 µM peptides concentration of mutated MERS-nsp 4-1 with the corresponding DMSO buffer concentration and imaged at 0 min, 1 min, 2 min and 5 min. **B-** GUV relative size. To measure the relative size of the GUVs, the perimeter is estimated by Rumanian's first approximation, the effective diameter is perimeter divided by π, the average standard deviation for both long and short measurements for a vesicle was also measured and averaged for each GUV for three separate experiments for 40 GUVs each. **C-** GUVs shape, to measure the shape of the GUVs, the ratio between longest and shortest radii were measured and averaged for each GUV for three separate experiments for 40 GUVs each. The scale bar indicates 20µm. Error bars shown are mean ± SEM. ($P > 0.05$; Linear Mixed). Coloured key features of the tested

peptide concentration are marked. Each colored group of four columns represents the data for a single peptide test at each time point. Left to right, 0,1, 2 & 5 min. Some error bars are too small to be observed. M1-M10: Mutant 1-Mutant 10.

4.4. Discussion

Bioinformatics of MERS and MHV CoVs suggested the occurrence of many possible membrane binding peptides in both the structural and non-structural proteins of the virus, consistent with the extensive modification cellular membranes in coronavirus infected cells. The studies in this chapter were done to confirm that these peptides did indeed have membrane binding or deformation properties. A particular interest was the fusion peptide in S protein as that has not yet been formally determined. In addition, as the nonstructural proteins were known to induce cellular membrane rearrangement, notably nsp3, nsp4 and nsp6 during the formation of viral ROs, associated with the formation of convoluted membranes and DMVs, the aim of the study was to identify possible membrane active peptides in these peptides too could be key to these activities. Highly conserved peptides with a high score for amphipathic domains were chosen as described in chapter 3 and synthesized and reconstituted into electroformed fluorescently labeled giant unilamellar vesicles (GUVs) and the change in size and shape of the vesicles was recorded.

4.4.1. DMSO effect on the GUVs size and shape.

Dimethyl sulfoxide (DMSO) was used as the common solvent (Yu and Quinn 1994) although it too can induce membrane fusion between phospholipids vesicles and cells (Ahkong et al. 1975) so the influence of various DMSO concentrations on the size and shape of the giant liposome was studied as a necessary control.

The results of the GUVs reconstitution assays and the statistical analysis showed that 0.5%, 1% and 5% DMSO buffers affected neither the size of the GUVs membrane nor their shape **Figures 4.1 A, B and C** consistent with membrane integrity preserved at low DMSO concentration (De La Serna et al, 2004). In higher DMSO concentration including the 13%, 14.7%, 15% and 25.5% DMSO buffers the size of the GUV membranes was changed **Figures 4.1 A, B and C** probably as a result of the decline in the amount of solvent at the membrane interface (Yamashita, Kinoshita and Yamazaki, 2000). High concentrations of DMSO were required to dissolve some of the peptides but a buffer only control was always included to ensure any effect seen was derived from the peptide and not the mobile phase.

4.4.2. Effect of MERS and MHV S2-derived peptides on the GUVs.

The results of the GUV assays showed clear size and deformation changes in the shape of the GUVs membrane due to MERS and MHV-putative FPs **Figures 4.2 A, B, C, D, E and F,** the increase in the size of which might be attributable to the binding of the peptides into the membrane, which would be predicted to lead to an increase in GUV surface area. The same effect on liposomes has been reported for other amphipathic membrane-inserting peptides such as melittin (Takahashi, et al 2013). Additionally, partition of the peptide into the external monolayer of the lipid membrane of the GUV, as well as potential electrostatic repulsion between the peptide and the membrane could be in play, as has been previously reported for a hydrophobic peptide partitioning into the membrane of an electrically neutral phospholipid membranes leading to increase the membrane area (Yamashita et al 2002). Another proposed mechanism for the GUV changed morphology is displacement of the lipid head group by insertion of the amphipathic helix into the

lipid membrane leading to membrane curvature. This proposed mechanism has been established for some proteins such as Sar1p (Lee et al 2005).

Recently, in a SARS study, a region of S (SFIEDLLFNKVTLADAGFMKQY) has been found to induce considerable membrane ordering in a calcium- dependent manner, specifically the LLF motif (Lai et al 2017). In the content of the full S the FP is helped in this function by different components that exist in the ectodomain of the fusion glycoprotein, often known as membrane-active regions, which together lead to the pre-transmembrane deformation (White et al 2008).

As a positive control in these experiments, the M2-infleunza peptide was used. This is a very well characterized peptide, a highly conserved amphipathic helix which has been shown to be sufficient for budding into GUVs (Rossman et al 2010). The GUV assay showed that there was a statistical significance in GUVs shape and formation of intraluminal-vesicles (ILVs) in 17 molar % cholesterol for this peptide as described (Rossman et al 2010) although no statistical significant change in GUVs size was apparent.

In addition to the FP peptides, MERS-HR1, MERS-SHCR and MHV-HR1 also caused GUV deformation and decreased their size. Their interaction with the GUVs was evidently by a different mechanism from the mechanism suggested above, making the GUVs become smaller in size and more rugged in shape after addition of the peptide **Figures 4.2 A, B, C, D, E and F** possibly consistent with fragmentation of the lipid bilayers after peptide insertion. Recently, by Cryo-EM studies, the S pre-fusion state of SARS, MERS-CoV, HCoV-NL63, MHV, HKU1 have been described (Wall et al 2016a; Yuan et al 2017; Kirchodefer et al 2016, Gui et al 2017). These studies show that the S1 subunit is located on top of the S2 stalk thereby applying a structural restriction on S2 subunit. The HR1 regions from the various human

coronaviruses are long helices consistent with these structures being critical to drive the conformational changes that accompany membrane fusion (Yuan et al 2017; Gui et al 2017). In addition, structural studies have identified amino acid substitutions in the S2 subunit and the HR1 motif, which disturb the post-fusion conformation more than the pre-fusion state, leading to a reduction of S-mediated membrane fusion (Wall et al 2017; Krueger et al 2001). The total architecture of the CoV S pre-fusion structures is similar to that of Influenza virus HA, although notably more complex and larger (Li 2016).

It was clear that some peptides showed notable effect on liposomes shape and size, such as MERS-CoV and MHV putative FPs, but others hardly exerted any effect in comparison including MERS and MHV-S2 derived peptides such as MERS-HR2, MERS-SPreTM, MERS-SC, MHV-SHCR, MHV-HR2 and MHV-SPreTM all of which did not cause any changes in the shape or size of the GUV. These peptides may not be membrane active, or might not work independently and may need the other parts of the protein in which they are found. However, it was noted that MHV-SC lead to membrane permeability leading to formation of cup-like GUVs which have been seen by others with peptides that are unstructured in solution but adopt alpha-helical structures once they bind to the lipid bilayers, such as for melittin (Naito et al 2000; Asthana, Yadav and Ghosh, 2004; Constantinescu and Lafleur, 2004). Other examples of cup-like shapes formed by peptides such as the MHV-SC include amphipathic antimicrobial peptides such as magainin and alamethicin (Matsuzaki, Yoneyama and Miyajima, 1997; Matsuzaki et al 1998; Wessman et al 2010). It would be interesting to test the selected peptides at different pH values and identify the effect of pH on the charge and amphipathic nature of them. The activity of a peptide can depend on different molecular properties including charge, pH, hydrophobicity

and amphipathicity (Yeaman and Yount, 2003). It has been shown that low pH increases the level of alpha helical secondary structure of a peptide thereby improving their propensity for membrane interaction (Malik et al 2016). In addition, it has been demonstrated that the terminal net charges impacts the aggregation tendency of hydrophobic peptides (Do et al 2013).

To address the key residues within the MERS putative fusion peptide FP a series of 5 additional peptides **Table 2.2** were included with the reconstituted GUVs, all at 10μM, and their shape and size measured as before. The rationale for choosing these residues is because these hydrophobic amino acids are known for their ability to bind to the membrane. In addition, structural, mutagenic and lipid mixing studies have provided some insight into how this highly-conserved segment functions (Madu et al 2009; Belouzard et al 2012). For example the critical LLF motif has been studied recently using electron spin resonance spectroscopy to reveal membrane ordering by these residues (Lai et al 2017).

The GUV assay, with statistical analysis, showed that while peptides 4 (L894A) and 6 (V898A) continued to show some GUV membrane deformation, albeit with different effects compared to the WT sequence, peptides 2 (I890A), 3 (L893A) and 5 (F895A) did not lead to appreciable deformation in shape or size over the course of the observation suggesting these residues are critical for activity **Figure 4.5A**. Interestingly, when aligned with other S sequences, positions Ile 890 and Leu 893 are wholly invariant while Phe 895 undergoes one highly conservative change to Tyr in the S protein of Bat HKU9 CoV **Figure 3.1**.

4.4.3. Effect of MERS and MHV M and E derived peptides on the GUVs.

MERS and MHV M-derived peptides including MERS-MPTM3, MERS-M Proline region, MHV-MTM3, MHV-MPTM3 and MHV-M Proline region, MERS-EPTM, MHV-ETM and MHV-EPTM were all tested on GUVs in different DMSO buffer concentrations. MERS-MPTM3, MERS-M Proline region and MHV-MPTM3 were positive in these assays while the MHV-M Proline region peptide showed the cup-like shape suggesting a permeability activity as suggested for the MHV-SC peptide. MERS-EPTM and MHV-ETM peptides had no influence on GUV membranes although MHV-EPTM deformed the shape of the GUV and decreased their size similar to that observed for the MERS-HR1 peptide.

4.4.4. Effect of MERS and MHV nsp3, nsp4 and nsp6 derived peptides on the GUVs.

CoVs nsp3, nsp4 and nsp6 are characterized by membrane spanning features and are considered the main drivers for directing the formation of replication organelles (ROs) (Angelini, Neuman and Buchmeier, 2014; Neuman, 2016). Nsp3 is a large multi-domain protein comprising 10-16 domains which performs numerous roles in the viral life cycle (Neuman and Buchmeier, 2016). Nsp3 can perform as a scaffold protein to interact with itself, other CoV nsps and host proteins (von Brunn et al 2007; Pfefferle et al 2011; Ma-Lauer et al 2016). Nsp3 is also crucial for the presence of CMs and DMVs in MHV, SARS-CoV and MERS-CoV (Snijder et al 2006; van Hemert et al 2008; Hagemeijer et al 2011; de Wilde et al 2013; Hagemeijer et al 2014). Predominantly, nsp3 is a key player in CoV replication, yet many roles of nsp3 remain to be explored.

Nsp3 spans the membrane two times and has one luminal loop, while nsp4 spans the membrane four times and has three luminal loops, finally, nsp6 contains three luminal loops and spans the membrane five times (Oostra et al 2007; Clementz et al 2008; Beachboard et al 2015). It is uncertain how the CoV integral proteins induce membrane modification or which regions of the proteins are responsible for DMV formation.

The GUV assay and the statistical analysis showed a significant variation of membrane binding in which the addition of peptides MERS-nsp 3-1, MERS-nsp 3-3 and MHV nsp 3-1 and nsp 3-2 lead to membrane deformity and decrease in GUV size compared to the control buffer whereas the addition of MHV-nsp 3-3 peptide showed no effect on GUV membranes, **Figure 4.8,** suggesting that MERS-nsp 3-1 MERS-nsp3-3 and MHV-nsp 3-1 and nsp 3-2 peptides are membrane active peptides while MHV-nsp 3-3 peptide is likely a non membrane active region.

Similarly, The GUV assay and the statistical analysis show a significant variation of membrane binding in which the addition of these peptides MERS-nsp 4-1, 4-2 and 4-3 and MHV-nsp 4-2 and nsp 4-3 lead to membrane deformity, pore formation and membrane permeability and decrease in GUV size compared to the control buffer whereas the addition of MHV-nsp 4-2 showed no effect on GUV membranes, **Figure 4.8,** suggesting that MERS-nsp 4 peptides and MHV-nsp 4-2 and 4-3 are membrane active peptides while MHV-nsp 4-1 peptide is likely not.

It has been shown that the minimal requisites for DMVs pairing seems to be the C-terminal third of nsp3 that comprise both transmembrane regions and the luminal ectodomain and the N-terminal region of nsp4 involving the first three transmembrane regions at least (Sparks, Lu and Denison, 2007; Hagemeijer et al 2014). As most of the tested peptides in this study are in the C-terminal region of

nsp3 and the nsp4-derived peptides are mostly in the N-terminal region see **Figures 3.10 and 3.11,** these findings are consistent with the importance of these segments in the viral life cycle as suggested.

Many studies have revealed that the MHV nsp4 luminal loop is essential for viral replication (Sparks, Lu and Denison, 2007; Beachboard, Anderson-Daniels and Denison, 2015). In addition, MHV and SARS nsp4 contain two and one N-glycosylated sites respectively in the first luminal loop (Clementz et al 2008; Gadlage et al 2010; Nagy and Pogany, 2012). Mutations in both N-glycosylated sites of MHV, the virus attenuated and DMV formation was hindered suggesting that nsp4 has an important role in ROs formation (Gadlage et al 2010; Beachboard, Anderson-Daniels and Denison, 2015). Recently, in MERS-CoV study, it was shown that MERS nsp3 and nsp4 are necessary and sufficient to induce all the membrane- rearrangement steps required for triggering DMV formation, probably through transformation of the ER membrane into a reticulovesicular network (RVN) comprised of DMV and modified ER (Oudshoorn et al 2017).

Alignment of the nsp6 amino acids sequences shows high conservation in the C-terminal hydrophobic region suggesting evolutionarily conserved functions (Baliji et al 2009). Peptides MHV-nsp 6-1, MERS-nsp 6-1 and MHV-nsp 6-2 show membrane pore formation and membrane deformity, suggesting them as a membrane active regions in the nsp6, consistent with this domain acting as a wedge-like amphipathic helix which can stimulate bending by inducing positive membrane curvature (McMahon and Gallop, 2005; McMahon, Kozlov and Martens, 2010; Lundin et al 2014). In comparison to MERS-nsp 6-2 which showed no membrane activity and was concluded to be a non-membrane active region.

4.4.5. Effect of MERS-nsp4-1 mutated peptides on the GUVs.

The GUV assay and the statistical analysis showed that most of the MERS-nsp 4-1 mutants had no impact on membrane binding or a pore formation as most of the mutants still able to induce a pore in the GUV membranes. However, mutant 6, the Valine (V276A) was unable to induce the pore in the GUV membrane **Figure 4.12**. The inability of the valine mutant to efficiently generate the cup like shape in the GUV assay may be in part attributable to an overall reduction in the amount of the MERS-nsp4-1 valine mutant binding to the membrane as a consequence of reduced hydrophobicity.

The MERS-nsp 4-1 peptide is loop1 of this protein (see **Figure 1.6)** and in the MHV study, it has been shown that mutations in nsp4 loop1 change DMV morphology and likely dysregulate nsp4 functions in DMV formation (Beachboard, Anderson-Daniels and Denison, 2015). Recently, it has been shown that, nsp4 alone is essential and adequate to generate membrane pairing in IBV (Doyle et al 2018) making this protein an attractive target for antiviral therapy.

5 Cloning and expression of MERS-S protein in human embryonic kidney cell line (HEK-293T cells).

5.1 Introduction

Coronavirus infection starts with the interaction of the viral spike protein, which protrude as trimers on the surface of CoV virions (Delmas and Laude, 1990), with host receptors such as hDPP receptor for MERS-CoV or hACE2 for SARS-CoV (Li et al 2003; Boheemen et al 2012; Ohnuma et al 2013). Each monomer consists of two subunits, S1, which is responsible for receptor binding and S2, which contains the membrane fusion machinery including the fusion peptide FP (Babcock et al 2004; Wong et al 2004). Membrane fusion is mediated by S protein activation following proteolytic cleavage and receptor binding, with or without pH triggering (Li et al 2006; White et al 2008). When viral fusion is activated in S proteins expressed at the cell surface, cell-cell fusion occurs with the formation of syncytia (Chan et al 2013).

Cleavage of the fusion protein is a well-known property of class I viral fusion proteins (White and Whittaker, 2016) and cleaved CoV-S exhibits a higher efficiency of cell-cell and virus-cell fusion and in cases where the protein is poorly cleaved, S can be activated by treatment with trypsin (Simmons et al 2004). Considerable effort has been made to identify and locate CoV FPs (Guillen et al 2008a; Guillen et al 2005; Guillén et al 2008b) but it remains the case that the precise location and sequences of many are still debatable (Belouzard et al 2012; Ou et al 2016). The identification and validation of the MERS FP was therefore of considerable interest.

Leading on from the results of Chapter 4, to confirm a role for the putative FP in a biological system and because the fusion peptide is crucial for S protein-mediated membrane fusion, a syncytium assay based on the expression of complete MERS-S protein was established, similar to that described for IBV (Yamada and Liu,

2009). Once established with the wild type protein, the assay acted as a baseline for the incorporation of mutations in the presumed FP sequence to explore whether any of them would change MERS-CoV S protein mediated cell-cell fusion. To enable this a complete S coding sequence was synthesized and cloned into a suitable expression vector, after which expression and biological activity was confirmed. This vector then acted as the template for various mutations designed to probe the identity of the MERS S FP.

The S coding region was expressed from the CAG promoter present in vector pTriEx1.1 **Figure 5.1**. The S sequence used were derived from the MERS-CoV: AHI48550.1, and purchased as two dsDNA fragments encoding the S1 and S2 subunits from Integrated DNA Technology (IDT). These two fragments were assembled using infusion cloning according to the manufacturers instruction protocol (Clontech) as discussed in Chapter 2 section 2.19. This method performs a directional cloning of inserts into any vector with high efficiency for any DNA fragment size. The technology depends on recognition and fusion of 15 bp overlap sequences at the ends of each of the target DNA fragments and linearized vector. These 15 bp overlaps are added during the dsDNA fragment design and are present in the sourced DNA. The pTriEx1.1 vector was chosen to clone MERS S protein as it was compatible with expression in both mammalian and insect cells, **Figures 5.1,** and was prepared by linearization with *Nco*I and *Xho*I restriction enzymes **Figure 5.2**. After the infusion reaction, the MERS-S-vector mixture was transformed into Stellar competent cells (*E. coli* HST08 strain) and colonies that grew overnight were colony screened using PCR with primers that flanked the site of insertion **Figure 5.3.** Positive colonies were grown for the extraction of plasmid DNA and positive plasmids send for sequencing according to the instructions on the Source Bioscience

website. A positive sequence encoding a full-length S protein was transfected into HEK-239T cells to test for expression of the S protein. In parallel, the presence of the receptor DPP4 was confirmed by staining with a DPP4 monoclonal antibody **Figure 5.7.** To assess the role of the residues identified in the peptide-GUV binding assay in syncytium formation each mutation was introduced into the S sequence as listed in **Table 2.12** in Chapter 2, section 2.12 by synthesizing and exchanging DNA fragments that contained the FP sequence between the *Eco*RI and *Nhe*I restriction sites present in the WT clone **Figure 5.4**. Ligations were transformed into Stellar competent cells (*E. coli* HST08 strain) and again screened by colony PCR, **Figure 5.5**. As before, positive colonies were sent for sequencing **Figure 5.6** and the assays developed with the WT sequence were repeated for each mutant **Figures 5.8 and 5.9**.

5.2 Results

5.3. In-Fusion cloning

In-Fusion cloning was utilized in this study. This technology assures directional cloning of DNA fragments into any vector with high cloning efficiency for different DNA fragment size. MERS-S was cloned so that it would be expressed as a C-terminal His tagged fusion protein following insertion between the *Nco*I and *Xho*I sites in the pTriEx1.1 vector - see **Figure 5.1.** The use of the epitope tag was part of the design to allow detection of any expressed proteins using SDS-PAGE analysis and western blot with His tag specific antibodies if required.

5.4. Transformation of In-Fusion products into competent *E. coli* cells

The In-Fusion reaction mixes were transformed into chemically competent Stellar™ *E. coli* cells and LB agar containing ampicillin was used to select the transformants. About 12 colonies were chosen randomly and screened by PCR using either T7 forward2 as a forward primer and TriExDOWN2 or fragment specific primers as the reverse primer **Table 2.13**. Then agarose gel electrophoresis was used to analyze the amplification products. Four of the screened colonies were positive for the correct sized WT ~ 4152 bp **Figures 5.3.** Similarly, for the mutants following exchange of a DNA fragment encoding the FP region **Figure 5.5.** LB broth containing ampicillin was inoculated by putative positive colonies and grown overnight at 37°C with shaking. Next day, plasmid DNA was purified using a Miniprep Kit following the manufacturer's protocol. The DNA was measured using the Nanodrop spectrophotometer and sequenced using Sanger Sequencing (Source BioScience) using T7 forward2 and TriExDOWN2 primers, **Figure 5.6**. Sequence

verified clones were thus generated for the parental MERS S sequence and for each of five mutants, which modified the FP sequence.

5.5. Immunofluorescent staining of HEK- 293T cells with Anti-DPP4

Coronaviruses use a variety of receptors ranging from sugars to extended cell surface proteins (reviewed in (Li, 2015) and the receptor for MERS infection has been identified as Dipeptidyl peptidase-4 (DPP4) found on a variety of cell types including epithelial cells of the respiratory tract (Boheemen et al 2012; Raj et al 2013).

To detect and confirm the presence of DPP4 receptor on HEK- 293T cells surface, verifying that the cells were a *bona fide* model for the induction of S mediated syncytia, HEK-293T cells were fixed and immunostained with an anti DPP4 antibody and suitable conjugate. The day before staining, 1.25 x 10^5 were seeded on glass coverslips in 12 well plate and incubated for 24 h at 37°C / 5% CO_2. Next day, the media was removed and cells washed twice with cold PBS for 5 minutes, then the cells were fixed with 3% formaldehyde for 1 h at room temperature. The cells were washed twice with wash buffer (3% BSA, 0.1 Tween-20 /PBS) then incubated with the primary Ab (Anti-DPP4 (Anti-CD26 Ab, ab119346 (Abcam) at a dilution of 1:20 for 1 h at room temperature. After incubation cells were washed twice with wash buffer and incubated with a secondary Ab (Anti-mouse Alexa Fluor 488) at 1:20 for 1 h at room temperature. The cells were washed twice with wash buffer for 15 min and counterstained with DAPI. The fixed cells were mounted by placing the cover slip upside down on a clean glass slide with a drop of Slowfade™ Gold antifade reagent before being imaged by an EVOS-FL digital fluorescent microscope, and the results showed and confirmed the presence of the DPP4 receptor on the HEK-293T cell

surface confirming reports that the kidney tissue expresses DPP4 (Boonacker and Van Noorden, 2003) **Figure 5.7**. Transfected COS7 cells could have acted as an independent positive control expressing DPP4 with non-transfected cells as the negative. Staining with the secondary Ab only would provide a suitable antibody control in all cases. Images were captured at 20X magnification.

5.6. Transfection of HEK-293 cells

Lenti-X 293T cells were cultured and maintained in Dulbecco's modified Eagle medium (DMEM) (Sigma Aldrich) supplemented with 10% fetal bovine serum (FBS) (GE Healthcare) and antibiotics penicillin/streptomycin (penicillin 100 U/ml, streptomycin 0.1 mg/ml; Gibco/Invitrogen) in 12 well plates. The cells were transfected with plasmid DNA to express WT or mutant MERS-S using Lipofectamine 3000 transfection reagent (Invitrogen) following the manufacturer's protocols. After incubation for 24 hr, cells were washed twice with cold PBS and fixed and permeabilized for immunostaining.

5.7. Immunofluorescent staining and fusion assay for WT MERS-S and mutants

To execute membrane fusion, S protein must be activated by receptor binding and proteolytic cleavage with or without pH triggering (Li et al 2006; White et al 2008). As it was unclear to what extent S would be cleaved in 293T cells the protocol made use of trypsin as a fusion trigger for the spike protein. Thus the ability of the WT and mutants to form syncytia were assessed in the presence of trypsin as described before (Madu et al 2009)**.**

A total of 1.25 x 10^5 293Tcells were seeded on glass coverslips sited in a 12 well plate and incubated for 24 hr at 37 ˚C / 5% CO_2. Next day, the cells were transfected with plasmid DNA to express the WT and mutant MERS-S proteins using Lipofectamine 3000 transfection reagent (Invitrogen) following the manufacturer's instruction protocol and incubated for 24hr at 37 ˚C / 5% CO_2. A control vector pTriEx1.1-GFP-His (a gift from B. Abdulsattar) which carried the Green Fluorescent Protein (GFP) gene was also transfected into cells and used to visualize the efficiency of transfection. Twenty four hours after the transfection, the medium was removed and the cells rinsed briefly with pH 5 buffer then incubated in the same buffer for 5 minutes at 22 ˚C. The acidic buffer was discharged and S cleavage was ensured by treated with 2 µg/ml of trypsin in Opti-MEM (Sigma Aldrich) for 30min at 37°C/ 5% CO_2 as previously described (Madu et al 2009). The media was then replaced with complete DMEM and the cells were further incubated at 37˚C / 5% CO_2 for 1 h. The cells were washed twice with cold PBS for 5 minutes, then fixed with fixation buffer (eBioscience™) for 1 hr at room temperature. The cells were then washed 2 x with permeabilization buffer (eBioscience™) for 5 min each at room temperature in the dark following the manufacturer's protocol. Cells were then incubated with the primary Ab (Anti-MERS-S, D12, Absolute Antibody) at 1:500 for 1 hr at room temperature and, following washing for 2 x 5 min with wash buffer they were incubated with a secondary Antibody conjugate (Alexa flour 488, Life technologies) 1:500 for 1 hr at room temperature. The cells were again washed twice with wash buffer for 5 min at room temperature in the dark after which a drop of Slowfade™ Gold antifade reagent was added on a clean glass slide and the coverslip was mounted upside down on the slide and imaged using an EVOS-FL digital fluorescence microscope **Figures 5.8 and 5.9**.

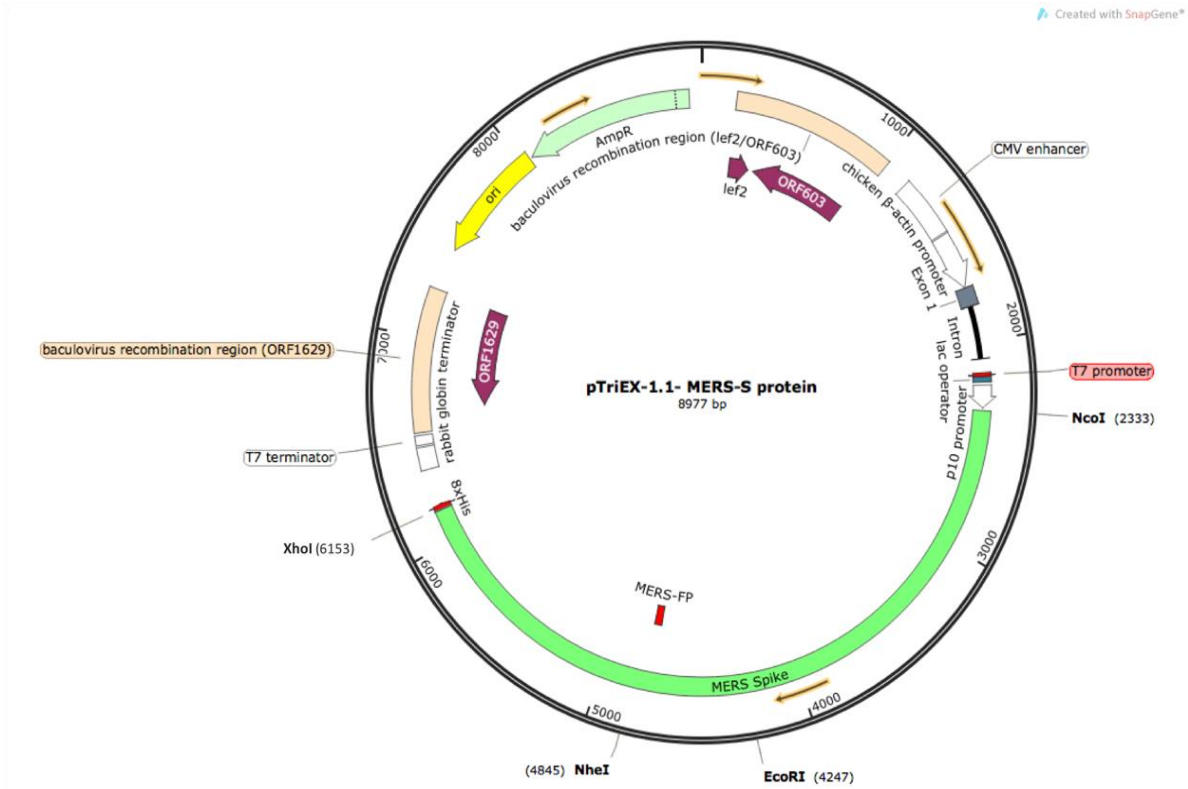

Figure 5.1: The cloning map for pTriEx1.1 with MERS-S. Key features of the plasmid are marked.

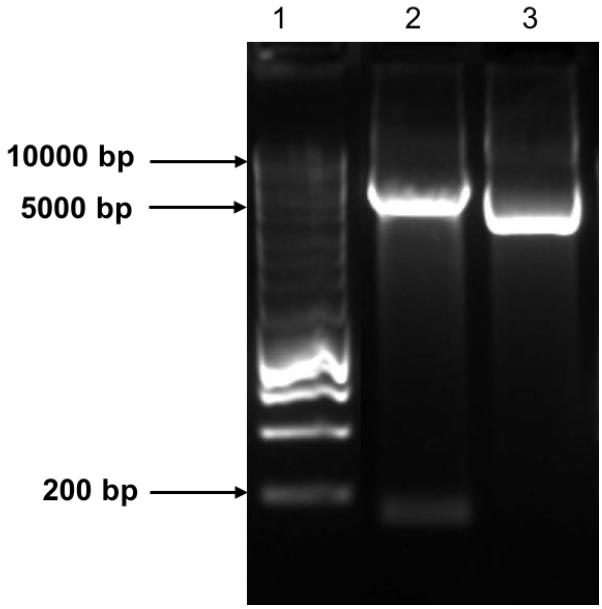

Figure 5.2: Gel electrophoresis of double digest of pTriEx1.1. Lane 1: Hyperladder 1kb, Lane 2: pTriEx1.1 vector digested with *Nco*I and *Xho*I (5155 bp). Lane 3: Uncut pTriEx1.1. vector (5301 bp). The excised 146bp *NcoI* and *XhoI* band represents the multicloning site that is exchanged for the S fragment in this case. The residual vector lacking this fragment was used for the cloning reaction. The image shown is a composite of individual lanes from a single gel where irrelevant lanes have been removed.

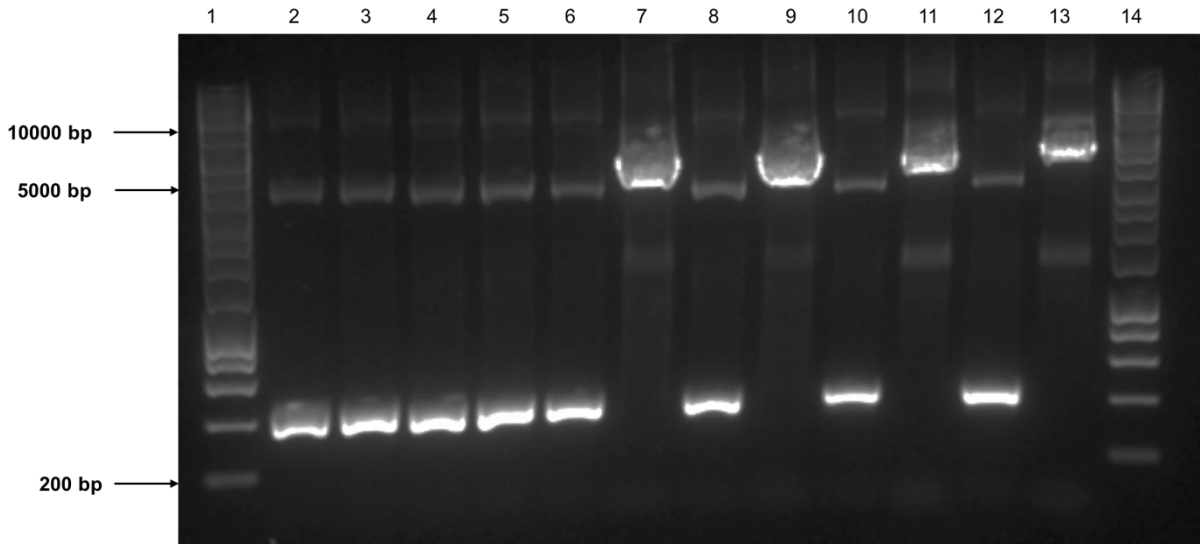

Figure 5.3: Gel electrophoresis of PCR of MERS-S in pTriEx1.1 plasmid. 12 colonies were screened for the presence of WT S (4152 bp). Lane 1: Hyperladder 1kb, Lane 2-13: The PCR product corresponding to 1-12 transformants. Lane 14: Hyperladder 1kb.

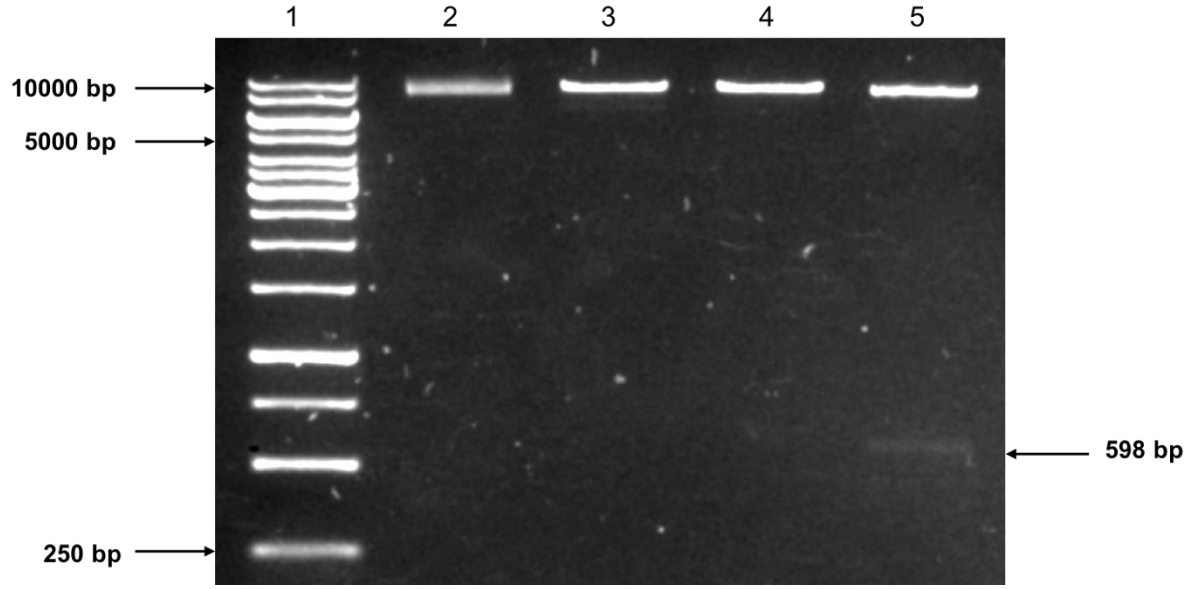

Figure 5.4: Gel electrophoresis of double digest of pTriEx1.1 for ligation cloning of mutated fragments. Lane 1: Hyperladder 1kb, Lane 2: pTriEx1.1-MERS-S (8977 bp). Lane 3: pTriEx1.1-MERS-S digested with *EcoRI*. Lane 4: pTriEx1.1-MERS-S digested with *Nhe*I. Lane 5: pTriEx1.1. MERS-S digested with *Eco*RI and *Nhe*I (8379 bp+598bp). The smaller excised *Nhe*I and EcoRI band represents the WT sequence that is exchanged for the S mutant fragments in this case. The residual vector lacking this fragment was used for the ligation reaction.

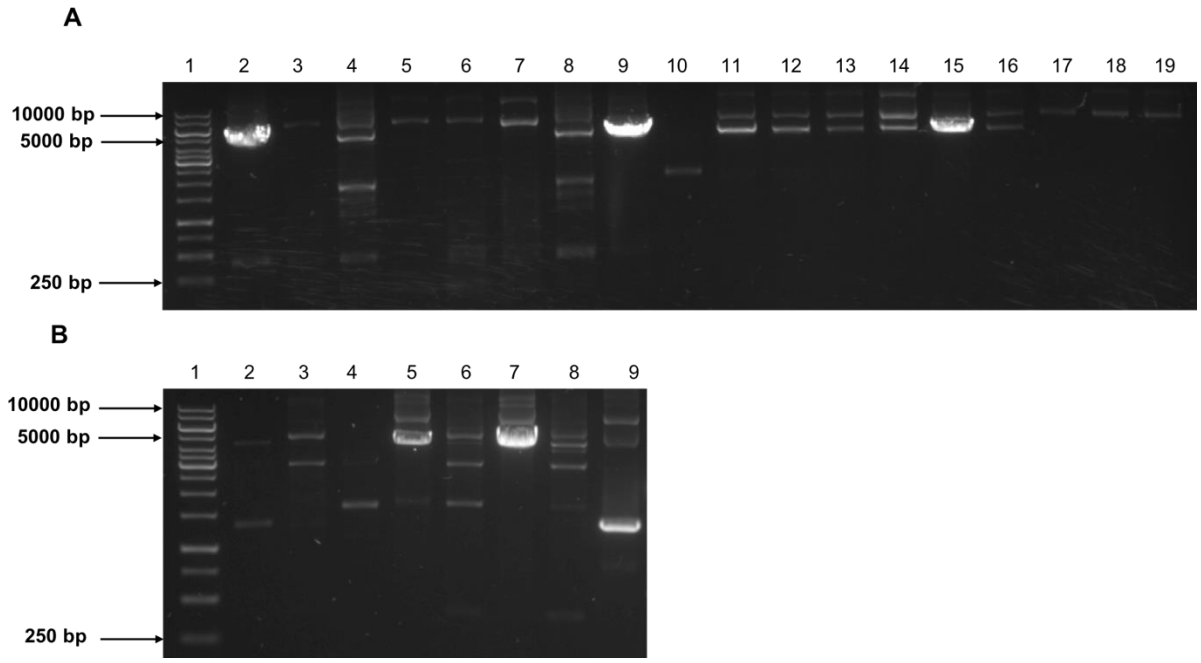

Figure 5.5: Gel electrophoresis of PCR screen for MERS-S mutations. A-18 colonies were screened for the presence of I890A, L893A, and L894A mutants. Lane 1: Hyperladder 1kb, Lane 2-19: The PCR product corresponding to 1-18 transformants. Tracks 2, 9 and 15 contain the correct target size amplicon**. B-** 8 colonies were screened for the presence of F895A and I890A+L893A+F985A mutants respectively. Lane 1: Hyperladder 1kb, Lane 2-9: The PCR product corresponding to 1-8 transformants. Tracks 5 and 7 have the correct sized amplicon.

Figure 5.6: Sequences alignment of 5 mutants with wild type MERS-S. Sequence of the 5 correctly sized isolates derived from the screen in Figure 5.5 were determined and aligned with the WT sequence using Snapgene software. Red boxes represent the introduced alanine mutations.

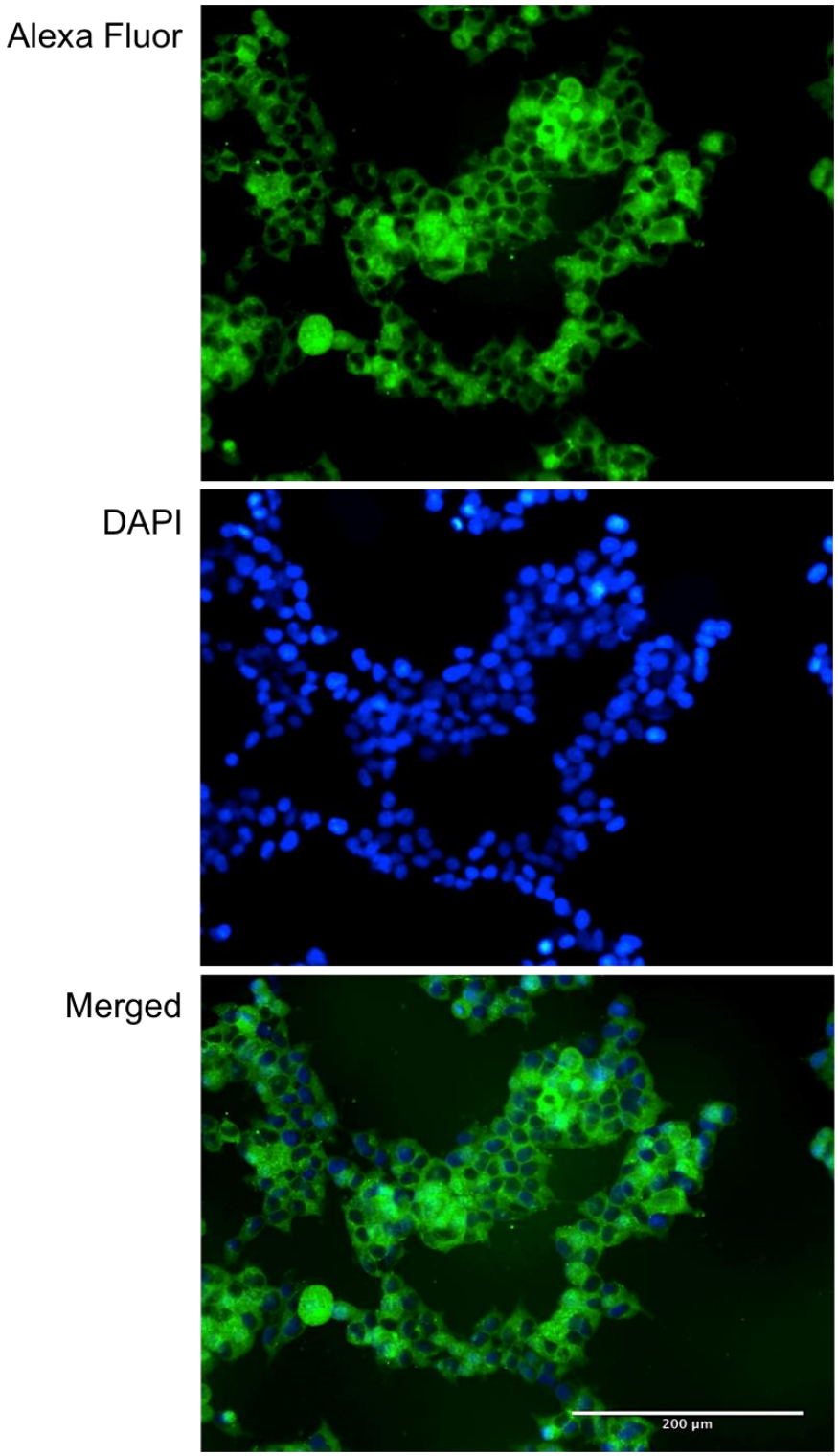

Figure 5.7: Confirmation of DPP4 receptor expression. HEK-239T cells were fixed with 3% formaldehyde and labeled with primary anti-DPP4 antibody, then incubated with secondary Alexa Fluor 488 goat anti mouse antibody (green). Nuclei were counterstained with DAPI (blue). Images were captured at 20X magnification power. The scale bar indicates 200 µm.

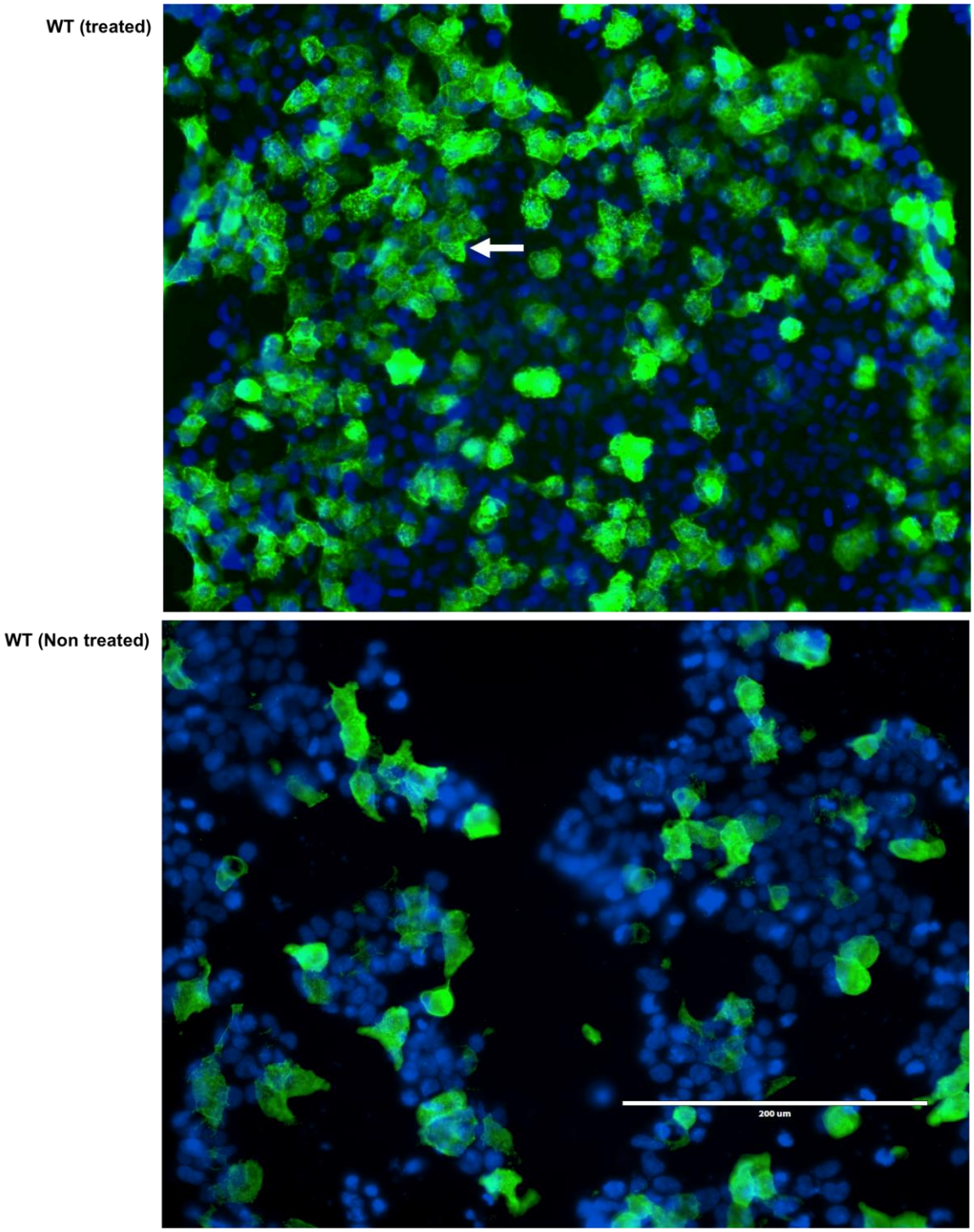

Figure 5.8: High magnification demonstration view of syncytium formation mediated by WT treated and non treated MERS-CoV spike proteins. HEK-239T cells were transfected with vectors encoding WT MERS-CoV S or one of the alanine mutants. The cells were treated with 2µg trypsin/ml for 30 minutes at 37 °C prior to a 5-minute acid pulse. Following recovery in complete DMEM for 1 h at 37 °C the cells processed and visualized as described. White arrow indicates the presence of syncytia induced by the wildtype. Images were captured at 20X magnification power. The scale bar indicates 200 µm.

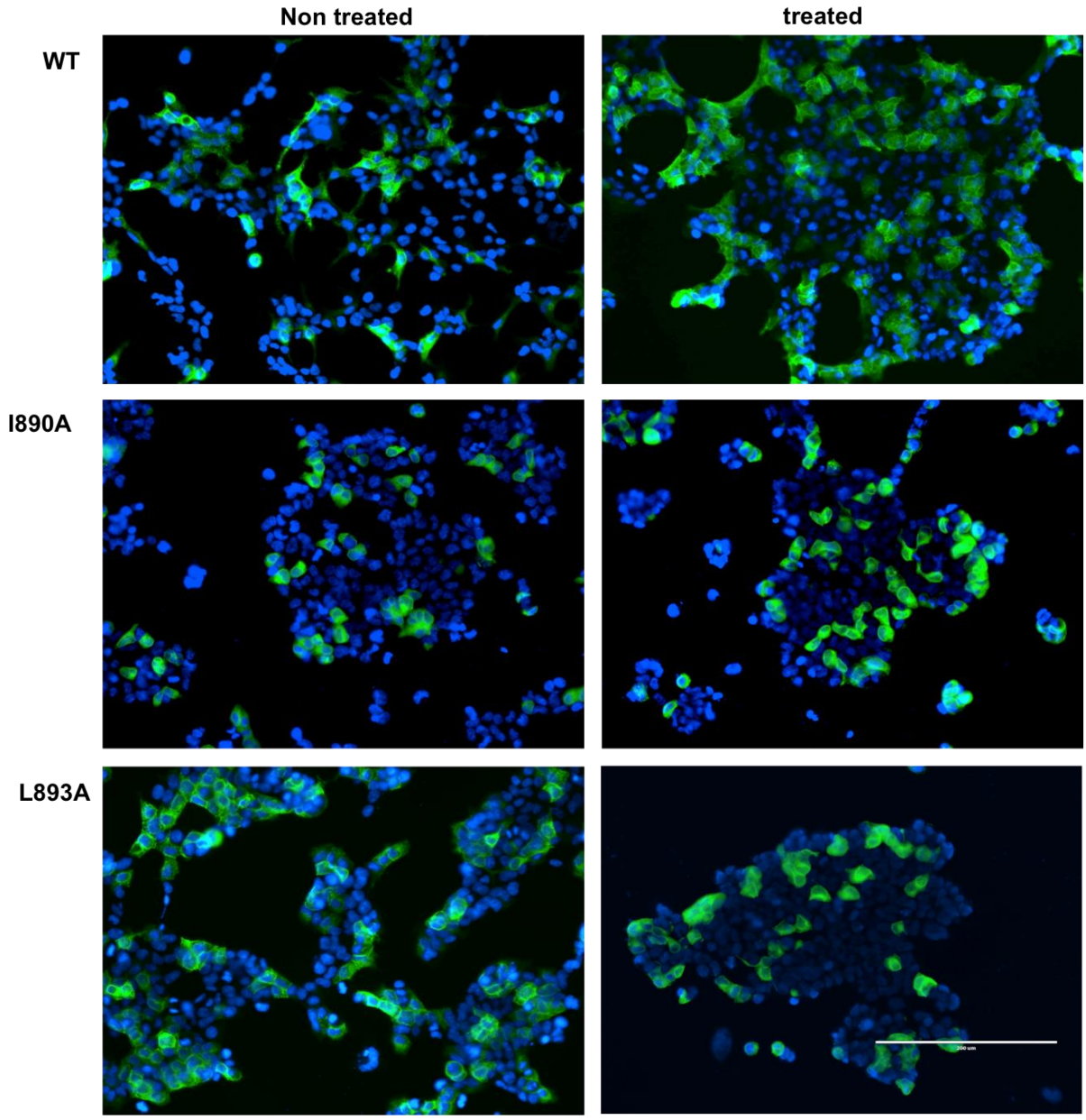

Figure 5.9: Syncytium formation mediated by WT or mutant MERS-CoV spike proteins. HEK-239T cells were transfected with vectors encoding WT MERS-CoV S or individual alanine mutants. The cells were either untreated or treated with 2µg trypsin/ml for 30 minutes at 37 °C prior to a 5-minute acid pulse. Following recovery in complete DMEM for 1 h at 37 °C the cells processed and visualized as described. Images were captured at 20X magnification power. The scale bar indicates 200 µm.

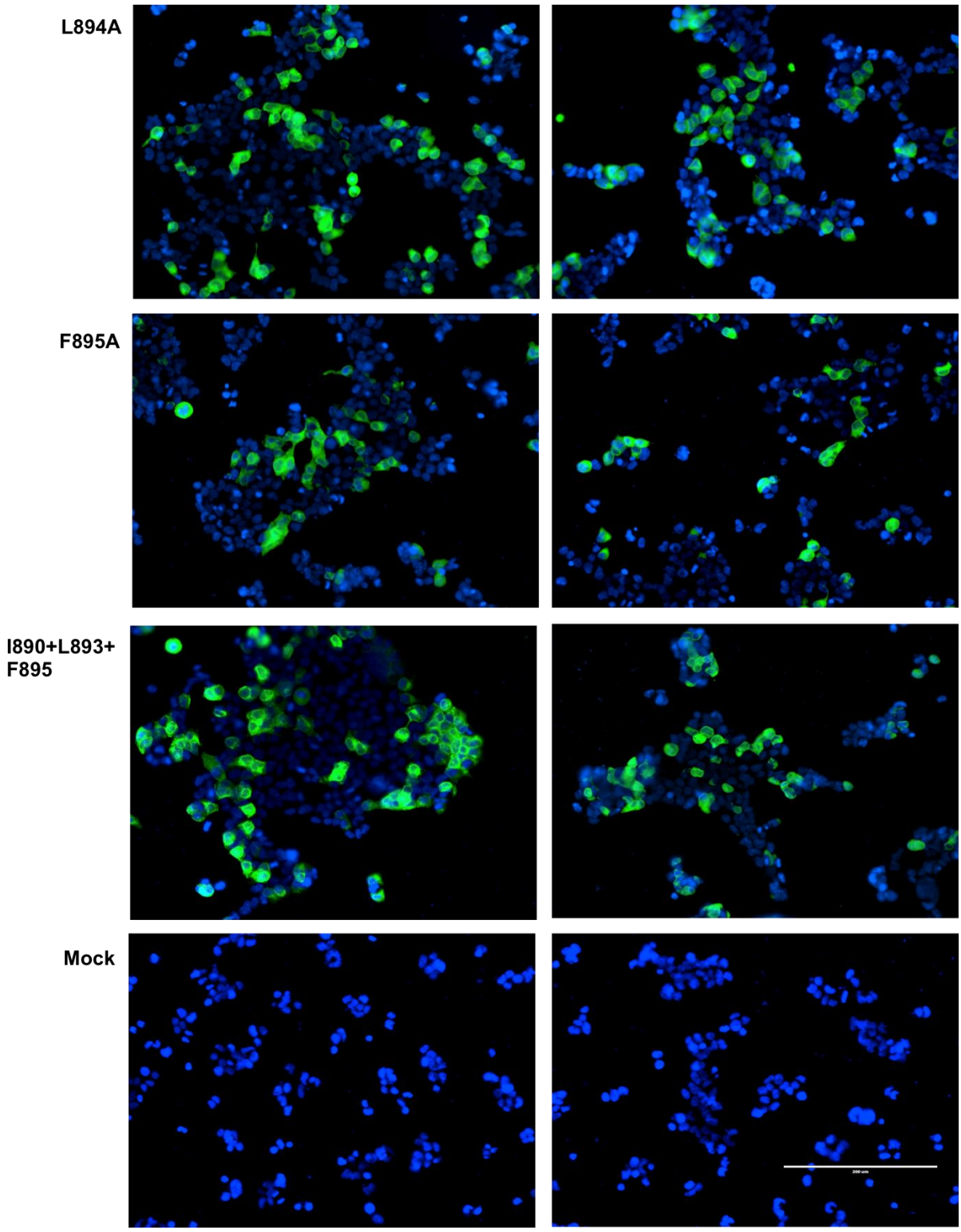

Figure 5.9 (continued): Syncytium formation mediated by WT or individual mutant MERS-CoV spike proteins. HEK-239T cells were transfected with vectors

encoding WT MERS-CoV S or alanine mutants. The cells were either untreated or treated with 2µg trypsin/ml for 30 minutes at 37 °C prior to a 5-minute acid pulse. Following recovery in complete DMEM for 1 h at 37 °C the cells processed and visualized as described. Images were captured at 20X magnification power. The scale bar indicates 200 µm.

5.8. Discussion

The studies in this chapter were carried out to investigate the putative fusion peptide of MERS-CoV S, which was tentatively identified in previous peptide studies. Despite fusion of the virus and host cell membranes mediated by the virus spike protein S, being a key step in the MERS CoV replication cycle the location of the fusion peptide within MERS S protein has not been precisely mapped. Isolated peptides and giant unilamellar vesicles (GUV) were used to demonstrate membrane binding for a peptide located near the N-terminus of the S2 domain in MERS-CoV as shown in Chapter 4. Key residues required for activity were mapped by amino acid replacement but their relevance *in vivo* remained to be tested. Here validation of the presumed FP function was sought by their introduction into a recombinant MERS S protein expressed in mammalian cells. Mutations preventing membrane binding *in vitro* as demonstrated in Chapter 4 also abolished S mediated syncytium formation **Figures 5.8 and 5.9** consistent with the identified peptide acting as the fusion peptide for the S protein of MERS-CoV.

To enable the work the sequence encoding MERS-CoV spike protein was synthesized *de novo* and cloned into the expression vector pTriEx 1.1. Mutants were synthesized and cloned similarly and all constructs were confirmed by DNA sequence prior to use. Plasmids encoding WT and mutant S were transfected in HEK-293T mammalian cells and their expression detected with a monoclonal antibody specific for S. The presence of the receptor DPP4 was confirmed by straining with a DPP4 monoclonal antibody **Figure 5.7**. When transfected cells were

cultured in the presence of trypsin, to ensure maturation of the spike protein when endogenous cleavage is inefficient (Millet et al 2016), and subject to an acid pulse followed by a period of recovery, profuse syncytia were observed consistent with S mediated fusion as shown in **Figures 5.8.** This figure, at high magnification to act as an example, clearly demonstrates syncytia formed in WT S or lack of syncytia, individual cell staining, in the L893A mutant. Qualitative microscopy analysis was performed to assess the average sizes of the syncytia produced following WT S or mutant expression. A more quantitative analysis of syncytia formation could have included measurement of luciferase activity, as previously described (Ou et al 2016). Once established this assay was used to assess the role of each of the residues identified in the peptide-GUV binding assays in syncytium formation. To do this, each mutation was introduced into the S sequence and the assays repeated with syncytium forming ability screened following acid pulse as before. In all cases, while the expression of MERS CoV S with mutations at I890A, L893A, L894A and F895A was not compromised by the introduced mutations, cell to cell fusion was not apparent following either post transfection treatment **Figure 5.9.** These data correlate with the membrane deformation activity of peptides including the same mutations and confirm the $I_{890}L_{893}F_{895}$ core identified by GUV binding as discussed in Chapter 4 as essential for activity as also critical for cell fusion.

The fusion protein S of coronavirus is essential for virus infectivity and antisera that block either receptor binding or fusion activity are protective (Channappanavar et al 2015; Volz et al 2015; Jiaming et al 2017). In addition S is a target for therapeutic intervention via peptides that compete with the fusion reaction and the cleavage between S1 and S2 (Du et al 2017). Work discussed in earlier chapters, based on the alignments of the spike protein of MERS with several other

coronavirus spike proteins, revealed a conserved sequence just downstream of the S2' cleavage site with homology to a sequence previously reported to contain the fusion peptide of SARS S (Madu et al 2009). Studies with the relevant peptide showed that it increased the size, and deformed the shape, of GUVs consistent with partition of the peptide into the external leaflet of the lipid membrane as has been reported for peptides derived from other amphipathic membrane-inserting proteins such as Melittin (Takahashi et al 2013) or Sar1p (Lee et al 2005).

Single amino acid substitution experiments revealed a key role in GUV deformation for hydrophobic amino acids Isoleucine, leucine and phenylalanine located in the central region of the putative fusion peptide as shown in Chapter 4 and the same residues were found to be critical for syncytium forming ability when incorporated into the full-length MERS S protein expressed in DPP4 expressing mammalian cells. Together, the experimental data for the MERS sequence coupled with the similarity of the defined sequence with the data obtained for SARS suggest that the sequence RSARSAIEDLLFDKV and particularly the core sequence IEDLLF constitute the fusion peptide for MERS coronavirus S protein.

6 Expression of MHV-E protein in HEK-293T and insect cells.

6.1. Introduction

As the MHV-EPTM synthetic peptide altered the GUVs membrane and showed membrane binding activity as described in Chapter 4, and to confirm a role for this peptide in a biological system, the E protein of MHV-A59 (Accession No. AY700211.1) was cloned for expression in a eukaryotic expression system suitable for testing the peptide sequence in the context of the complete protein. To do this the E gene was amplified by PCR from cDNA using the primers listed in **Table 2.9** in Chapter 2, section 2.12.1 using the CloneAmp HiFi PCR Premix following the manufacturer's protocol as described in Chapter 2, section 2.15. The purified PCR product was digested using enzymes whose sites were present in the PCR primers, for *NcoI* and *XhoI* restriction enzymes as described in Chapter 2, section 2.16 and the digested product was extracted after agarose gel electrophoresis using a gel extraction kit. The pTriEx1.1 vector was also linearized using *Nco*I and *Xho*I restriction enzymes. A T4 DNA ligation kit was then utilized for ligation following the manufacturer's instructions and the ligation reaction was transformed into Stellar™ competent cells (*E.coli* HST08 strain).

To check for the presence of the MHV-E gene, colony PCR was carried out using the forward and reverse primers listed in **Table 2.9**, **Figure 6.3,** and then an isolate with the correct sized insert was picked and sent for DNA sequencing with each primer listed in **Table 2.9**. In the original design, MHV-E was cloned so that it would be expressed as an N-terminal HSV tagged and C-terminal His tagged fusion protein following insertion between the *Nco*I and *Xho*I restriction sites see- **Figure 6.1,** the HSV tag and *Nco*I site being included in the forward primer used for the

PCR. Both sites were included as tags as it was unclear which would be most suitable for the detection of the tagged E protein following expression in eukaryotic cells. On subsequent analysis, it was found that the HSV tag did not work well i.e. it could not be detected routinely by western blot analysis and later constructs used only the C-terminal His tag. The use of the epitope tags was part of the design to allow detection of any expressed proteins using SDS-PAGE analysis and western blot with HSV and His tag specific antibodies.

Following confirmation of the WT sequence, to assess the role of the peptide sequence on protein expression and localization, a set of mutations was introduced into the E sequence by exchanging key hydrophobic amino acids for alanine and, following expression of each mutant, a subcellular fractionation assay was performed. Eight such mutations were synthesized and ordered as synthetic DNA fragments from Integrated DNA Technology (IDT) as listed in the **Table 2.10** and **Figure 6.6.** All eight MHV-E mutants in this study were cloned as described for the WT sequence except that no HSV tag was used. Each was designed to be expressed as a C-terminal His tagged fusion protein following insertion between the *Nco*I and *Xho*I sites of the pTriEx1.1 vector. All constructs were confirmed by double digest by *NcoI* and *Xho*I restriction enzymes **Figure 6.7** and by DNA sequencing using the T7 forward2 primer and the TriExDOWN2 reverse primer **Figure 6.8** prior to use. The analysis of these mutants was comprehensive and included transfection into HEK-293T cells for immunofluorescent as described in Chapter 2, sections 2.23.2 and 2.23.3, shown in **Figure 6.9**. In addition, recombinant baculoviruses were constructed for the WT E and all mutants with each of the vectors described following transfection into *Sf9* cells with baculovirus genomic DNA as described in Chapter 2, section 2.23.7. Recombinant viruses were amplified by successive

passage until the observed cytopathic effect was clear and high titer baculovirus stocks were harvested and stored at 4˚C. Expression in insect cells is typically efficient allowing a biochemical approach to the cellular location of MHV E and its mutants.

6.2 Results

6.2.1. Construction of MHV-E in pTriEx1.1 vector.

Wild-type E and all eight MHV-E mutants in this study were cloned and expressed as C-terminal His tagged fusion proteins by insertion between the *Nco*I and *Xho*I sites in pTriEx1.1 vector **Figure 6.1.**

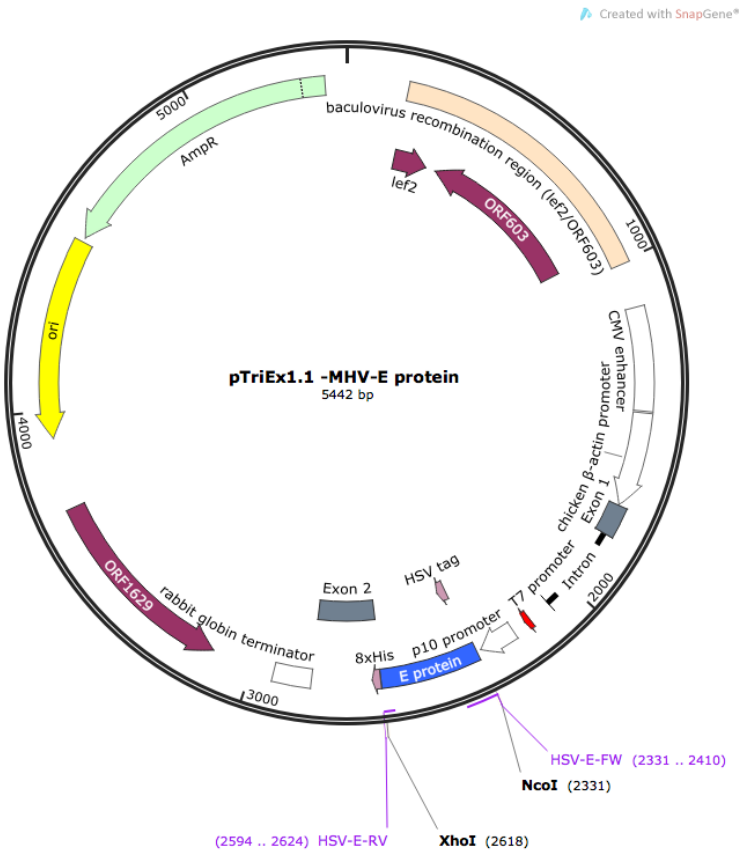

Figure 6.1: The cloning map for pTriEx1.1 with MHV-E. Key features of the plasmid are marked.

6.2.1.2 PCR amplification of DNA fragments from cDNA of MHV-A59

The cloning process was executed by amplifying the E gene from MHV-A59 cDNA by PCR using the specific forward and reverse primers detailed in listed in **Table 2.9**, as described in section 2.15. The PCR products were visualized by agarose gel electrophoresis and the DNA band size was established using a 1kb DNA ladder **Figure 6.3.** PCR products were purified using a gel extraction kit and the DNA concentration was measured using a Nanodrop spectrophotometer. pTriEx1.1 vector and PCR product were linearized using *Nco*I and *Xho*I restriction enzymes following the manufacturer's protocol **Figures 6.2** and **6.4**.

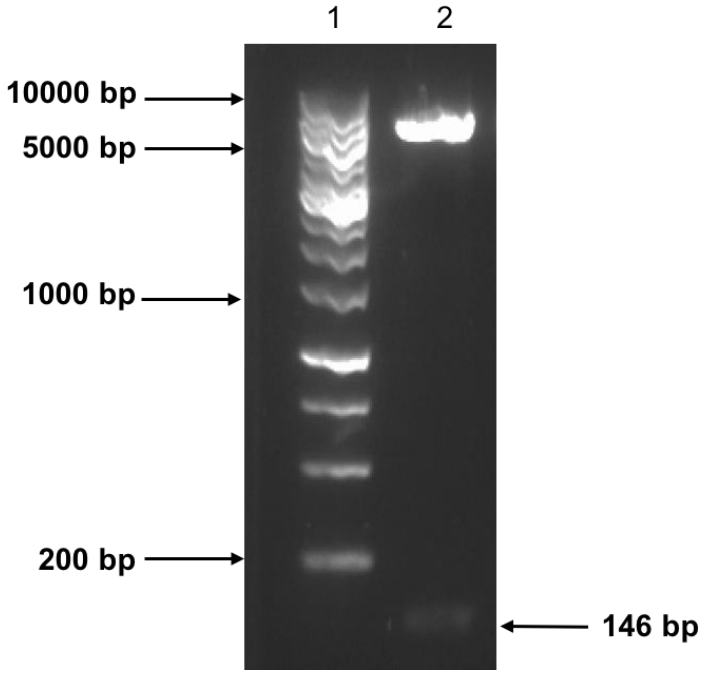

Figure 6.2: Gel electrophoresis of the double digest of pTriEx1.1. Lane 1: Hyperladder 1kb, Lane 2: pTriEx1.1 vector digested with *Nco*I and *Xho*I (5155 bp). The excised 146bp *Nco*I and *Xho*I band represents the multicloning sites that is exchanged for the E fragment as a result of the cloning. The residual vector lacking this fragment was used for the ligation reaction.

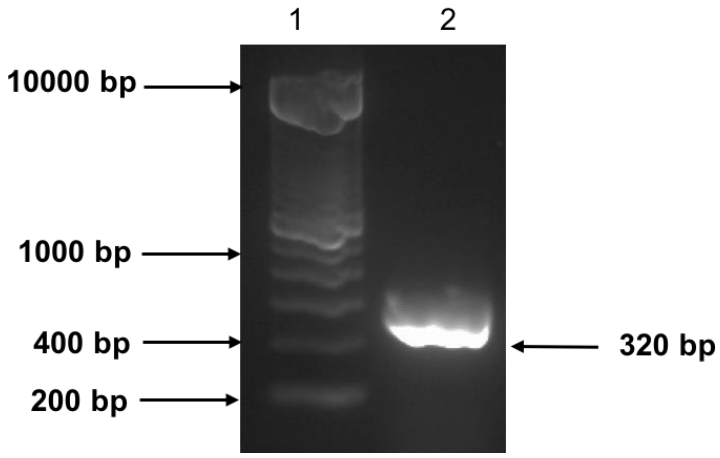

Figure 6.3: Amplification MHV-E protein from cDNA of MHV-A59. cDNA of MHV-A59 was used as a template to amplify E coding region. Lane 1: Hyperladder 1kb, Lane 2: E gene (320 bp).

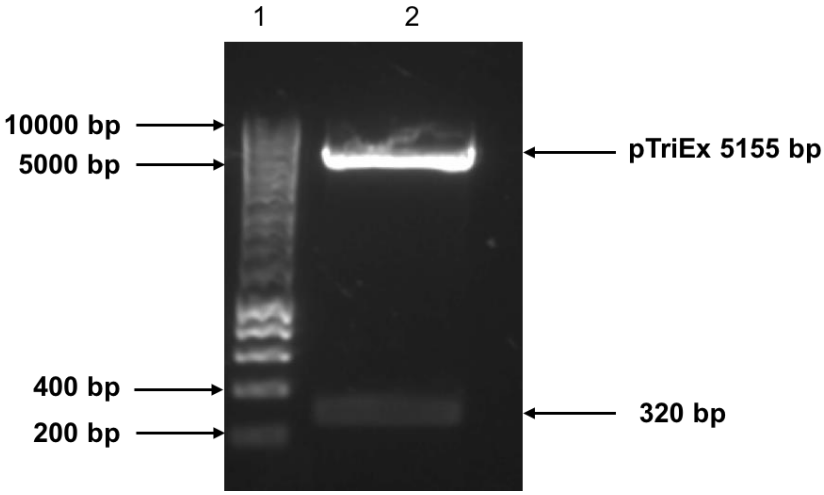

Figure 6.4: Gel electrophoresis of the ligation mixture of pTriEx1.1 and the MHV E gene. Lane 1: Hyperladder 1kb, Lane 2: pTriEx1.1-E and the eluted MHV E fragment, both obtained by restriction digest with *Nco*I and *Xho*I (320 bp).

6.2.1.3 Transformation of T4 ligation products into competent *E. coli* HST08 strain

A T4 DNA ligation kit (Thermo Fisher Scientific) was used to ligate the restriction enzyme generated DNA fragments following manufacturer's protocol. The cloning reaction was completed followed by chemically transformation into Stellar™ competent cells (*E. coli* HST08 strain) and plated on Ampicillin/LB agar to select transformants. About 30 random colonies were screened by colony PCR using T7 forward2 and TriExDOWN2 reverse primers, **Figure 6.5** shows 30 colonies screened by colony PCR for the presence of the E protein gene with an anticipated correct size of ~320bp. Subsequently, double digestion was carried out on selected plasmid preparations to confirm the presence of the desired DNA fragments in the pTriEx1.1 vector. Eight different mutant E fragments were cloned similarly. **Figure 6.7** shows 8 isolates screened by double digestion by *Nco*I and *Xho*I restriction enzymes for the 8 E mutants which show the correct size insert of ~ 320bp except in the case of the deleted EPTM construct where the anticipated size is 239bp. All clones were send for DNA sequencing prior to conducting any further experiments and the results aligned to the wildtype sequence. The data confirmed the presence of the desired mutations as designed in all the clones tested **Figure 6.8**.

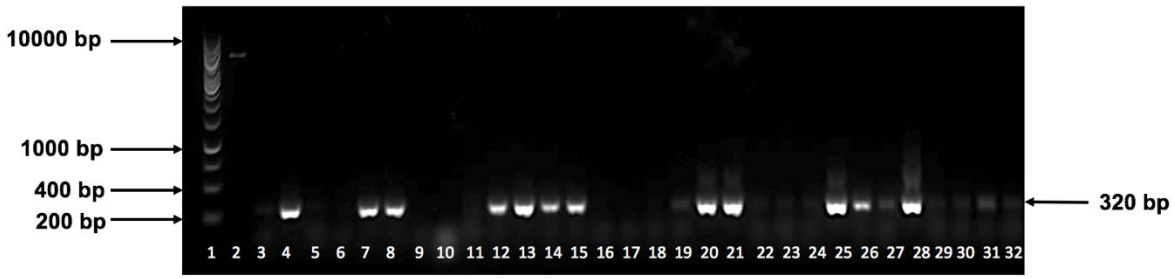

Figure 6.5: Gel electrophoresis of colony PCR of E protein in pTriEx1.1. Lane 1: Hyperladder 1kb, Lane 3- 32: The colony PCR product corresponding to 1-30 transformants, the correct size of E is (320 bp).

```
      50                64
WT    LVLSPSIYLYDRSKQ
L50   A***************
V51   *A**************
L52   **A*************
P54   ****A**********
Y57   *******A*******
Y59   *********A*****
ALL   AAA*A**A*A*****
Del   ---------------
```

Figure 6.6: Sequences of residues 50 to 64 in wild-type MHV-E protein and the alanine substitution mutants designed to probe hydrophobic amino acid function. The dashed line represents the deletion of the entire region.

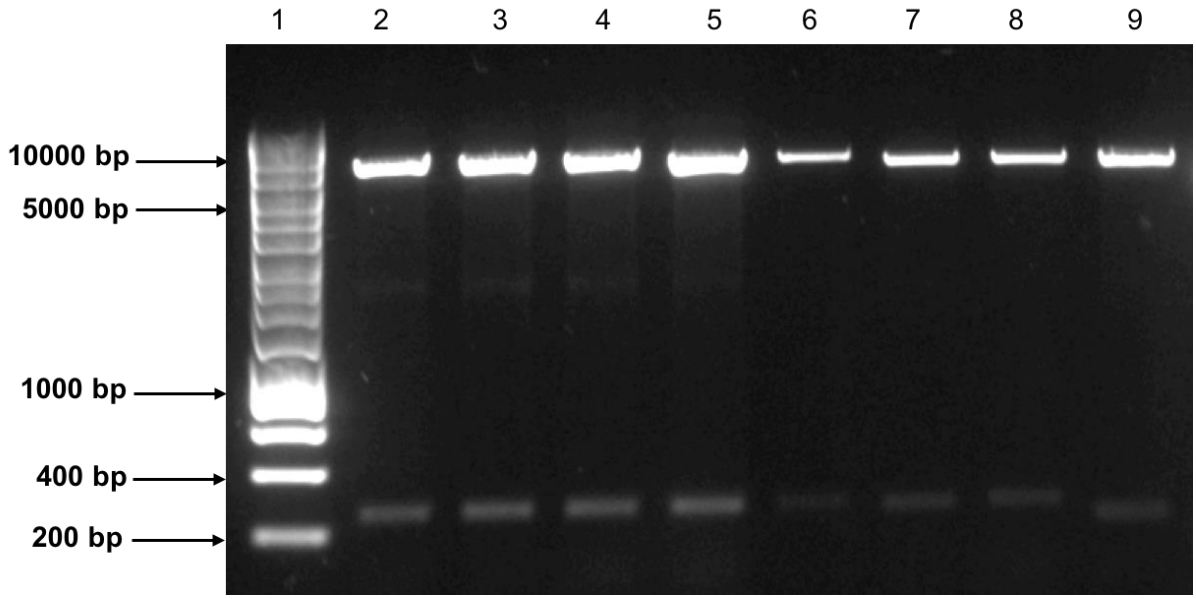

Figure 6.7: Gel electrophoresis of double digestion with *Nco*I and *Xho*I products of MHV-E mutants showing the desired DNA fragments. Lane1: Hyperladder 1kb, lane 2: pTriEx 1.1+MHV-E (L50A mutant), lane 3: pTriEx 1.1 + MHV-E (V51A mutant), lane 4: pTriEx 1.1 + MHV-E (L52A mutant), lane 5: pTriEx 1.1 + MHV-E (P54A mutant), lane 6: pTriEx 1.1 + MHV-E (Y57A mutant), lane 7: pTriEx 1.1 + MHV-E (Y59A mutant), lane 8: pTriEx 1.1 + MHV-E (all mutants), lane 9: pTriEx 1.1 + MHV-E (deleted EPTM mutant). All the released band sizes agree with the fragments as designed.

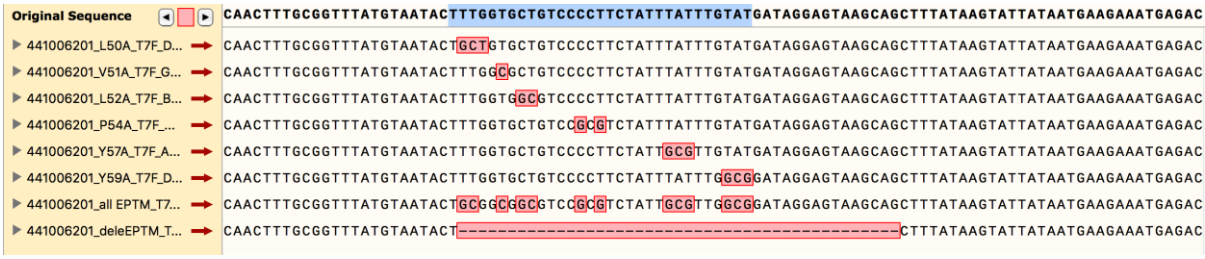

Figure 6.8: Sequence alignment of 8 mutants with wild type MHV-E. The sequence of the 8 isolates was aligned with wild type using Snapgene software. Red boxes represent the introduced alanine mutations and the dashed line represents the deletion of the entire region.

6.2.1.4 Protein expression of the 8 mutations of MHV-E in the HEK-293T cells.

6.2.1.5 Transfection of HEK-293T cells

HEK- 293T cells were cultured and maintained in Dulbecco's modified Eagle medium (DMEM) (Sigma Aldrich) supplemented with 10% fetal bovine serum (FBS) (GE Healthcare), and antibiotics penicillin/streptomycin (penicillin 100 U/ml, streptomycin 0.1 mg/ml; Gibco/Invitrogen) on glass coverslips in a 12 well plate. The cells were transfected with plasmid DNA to express wildtype or mutant MHV-E genes using the Lipofectamine 3000 transfection reagent (Invitrogen) following the manufacturer's protocol.

One day before transfection, 1.25 x 10^5 HEK-293Tcells were seeded into 12 well plates containing a glass coverslip in each well and incubated for 24 hr at 37 ˚C / 5% CO_2. Next day, the cells were transfected with the wildtype or mutant MHV-E plasmids and incubated for 24 hr at 37 ˚C / 5% CO_2. A control vector pTriEx1.1-GFP-His (a gift from B. Abdulsattar) which carried the Green Fluorescent Protein (GFP) gene was also transfected into cells and used to visualize the efficiency of transfection. Transfection efficiency was typically 30-50% of cells and was sufficiently high for an analysis of MHV E protein expression without further optimization. Twenty four hours after the transfection, the media was removed and the cells washed twice with cold PBS for 5 minutes, then the cells were fixed in fixation buffer (eBioscience™) for 1 hr at room temperature. The cells were then permeabilized using 1x permeabilization buffer (eBioscience™) for 5 min at room temperature in the dark following the manufacturer's instructions. Fixed and permeabilized cells were incubated with the Anti-His–Alexa Fluor 488 conjugate Ab (4E3D10HH2/E3, ThermoFisher Scientific) for 1 hr at room temperature diluted 1:100 in 1x permeabilization buffer. The cells were washed 2 x with wash buffer for 15 min at

room temperature in the dark and counterstained with DAPI. The fixed cells were mounted by placing the cover slip upside down on a clean glass slide with a drop of Slowfade™ Gold antifade reagent before being imaged by an EVOS-FL digital fluorescence microscope. Typically, images were captured at 20X magnification power and further manipulated, if, required using ImageJ software **Figure 6.9**.

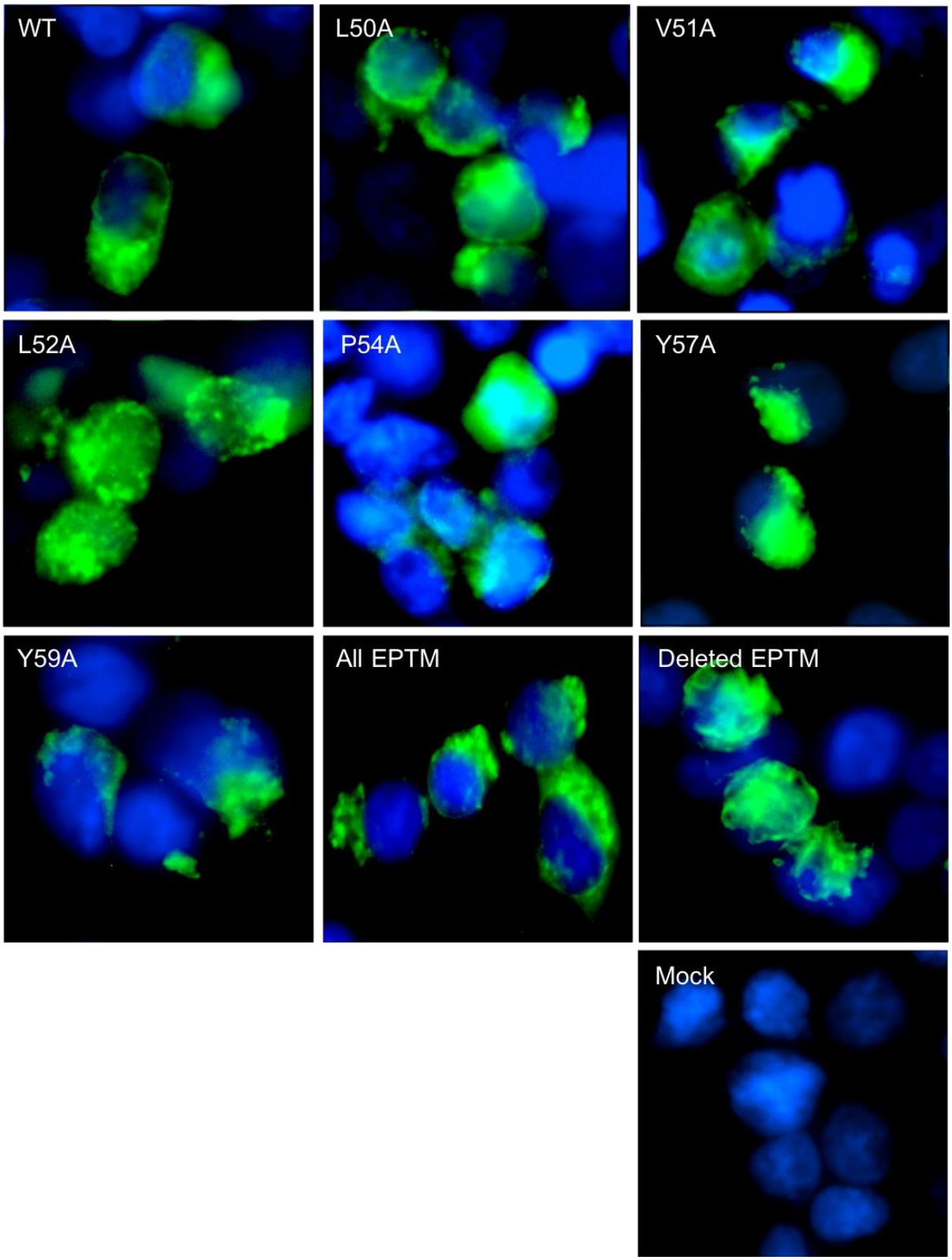

Figure 6.9: Immunofluorescent staining of MHV E protein expression in HEK-293T cells. Cells were transfected with pTriEx 1.1 vectors encoding WT MHV-CoV E or various alanine mutants, fixed and permeabilized and detected with anti-His Ab conjugated to Alexa Flour 488 (green). Nuclei were counterstained with DAPI (blue).

In the transfected HEK-293T cells WT MHV E protein was found distributed evenly throughout the cytoplasm with a slight concentration near the nucleus, probably the Golgi body. All mutant E expression was positive with little diminution of the overall signal but in most cases the pattern of staining was altered to a more granular punctate staining. This is particularly notable for mutation L52A where almost all of the fluorescent signal was associated with a punctate pattern. This is the first data to suggest that mutations identified as causing membrane association in an isolated peptide also influence the behaviour of the complete protein in a physiologically relevant environment. However, as a more quantitative measure of membrane association would be valuable, a more productive protein expression system, expression in insect cells, was also investigated.

6.2.1.6 Protein expression of the 8 mutations of MHV-E in the insect cell line.

6.2.1.7 Baculovirus expression system

The baculovirus-insect cell system has been a beneficial tool for the expression of many recombinant proteins. This system has been utilized widely to produce different types of vaccines such as surface displayed vaccine, recombinant proteins and baculovirus based VLPs (Ernst et al 2000; Latham and Galarza, 2001; Treanor et al 2006; Bright et al 2007; Gwon et al 2016). The *Autogarapha californica multiple nuclear polyhedrosis virus* (AcMNPV) was first used in 1983 to generate human IFN (beta) (Smith, Summers and Fraser, 1983). Baculoviruses encode a large genome of double stranded circular DNA (~130 kb in size) including 156 predicted coding genes (Ayres et al 1994). Baculoviruses have a rod shape nucleocapsid ranging from 250-300 nm in length and 30-60 nm in diameter and are

pathogenic for insect cells specifically of the orders *Hymenoptra*, *Diptera* and *Lepidoptera* (Hernious et al 2011). AcMNPV cell entry is mediated by the gp64 glycoprotein, which is both essential and adequate for receptor binding and fusion in both insect and mammalian cells (Rosen, Stapleton and McLinden, 1993; Monsma, Oomens and Blissard, 1996). AcMNPV is widely used as a gene delivery agent as well as for the expression of recombinant proteins (Chen et al 2011). Generally, there are two procedures of recombinant formation varying only in the location of the target gene incorporation into the baculovirus genome. The most prevalent method of recombination is introduction of the cloned gene into viral DNA using a transfer vector in insect cells where the recombination process occurs. The linear viral DNA genome used in this event is incapable of initiating an infection unless rescued to the circular form by recombination with a transfer vector (Kitts 1993; Zhao 2003). This method is effective and depends on two factors: the quality of the linear viral DNA, which should be high to allow the least possibility of recirculation by non-required recombination events (Jones and Morikawa, 1996). The second factor is the construction of a transfer vector in which the target gene is positioned under the control of a powerful baculoviral promotor. A second technique of recombinant baculovirus formation, direct incorporation of the gene of interest into a baculovirus vector (bacmid) based on recombination in *E.coli* has also been described (Luckow et al 1993). Here the recombination event is carried out by site directed transposition in *E.coli* where the baculovirus genome is held as a bacterial artificial chromosome (bacmid). In this case a transfer vector is also used but it must be enabled for the transposition event. Both recombination systems result in the gene of interest incorporated into the baculovirus genome where it is subsequently expressed as part of the late replication cycle. The transposase system is popular as it is done entirely

by plate genetics, using antibiotics to select the final recombinant form, but the resulting recombinants have been described as unstable in a number of cases (Pijlman et al 2001; Pijlman, van Schinjndel and Vlak, 2003).

6.2.1.8 Transfection of Sf9 cells and production of MHV-E recombinant baculoviruses.

Recombinant baculoviruses expressing MHV E WT and each mutant were constructed as described in Chapter 2, section 2.23.7. To examine protein expression from each recombinant, a 6 well plate 1 x 10^6 Sf9 cells was infected with each of the recombinant virus stocks at high MOI. After 1 hour at room temperature the wells were supplemented with 2 ml of complete insect cell media and incubation continued at 27 ˚C for 3 days when cytopathic effect was observed by light microscopy. The infected cells were harvested and the cell pellets were used to confirm protein expression using western blot analysis as described in Chapter 2 section 2.25 **Figure 6.10**. All proteins were expressed at the molecular weight expected but the expression level varied with mutation. Half of the mutants expressed at the same level as the wild type but mutations L50A, V51A, L52A and Y57A were expressed at reduced level consistent with a role of these residues in protein folding and stability. Expression differences were not the result of different baculovirus infection efficiencies as the same blot was stripped as described in section 2.26 by incubation in stripping buffer (100 mM ß-mercaptoethanol, 2% SDS, 62.5 mM Tris-Hcl) at pH 6.7 for 30 minutes at 50 ˚C. After stripping, a second western blot analysis was carried out as described in section 2.25 by incubation of the membrane with an anti-gp64 Ab, (Lu et al 2002) followed by incubation with a secondary anti-mouse conjugate. The blot for the major baculovirus glycoprotein,

gp64, showed near equivalent infection in all cases. The effect of Sf9 cells apoptosis on subcellular distribution of E protein and its mutants was not considered.

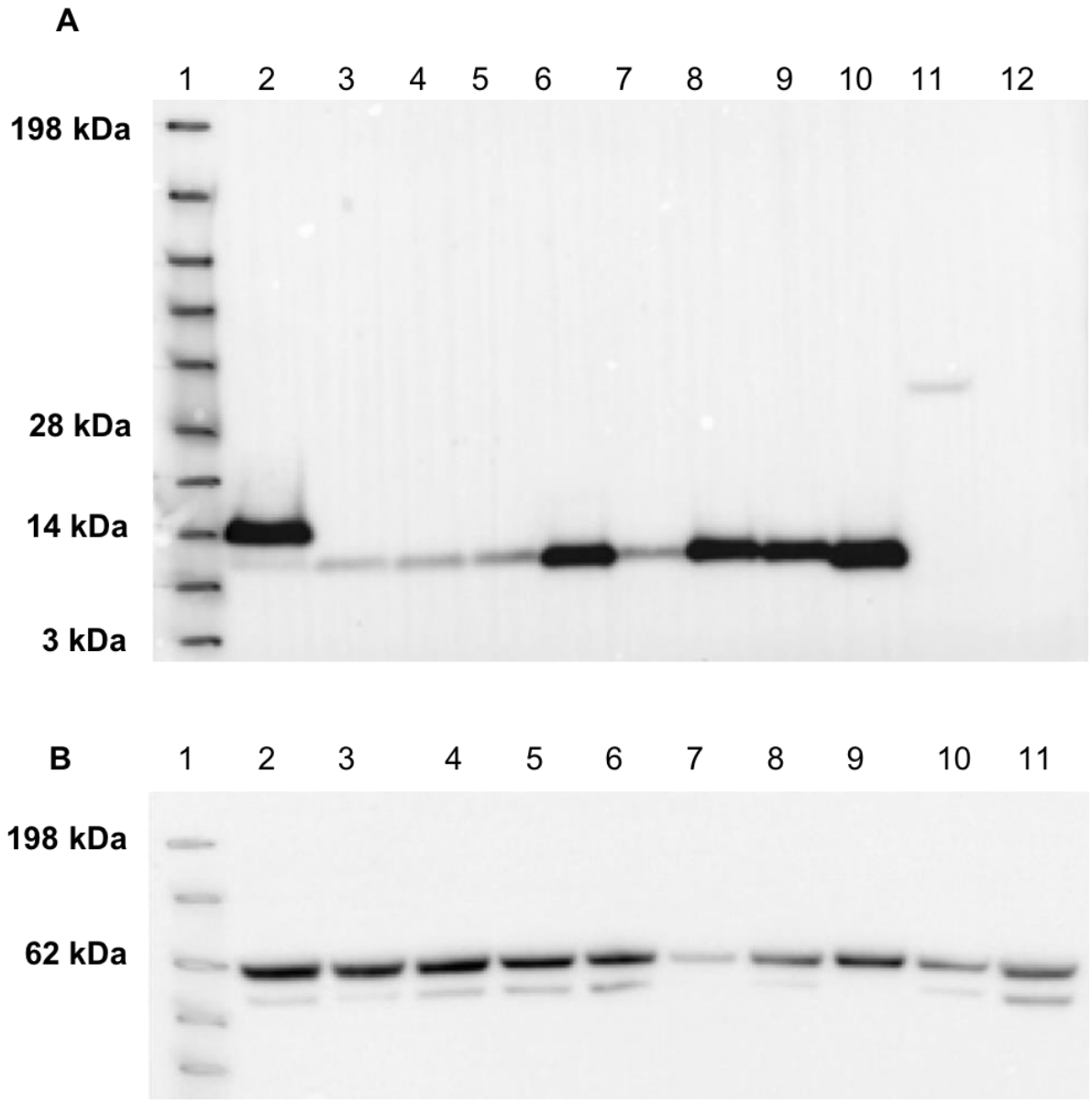

Figure 6.10: Western blot analysis of recombinant WT MHV-E protein expression and eight mutants following expression in insect cells. A- Lane 1: See Blue™ Plus2 Pre-Stained Protein Standard (Invitrogen), lane 2: WT E, lane 3: L50A mutant, lane 4: V51A mutant, lane 5: L52A mutant, lane 6: P54A mutant, lane 7: Y57A mutant, lane 8: Y59A mutant, lane 9: all mutants, lane 10: deleted EPTM mutant, lane 11: GFP-His tagged (positive control), lane 12: negative control (uninfected cells). B- Western blot analysis of the baculovirus surface glycoprotein gp64 protein as an infection control (64 kDa) for the same membrane as (**A**). NB. A ubiquitous cellular protein marker such as actin could also have served as a loading control.

6.2.1.9 Effect of 8 mutations of on protein cellular localization of MHV-E.

6.2.1.9.1 Differential centrifugation

To investigate in more detail whether the mutations introduced into MHV-E resulted in an effect on cellular localization, plausibly by altered membrane association, cell fractionation of MHV WT E and its mutants was performed using a differential centrifugation assay following expression of the recombinant MHV-E proteins in Sf9 cells.

2.5x10^6 *Sf9* cells were seeded in T25 flasks as monolayers and incubated for 1 hr to allow the cells to adhere at room temperature. Then cells were infected with recombinant baculoviruses at high MOI and incubated for 72hr at 27˚C. The infected cells were harvested by loosening the monolayer into the media and collected by centrifugation at 4000 rpm / 20 minutes/ 4 ˚C. The cell pellets were resuspended with 500µl cold PBS and lysed by sonication for 10 min at 20 second intervals with an 80% amplitude. No detergent was used in these preparations. The cell lysates were centrifuged at low speed 10,000 rpm / 15 min / 4 ˚C using a bench top centrifuge to remove unbroken cells and large debris and the samples kept as low speed (LS) pellets. The supernatants were collected and centrifuged at high speed, 50,000 rpm/ 90 minutes/ 4 ˚C, using the Beckman TL-100 ultracentrifuge, and the supernatants and pellets were collected as high speed supernatants and pellets (HSP) respectively. The low speed pellet and high speed pellet fractions were all tested for MHV E protein expression and localization by western blot with the His-tag antibody as before **Figure 6.11**.

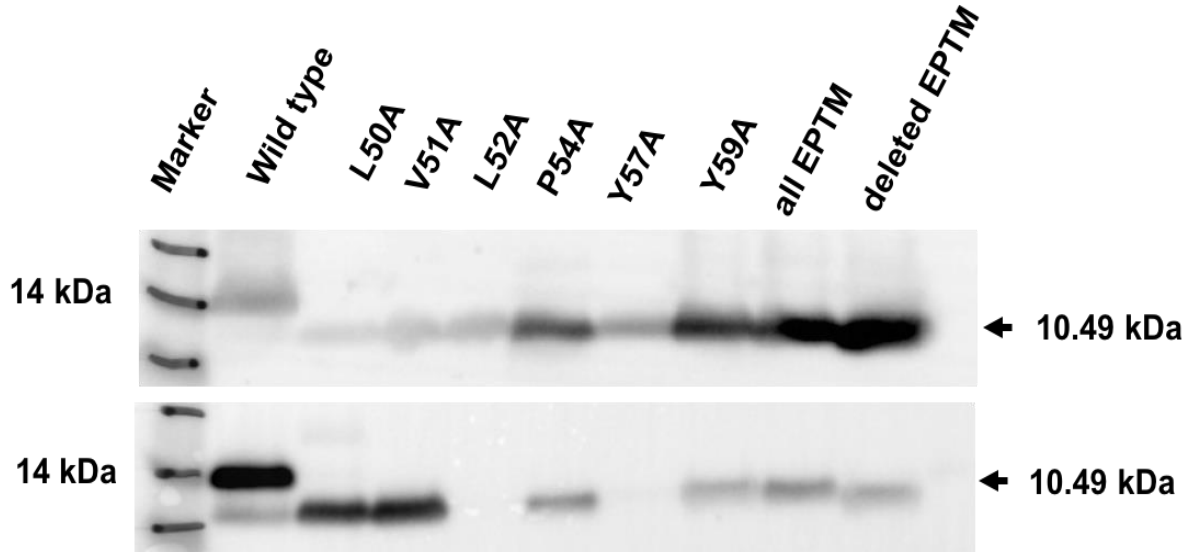

Figure 6.11: Western blot analysis of recombinant WT MHV-E protein expression and eight mutants following expression in insect cells and partition among membrane fractions (differential centrifugation). The altered distribution of E dependent on peptide sequence is clear. Above and below images represent the low and high speed pellets gels respectively.

The expression of the wild type MHV E was found to be associated most strongly with the HSP fraction, which should include the ER-membranes, consistent with its known primary localization in expressing cells (Venkatagopalan et al 2015). Similarly, mutations L50A and V51A partitioned mainly in the HSP fraction although expression levels overall were reduced. Strikingly the “all” mutant, in which all targeted residues were mutated to Alanine and “del” mutant in which the target peptide was deleted from MHV E were found almost exclusively in the LS pellet fraction, despite high levels of expression. The remaining mutations Leucine L52A, P54A, Y57A and Y59A also associated preferentially with the LSP which should include broken cells, nuclei and cytoskeletal components although expression level was low in some cases, notably L52A and Y57A, which may have had some effect on the relative partition. Nevertheless, these data show a role for the targeted residues in distribution of the MHV E protein among the membrane fractions of the expressing insect cells.

6.3 Discussion

The studies in this chapter were performed in order to demonstrate the cellular localization of, and the contribution of some residues to, the membrane association enabled by the post transmembrane region of MHV-E, which is located in the C-terminal domain. CoV-E proteins consists from a short hydrophobic amino terminal region, a hydrophobic transmembrane region, and a carboxy terminal region that encompass the majority of the protein (Torres et al 2007). In coronaviruses where it has been examined, E protein is predominantly located in the ERGIC and Golgi and the protein has been shown not to traffic to the infected cell surface (Venkatagopalan et al 2015).

The results of the *in vitro* assays with isolated peptide and GUV binding suggested that the post TM region of MHV-E has membrane binding activity, as described in Chapter 4. However, while indicative of a function, studies of isolated peptides cannot be directly correlated with the role of the same sequence within the full length protein until the sequence identified is mutated in the context of full length E. To accomplish this, the WT MHV-E protein and an additional eight mutants targeting the post TM region of E were designed and generated to test the effect of these mutations on the cellular localization of E *in vivo*. The successful constructions of MHV-E tagged at the C-terminus with the His-tag in the pTriEx 1.1 plasmid vector was achieved based on T4 ligation cloning as described in Chapter 2 section 2.18 and the final constructs were confirmed by DNA sequencing. Concerning the mutational analysis, eight mutations were constructed in the WT sequence E in same way including L50A, V51A, L52A, P54A, Y57A and Y59A in addition to a combination of these mutants (“all”) as well as deletion of the whole EPTM region. If, as

suggested by the peptide analysis, this sequence was a *bona fide* membrane binding region then the expectation was that some or all of these mutants might result in a redistribution of E protein in cells following expression.

Expression *in vivo* was achieved by transfection of MHV-E-His-tagged protein and eight mutants in HEK-293T mammalian cells as described in Chapter 2 section 2.23.2 and immunofluorescent staining was done as described in section 2.23.3. In addition, expression of WT E and the mutants *in vivo* was carried out using the recombinant baculovirus system leading to the expression of MHV-E-His tagged fusion protein in infected *Sf*9 cells as described in Chapter 2 section 2.23.8. Differential centrifugation experiments were done to demonstrate the effect of the mutations after expression of these proteins in the insect cells.

The observations for the immunofluorescent staining results revealed different protein cellular localization and cellular redistribution for the mutants compared to the WT MHV E protein **Figure 6.9** as shown for L50A, L52A, all EPTM, and the deleted mutant, all of which caused a more punctate protein staining pattern in the cellular cytoplasm. The Y59A mutant appeared to show more protein accumulation in Golgi region.

Following construction of recombinant baculoviruses and confirmation of their expression of E, the expressed protein expression level was analysed by western blot which revealed different protein expression levels for the WT MHV E compared to the mutants. **Figure 6.10** showed poor levels of protein expression for L50A, V51A, L52A, Y57A while P54A, Y59A, all mutants and deleted EPTM mutants showed similar protein expression to the WT E expression. The detection of a faster migrating band in the deleted EPTM mutant was clear in comparison to the WT.

Additionally, minor migration differences in the mutations that exchanged a hydrophobic amino acid for alanine were also apparent consistent with changes in overall protein molecular weight and/or SDS binding which cause proteins to migrate differently. As the transcription unit is unchanged in all of the constructs the lower expression level is indicative of degradation, plausibly as a result of misdirected membrane binding.

The results from western blot analysis of the fractions obtained by differential centrifugation confirmed a different cellular distribution. ImageJ (Schneider, Rasband and Eliceiri, 2012) was used to calculate the relative level of protein expression in the fractions obtained by differential centrifugation through a comparison of the area of band intensity for the low speed pellet compared to the high speed pellet **Figure 6.12**.

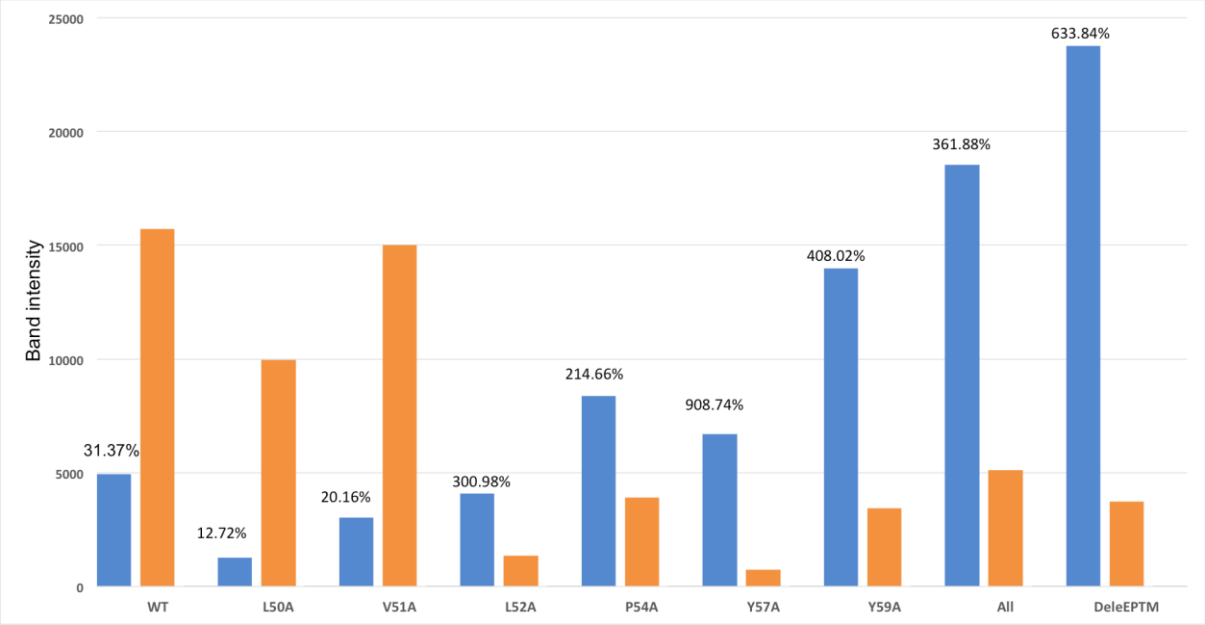

Figure 6.12: Relative intensity of recombinant WT MHV-E protein expression and eight mutants following partition among membrane fractions (differential centrifugation). The samples are indicated. Low speed pellet (blue) compared to the high speed pellet (orange) as detected by western blot.

The WT, L50A and V51A samples were predominantly associated with the HS fraction with only 31.37%, 12.72 % and 20.16% respectively in the LS pellet. The poorly expressing L52A and Y57A mutants were hardly present in the high-speed pellet fractions as shown in **Figures 6.11 and 6.12**, the predominant association was with the LS fraction**.** In these mutations loss of expression level is accompanied by a changed cellular localization suggesting the two observations maybe linked and that the protein was misfolded. However, those mutants where expression level was similar to the WT, that is P54A, Y59A, “all” and “deleted”, also demonstrated altered fractionation profiles with a much high proportion of the total protein being found in the LS pellet fraction, all indicative of aggregation and a failure to progress in with ER. In the case of these mutant’s alteration in the cellular localization of E was clear but was not associated with degradation. It is notable that the majority of the mutations introduced redistribute the E protein to the LS fraction irrespective of a role in overall yield, consistent with a common function for the peptide sequence. These data are consistent with a physiological role in membrane binding in the virus life cycle for the residues identified by peptide analysis. The subcellular fractionation represented by the low and high speed fractions could be confirmed by probing for different subcellular markers including markers of the ER (e.g. Erp7), Golgi (e.g. Golgi-58K) and ERGIC (e.g. ERGIC-53) (Nal et al 2005).

These data are supported by studies of E function in other coronaviruses. In the case of SARS CoV, the C-terminal motif of E is responsible for re-orienting the plasma membrane in the Golgi region (Cohen, Lin and Machamer, 2011). Mutations in the motif concerned that were intended to raise its α-helical content impaired localization to membranes (Cohen, Lin and Machamer, 2011). The C-terminal

domain of E is also significant for its interactions with the M protein on the cytoplasmic side of the ERGIC (Lim & Liu 2001; Hogue & Machamer 2008; Bos et al 1996) although that interaction was not tested here as no M protein was co-expressed. The M-E interactions has been suggested to be the main leader for envelope formation (de Haan et al 2000) and it has been suggested that E protein induces membrane curvature and subsequent viral particle scission as mutation in the MHV E C-terminal domain disrupts viral assembly and maturation (Fischer *et al*, 1998). It has been shown that the C-terminal region of SARS-E protein interacts with cellular proteins such as the PALS1 (Teoh et al 2010) and with nsp3 domains (Álvarez et al 2010). To what extent these interactions may also occur in insect cells leading to an altered membrane distribution is not clear. That E is an important protein has been shown in SARS-CoV where deletion of E protein was found to diminish pathogenicity and mortality (DeDiego et al 2014). In cellular studies, E protein has been linked to upregulation of the inflammatory host response and downregulation of the cell stress response (DeDiego et al 2011). The critical regions in the SARS-E protein that define virulence have been mapped as the TM domain (Torres, Briggs and Arkin, 2002) and the C-terminal domain (Regla-Nava et al 2015). Its membrane binding activity has also been suggested as it has been shown that E alters membrane permeability when expressed in mammalian cells and *E.coli* (Liao et al 2004). Channel activity has also been shown in an artificial cell membrane (Wilson et al 2004; Torres et al 2007), driven by pentameric oligomers of E (Torres et al 2006; Pervushin et al 2009). Some mapping of membrane interaction has been done showing, in SARS CoV, that the residues which bound to the surface of the micelle included Tyrosine-59, Valine-52 and Lys-63 (Li et al 2014). These residues are equivalent in MHV, which may suggest similar effects, as seen here for Y59A.

In MERS E has also been suggested as a vaccine candidate as possible B-cell epitopes have been predicted with high antigenicity and appropriate length (amino acids 58-82) (Xie et al 2018). The data here on baculovirus expression would suggest that E protein expression can be achieved with tags suitable for rapid purification. Thus, purified E could be assessed as a vaccine candidate, possibly as a high speed membrane fraction of expression cells.

7 General discussion

Viruses depend on the host's translation machinery for their replication requirements and this is usually achieved by the virus hijacking many cellular processes. Inducing cellular membrane remolding after viral protein expression is a good example of the ability of +ssRNA viruses to utilize cellular processes (Miller and Krijnse-Locker, 2008; Netherton and Wileman, 2011). This rearrangement of cellular membrane is a crucial step in viral replication cycle since these modified membranes are the sites for the localization of all viral constituents needed for viral RNA synthesis. In addition, they provide protection from the host innate immune system (den Boon and Ahlquist 2010a; Neufeldt et al 2016). The mechanisms used for inducing rearrangement of cellular membranes are not yet fully understood.

Within the *Coronaviridae* there are two important emerging viruses, SARS-related CoV and MERS-related CoV. Both can cross the species barrier and cause pathology in a new target species. There is no effective treatment or licensed vaccine for either virus, emphasizing the need to further understand CoV biology as a route to improve future intervention (van Doremalen and Munster 2015; Baseler et al 2016). Despite coronavirus diversity, they share some common features including the production, in infected cells, of elaborate membrane structures. Membranes represent both an obstacle and an aid to coronavirus replication and in consequence, virus encoded structural and nonstructural proteins have membrane binding properties.

As coronaviruses are enveloped viruses, viral membrane fusion with the host cell is an essential step in the replication cycle to deliver genomic RNA into the host cell cytoplasm, ultimately resulting in the initiation of replication (White et al 2008). For coronaviruses, the definitive player in the entry event is the spike fusion protein

(S) as it mediates both cell binding and membrane fusion processes (White and Whittaker, 2016). Despite this centrality, the location of the fusion peptide within the CoV-S protein has not been precisely located. In this study the main aim was to investigate the membrane active regions predicted in coronaviruses proteins and more specifically to locate the fusion peptide within the CoV-S protein in term of location and sequence. The study used MERS-CoV and MHV-A59 as model coronaviruses to investigate membrane active regions suggested by bioinformatics analysis to occur in both structural and nonstructural proteins.

The bioinformatics results revealed several highly conserved amphipathic regions in the selected coronavirus proteins. In addition, the results showed that at least part of the CoV putative fusion peptide maybe located near the N-terminus of S2 where a conserved motif RSARSAIEDLLFDKV with properties consistent with those expected of an FP occurs across the coronavirus family - see **Figure 3.1.** Within this sequence the core motif IEDLLF includes only infrequent and conservative replacements (Madu et al 2009; Belouzard et al 2012). Similarly, bioinformatics analysis identified clusters of conserved cysteines at the N-terminus of the S2 endodomain, a region that is important for syncytium formation during viral infection, possibly via the palmitoylation of S (Thorp et al 2006)

Bioinformatics analysis of nsp3, nsp4 and nsp6 revealed several conserved sites that may be crucial for nsp3, nsp4 and nsp6 function see - **Figures 3.10, 3.13 and 3.16** including the highly conserved C-terminal regions of nsp4 and nsp6 which are found in almost all viruses. Cysteine residues within the C-terminus of nsp6, particularly the “G (X) C (X) G” motif have been hypothesized to be modified by palmitoylation further suggesting that this region has a role in protein-membrane or protein-protein interactions during viral assembly (Baliji et al 2009).

Based on the bioinformatics analysis several peptides from MERS-CoV and MHV-A59 were chosen for *in vitro* analysis. These peptides represent conserved and predicted amphipathic helices of the S2, M, E, nsp3, nsp4, and nsp6 proteins of both viruses. Some of these peptides dissolved completely in a buffer containing 0.1 mM sucrose, 0.1 mM glucose, and 0.5% DMSO concentration**.** However, several peptides had to be excluded from the study due to their poor solubility, even in 100% DMSO or due to their formation of a gel **Table 2.5**. Those peptides that were soluble were then tested for formal membrane binding and/or distortion by incubation with GUVs, an established assay for membrane perturbation.

The GUV assay results showed that the putative MERS-FP and MHV-FP deformed the GUV membrane leading to an increase in their size **Figure 4.2**. To define their key role in activity, single amino acid substitution experiments were done and revealed a role for hydrophobic amino acids isoleucine, leucine and phenylalanine, all located in the central region of the putative fusion peptide **Figure 4.5.** This is consistent with a published study that revealed that the segment located immediately downstream of the S2 cleavage site in SARS S, “SFIEDLLFNKVTLADAGF” showed membrane-interacting properties (Madu et al 2009). Recently, using cryo-EM, the details of the pre-fusion conformation of the ectodomain of a few coronavirus S proteins including MERS-CoV, SARS-CoV, HCoV-NL63, HCoV-HKU1 and MHV have been revealed. These suggest that the FP sequence maybe exposed at the surface of the protein in the pre-fusion state (Gui et al 2017; Yuan et al 2017; Walls et al 2016a; Kirchdoerfer et al 2016). Interestingly the putative FP is downstream of the second S2’ cleavage site in S and is unusual as other class I viral fusion proteins generally require only one, not two cleavage sites for exposure and activity (Millet and Whittaker, 2018).

The relevance of the key role residues identified of the putative CoV-FP *in vitro* were tested *in vivo* by their introduction into recombinant MERS S protein expressed in mammalian cells - **Figure 5.7**. Mutations preventing membrane binding *in vitro* also abrogate S mediated syncytium formation - **Figure 5.7** consistent with the identified peptide acting as the fusion peptide for the S protein of MERS-CoV.

Another membranotropic region in the C-terminal segment of MHV-A59 E protein corresponding to the residues between 50-64 was identified using the GUV assay - **Figure 4.7**. To confirm this result in a physiologically relevant environment, this sequence too was mutated in the context of the complete E protein. A set of mutations was introduced into the MHV-E sequence by exchanging key hydrophobic amino acids for alanine and, following expression of each mutant in transfected mammalian cells, immune fluorescence microscopy was used to examine cellular distribution. WT MHV E protein was found distributed evenly throughout the cytoplasm with a slight concentration near the nucleus, probably the Golgi body. In most cases the pattern of staining was altered to a more granular punctate staining in the case of the introduced mutations. This is particularly notable for mutation L52A where almost all of the fluorescent signal was associated with a punctate staining pattern - **Figure 6.9**

WT MHV E and its mutants were also examined by biochemical fractionation following high levels expression in insect cells. **Figure 6.10** showed an effect of the level of protein expression for mutants L50A, V51A, L52A, Y57A while mutants P54A, Y59A, a multiple mutant and a deleted EPTM mutant showed similar protein expression levels to the WT. This data suggested protein degradation, consistent with misdirected membrane binding in the case of the severely affected mutations.

Subcellular fractionation of cellular extracts by differential centrifugation confirmed a re-distribution into low speed or high speed membrane fractions associated with some of the mutations made - **Figure 6.12.** Interestingly there was a correlation of those mutations with lower expression levels with a changed cellular localization suggesting the two observations maybe linked. These results are supported by studies of E protein function in other coronaviruses where, for example, the C-terminal motif of SARS-E has been shown to be responsible for re-orienting the plasma membrane in the Golgi region (Cohen, Lin and Machamer, 2011). Mutations in the motif concerned, intended to raise the α-helix content, impaired localization (Cohen, Lin and Machamer, 2011) echoing the data obtained here. In addition, residues Tyrosine-59, Valine-52 and Lys-63 have been directly implicated in binding to the surface of micelles (Li *et al*, 2014). Recently, an NMR spectroscopy study showed that a 9 residue peptide TK9 (T^{55}VYVYSRVK^{63}) from SARS-E, located in the α helical segment of the C-terminus, has a key role in the membrane recognition and subsequent disturbance (Ghosh, Bhattacharyya and Bhunia, 2018). This is consistent with the C-terminal domain of E protein being crucial for viral assembly and virus trafficking (Corse and Machamer, 2002b; Ruch and Machamer, 2011). Together these data support the identification and properties of the E peptide identified here as a *bona fide* membrane binding region of consequence to the virus.

The overall outcome of the work in this thesis can be summarized in three points:

- Bioinformatics analysis was used to identify the membrane binding proteins of MERS-CoV and MHV and to obtain candidate sequences as peptides for biochemical tests using a cell-mimicking compartment

assay (Giant Unilamellar Vesicles, GUVs). GUVs were formed and the ability of selected peptides to change their shape and size was determined experimentally.

- A region was identified in the S protein of CoVs that has many features consistent with the FPs of some classical class I viral fusion proteins and this peptide was confirmed as a plausible FP by both *in vitro* and *in vivo* analysis. A sequence recognized in the MHV-E protein was also confirmed as being a membrane active region consistent with a role in viral assembly or release.
- Additionally, several membrane interacting regions of the MERS-CoV and MHV-A59 nonstructural proteins, nsp3, nsp4, and nsp6 were identified consistent with their role in DMV formation during the virus replication cycle.

The results of the thesis underpin possible future research into the membrane fusion and modulation mechanisms of coronaviruses. Understanding these mechanisms will not only allow us to gain insight into their complicated biology, but may also suggest new targets for antiviral therapy against CoVs infections. Both structural and non-structural proteins contribute to membrane reorganization and viral protein interaction with membranes occurs at several stages of the virus replication cycle offering multiple targets for intervention. However, the precise role of each protein and of individual domains within each protein in contacting the membrane and initiating its deformation remains work in progress and may vary across the family.

Certainty over the mechanism of action of membrane of some membrane active peptides has improved considerably in the case of those sequences located in

the structural proteins as a number of protein structures now exist, including structures for large molecules and multimeric assemblies such as the spike protein trimer, obtained by cryo-electron microscopy. Models for the mechanism of protein function based on such structures allows them to be tested. Improved understanding also applies to the non-structural proteins in that certain combinations of proteins, notably nsp3, 4 and 6, can produce membrane deformation and structures that resemble those formed during virus infection when expressed alone. However, the precise contribution of each protein and the role of host proteins in the overall process remain to be determined. Ironically, it is the membrane binding properties of the proteins that makes them difficult targets for structural biology.

Regardless of the precise mechanisms of membrane curvature the central role of membrane perturbation in the coronavirus replication cycle suggests itself as a target for designed intervention. A lack of membrane structures would clearly prevent virus replication but more reasonably even a partial inhibition might result in revelation of the replicative intermediates to the immune system and accelerate virus clearance. Study of the membrane reorganization associated with coronavirus infection is therefore likely to contribute to a greater understanding of membrane biogenesis in general and to offer opportunities for rational design. It is worth noting that, as a universal feature of coronavirus replication, inhibition of membrane reorganization would likely apply to future zoonotic outbreak strains as well as to established and characterized viruses.

Appendix

Appendix 1: Pairwise comparisons of time and treatment of the effects of all DMSO buffers on GUV size[a].

Time (min)	(I) treatment	(J) treatment	Mean Difference (I-J)	Std. Error	df	Sig.[d]	95% Confidence Interval for Difference[d]	
							Lower Bound	Upper Bound
1.0	0.5% DMSO buffer	13%DMSO buffer	.557[*, b, c]	.083	270.083	.000	.303	.811
		14.7%DMSO buffer	.631[*, b, c]	.083	269.270	.000	.377	.884
		15% DMSO buffer	.543[*, b, c]	.085	284.161	.000	.283	.802
		17% DMSO buffer	.646[*, b, c]	.083	271.474	.000	.392	.901
		25.5% DMSO buffer	1.211[*, b, c]	.083	269.538	.000	.957	1.464
		5% DMSO buffer	.023[b, c]	.083	269.291	1.000	-.230	.277
		1% DMSO buffer	.065[b, c]	.062	191.58	1.000	-.111	.241
2.0	0.5% DMSO buffer	13%DMSO buffer	.865[*, b, c]	.091	271.843	.000	.586	1.143
		14.7%DMSO buffer	.809[*, b, c]	.091	272.080	.000	.531	1.088
		15% DMSO buffer	1.015[*, b, c]	.093	285.128	.000	.731	1.299
		17% DMSO buffer	.918[*, b, c]	.091	273.149	.000	.639	1.197
		25.5% DMSO buffer	1.429[*, b, c]	.091	271.331	.000	1.150	1.708
		5% DMSO buffer	.114[b, c]	.091	271.100	1.000	-.164	.393
		1% DMSO buffer	.065[b, c]	.085	194.800	1.000	-.177	.306
5.0	0.5% DMSO buffer	13%DMSO buffer	.933[*, b, c]	.114	270.756	.000	.584	1.283
		14.7%DMSO buffer	.844[*, b, c]	.114	270.174	.000	.495	1.193

	15% DMSO buffer	1.333[*, b, c]	.115	280.969	.000	.980	1.687
	17% DMSO buffer	1.096[*, b, c]	.114	271.754	.000	.746	1.446
	25.5% DMSO buffer	1.579[*, b, c]	.114	270.366	.000	1.230	1.928
	5% DMSO buffer	.041[b, c]	.114	270.190	1.000	-.309	.390
	1% DMSO buffer	.065[b, c]	.106	194.657	1.000	-.235	.365

Based on estimated marginal means

*. The mean difference is significant at the .05 level.

a. Dependent Variable: Effective diameter (size).

b. An estimate of the modified population marginal mean (I).

c. An estimate of the modified population marginal mean (J).

d. Adjustment for multiple comparisons: Bonferroni.

Appendix 2: Pairwise comparisons of time and treatment of the effects of all DMSO buffers on GUV shape[a].

Time (min)	(I) treatment	(J) treatment	Mean Difference (I-J)	Std. Error	df	Sig.[d]	95% Confidence Interval for Difference[d]	
							Lower Bound	Upper Bound
1.0	0.5% DMSO buffer	13%DMSO buffer	-.011[b, c]	.006	262.047	1.000	-.029	.006
		14.7%DMSO buffer	-.009[b, c]	.006	263.336	1.000	-.027	.009
		15% DMSO buffer	-.011[b, c]	.006	265.522	1.000	-.029	.007
		17% DMSO buffer	-.006[b, c]	.006	264.054	1.000	-.024	.012
		25.5% DMSO buffer	-.021[b, c, *]	.006	264.440	.011	-.039	-.003
		5% DMSO buffer	.005[b, c]	.006	268.575	1.000	-.014	.023
		1% DMSO buffer	.000[b, c]	.003	193.945	1.000	-.010	.009
2.0	0.5% DMSO buffer	13%DMSO buffer	-.015[b, c]	.009	271.776	1.000	-.042	.012
		14.7%DMSO buffer	-.005[b, c]	.009	272.854	1.000	-.032	.022
		15% DMSO buffer	-.014[b, c]	.009	274.693	1.000	-.041	.012

		17% DMSO buffer	-.001[b, c]	.009	273.456	1.000	-.028	.026
		25.5% DMSO buffer	-.022[b, c]	.009	273.781	.216	-.049	.004
		5% DMSO buffer	.007[b, c]	.009	277.289	1.000	-.020	.034
		1% DMSO buffer	.000[b, c]	.004	194.435	1.000	-.010	.010
5.0	0.5% DMSO buffer	13%DMSO buffer	-.013[b, c]	.012	269.149	1.000	-.049	.023
		14.7%DMSO buffer	-.005[b, c]	.012	269.832	1.000	-.041	.031
		15% DMSO buffer	-.015[b, c]	.012	271.000	1.000	-.051	.021
		17% DMSO buffer	-.004[b, c]	.012	270.214	1.000	-.040	.032
		25.5% DMSO buffer	-.036[b, c]	.012	270.420	.050	-.072	1.291E-6
		5% DMSO buffer	.007[b, c]	.012	272.651	1.000	-.029	.043
		1% DMSO buffer	.000[b, c]	.003	194.105	1.000	-.010	.010

Based on estimated marginal means

*. The mean difference is significant at the .05 level.

a. Dependent Variable: Ratio A/B (shape).

b. An estimate of the modified population marginal mean (I).

c. An estimate of the modified population marginal mean (J).

d. Adjustment for multiple comparisons: Bonferroni.

Appendix 3: Pairwise comparisons of time and treatment of effect of MERS and MHV S2-derived peptides in 0.5% DMSO buffer on GUV size[a].

Time (min)	(I) treatment	(J) treatment	Mean Difference (I-J)	Std. Error	df	Sig.[d]	95% Confidence Interval for Difference[d]	
							Lower Bound	Upper Bound
1.0	0.5% DMSO buffer	MERS-FP	-.866[*, b, c]	.148	311.174	.000	-1.332	-.400
		MERS-SC	-.039[b, c]	.147	307.744	1.000	-.503	.425
		MERS-SHCR	.360[b, c]	.148	310.085	.433	-.106	.825
		MHV-FP	-.557[*, b, c]	.147	307.194	.005	-1.020	-.093

		MHV-SHCR	.267[b, c]	.147	307.493	1.000	-.197	.730
		M2-infleunza	-.204[, b, c]	.217	119.171	1.000	-.729	.322
2.0	0.5% DMSO buffer	MERS-FP	-1.283[*, b, c]	.184	314.256	.000	-1.864	-.701
		MERS-SC	.042[b, c]	.184	311.440	1.000	-.538	.621
		MERS-SHCR	.618[*, b, c]	.184	313.360	.025	.037	1.198
		MHV-FP	-.667[*, b, c]	.184	310.989	.009	-1.246	-.088
		MHV-SHCR	.310[b, c]	.184	311.234	1.000	-.269	.890
		M2-infleunza	-.196[, b, c]	.239	122.850	1.000	-.776	.383
5.0	0.5% DMSO buffer	MERS-FP	-1.935[*, b, c]	.176	312.226	.000	-2.490	-1.381
		MERS-SC	-.100[b, c]	.175	309.257	1.000	-.652	.453
		MERS-SHCR	.716[*, b, c]	.176	311.282	.002	.162	1.270
		MHV-FP	-1.273[*, b, c]	.175	308.781	.000	-1.825	-.720
		MHV-SHCR	.282[b, c]	.175	309.040	1.000	-.270	.835
		M2-infleunza	-.368[, b, c]	.286	118.184	.603	-1.063	.327

Based on estimated marginal means

*. The mean difference is significant at the .05 level.

a. Dependent Variable: Effective diameter (size).

b. An estimate of the modified population marginal mean (I).

c. An estimate of the modified population marginal mean (J).

d. Adjustment for multiple comparisons: Bonferroni.

Appendix 4: Pairwise comparisons of time and treatment of effect of the effect of MERS and MHV S2-derived peptides in 0.5% DMSO buffer on GUV shape[a].

Time (min)	(I) treatment	(J) treatment	Mean Difference (I-J)	Std. Error	df	Sig.[d]	95% Confidence Interval for Difference[d]	
							Lower Bound	Upper Bound
1.0	0.5% DMSO buffer	MERS-FP	.059[*, b, c]	.009	317.203	.000	-.086	-.032
		MERS-SC	.003[b, c]	.009	306.657	1.000	-.024	.030
		MERS-SHCR	-.017[b, c]	.009	307.088	1.000	-.044	.010
		MHV-FP	-.037[*, b, c]	.009	309.654	.000	-.065	-.010
		MHV-SHCR	-.008[b, c]	.009	306.636	1.000	-.035	.019
		M2-infleunza	-.054[*, b, c]	.011	117.814	.000	-.080	-.027
2.0	0.5% DMSO buffer	MERS-FP	-.061[*, b, c]	.009	318.093	.000	-.089	-.034
		MERS-SC	.007[b, c]	.009	307.582	1.000	-.020	.034
		MERS-SHCR	-.011[b, c]	.009	308.011	1.000	-.039	.016
		MHV-FP	-.030[*, b, c]	.009	310.568	.014	-.058	-.003
		MHV-SHCR	-.006[b, c]	.009	307.561	1.000	-.033	.022
		M2-infleunza	-.056[*, b, c]	.010	119.020	.000	.016	.069
5.0	0.5% DMSO buffer	MERS-FP	-.080[*, b, c]	.011	317.643	.000	-.115	-.045
		MERS-SC	.007[b, c]	.011	309.596	1.000	-.028	.041
		MERS-SHCR	-.009[b, c]	.011	309.922	1.000	-.044	.026
		MHV-FP	-.043[*, b, c]	.011	311.872	.003	-.078	-.008
		MHV-SHCR	-.011[b, c]	.011	309.579	1.000	-.046	.024
		M2-infleunza	-.046[*, b, c]	.014	117.161	.005	-.081	-.011

Based on estimated marginal means

*. The mean difference is significant at the .05 level.

a. Dependent Variable: Ratio A/B (shape).

b. An estimate of the modified population marginal mean (I).

c. An estimate of the modified population marginal mean (J).

d. Adjustment for multiple comparisons: Bonferroni.

Appendix 5: Pairwise comparisons of time and treatment of effect of MERS-HR1, MERS-SPreTM in 5% DMSO buffer on GUV size[a].

Time (min)	(I) treatment	(J) treatment	Mean Difference (I-J)	Std. Error	df	Sig.[d]	95% Confidence Interval for Difference[d]	
							Lower Bound	Upper Bound
1.0	5% DMSO buffer	MERS-HR1	.460[*b, c]	.100	139.165	.000	.219	.702
		MERS-SPreTM	.003[b, c]	.092	116.326	1.000	-.221	.227
2.0	5% DMSO buffer	MERS-HR1	.615[*, b, c]	.110	137.758	.000	.347	.882
		MERS-SPreTM	.022[b, c]	.104	116.836	1.000	-.230	.274
5.0	5% DMSO buffer	MERS-HR1	.644[*, b, c]	.108	137.742	.000	.381	.907
		MERS-SPreTM	.105[b, c]	.102	116.448	.918	-.143	.352

Based on estimated marginal means
*. The mean difference is significant at the .05 level.
a. Dependent Variable: Effective diameter (size).
b. An estimate of the modified population marginal mean (I).
c. An estimate of the modified population marginal mean (J).
d. Adjustment for multiple comparisons: Bonferroni.

Appendix 6: Pairwise comparisons of time and treatment of effect of MERS-HR1, MERS-SPreTM in 5% DMSO buffer on GUV shape[a].

Time (min)	(I) treatment	(J) treatment	Mean Difference (I-J)	Std. Error	df	Sig.[d]	95% Confidence Interval for Difference[d]	
							Lower Bound	Upper Bound
1.0	5% DMSO buffer	MERS-HR1	-.021[*, b, c]	.004	120.834	.000	-.031	-.010
		MERS-SPreTM	-.004[b, c]	.004	117.387	.965	-.015	.006
2.0	5% DMSO buffer	MERS-HR1	-.019[*, b, c]	.004	121.652	.000	-.028	-.010
		MERS-SpreTM	-.005[b, c]	.004	117.806	.592	-.014	.004
5.0	5% DMSO buffer	MERS-HR1	-.021[*, b, c]	.004	121.552	.000	-.032	-.010
		MERS-SPreTM	-.007[b, c]	.004	118.157	.349	-.018	.004

Based on estimated marginal means
*. The mean difference is significant at the .05 level.
a. Dependent Variable: Ratio A/B (shape).
b. An estimate of the modified population marginal mean (I).

c. An estimate of the modified population marginal mean (J).

d. Adjustment for multiple comparisons: Bonferroni.

Appendix 7: Pairwise comparisons of time and treatment of effect of MHV-HR1 in 25.5% DMSO on GUV size[a].

Time (min)	(I) treatment	(J) treatment	Mean Difference (I-J)	Std. Error	df	Sig.[d]	95% Confidence Interval for Difference[d]	
							Lower Bound	Upper Bound
1.0	25.5% DMSO buffer	MHV-HR1	-.107[b, c]	.103	78.613	.303	-.311	.098
2.0	25.5% DMSO buffer	MHV-HR1	-.267[b, c]	.144	78.954	.068	-.554	.020
5.0	25.5% DMSO buffer	MHV-HR1	-.229[b, c]	.124	77.155	.068	-.475	.017

Based on estimated marginal means

a. Dependent Variable: Effective diameter (size).

b. An estimate of the modified population marginal mean (I).

c. An estimate of the modified population marginal mean (J).

d. Adjustment for multiple comparisons: Bonferroni.

Appendix 8: Pairwise comparisons of time and treatment of effect of MHV-HR1 in 25.5% DMSO on GUV shape[a].

Time (min)	(I) treatment	(J) treatment	Mean Difference (I-J)	Std. Error	df	Sig.[d]	95% Confidence Interval for Difference[d]	
							Lower Bound	Upper Bound
1.0	25.5% DMSO buffer	MHV-HR1	-.008[b, c]	.010	63.406	.439	-.029	.013
2.0	25.5% DMSO buffer	MHV-HR1	-.052[b, c, *]	.020	74.225	.011	-.092	-.012
5.0	25.5% DMSO buffer	MHV-HR1	-.017[b, c]	.020	73.666	.412	-.057	.024

Based on estimated marginal means *.

The mean difference is significant at the .05 level.

a. Dependent Variable: Ratio A/B (shape).

b. An estimate of the modified population marginal mean (I).

c. An estimate of the modified population marginal mean (J).

d. Adjustment for multiple comparisons: Bonferroni.

Appendix 9: Pairwise comparisons of time and treatment of the effect of MERS-S2 and MHV-S2 derived peptides in 1% DMSO on GUV size[a].

Time (min)	(I) treatment	(J) treatment	Mean Difference (I-J)	Std. Error	df	Sig.[d]	95% Confidence Interval for Difference[d]	
							Lower Bound	Upper Bound
1.0	1% DMSO buffer	MERS S-HR2	.006 [b, c]	.010	317.675	1.000	-.025	.036
		MHV S-HR2	.001 [b, c]	.010	317.737	1.000	-.030	.031
		MHV S-PreTM	.001 [b, c]	.010	323.010	1.000	-.029	.032
		MHV SC	-.015 [b, c]	.010	342.249	1.000	-.047	.017
2.0	1% DMSO buffer	MERS S-HR2	.005 [b, c]	.010	317.829	1.000	-.026	.036
		MHV S-HR2	.000 [b, c]	.010	317.892	1.000	-.031	.031
		MHV S-PreTM	.001 [b, c]	.010	323.161	1.000	-.030	.032
		MHV SC	-.012 [b, c]	.010	342.425	1.000	-.044	.020
5.0	1% DMSO buffer	MERS S-HR2	.006 [b, c]	.029	312.880	1.000	-.085	.097
		MHV S-HR2	.000 [b, c]	.029	312.893	1.000	-.091	.091
		MHV S-PreTM	-.002 [b, c]	.029	314.002	1.000	-.093	.089
		MHV SC	-.015 [b, c]	.029	318.213	1.000	-.106	.076

Based on estimated marginal means
a. Dependent Variable: Effective diameter (size).
b. An estimate of the modified population marginal mean (I).
c. An estimate of the modified population marginal mean (J).
d. Adjustment for multiple comparisons: Bonferroni.

Appendix 10: Pairwise comparisons of time and treatment of the effect of MERS-S2 and MHV-S2 derived peptides in 1% DMSO on GUV shape[a].

Time (min)	(I) treatment	(J) treatment	Mean Difference (I-J)	Std. Error	df	Sig.[d]	95% Confidence Interval for Difference[d]	
							Lower Bound	Upper Bound
1.0	1% DMSO buffer	MERS S-HR2	.000[b, c]	.000	310.422	1.000	-.001	.001
		MHV S-HR2	-.001[b, c]	.000	312.330	1.000	-.002	.000
		MHV S-PreTM	.000[b, c]	.000	310.405	1.000	-.001	.001
		MHV SC	.000[b, c]	.000	310.445	1.000	-.001	.001
2.0	1% DMSO buffer	MERS S-HR2	.000[b, c]	.000	310.433	1.000	-.001	.001
		MHV S-HR2	-.001[b, c]	.000	312.340	1.000	-.002	.000
		MHV S-PreTM	.000[b, c]	.000	310.415	1.000	-.001	.001
		MHV SC	.000[b, c]	.000	310.456	1.000	-.001	.001
5.0	1% DMSO buffer	MERS S-HR2	.000[b, c]	.001	311.081	1.000	-.002	.002
		MHV S-HR2	-.001[b, c]	.001	311.838	1.000	-.003	.002
		MHV S-PreTM	.000[b, c]	.001	311.075	1.000	-.002	.002
		MHV SC	.000[b, c]	.001	311.090	1.000	-.002	.002

Based on estimated marginal means
a. Dependent Variable: Ratio A/B (shape).
b. An estimate of the modified population marginal mean (I).
c. An estimate of the modified population marginal mean (J).
d. Adjustment for multiple comparisons: Bonferroni.

Appendix 11: Pairwise comparisons of time and treatment of the effects of MERS-FP in 1µM on GUV size[a].

Time (min)	(I) treatment	(J) treatment	Mean Difference (I-J)	Std. Error	df	Sig.[d]	95% Confidence Interval for Difference[d]	
							Lower Bound	Upper Bound
.0	MERS-FP (1µM)	0.5%DMSO buffer	-.364[b, c]	.692	77.496	.601	-1.742	1.015
5.0	MERS-FP (1µM)	0.5%DMSO buffer	-.345[b, c]	.691	77.494	.619	-1.722	1.031

Based on estimated marginal means
a. Dependent Variable: Effective diameter (size).
b. An estimate of the modified population marginal mean (I).
c. An estimate of the modified population marginal mean (J).
d. Adjustment for multiple comparisons: Bonferroni.

Appendix 12: Pairwise comparisons of time and treatment of the effects of MERS-FP in 1μM on GUV shape[a].

Time (min)	(I) treatment	(J) treatment	Mean Difference (I-J)	Std. Error	df	Sig.[d]	95% Confidence Interval for Difference[d]	
							Lower Bound	Upper Bound
.0	MERS-FP (1μM)	0.5%DMSO buffer	-.016[* b, c]	.002	76.294	.000	-.021	-.011
5.0	MERS-FP (1μM)	0.5%DMSO buffer	-.021[* b, c]	.004	77.226	.000	-.029	-.013

Based on estimated marginal means
*. The mean difference is significant at the .05 level.
a. Dependent Variable: Ratio A/B (shape).
b. An estimate of the modified population marginal mean (I).
c. An estimate of the modified population marginal mean (J).
d. Adjustment for multiple comparisons: Bonferroni.

Appendix 13: Pairwise comparisons of time and treatment of the effect of MERS-FP in 0.1μM on GUV size[a].

Time (min)	(I) treatment	(J) treatment	Mean Difference (I-J)	Std. Error	df	Sig.[d]	95% Confidence Interval for Difference[d]	
							Lower Bound	Upper Bound
.0	0.5% DMSO buffer	MERS-FP (0.1μM)	-1.044[b, c]	.764	77.493	.176	-2.566	.478
5.0	0.5% DMSO buffer	MERS-FP (0.1μM)	-1.000[b, c]	.765	77.495	.195	-2.523	.524

Based on estimated marginal means
a. Dependent Variable: Effective diameter (size).
b. An estimate of the modified population marginal mean (I).
c. An estimate of the modified population marginal mean (J).
d. Adjustment for multiple comparisons: Bonferroni.

Appendix 14: Pairwise comparisons of time and treatment of the effect of MERS-FP in 0.1µM on GUV shape[a].

Time (min)	(I) treatment	(J) treatment	Mean Difference (I-J)	Std. Error	df	Sig.[d]	95% Confidence Interval for Difference[d]	
							Lower Bound	Upper Bound
.0	0.5% DMSO buffer	MERS-FP (0.1µM)	1.653E-11 [b, c]	.000	78.000	1.000	-4.934E-7	4.934E-7
5.0	0.5% DMSO buffer	MERS-FP (0.1µM)	.007 [b, c]	.004	78.000	.102	-.001	.014

Based on estimated marginal means
a. Dependent Variable: ratio A/B (shape).
b. An estimate of the modified population marginal mean (I).
c. An estimate of the modified population marginal mean (J).
d. Adjustment for multiple comparisons: Bonferroni.

Appendix 15: Pairwise comparisons of time and treatment of the effect of MHV-FP in 1µM on GUV size[a].

Time (min)	(I) treatment	(J) treatment	Mean Difference (I-J)	Std. Error	df	Sig.[d]	95% Confidence Interval for Difference[d]	
							Lower Bound	Upper Bound
.0	0.5%DMSO buffer	MHV-FP (1µM)	2.052E-10 [b, c]	.000	78.000	1.000	-2.056E-5	2.056E-5
5.0	0.5%DMSO buffer	MHV-FP (1µM)	.038 [b, c]	.035	78.000	.279	-.031	.107

Based on estimated marginal means
a. Dependent Variable: Effective diameter (size).
b. An estimate of the modified population marginal mean (I).
c. An estimate of the modified population marginal mean (J).
d. Adjustment for multiple comparisons: Bonferroni.

Appendix 16: Pairwise comparisons of time and treatment of the effect of MHV-FP in 1µM on GUV shape[a].

Time (min)	(I) treatment	(J) treatment	Mean Difference (I-J)	Std. Error	df	Sig.[b]	95% Confidence Interval for Difference[b]	
							Lower Bound	Upper Bound
.0	0.5%DMSO buffer	MHV-FP (1µM)	3.436	.000	1174816	1.000	-7.604E-7	7.605E-7
5.0	0.5%DMSO buffer	MHV-FP (1µM)	.006	.004	78.000	.083	-.001	.014

Based on estimated marginal means
a. Dependent Variable: Ratio A/B (shape).
b. Adjustment for multiple comparisons: Bonferroni.

Appendix 17: Pairwise comparisons of time and treatment of the effect of MHV-FP in 0.1µM on GUV size[a].

Time (min)	(I) treatment	(J) treatment	Mean Difference (I-J)	Std. Error	df	Sig.[b]	95% Confidence Interval for Difference[b]	
							Lower Bound	Upper Bound
.0	0.5%DMSO buffer	MHV-FP (0.1µM)	2.052E-10	.000	78.000	1.000	-2.056E-5	2.056E-5
5.0	0.5%DMSO buffer	MHV-FP (0.1µM)	.038	.035	78.000	.279	-.031	.107

Based on estimated marginal means
a. Dependent Variable: Effective diameter (size).
b. Adjustment for multiple comparisons: Bonferroni.

Appendix 18: Pairwise Comparisons of time and treatment of the effect of MHV-FP in 0.1µM on GUV shape[a].

Time (min)	(I) treatment	(J) treatment	Mean Difference (I-J)	Std. Error	df	Sig.[b]	95% Confidence Interval for Difference[b]	
							Lower Bound	Upper Bound
.0	0.5% DMSO buffer	MHV-FP (0.1µM)	3.436	.000	78.000	1.000	-7.60	7.60
5.0	0.5% DMSO buffer	MHV-FP (0.1µM)	.006	.004	78.000	.083	-.001	.014

Based on estimated marginal means

a. Dependent Variable: Ratio A/B (shape).

b. Adjustment for multiple comparisons: Bonferroni.

Appendix 19: Pairwise comparisons of time and treatment of the effect of mutated MERS-FP on GUV size[a].

Time (min)	(I) treatment	(J) treatment	Mean Difference (I-J)	Std. Error	df	Sig.[b]	95% Confidence Interval for Difference[b]	
							Lower Bound	Upper Bound
1.0	5% DMSO buffer	MERS-FP peptide 5	.081	.087	271.456	1.000	-.185	.347
		MERS-FP peptide 4	.683*	.087	273.692	.000	.416	.949
		MERS-FP peptide 6	.198	.088	278.788	.513	-.070	.467
		MERS-FP peptide 3	-.013	.087	271.444	1.000	-.279	.253
		MERS-FP peptide 2	.017	.087	272.840	1.000	-.249	.283
		MERS-FP peptide 1	-.866*	.148	311.174	.000	-1.332	-.400
2.0	5% DMSO buffer	MERS-FP peptide 5	.108	.088	272.112	1.000	-.162	.378
		MERS-FP peptide 4	.869*	.088	274.321	.000	.599	1.140
		MERS-FP peptide 6	.367*	.089	279.357	.001	.094	.639
		MERS-FP peptide 3	-.020	.088	272.101	1.000	-.290	.250
		MERS-FP peptide 2	.010	.088	273.480	1.000	-.260	.281
		MERS-FP peptide 1	-1.283*	.184	314.256	.000	-1.864	-.701
5.0	5% DMSO buffer	MERS-FP peptide 5	.115	.097	272.075	1.000	-.183	.412
		MERS-FP peptide 4	1.061*	.097	274.075	.000	.762	1.359
		MERS-FP peptide 6	.606*	.098	278.627	.000	.306	.906
		MERS-FP peptide 3	-.013	.097	272.065	1.000	-.310	.285
		MERS-FP peptide 2	-.010	.097	273.310	1.000	-.308	.288
		MERS-FP peptide 1	-1.935*	.176	312.226	.000	-2.490	-1.381

Based on estimated marginal means
*. The mean difference is significant at the .05 level.
a. Dependent Variable: Effective diameter (size).
b. Adjustment for multiple comparisons: Bonferroni.

Appendix 20: Pairwise comparisons of time and treatment of the effect of mutated MERS-FP on GUV shape[a].

Time (min)	(I) treatment	(J) treatment	Mean Difference (I-J)	Std. Error	df	Sig.[b]	95% Confidence Interval for Difference[b]	
							Lower Bound	Upper Bound
1.0	5% DMSO buffer	MERS-FP peptide 5	-.002	.004	270.383	1.000	-.014	.010
		MERS-FP peptide 4	-.025*	.004	270.384	.000	-.037	-.013
		MERS-FP peptide 6	-.020*	.004	269.841	.000	-.032	-.008
		MERS-FP peptide 3	-.001	.004	269.700	1.000	-.013	.011
		MERS-FP peptide 2	5.985E.	.004	270.365	1.000	-.012	.012
		MERS-FP peptide 1	059	.009	317.203	.000	-.086	-.032
2.0	5% DMSO buffer	MERS-FP peptide 5	-.005	.004	271.546	1.000	-.018	.009
		MERS-FP peptide 4	-.029*	.004	271.547	.000	-.043	-.016
		MERS-FP peptide 6	-.035*	.004	271.054	.000	-.049	-.022
		MERS-FP peptide 3	-.001	.004	270.927	1.000	-.014	.013
		MERS-FP peptide 2	7.338E-	.004	271.529	1.000	-.013	.014
		MERS-FP peptide 1	-.061*	.009	318.093	.000	-.089	-.034
5.0	5% DMSO buffer	MERS-FP peptide 5	-.003	.005	270.882	1.000	-.019	.012
		MERS-FP peptide 4	-.031*	.005	270.883	.000	-.046	-.015
		MERS-FP peptide 6	-.048*	.005	270.466	.000	-.064	-.032
		MERS-FP peptide 3	-.001	.005	270.359	1.000	-.016	.015
		MERS-FP peptide 2	-.002	.005	270.868	1.000	-.017	.014
		MERS-FP peptide 1	-.080*	.011	317.643	.000	-.115	-.045

Based on estimated marginal means

*. The mean difference is significant at the .05 level.

a. Dependent Variable: Ratio A/B (shape).

b. Adjustment for multiple comparisons: Bonferroni.

Appendix 21: Pairwise comparisons of time and treatment of the effect of MERS-MPTM3 on 17% DMSO buffer GUV size[a].

Time (min)	(I) treatment	(J) treatment	Mean Difference (I-J)	Std. Error	df	Sig.[d]	95% Confidence Interval for Difference[d]	
							Lower Bound	Upper Bound
1.0	17% DMSO buffer	MERS-MPTM3	.168[b, c]	.092	77.881	.072	-.015	.352
2.0	17% DMSO buffer	MERS-MPTM3	.205[b, c, *]	.100	78.820	.043	.007	.403
5.0	17% DMSO buffer	MERS-MPTM3	.250[b, c, *]	.125	77.111	.049	.001	.499

Based on estimated marginal means
*. The mean difference is significant at the .05 level.
a. Dependent Variable: Effective diameter (size).
b. An estimate of the modified population marginal mean (I).
c. An estimate of the modified population marginal mean (J).
d. Adjustment for multiple comparisons: Bonferroni.

Appendix 22: Pairwise Comparisons of treatment and time of the effect of MERS-MPTM3 in 17% DMSO buffer GUV shape[a].

Time (min)	(I) treatment	(J) treatment	Mean Difference (I-J)	Std. Error	df	Sig.[d]	95% Confidence Interval for Difference[d]	
							Lower Bound	Upper Bound
1.0	17% DMSO buffer	MERS-MPTM3	-.005[b, c]	.005	75.730	.347	-.014	.005
2.0	17% DMSO buffer	MERS-MPTM3	-.003[b, c]	.005	75.028	.601	-.013	.008
5.0	17% DMSO buffer	MERS-MPTM3	-.007[b, c]	.006	77.597	.300	-.019	.006

Based on estimated marginal means
a. Dependent Variable: Ratio A/B (shape).
b. An estimate of the modified population marginal mean (I).
c. An estimate of the modified population marginal mean (J).
d. Adjustment for multiple comparisons: Bonferroni.

Appendix 23: Pairwise comparisons of time and treatment of the effects of MERS M Proline in 14.7% DMSO buffer on GUV size[a].

Time (min)	(I) treatment	(J) treatment	Mean Difference (I-J)	Std. Error	df	Sig.[d]	95% Confidence Interval for Difference[d]	
							Lower Bound	Upper Bound
1.0	14.7%DMSO buffer	MERS-M Proline	.197[*, b, c]	.080	76.394	.016	.038	.356
2.0	14.7%DMSO buffer	MERS-M Proline	.367[*, b, c]	.084	77.441	.000	.200	.534
5.0	14.7%DMSO buffer	MERS-M Proline	.575[*, b, c]	.089	77.325	.000	.398	.752

Based on estimated marginal means
*. The mean difference is significant at the .05 level.
a. Dependent Variable: Effective diameter (size).
b. An estimate of the modified population marginal mean (I).
c. An estimate of the modified population marginal mean (J).
d. Adjustment for multiple comparisons: Bonferroni.

Appendix 24: Pairwise comparisons of time and treatment of the effect of MERS-M Proline in 14.7% DMSO buffer on GUV shape[a].

Time (min)	(I) treatment	(J) treatment	Mean Difference (I-J)	Std. Error	df	Sig.[d]	95% Confidence Interval for Difference[d]	
							Lower Bound	Upper Bound
1.0	14.7%DMSO buffer	MERS-M Proline	-.023[*, b, c]	.006	75.741	.001	-.035	-.010
2.0	14.7%DMSO buffer	MERS-M Proline	-.030[*, b, c]	.008	77.611	.000	-.045	-.014
5.0	14.7%DMSO buffer	MERS-M Proline	-.036[*, b, c]	.009	75.262	.000	-.055	-.018

Based on estimated marginal means
*. The mean difference is significant at the .05 level.
a. Dependent Variable: Ratio A/B (shape).
b. An estimate of the modified population marginal mean (I).
c. An estimate of the modified population marginal mean (J).
d. Adjustment for multiple comparisons: Bonferroni.

Appendix 25: Pairwise comparisons of time and treatment of the effect of MHV-MTM3 and MHV-M Proline region in 1% DMSO buffer on GUV size[a].

Time (min)	(I) treatment	(J) treatment	Mean Difference (I-J)	Std. Error	df	Sig.[b]	95% Confidence Interval for Difference[b]	
							Lower Bound	Upper Bound
1.0	1% DMSO buffer	MHV M-TM3	.007	.010	332.065	1.000	-.024	.038
		MHV-M Proline	.007	.010	313.467	1.000	-.024	.037
2.0	1% DMSO buffer	MHV M-TM3	.006	.010	332.220	1.000	-.025	.038
		MHV-M Proline	.006	.010	313.629	1.000	-.025	.037
5.0	1% DMSO buffer	MHV M-TM3	.006	.029	315.951	1.000	-.085	.098
		MHV-M Proline	-.048	.029	312.007	1.000	-.139	.042

Based on estimated marginal means
a. Dependent Variable: Effective diameter (size).
b. Adjustment for multiple comparisons: Bonferroni.

Appendix 26: Pairwise comparisons of time and treatment of the effect of MHV-MTM3 and MHV-M Proline region in 1% DMSO buffer on GUV shape[a].

Time (min)	(I) treatment	(J) treatment	Mean Difference (I-J)	Std. Error	df	Sig.[b]	95% Confidence Interval for Difference[b]	
							Lower Bound	Upper Bound
1.0	1% DMSO buffer	MHV M-TM3	.000	.000	310.474	1.000	-.001	.001
		MHV-M Proline	.000	.000	310.143	1.000	-.001	.001
2.0	1% DMSO buffer	MHV M-TM3	.000	.000	310.485	1.000	-.001	.001
		MHV-M Proline	.000	.000	310.154	1.000	-.001	.001
5.0	1% DMSO buffer	MHV M-TM3	.000	.001	311.102	1.000	-.002	.003
		MHV-M Proline	-.001	.001	310.971	1.000	-.004	.001

Based on estimated marginal means
a. Dependent Variable: Ratio A/B (shape).
b. Adjustment for multiple comparisons: Bonferroni.

Appendix 27: Pairwise comparisons of time and treatment of the effects of MHV-MPTM3 in 15% DMSO buffer on GUV size[a].

Time (min)	(I) treatment	(J) treatment	Mean Difference (I-J)	Std. Error	df	Sig.[d]	95% Confidence Interval for Difference[d]	
							Lower Bound	Upper Bound
1.0	15% DMSO buffer	MHV-MPTM3	.357[*, b, c]	.103	80.969	.001	.151	.563
2.0	15% DMSO buffer	MHV-MPTM3	.144[b, c]	.126	81.977	.256	-.106	.394
5.0	15% DMSO buffer	MHV-MPTM3	.153[b, c]	.137	79.311	.267	-.119	.425

Based on estimated marginal means
*. The mean difference is significant at the .05 level.
a. Dependent Variable: Effective diameter (size).
b. An estimate of the modified population marginal mean (I).
c. An estimate of the modified population marginal mean (J).
d. Adjustment for multiple comparisons: Bonferroni.

Appendix 28: Pairwise comparisons of time and treatment of the effects of MHV-MPTM3 in 15% DMSO buffer on GUV shape[a].

Time (min)	(I) treatment	(J) treatment	Mean Difference (I-J)	Std. Error	df	Sig.[d]	95% Confidence Interval for Difference[d]	
							Lower Bound	Upper Bound
1.0	15% DMSO buffer	MHV-MPTM3	-.003[b, c]	.005	76.478	.542	-.014	.007
2.0	15% DMSO buffer	MHV-MPTM3	.004[b, c]	.007	77.380	.594	-.010	.017
5.0	15% DMSO buffer	MHV-MPTM3	-.005[b, c]	.007	75.561	.441	-.020	.009

Based on estimated marginal means
a. Dependent Variable: Ratio A/B (shape).
b. An estimate of the modified population marginal mean (I).
c. An estimate of the modified population marginal mean (J).
d. Adjustment for multiple comparisons: Bonferroni.

Appendix 29: Pairwise comparisons of time and treatment of the effects of MERS-EPTM in 13% DMSO buffer on GUV size[a].

Time (min)	(I) treatment	(J) treatment	Mean Difference (I-J)	Std. Error	df	Sig.[d]	95% Confidence Interval for Difference[d]	
							Lower Bound	Upper Bound
1.0	13%DMSO buffer	MERS-EPTM	.068[b, c]	.177	91.579	.704	-.284	.419
2.0	13%DMSO buffer	MERS-EPTM	.004[b, c]	.175	92.045	.981	-.344	.353
5.0	13%DMSO buffer	MERS-EPTM	-.077[b, c]	.194	90.765	.693	-.462	.308

Based on estimated marginal means
a. Dependent Variable: Effective diameter (size).
b. An estimate of the modified population marginal mean (I).
c. An estimate of the modified population marginal mean (J).
d. Adjustment for multiple comparisons: Bonferroni.

Appendix 30: Pairwise comparisons of time and treatment of the effects of MERS-EPTM in 13% DMSO buffer on GUV shape[a].

Time (min)	(I) treatment	(J) treatment	Mean Difference (I-J)	Std. Error	df	Sig.[d]	95% Confidence Interval for Difference[d]	
							Lower Bound	Upper Bound
1.0	13%DMSO buffer	MERS-EPTM	.004[b, c]	.005	76.503	.435	-.006	.014
2.0	13%DMSO buffer	MERS-EPTM	.013[b, c]	.007	78.170	.062	-.001	.027
5.0	13%DMSO buffer	MERS-EPTM	.011[b, c]	.008	77.940	.185	-.005	.027

Based on estimated marginal means
a. Dependent Variable: Ratio A/B (shape).
b. An estimate of the modified population marginal mean (I).
c. An estimate of the modified population marginal mean (J).
d. Adjustment for multiple comparisons: Bonferroni.

Appendix 31: Pairwise comparisons of time and treatment of the effects of MHV-ETM in 1% DMSO buffer on GUV size[a].

Time (min)	(I) treatment	(J) treatment	Mean Difference (I-J)	Std. Error	df	Sig.[b]	95% Confidence Interval for Difference[b]	
							Lower Bound	Upper Bound
1.0	1% DMSO buffer	MHV-ETM	.002	.010	318.393	1.000	-.029	.032
2.0	1% DMSO buffer	MHV-ETM	.002	.010	318.547	1.000	-.029	.033
5.0	1% DMSO buffer	MHV-ETM	.002	.029	313.030	1.000	-.089	.093

Based on estimated marginal means
a. Dependent Variable: Effective diameter (size).
b. Adjustment for multiple comparisons: Bonferroni.

Appendix 32: Pairwise comparisons of time and treatment of the effects of MHV-ETM at 1% DMSO buffer on GUV shape[a].

Time (min)	(I) treatment	(J) treatment	Mean Difference (I-J)	Std. Error	df	Sig.[b]	95% Confidence Interval for Difference[b]	
							Lower Bound	Upper Bound
1.0	1% DMSO buffer	MHV-ETM	.000	.000	310.387	1.000	-.001	.001
2.0	1% DMSO buffer	MHV-ETM	.000	.000	310.397	1.000	-.001	.001
5.0	1% DMSO buffer	MHV-ETM	.000	.001	311.067	1.000	-.002	.002

Based on estimated marginal means
a. Dependent Variable: Ratio A/B (shape).
b. Adjustment for multiple comparisons: Bonferroni.

Appendix 33: Pairwise comparisons of time and treatment of the effects of MHV-EPTM at 0.5% DMSO buffer on GUV size[a].

Time (min)	(I) treatment	(J) treatment	Mean Difference (I-J)	Std. Error	df	Sig.[d]	95% Confidence Interval for Difference[d]	
							Lower Bound	Upper Bound
1.0	0.5% DMSO buffer	MHV-E PTM	.435[*, b, c]	.089	78.126	.000	.258	.612
2.0	0.5% DMSO buffer	MHV-E PTM	.543[*, b, c]	.092	77.870	.000	.361	.726
5.0	0.5% DMSO buffer	MHV-E PTM	.515[*, b, c]	.095	77.927	.000	.326	.704

Based on estimated marginal means
*. The mean difference is significant at the .05 level.
a. Dependent Variable: Effective diameter (size).
b. An estimate of the modified population marginal mean (I).
c. An estimate of the modified population marginal mean (J).
d. Adjustment for multiple comparisons: Bonferroni.

Appendix 34: Pairwise comparisons of time and treatment of the effects of MHV-EPTM at 0.5% DMSO buffer on GUV shape[a].

Time (min)	(I) treatment	(J) treatment	Mean Difference (I-J)	Std. Error	df	Sig.[d]	95% Confidence Interval for Difference[d]	
							Lower Bound	Upper Bound
1.0	0.5% DMSO buffer	MHV-E PTM	.012[*, b, c]	.003	85.346	.000	.006	.018
2.0	0.5% DMSO buffer	MHV-E PTM	.015[*, b, c]	.005	88.466	.002	.006	.024
5.0	0.5% DMSO buffer	MHV-E PTM	.016[*, b, c]	.004	91.901	.000	.008	.023

Based on estimated marginal means
*. The mean difference is significant at the .05 level.
a. Dependent Variable: Ratio A/B (shape).
b. An estimate of the modified population marginal mean (I).
c. An estimate of the modified population marginal mean (J).
d. Adjustment for multiple comparisons: Bonferroni.

Appendix 35: Pairwise comparisons of time and treatment of the effects of MERS and MHV-nsp 3, nsp 4, and nsp 6 in at 10 µM and 0.5% DMSO on GUV size[a].

Time (min)	(I) treatment	(J) treatment	Mean Difference (I-J)	Std. Error	df	Sig.[b]	95% Confidence Interval for Difference[b]	
							Lower Bound	Upper Bound
1.0	0.5% DMSO buffer	MERS-nsp 4-3	-.556*	.099	474.963	.000	-.891	-.221
		MERS-nsp 6-1	.017	.100	486.622	1.000	-.322	.355
		MERS-nsp 6-2	.010	.098	464.044	1.000	-.322	.341
		MERS-nsp 3-1	.853*	.101	500.949	.000	.510	1.196
		MERS-nsp 3-3	.651*	.100	486.409	.000	.313	.990
		MHV-nsp 4-1	.060	.098	470.113	1.000	-.274	.394
		MHV-nsp 4-2	.299	.098	463.188	.154	-.032	.631
		MHV-nsp 6-2	.291	.098	464.336	.208	-.041	.622
		MHV-nsp 3-1	.693*	.098	465.501	.000	.360	1.025
		MHV-nsp 3-3	.195	.099	477.249	1.000	-.141	.531
		MHV-nsp 3-2	.507*	.101	501.903	.000	.164	.850
2.0	0.5% DMSO buffer	MERS-nsp 4-3	-.590*	.111	475.880	.000	-.966	-.214
		MERS-nsp 6-1	.115	.112	486.556	1.000	-.264	.494
		MERS-nsp 6-2	.103	.110	465.937	1.000	-.270	.476
		MERS-nsp 3-1	1.166*	.113	499.760	.000	.784	1.549
		MERS-nsp 3-3	.856*	.112	486.360	.000	.477	1.235
		MHV-nsp 4-1	.026	.110	471.458	1.000	-.349	.401
		MHV-nsp 4-2	.516*	.110	465.160	.000	.143	.889
		MHV-nsp 6-2	.507*	.110	466.202	.000	.134	.880
		MHV-nsp 3-1	.970*	.110	467.261	.000	.596	1.343
		MHV-nsp 3-3	.320	.111	477.969	.272	-.056	.697
		MHV-nsp 3-2	.751*	.113	500.643	.000	.368	1.134
5.0	0.5% DMSO buffer	MERS-nsp 4-3	-.827*	.121	474.255	.000	-1.236	-.417
		MERS-nsp 6-1	.055	.122	483.951	1.000	-.357	.468
		MERS-nsp 6-2	.029	.120	465.251	1.000	-.378	.436
		MERS-nsp 3-1	1.233*	.123	495.984	.000	.817	1.649
		MERS-nsp 3-3	.975*	.122	483.773	.000	.562	1.387
		MHV-nsp 4-1	-.071	.120	470.247	1.000	-.480	.337
		MHV-nsp 4-2	.571*	.120	464.548	.000	.164	.978
		MHV-nsp 6-2	.613*	.120	465.491	.000	.206	1.020
		MHV-nsp 3-1	.998*	.120	466.449	.000	.591	1.405
		MHV-nsp 3-3	.253	.121	476.150	1.000	-.157	.663
		MHV-nsp 3-2	.769*	.123	496.790	.000	.353	1.185

Based on estimated marginal means

*. The mean difference is significant at the .05 level.

a. Dependent Variable: Effective diameter (size).

b. Adjustment for multiple comparisons: Bonferroni.

Appendix 36: Pairwise comparisons of time and treatment of the effects of MERS and MHV-nsp 3, nsp 4, and nsp 6 in in 10 μM and 0.5% DMSO on GUV shape[a].

Time (min)	(I) treatment	(J) treatment	Mean Difference (I-J)	Std. Error	df	Sig.[b]	95% Confidence Interval for Difference[b]	
							Lower Bound	Upper Bound
1.0	0.5% DMSO buffer	MERS-nsp 4-3	.008	.004	484.565	1.000	-.005	.021
		MERS-nsp 6-1	.012	.004	483.319	.125	-.001	.025
		MERS-nsp 6-2	.003	.004	479.903	1.000	-.021	.017
		MERS-nsp 3-1	-.001	.004	476.419	1.000	-.014	.012
		MERS-nsp 3-3	-.006	.004	476.570	1.000	-.019	.008
		MHV-nsp 4-1	.000	.004	476.839	1.000	-.013	.013
		MHV-nsp 4-2	.004	.004	473.047	1.000	-.009	.017
		MHV-nsp 6-2	.011	.004	486.483	.488	-.003	.024
		MHV-nsp 3-1	.003	.004	468.511	1.000	-.010	.016
		MHV-nsp 3-3	.005	.004	485.420	1.000	-.009	.018
		MHV-nsp 3-2	.003	.004	475.090	1.000	-.011	.016
2.0	0.5% DMSO buffer	MERS-nsp 4-3	.012	.004	485.462	.585	-.003	.027
		MERS-nsp 6-1	.016*	.004	484.328	.031	.001	.030
		MERS-nsp 6-2	.003	.004	471.442	1.000	-.012	.017
		MERS-nsp 3-1	.001	.004	478.060	1.000	-.014	.016
		MERS-nsp 3-3	-.004	.004	478.196	1.000	-.019	.011
		MHV-nsp 4-1	.003	.004	478.440	1.000	-.012	.017
		MHV-nsp 4-2	.008	.004	475.005	1.000	-.007	.023
		MHV-nsp 6-2	.011	.004	487.209	.873	-.004	.026
		MHV-nsp 3-1	.001	.004	470.902	1.000	-.013	.016
		MHV-nsp 3-3	.006	.004	486.241	1.000	-.009	.021
		MHV-nsp 3-2	.003	.004	476.855	1.000	-.012	.018
5.0	0.5% DMSO buffer	MERS-nsp 4-3	.012	.005	481.420	.517	-.003	.028
		MERS-nsp 6-1	.016*	.005	480.353	.032	.001	.032
		MERS-nsp 6-2	.003	.005	474.481	1.000	-.012	.019
		MERS-nsp 3-1	-.001	.005	474.458	1.000	-.017	.014
		MERS-nsp 3-3	-.001	.005	474.587	1.000	-.016	.015
		MHV-nsp 4-1	.003	.005	474.816	1.000	-.012	.019
		MHV-nsp 4-2	.004	.005	471.588	1.000	-.012	.019
		MHV-nsp 6-2	.009	.005	483.064	1.000	-.007	.024
		MHV-nsp 3-1	.003	.005	467.736	1.000	-.013	.018
		MHV-nsp 3-3	.006	.005	482.152	1.000	-.010	.022
		MHV-nsp 3-2	.004	.005	473.326	1.000	-.011	.020

Based on estimated marginal means

*. The mean difference is significant at the .05 level.

a. Dependent Variable: Ratio AB (shape).

b. Adjustment for multiple comparisons: Bonferroni.

Appendix 37: Pairwise comparisons of time and treatment of the effects of MERS and MHV-nsp 4, and nsp6 in in 0.5 µM and 1% DMSO buffer on GUV size[a].

Time (min)	(I) treatment	(J) treatment	Mean Difference (I-J)	Std. Error	df	Sig.[b]	95% Confidence Interval for Difference[b]	
							Lower Bound	Upper Bound
1.0	1% DMSO buffer	MERS-nsp 4-1	.065	.062	191.858	1.000	-.111	.241
		MERS-nsp 4-2	.410*	.062	190.968	.000	.235	.586
		MHV-nsp 4-3	.029	.062	193.051	1.000	-.147	.205
		MHV-nsp 6-1	-.059	.062	195.371	1.000	-.237	.118
2.0	1% DMSO buffer	MERS-nsp 4-1	.065	.085	194.800	1.000	-.177	.306
		MERS-nsp 4-2	.617*	.085	194.063	.000	.376	.857
		MHV-nsp 4-3	.056	.085	195.792	1.000	-.186	.297
		MHV-nsp 6-1	-.084	.085	197.735	1.000	-.326	.159
5.0	1% DMSO buffer	MERS-nsp 4-1	.065	.106	194.657	1.000	-.235	.365
		MERS-nsp 4-2	.827*	.106	194.114	.000	.527	1.127
		MHV-nsp 4-3	.069	.106	195.388	1.000	-.231	.370
		MHV-nsp 6-1	-.111	.106	196.823	1.000	-.412	.190

Based on estimated marginal means
*. The mean difference is significant at the .05 level.
a. Dependent Variable: Effective diameter (size).
b. Adjustment for multiple comparisons: Bonferroni.

Appendix 38: Pairwise comparisons of time and treatment of the effects of MERS and MHV-nsp 4, and nsp 6 in in 0.5 µM and 1% DMSO buffer on GUV shape[a].

Time min)	(I) treatment	(J) treatment	Mean Difference (I-J)	Std. Error	df	Sig.[b]	95% Confidence Interval for Difference[b]	
							Lower Bound	Upper Bound
1.0	1% DMSO buffer	MERS-nsp 4-1	-.006	.003	194.033	.769	-.015	.004
		MERS-nsp 4-2	-.006	.003	194.416	.703	-.016	.003
		MHV-nsp 4-3	.000	.003	193.945	1.000	-.010	.009
		MHV-nsp 6-1	-.006	.003	194.956	.816	-.015	.004
2.0	1% DMSO buffer	MERS-nsp 4-1	-.006	.004	194.516	.968	-.016	.004
		MERS-nsp 4-2	-.007	.004	194.874	.464	-.017	.003
		MHV-nsp 4-3	.000	.004	194.435	1.000	-.010	.010
		MHV-nsp 6-1	-.009	.004	195.379	.123	-.019	.001
5.0	1% DMSO buffer	MERS-nsp 4-1	-.006	.003	194.188	1.000	-.016	.004
		MERS-nsp 4-2	-.009	.004	194.554	.076	-.019	.000
		MHV-nsp 4-3	.000	.003	194.105	1.000	-.010	.010
		MHV-nsp 6-1	-.011*	.004	195.070	.029	-.021	-.001

Based on estimated marginal means
*. The mean difference is significant at the .05 level.
a. Dependent Variable: Ratio A/B (shape).
b. Adjustment for multiple comparisons: Bonferroni.

Appendix 39: Pairwise comparisons of time and treatment of the effects of MERS and MHV-nsp 4, and nsp 6 in in 1µM and 5% DMSO buffer on GUV size [a].

Time (min)	(I) treatment	(J) treatment	Mean Difference (I-J)	Std. Error	df	Sig.[b]	95% Confidence Interval for Difference[b]	
							Lower Bound	Upper Bound
.0	5% DMSO buffer	MERS-nsp 4-1	.095	.511	154.990	1.000	-1.271	1.461
		MHV-nsp 4-3	-.307	.511	154.990	1.000	-1.673	1.059
		MHV-nsp 6-1	-.307	.511	154.990	1.000	-1.673	1.059
5.0	5% DMSO buffer	MERS-nsp 4-1	.078	.512	154.996	1.000	-1.290	1.446
		MHV-nsp 4-3	-.349	.512	154.996	1.000	-1.717	1.018
		MHV-nsp 6-1	-.349	.512	154.996	1.000	-1.717	1.018

Based on estimated marginal means
a. Dependent Variable: Effective diameter (size).
b. Adjustment for multiple comparisons: Bonferroni.

Appendix 40: Pairwise comparisons of time and treatment of the effects of MERS and MHV-nsp 4, and nsp 6 in in 1µM and 5% DMSO buffer on GUV shape[a].

Time (min)	(I) treatment	(J) treatment	Mean Difference (I-J)	Std. Error	df	Sig.[b]	95% Confidence Interval for Difference[b]	
							Lower Bound	Upper Bound
.0	5% DMSO buffer	MERS-nsp 4-1	.001	.001	152.659	.643	-.001	.003
		MHV-nsp 4-3	.000	.001	152.659	1.000	-.001	.002
		MHV-nsp 6-1	.001	.001	152.659	1.000	-.001	.002
5.0	5% DMSO buffer	MERS-nsp 4-1	-.002	.002	155.522	1.000	-.007	.003
		MHV-nsp 4-3	-.001	.002	155.522	1.000	-.007	.004
		MHV-nsp 6-1	.001	.002	155.522	1.000	-.005	.006

Based on estimated marginal means
a. Dependent Variable: Ratio A/B (shape).
b. Adjustment for multiple comparisons: Bonferroni.

Appendix 41: Pairwise comparisons of time and treatment of the effects of MERS and MHV-nsp 4, and nsp 6 in in 0.25 µM and 1% DMSO buffer on GUV size [a].

Time (min)	(I) treatment	(J) treatment	Mean Difference (I-J)	Std. Error	df	Sig.[b]	95% Confidence Interval for Difference[b]	
							Lower Bound	Upper Bound
.0	1%DMSO buffer	MERS-nsp 4-1	.199	.674	154.986	1.000	-1.602	2.001
		MHV- nsp 4-3	-.476	.674	154.986	1.000	-2.277	1.325
		MHV- nsp 6-1	-1.626	.674	154.986	.102	-3.427	.176
5.0	1%DMSO buffer	MERS-nsp 4-1	.199	.676	154.996	1.000	-1.607	2.005
		MHV- nsp 4-3	-.438	.676	154.996	1.000	-2.244	1.368
		MHV- nsp 6-1	-1.588	.676	154.996	.120	-3.394	.218

Based on estimated marginal means
a. Dependent Variable: Effective diameter (size).
b. Adjustment for multiple comparisons: Bonferroni.

Appendix 42: Pairwise comparisons of time and treatment of the effects of MERS and MHV-nsp 4, and nsp 6 in in 0.25 µM and 1% DMSO buffer on GUV shape[a].

Time (min)	(I) treatment	(J) treatment	Mean Difference (I-J)	Std. Error	df	Sig.[b]	95% Confidence Interval for Difference[b]	
							Lower Bound	Upper Bound
.0	1%DMSO buffer	MERS-nsp 4-1	-3.603E+16	3.271E+10	128.176	1.000	-3.602	-3602
		MHV- nsp 4-3	-3.603E+16	3.409E+10	151.228	1.000	-3.602	-3602
		MHV- nsp 6-1	-3603E+16	2.430E+10	156.067	1.000	-3.602	-3602
5.0	1%DMSO buffer	MERS-nsp 4-1	2.359E-	.000	2E+63	1.000	2.303E-	2.415 E-16
		MHV- nsp 4-3	2.356E-	.000	2E+63	1.000	2.299E-	2.412 E-16
		MHV- nsp 6-1	1.109E-	.000	2E+63	1.000	1.103E-	1.114 E-15

Based on estimated marginal means
a. Dependent Variable: Ratio A/B (shape).
b. Adjustment for multiple comparisons: Bonferroni.

Appendix 43: Pairwise comparisons of time and treatment of the effects of MERS and MHV-nsp 4, and nsp 6 in in 0.125 µM and 0.5% DMSO buffer on GUV size [a].

Time (min)	(I) treatment	(J) treatment	Mean Difference (I-J)	Std. Error	df	Sig.[b]	95% Confidence Interval for Difference[b]	
							Lower Bound	Upper Bound
.0	0.5% DMSO buffer	MERS-nsp 4-1	-.608	.591	154.990	1.000	-2.189	.972
		MHV- nsp 6-1	-6.926	.591	154.990	1.000	-2.249	.911
		MHV- nsp 3-4	-.669	.591	154.990	1.000	-2.249	.911
5.0	0.5% DMSO buffer	MERS-nsp 4-1	-.570	.592	154.996	1.000	-2.153	1.012
		MHV- nsp 6-1	-.632	.592	154.996	1.000	-2.214	.951
		MHV- nsp 3-4	-.632	.592	154.996	1.000	-2.214	.951

Based on estimated marginal means
a. Dependent Variable: Effective diameter (size).
b. Adjustment for multiple comparisons: Bonferroni.

Appendix 44: Pairwise comparisons of time and treatment of the effects of MERS and MHV-nsp 4, and nsp 6 in in 0.125 µM and 0.5% DMSO buffer on GUV shape[a].

Time (min)	(I) treatment	(J) treatment	Mean Difference (I-J)	Std. Error	df	Sig.[b]	95% Confidence Interval for Difference[b]	
							Lower Bound	Upper Bound
.0	0.5% DMSO buffer	MERS-nsp 4-1	3.767E-11	.000	156.000	1.000	-4.668E-7	4.669E-7
		MHV- nsp 6-1	3.777E-11	.000	156.000	1.000	-4.673E-7	4.673E-7
		MHV- nsp 3-4	3.776E-11	.000	156.000	1.000	-4.672E-7	4.673E-7
5.0	0.5% DMSO buffer	MERS-nsp 4-1	.006	.003	156.000	.085	.000	.013
		MHV- nsp 6-1	.006	.003	156.000	.085	.000	.013
		MHV- nsp 3-4	.006	.003	156.000	.085	.000	.013

Based on estimated marginal means
a. Dependent Variable: Ratio A/B (shape).
b. Adjustment for multiple comparisons: Bonferroni.

Appendix 45: Pairwise comparisons of time and treatment of the effects of MHV-nsp 4-3 and nsp6-1 together in in 1 µM and 5% DMSO buffer on GUV size [a].

Time (min)	(I) treatment	(J) treatment	Mean Difference (I-J)	Std. Error	df	Sig.[b]	95% Confidence Interval for Difference[b]	
							Lower Bound	Upper Bound
.0	5% DMSO buffer	MHV 4-3 & 6-1	.438	2.512	76.512	1.000	-3.208	-1.021
5.0	5% DMSO buffer	MHV 4-3 & 6-1	-.438	2.512	76.512	1.000	-3.533	-.800

Based on estimated marginal means
a. Dependent Variable: Effective diameter (size).
b. Adjustment for multiple comparisons: Bonferroni.

Appendix 46: Pairwise comparisons of time and treatment of the effects of MHV-nsp 4-3 and MHV-nsp6-1 together in 1 µM and 5% DMSO buffer on GUV shape[a].

Time (min)	(I) treatment	(J) treatment	Mean Difference (I-J)	Std. Error	df	Sig.[b]	95% Confidence Interval for Difference[b]	
							Lower Bound	Upper Bound
.0	5% DMSO buffer	MHV 4-3 & 6-1	.001	.001	76.082	.266	-.001	.002
5.0	5% DMSO buffer	MHV 4-3 & 6-1	-.006	.004	76.707	.464	-.016	.004

Based on estimated marginal means
a. Dependent Variable: Ratio A/B (shape).
b. Adjustment for multiple comparisons: Bonferroni.

Appendix 47: Pairwise comparisons of time and treatment of the effects of mutated MERS-nsp4-1 in 0.5 μM and 1% DMSO buffer on GUV size[a].

Time (min)	(I) treatment	(J) treatment	Mean Difference (I-J)	Std. Error	df	Sig.[b]	95% Confidence Interval for Difference[b]	
							Lower Bound	Upper Bound
1.0	1% DMSO buffer	MERS-nsp4-1 M7	.004	.003	437.900	1.000	-.006	.015
		MERS-nsp4-1 M10	.003	.003	470.913	1.000	-.008	.014
		MERS-nsp4-1 M4	.004	.003	450.077	1.000	-.007	.014
		MERS-nsp4-1 M3	.004	.003	435.517	1.000	-.006	.015
		MERS-nsp4-1 M8	.004	.003	443.707	1.000	-.007	.014
		MERS-nsp4-1 M6	.003	.003	464.754	1.000	-.008	.014
		MERS-nsp4-1 M5	.004	.003	435.247	1.000	-.006	.015
		MERS-nsp4-1 M9	.003	.003	464.281	1.000	-.008	.014
		MERS-nsp4-1 M2	.004	.003	444.738	1.000	-.007	.014
		MERS-nsp4-1 M1	.006	.003	428.086	1.000	-.005	.016
2.0	1% DMSO buffer	MERS-nsp4-1 M7	.004	.003	437.300	1.000	-.007	.014
		MERS-nsp4-1 M10	.003	.003	470.030	1.000	-.008	.013
		MERS-nsp4-1 M4	.003	.003	449.368	1.000	-.007	.014
		MERS-nsp4-1 M3	.004	.003	434.940	1.000	-.007	.015
		MERS-nsp4-1 M8	.004	.003	443.055	1.000	-.007	.014
		MERS-nsp4-1 M6	.003	.003	463.920	1.000	-.008	.014
		MERS-nsp4-1 M5	.004	.003	434.673	1.000	-.007	.015
		MERS-nsp4-1 M9	.003	.003	463.451	1.000	-.008	.014
		MERS-nsp4-1 M2	.003	.003	444.077	1.000	-.007	.014
		MERS-nsp4-1 M1	.005	.003	427.579	1.000	-.005	.016
5.0	1% DMSO buffer	MERS-nsp4-1 M7	.004	.003	437.522	1.000	-.007	.015
		MERS-nsp4-1 M10	.003	.003	470.357	1.000	-.008	.014
		MERS-nsp4-1 M4	.003	.003	449.630	1.000	-.007	.014
		MERS-nsp4-1 M3	.004	.003	435.154	1.000	-.006	.015
		MERS-nsp4-1 M8	.004	.003	443.296	1.000	-.007	.014
		MERS-nsp4-1 M6	.003	.003	464.229	1.000	-.008	.014
		MERS-nsp4-1 M5	.004	.003	434.885	1.000	-.006	.015
		MERS-nsp4-1 M9	.003	.003	463.758	1.000	-.008	.014
		MERS-nsp4-1 M2	.004	.003	444.321	1.000	-.007	.014
		MERS-nsp4-1 M1	.005	.003	427.767	1.000	-.005	.016

Based on estimated marginal means

a. Dependent Variable: Effective diameter (size).

b. Adjustment for multiple comparisons: Bonferroni.

Appendix 48: Pairwise comparisons of time and treatment of the effects of mutated MERS-nsp4-1 in 0.5 µM and 1% DMSO buffer on GUV shape[a].

Time (min)	(I) treatment	(J) treatment	Mean Difference (I-J)	Std. Error	df	Sig.[b]	95% Confidence Interval for Difference[b]	
							Lower Bound	Upper Bound
.0	1% DMSO buffer	MERS-nsp4-1 M7	4.551E-5	.000	434.345	.870	-1.724E-5	.000
		MERS-nsp4-1 M10	3.685E-5	.000	434.108	1.000	-2.590E-5	9.959E-5
		MERS-nsp4-1 M4	1.488E-5	.000	433.521	1.000	-4.784E-5	7.759E-5
		MERS-nsp4-1 M3	4.551E-5	.000	434.345	.870	-1.724E-5	.000
		MERS-nsp4-1 M8	3.309E-5	.000	434.006	1.000	-2.965E-5	9.583E-5
		MERS-nsp4-1 M6	4.551E-5	.000	434.345	.870	-1.724E-5	.000
		MERS-nsp4-1 M5	1.166E-5	.000	433.437	1.000	-5.105E-5	7.437E-5
		MERS-nsp4-1 M9	2.215E-5	.000	433.713	1.000	-4.058E-5	8.487E-5
		MERS-nsp4-1 M2	4.005E-5	.000	434.195	1.000	-2.270E-5	.000
		MERS-nsp4-1 M1	1.425E-5	.000	433.505	1.000	-4.846E-5	7.697E-5
2.0	1% DMSO buffer	MERS-nsp4-1 M7	3.492E-7	.000	435.624	1.000	-5.835E-5	5.905E-5
		MERS-nsp4-1 M10	-8.318E-6	.000	435.370	1.000	-6.701E-5	5.037E-5
		MERS-nsp4-1 M4	-3.029E-5	.000	434.742	1.000	-8.895E-5	2.837E-5
		MERS-nsp4-1 M3	3.492E-7	.000	435.624	1.000	-5.835E-5	5.905E-5
		MERS-nsp4-1 M8	-1.207E-5	.000	435.261	1.000	-7.075E-5	4.661E-5
		MERS-nsp4-1 M6	3.492E-7	.000	435.624	1.000	-5.835E-5	5.905E-5
		MERS-nsp4-1 M5	-3.351E-5	.000	434.652	1.000	-9.216E-5	2.514E-5
		MERS-nsp4-1 M9	-2.302E-5	.000	434.947	1.000	-8.169E-5	3.565E-5
		MERS-nsp4-1 M2	-5.114E-6	.000	435.464	1.000	-6.381E-5	5.358E-5
		MERS-nsp4-1 M1	-3.091E-5	.000	434.725	1.000	-8.957E-5	2.774E-5
5.0	1% DMSO buffer	MERS-nsp4-1 M7	1.420E-5	.000	436.512	1.000	-4.471E-5	7.311E-5
		MERS-nsp4-1 M10	5.530E-6	.000	436.259	1.000	-5.337E-5	6.443E-5
		MERS-nsp4-1 M4	-1.644E-5	.000	435.633	1.000	-7.531E-5	4.242E-5
		MERS-nsp4-1 M3	1.420E-5	.000	436.512	1.000	-4.471E-5	7.311E-5
		MERS-nsp4-1 M8	1.776E-6	.000	436.151	1.000	-5.712E-5	6.067E-5
		MERS-nsp4-1 M6	1.420E-5	.000	436.512	1.000	-4.471E-5	7.311E-5
		MERS-nsp4-1 M5	-1.966E-5	.000	435.544	1.000	-7.852E-5	3.920E-5
		MERS-nsp4-1 M9	-9.171E-6	.000	435.838	1.000	-6.805E-5	4.971E-5
		MERS-nsp4-1 M2	8.734E-6	.000	436.352	1.000	-5.017E-5	6.764E-5
		MERS-nsp4-1 M1	-1.706E-5	.000	435.616	1.000	-7.593E-5	4.180E-5

Based on estimated marginal means
a. Dependent Variable: Ratio A/B (shape).
b. Adjustment for multiple comparisons: Bonferroni.

References

Adams, M. & C. E. (2012) ‘Ratification vote on taxonomic proposals to the International Committe on Taxonomy of Viruses (2012)’, *Archives of Virology*, 157, pp. 1411–1422.

Agnello, V. *et al* (1999) ‘Hepatitis C virus and other Flaviviridae viruses enter cells via low density lipoprotein receptor’, *Pnas*, 96(22), pp. 12766–12771.

Ahkong, Q. F. *et al* (1975) ‘Mechanisms of cell fusion’, *Nature*. Nature Publishing Group, 253, p. 194.

Aimon, S. *et al* (2011) ‘Functional Reconstitution of a Voltage-Gated Potassium Channel in Giant Unilamellar Vesicles’, *PLoS ONE*, 6(10).

Akashi, K. *et al* (1996) ‘Preparation of Giant Liposomes in Physiological Conditions and Their Characterization under an Optical Microscope’, 71(December), pp. 3242–3250.

Al-Mulla, H. M. N. *et al* (2014) ‘Competitive fitness in coronaviruses is not correlated with size or number of double-membrane vesicles under reduced-temperature growth conditions’, *mBio*, 5(2), pp. 1–9.

Alberts, B., Lewis, j., & Bray, D. (1994) *Molecular biology of the cell.* 3rd edn. New York: Garland Publishing.

Alexander, S. and Elder, J. H. (1984) ‘Carbohydrate dramatically influences immune reactivity of antisera to viral glycoprotein antigens’, *Science*, 226(4680), pp. 1328–1330.

Álvarez, E. *et al* (2010) ‘The envelope protein of severe acute respiratory syndrome

coronavirus interacts with the non-structural protein 3 and is ubiquitinated', *Virology*. Elsevier Inc., 402(2), pp. 281–291.

Angelini, M. and Akhlaghpour, M. (2013) 'Severe Acute Respiratory Syndrome Coronavirus Nonstructural Proteins 3, 4, and 6 Induce Double-Membrane Vesicles', *MBio*, 4(4), pp. 1–10.

Angelini, M. M., Neuman, B. W. and Buchmeier, M. J. (2014) 'Untangling membrane rearrangement in the nidovirales.', *DNA and cell biology*, 33(3), pp. 122–7.

Angelova, M. I. (1986) 'Liposome electroformation', *Perspectives in Supramolecular Chemistry: Giant Vesicles*, 6, pp. 26–36.

Angelova, M. I. and Dimitrov, D. S. (1986) 'Liposome Electro formation', *Faraday Discuss. Chem. SO*, 81, pp. 303–311.

Antonny, B. (2006) 'Membrane deformation by protein coats', *Current Opinion in Cell Biology*, 18(4), pp. 386–394. doi: 10.1016/j.ceb.2006.06.003.

Arbely, E. *et al* (2004) 'A highly unusual palindromic transmembrane helical hairpin formed by SARS coronavirus E protein', *Journal of Molecular Biology*, 341(3), pp. 769–779.

Armstrong J., Niemann H., Smeekens, S., Rottier., P., and Warren., G. (1984) 'Sequence and topology of a model intracellular membrane protein,E1 glycoprotein, from a coronavirus', *Nature*, 308(5961), pp. 751–752.

Arndt, A. L., Larson, B. J. and Hogue, B. G. (2010) 'A Conserved Domain in the Coronavirus Membrane Protein Tail Is Important for Virus Assembly', *Journal of Virology*, 84(21), pp. 11418–11428.

Asthana, N., Yadav, S. P. and Ghosh, J. K. (2004) 'Dissection of antibacterial and toxic activity of melittin: A leucine zipper motif plays a crucial role in determining its hemolytic activity but not antibacterial activity', *Journal of Biological Chemistry*, 279(53), pp. 55042–55050.

Ayres, M. D. *et al* (1994) 'The Complete DNA Sequence of Autographa californica Nuclear Polyhedrosis Virus', *Virology*, 202(2), pp. 586–605.

Babcock, G. J. *et al* (2004) 'Amino Acids 270 to 510 of the Severe Acute Respiratory Syndrome Coronavirus Spike Protein Are Required for Interaction with Receptor', *Journal of Virology*, 78(9), pp. 4552–4560.

Bacia, K. *et al* (2004) 'SNAREs prefer liquid-disordered over "raft" (liquid-ordered) domains when reconstituted into giant unilamellar vesicles', *Journal of Biological Chemistry*, 279(36), pp. 37951–37955.

Bailey, A. L. *et al* (1997) 'Membrane fusion with cationic liposomes: effects of target membrane lipid composition', *Biochemistry*, 36(7), pp. 1628–1634.

Bale, S. *et al* (2011) 'Ebola virus glycoprotein needs an additional trigger, beyond proteolytic priming for membrane fusion', *PLoS Neglected Tropical Diseases*, 5(11), pp. 1–6.

Baliji, S., Cammer, S. a, *et al* (2009) 'Detection of nonstructural protein 6 in murine coronavirus-infected cells and analysis of the transmembrane topology by using bioinformatics and molecular approaches.', *Journal of virology*, 83(13), pp. 6957–62.

Baliji, S., Cammer, S. A., *et al* (2009) 'Detection of nonstructural protein 6 in murine coronavirus-infected cells and analysis of the transmembrane topology by using bioinformatics and molecular approaches', *J Virol*, 83(13), pp. 6957–6962.

Baseler, L., de Wit, E. and Feldmann, H. (2016) ‘A Comparative Review of Animal Models of Middle East Respiratory Syndrome Coronavirus Infection’, *Veterinary Pathology*, 53(3), pp. 521–531.

Baumgart, T. *et al* (2007) ‘Fluorescence probe partitioning between Lo membranes /Ld phases in lipid’, *Biochimica et biophysica acta*, 1768(9), pp. 2182–2194.

Beachboard, D. C., Anderson-Daniels, J. M. and Denison, M. R. (2015) ‘Mutations across Murine Hepatitis Virus nsp4 Alter Virus Fitness and Membrane Modifications’, *Journal of Virology*, 89(4), pp. 2080–2089.

Belouzard, S. *et al* (2012) ‘Mechanisms of coronavirus cell entry mediated by the viral spike protein.’, *Viruses*, 4(6), pp. 1011–1033.

Belouzard, S., Chu, V. C. and Whittaker, G. R. (2009) ‘Activation of the SARS coronavirus spike protein via sequential proteolytic cleavage at two distinct sites.’, *Proceedings of the National Academy of Sciences of the United States of America*, 106(14), pp. 5871–6.

Bender, S. J. *et al* (2010) ‘Murine coronavirus receptors are differentially expressed in the central nervous system and play virus strain-dependent roles in neuronal spread.’, *Journal of virology*, 84(21), pp. 11030–11044.

Berger, K. L. *et al* (2009) ‘Roles for endocytic trafficking and phosphatidylinositol 4-kinase III alpha in hepatitis C virus replication’, *Proceedings of the National Academy of Sciences*, 106(18), pp. 7577–7582.

Bhatia, T. *et al* (2015) ‘Preparing giant unilamellar vesicles (GUVs) of complex lipid mixtures on demand: Mixing small unilamellar vesicles of compositionally heterogeneous mixtures’, *Biochimica et Biophysica Acta (BBA) - Biomembranes*.

Elsevier B.V., 1848(12), pp. 3175–3180.

Boheemen, S. Van *et al* (2012) 'Genomic Characterization of Newly Discovered Coronavirus Associated with Acute Respiratory Distress Syndrome in Humans', *mBio*, 3(6), pp. e00473-12.

Bolles, M., Donaldson, E. and Baric, R. (2011) 'SARS-CoV and emergent coronaviruses: Viral determinants of interspecies transmission', *Current Opinion in Virology*, 1(6), pp. 624–634.

den Boon, J. A. and Ahlquist, P. (2010) 'Organelle-Like Membrane Compartmentalization of Positive-Strand RNA Virus Replication Factories', *Annual Review of Microbiology*. Annual Reviews, 64(1), pp. 241–256.

den Boon, J. A., Diaz, A. and Ahlquist, P. (2010) 'Cytoplasmic viral replication complexes', *Cell Host and Microbe*. Elsevier Inc., 8(1), pp. 77–85.

Bos, E. C. *et al* (1997) 'A subgenomic mRNA transcript of the coronavirus mouse hepatitis virus strain A59 defective interfering (DI) RNA is packaged when it contains the DI packaging signal', *J Virol*, 71(7), pp. 5684–5687.

Bos, E. C. W. *et al* (1995) 'Mutational analysis of the murine coronavirus spike protein: Effect on cell-to-cell fusion', *Virology*, 214(2), pp. 453–463.

Bos, E. C. W. *et al* (1996) 'The production of recombinant infectious DI-particles of a murine coronavirus in the absence of helper virus', *Virology*, 218(1), pp. 52–60.

Boscarino, J. a *et al* (2008) 'Envelope Protein Palmitoylations Are Crucial for Murine Coronavirus Assembly', *Journal of Virology*, 82(6), pp. 2989–2999.

Bosch, B. J. & Rottier, P. (2008) 'Nidovirus entry into cells.', in *Nidoviruses*.

Washington, D.C: ASM Press, pp. 157–178.

Bosch, B. J. *et al* (2003) 'The Coronavirus Spike Protein Is a Class I Virus Fusion Protein : Structural and Functional Characterization of the Fusion Core Complex', *Journal of virology*, 77(16), pp. 8801–8811.

Bosch, B. J. *et al* (2005) 'Spike protein assembly into the coronavirion: Exploring the limits of its sequence requirements', *Virology*, 334(2), pp. 306–318.

Bosch, B. J., Bartelink, W. and Rottier, P. J. M. (2008) 'Cathepsin L functionally cleaves the severe acute respiratory syndrome coronavirus class I fusion protein upstream of rather than adjacent to the fusion peptide.', *Journal of virology*, 82(17), pp. 8887–8890.

Boucrot, E. *et al* (2012) 'Membrane fission is promoted by insertion of amphipathic helices and is restricted by crescent BAR domains', *Cell*, 149(1), pp. 124–136.

Bouvrais, H. *et al* (2008) 'Softening of POPC membranes by magainin', *Biophysical Chemistry*, 137(1), pp. 7–12.

Braakman, I. and van Anken, E. (2000) 'Folding of viral envelope glycoproteins in the endoplasmic reticulum.', *Traffic (Copenhagen, Denmark)*, 1(7), pp. 533–539.

Brandão, P. E. *et al* (2016) 'Complete Genome Sequence of a Brazil-Type Avian coronavirus Detected in a Chicken', *Genome Announcements*, 4(5), pp. 15–16.

Bredenbeek, P. J. *et al* (1990) 'The primary structure and expression of the second open reading frame of the polymerase gene of the coronavirus MHV-A59; a highly conserved polymerase is expressed by an efficient ribosomal frameshifting mechanism', *Nucleic Acids Research*, 18(7), pp. 1825–1832.

Bright, R. A. *et al* (2007) ‘Influenza virus-like particles elicit broader immune responses than whole virion inactivated influenza virus or recombinant hemagglutinin’, *Vaccine*, 25(19), pp. 3871–3878.

von Brunn, A. *et al* (2007) ‘Analysis of intraviral protein-protein interactions of the SARS coronavirus ORFeome’, *PLoS ONE*, 2(5).

Caponea, S. *et al* (2008) ‘pH-sensitive vesicles containing a lipidic β-amino acid with two hydrophobic chains’, *Chemistry and Biodiversity*, 5(1), pp. 16–30.

Carvalho, K. *et al* (2008) ‘Giant unilamellar vesicles containing phosphatidylinositol(4,5)bisphosphate: characterization and functionality.’, *Biophysical journal*, 95(9), pp. 4348–60.

Castaño-Rodriguez, C. *et al* (2018) ‘Role of Severe Acute Respiratory Syndrome Coronavirus Viroporins E, 3a, and 8a in Replication and Pathogensis’, *MBio*, 9(3), pp. 1–23.

Chambers, P., Pringle, C. R. and Easton, A. J. (1990) ‘Heptad repeat sequences are located adjacent to hydrophobic regions in several types of virus fusion glycoproteins’, *Journal of General Virology*, 71(12), pp. 3075–3080.

Chan, J. F. W. *et al* (2013) ‘Differential cell line susceptibility to the emerging novel human betacoronavirus 2c EMC/2012: Implications for disease pathogenesis and clinical manifestation’, *Journal of Infectious Diseases*, 207(11), pp. 1743–1752.

Chang, K. W., Sheng, Y. W. and Gombold, J. L. (2000) ‘Coronavirus-induced membrane fusion requires the cysteine-rich domain in the spike protein’, *Virology*, 269(1), pp. 212–224.

Channappanavar, R. *et al* (2015) ‘Protective effect of intranasal regimens containing peptidic middle east respiratory syndrome coronavirus fusion inhibitor against MERS-CoV infection’, *Journal of Infectious Diseases*, 212(12), pp. 1894–1903.

Chen, B. J. *et al* (2008) ‘The influenza virus M2 protein cytoplasmic tail interacts with the M1 protein and influences virus assembly at the site of virus budding.’, *Journal of virology*, pp. 10059–10070.

Chen, C. Y. *et al* (2011) ‘Baculovirus as a gene delivery vector: Recent understandings of molecular alterations in transduced cells and latest applications’, *Biotechnology Advances*. Elsevier Inc., 29(6), pp. 618–631.

Chen, S. C. *et al* (2009) ‘Expression and membrane integration of SARS-CoV e protein and its interaction with M protein’, *Virus Genes*, 38(3), pp. 365–371.

Chen, Y. *et al* (2013) ‘Crystal Structure of the Receptor-Binding Domain from Newly Emerged Middle East Respiratory Syndrome Coronavirus’, *Journal of Virology*, 87(19), pp. 10777–10783.

Choe, Y. *et al* (2006) ‘Substrate profiling of cysteine proteases using a combinatorial peptide library identifies functionally unique specificities’, *Journal of Biological Chemistry*, 281(18), pp. 12824–12832.

Clementz, M. A. *et al* (2008) ‘Mutation in murine coronavirus replication protein nsp4 alters assembly of double membrane vesicles’, *Virology*, 375(1), pp. 118–129.

Cohen, J. R., Lin, L. D. and Machamer, C. E. (2011) ‘Identification of a Golgi Complex-Targeting Signal in the Cytoplasmic Tail of the Severe Acute Respiratory Syndrome Coronavirus Envelope Protein’, *Journal of Virology*, 85(12), pp. 5794–5803.

Coleman, C. M. and Frieman, M. B. (2014) ‘Coronaviruses: Important Emerging Human Pathogens’, *Journal of Virology*, 88(10), pp. 5209–5212.

Coley, S. E. *et al* (2005) ‘Recombinant mouse hepatitis virus strain A59 from cloned, full-length cDNA replicates to high titers in vitro and is fully pathogenic in vivo’, *Journal of Virology*, 79(5), pp. 3097–3106.

Constantinescu, I. and Lafleur, M. (2004) ‘Influence of the lipid composition on the kinetics of concerted insertion and folding of melittin in bilayers’, *Biochimica et Biophysica Acta - Biomembranes*, 1667(1), pp. 26–37.

Corse, E. and Machamer, C. E. (2002a) ‘Infectious Bronchitis Virus E Protein Is Targeted to the Golgi Complex and Directs Release of Virus-Like Particles’, *Journal of Virology*, 74(9), pp. 4319–4326.

Corse, E. and Machamer, C. E. (2002b) ‘The Cytoplasmic Tail of Infectious Bronchitis Virus E Protein Directs Golgi Targeting’, *Society*, 76(3), pp. 1273–1284.

Cottam, E. M. *et al* (2011) ‘Coronavirus nsp6 proteins generate autophagosomes from the endoplasmic reticulum via an omegasome intermediate’, *Autophagy*, 7(11), pp. 1335–1347.

Cottam, E. M., Whelband, M. C. and Wileman, T. (2014) ‘Coronavirus NSP6 restricts autophagosome expansion’, *Autophagy*, 10(8), pp. 1426–1441.

Dalziel, R. G. *et al* (1986) ‘Site-specific alteration of murine hepatitis virus type 4 peplomer glycoprotein E2 results in reduced neurovirulence’, *J Virol*, 59(2), pp. 463–471.

DeDiego, M. L. *et al* (2011) ‘Severe acute respiratory syndrome coronavirus

envelope protein regulates cell stress response and apoptosis', *PLoS Pathogens*, 7(10).

DeDiego, M. L. *et al* (2014) 'Coronavirus virulence genes with main focus on SARS-CoV envelope gene', *Virus Research*, 194, pp. 124–137.

Delang, L., Paeshuyse, J. and Neyts, J. (2012) 'The role of phosphatidylinositol 4-kinases and phosphatidylinositol 4-phosphate during viral replication', *Biochemical Pharmacology*. Elsevier Inc., 84(11), pp. 1400–1408.

Delmas, B. and Laude, H. (1990) 'Assembly of coronavirus spike protein into trimers and its role in epitope expression.', *J. Virol.*, 64(11), pp. 5367–5375.

Derganc, J., Antonny, B. and Čopič, A. (2013) 'Membrane bending: The power of protein imbalance', *Trends in Biochemical Sciences*, 38(11), pp. 576–584.

Desplanques, A. S. *et al* (2008) 'Plasma membrane cholesterol is required for efficient pseudorabies virus entry', *Virology*, 376(2), pp. 339–345.

Diaz, A., Wang, X. and Ahlquist, P. (2010) 'Membrane-shaping host reticulon proteins play crucial roles in viral RNA replication compartment formation and function', *Proceedings of the National Academy of Sciences*, 107(37), pp. 16291–16296.

Diguet, A. *et al* (2012) 'UV-induced bursting of cell-sized multicomponent lipid vesicles in a photosensitive surfactant solution', *Journal of the American Chemical Society*, 134(10), pp. 4898–4904.

Do, T. D. *et al* (2013) 'Effects of pH and charge state pn peptide Assembly: The YVIFL Model System'. J.*Phys.Chem.B.* 117, 10759-10768.

van Doremalen, N. and Munster, V. J. (2015) ‘Animal models of Middle East respiratory syndrome coronavirus infection’, *Antiviral Research*. Elsevier B.V., 122, pp. 28–38.

Doyle, N. *et al* (2018) ‘Infectious Bronchitis Virus Nonstructural Protein 4 Alone Induces Membrane Pairing’, *Viruses*, 10(9), p. 477.

Drosten, C. (2003) ‘Identification of a novel coronavirus in patients with severe acute respiratory syndrome’, *N. Engl. J. Med.*, 348, pp. 1967–1976.

Du, L. *et al* (2017) ‘MERS-CoV spike protein: a key target for antivirals’, *Expert Opinion on Therapeutic Targets*, 21(2), pp. 131–143.

Dveksler, G. S. *et al* (1991) ‘Cloning of the mouse hepatitis virus (MHV) receptor: expression in human and hamster cell lines confers susceptibility to MHV.’, *Journal of virology*, 65(12), pp. 6881–91.

Dyall, J. *et al* (2014) ‘Repurposing of clinically developed drugs for treatment of Middle East respiratory syndrome coronavirus infection’, *Antimicrobial Agents and Chemotherapy*, 58(8), pp. 4885–4893.

Dyall, J. *et al* (2017) ‘Middle East Respiratory Syndrome and Severe Acute Respiratory Syndrome: Current Therapeutic Options and Potential Targets for Novel Therapies’, *Drugs*. Springer International Publishing, 77(18), pp. 1935–1966.

Earp, L. J. *et al* (2005) ‘The many mechanisms of viral membrane fusion proteins.’, *Current topics in microbiology and immunology*. The Authors, 285(13), pp. 25–66.

Eckert, D. M. and Kim, P. S. (2001) ‘Mechanisms of Viral Membrane Fusion and Its Inhibition’, *Annual Review of Biochemistry*, 70(1), pp. 777–810.

Elshabrawy, H. A. *et al* (2012) 'Human Monoclonal Antibodies against Highly Conserved HR1 and HR2 Domains of the SARS-CoV Spike Protein Are More Broadly Neutralizing', *PLoS ONE*, 7(11), pp. 1–9.

Engelman, D. M. (2005) 'Membranes are more mosaic than fluid', *Nature*, 438(7068), pp. 578–580.

Ernst, W. J. *et al* (2000) 'Expanding baculovirus surface display. Modification of the native coat protein gp64 of Autographa californica NPV', *European Journal of Biochemistry*, 267(13), pp. 4033–4039.

Escors, D. *et al* (2002) 'Organization of Two Transmissible Gastroenteritis Coronavirus Membrane Protein Topologies within the Virion and Core', *Journal of Virology*, 75(24), pp. 12228–12240.

Ewers, H. *et al* (2010) 'GM1 structure determines SV40-induced membrane invagination and infection.', *Nature cell biology*, 12(1), pp. 11–18; sup pp 1-12.

Fehr, A. R. and Perlman, S. (2015) 'Coronaviruses', *Methods Mol Biol*, 1282, pp. 1–23.

Fischer, F. *et al* (1998) 'Analysis of constructed E gene mutants of mouse hepatitis virus confirms a pivotal role for E protein in coronavirus assembly.', *Journal of virology*, 72(10), pp. 7885–94.

Fung, T. S., Liao, Y. and Liu, D. X. (2016) 'Regulation of stress responses and translational control by coronavirus', *Viruses*, 8(7), pp. 1–15.

Gadlage, M. J. *et al* (2010) 'Murine hepatitis virus nonstructural protein 4 regulates virus-induced membrane modifications and replication complex function', *J Virol*,

84(1), pp. 280–290.

Gagneten, S. *et al* (1995) ‘Interaction of mouse hepatitis virus (MHV) spike glycoprotein with receptor glycoprotein MHVR is required for infection with an MHV strain that expresses the hemagglutinin-esterase glycoprotein.’, *Journal of virology*, 69(2), pp. 889–895.

Gallagher, T. M. (1997) ‘A Role for Naturally Occurring Variation of the Murine Coronavirus Spike Protein in Stabilizing Association with the Cellular Receptor’, *Journal of Virology*, 71(4), pp. 3129–3137.

Gao, J. *et al* (2013) ‘Structure of the fusion core and inhibition of fusion by a heptad repeat peptide derived from the S protein of Middle East respiratory syndrome coronavirus.’, *Journal of virology*, 87(24), pp. 13134–40.

Ghosh, A., Bhattacharyya, D. and Bhunia, A. (2018) ‘Structural insights of a self-assembling 9-residue peptide from the C-terminal tail of the SARS corona virus E-protein in DPC and SDS micelles: A combined high and low resolution spectroscopic study’, *Biochimica et Biophysica Acta - Biomembranes*. Elsevier, 1860(2), pp. 335–346.

Girard, P. *et al* (2004) ‘A new method for the reconstitution of membrane proteins into giant unilamellar vesicles’, *Biophysical Journal*, 87(1), pp. 419–429.

Godeke, G. J. *et al* (2000) ‘Assembly of spikes into coronavirus particles is mediated by the carboxy-terminal domain of the spike protein.’, *Journal of virology*, 74(3), pp. 1566–71.

Gorbalenya, A. E. *et al* (2006) ‘Nidovirales: Evolving the largest RNA virus genome’, *Virus Research*, 117(1), pp. 17–37.

Gouttenoire, J. *et al* (2009) ‘An Amphipathic -Helix at the C Terminus of Hepatitis C Virus Nonstructural Protein 4B Mediates Membrane Association’, *Journal of Virology*, 83(21), pp. 11378–11384.

Gui, M. *et al* (2017) ‘Cryo-electron microscopy structures of the SARS-CoV spike glycoprotein reveal a prerequisite conformational state for receptor binding’, *Cell Research*. Nature Publishing Group, 27(1), pp. 119–129.

Guille’n, Pe´rez-Berna´, Miguel R. Moreno, J. V. (2005) ‘Identification of the Membrane-Active Regions of the Severe Acute Respiratory Syndrome Coronavirus Spike Membrane Glycoprotein Using a 16/18-Mer Peptide Scan: Implications for the Viral Fusion Mechanism Jaime’, *Journal of Virology*, 79(3), pp. 1743–1752.

Guille’n, J. *et al* (2008a) ‘Structural and dynamic characterization of the interaction of the putative fusion peptide of the S2 SARS-CoV virus protein with lipid membranes’, *J Phys Chem B*, 112(23), pp. 6997–7007.

Guillén, J. *et al* (2008b) ‘A second SARS-CoV S2 glycoprotein internal membrane-active peptide. Biophysical characterization and membrane interaction’, *Biochemistry*, 47(31), pp. 8214–8224.

Gwon, Y. D. *et al* (2016) ‘Immunogenicity of Virus Like Particle Forming Baculoviral DNA Vaccine against Pandemic Influenza H1N1’, *PloS one*, 11(5), p. e0154824.

de Haan, Cornelis A. M., & Rottier, P. J. *et al* (1998) ‘Structural Requirements for O -Glycosylation of the Mouse Hepatitis Virus Membrane Protein. *Journal of Biological Chemistry*, 273(45), pp. 29905–29914.

de Haan, Cornelis A. M., & Rottier, P. J. (2005) ‘de Haan, C.A. and Rottier, P.J., 2005. Molecular interactions in the assembly of coronaviruses. *advances in virus*

research, (64), pp. 165–230.

de Haan, C. A. *et al* (1999) ‘Mapping of the coronavirus membrane protein domains involved in interaction with the spike protein’, *J Virol*, 73(9), pp. 7441–7452.

de Haan, C. A. M. *et al* (2004) ‘Cleavage inhibition of the murine coronavirus spike protein by a furin-like enzyme affects cell-cell but not virus-cell fusion.’, *Journal of Virology*, 78(11), pp. 6048–6054.

de Haan, C. A. M. *et al* (2003) ‘The glycosylation status of the murine hepatitis coronavirus M protein affects the interferogenic capacity of the virus in vitro and its ability to replicate in the liver but not the brain’, *Virology*, 312(2), pp. 395–406.

de Haan, C. A. M., Vennema, H. and Rottier, P. J. M. (2000) ‘Assembly of the coronavirus envelope: homotypic interactions between the M proteins’, *Journal of virology*, 74(11), pp. 4967–4978.

Hagemeijer, M. C., Ulasli, M., Vonk, A. M., Reggiori, F., Rottier, P. J. M. and de Haan, C. a M. (2011) ‘Mobility and interactions of coronavirus nonstructural protein 4. *Journal of virology*, 85(9), pp. 4572–4577.

Hagemeijer, M. C. *et al* (2014) ‘Membrane rearrangements mediated by coronavirus nonstructural proteins 3 and 4’. *Virology*, 459, pp. 125–135.

Hagemeijer, M. C., Rottier, P. J. M. and de Haan, C. A. M. (2012) ‘Biogenesis and dynamics of the coronavirus replicative structures.’, *Viruses*, 4(11), pp. 3245–69.

Haluska, C. K. *et al* (2006) ‘Time scales of membrane fusion revealed by direct imaging of vesicle fusion with high temporal resolution.’, *Proceedings of the National Academy of Sciences of the United States of America*, 103(43), pp. 15841–6.

Harrison, S. C. (2015) ‘Viral membrane fusion’, *Virology*. Elsevier, 479–480, pp. 498–507.

Hasemann, C. A. and Capra, J. D. (1990) ‘High-level production of a functional immunoglobulin heterodimer in a baculovirus expression system.’, *Proceedings of the National Academy of Sciences*, 87(May), pp. 3942–3946.

Heaton, N. S. and Randall, G. (2011) ‘Multifaceted roles for lipids in viral infection’, *Trends in Microbiology*, pp. 368–375.

van Hemert, M. J. *et al* (2008) ‘SARS-coronavirus replication/transcription complexes are membrane-protected and need a host factor for activity in vitro’, *PLoS Pathogens*, 4(5).

Hernious, E., Theilmann, D.A., Blissard, G.W., Beenel, J.J, Basil, A., Harridon, R.L., Bonning, B.C., Vlak, J.M, J. (2011). *Baculoviridae. Virus*

Taxnomy:Calssfication and Nomenclature of viruses.

Heuvingh, J., Pincet, F. and Cribier, S. (2004) ‘Hemifusion and fusion of giant vesicles induced by reduction of inter-membrane distance’, *European Physical Journal E*, 14(3), pp. 269–276.

Hingley, S. T. *et al* (2002) ‘The virulence of mouse hepatitis virus strain A59 is not dependent on efficient spike protein cleavage and cell-to-cell fusion’, *Journal of NeuroVirology*, 8(5), pp. 400–410.

Hishida, M., Seto, H. and Yoshikawa, K. (2005) ‘Smooth/rough layering in liquid-crystalline/gel state of dry phospholipid film, in relation to its ability to generate giant vesicles’, *Chemical Physics Letters*, 411(1–3), pp. 267–272.

van der Hoeven, B. *et al* (2016) 'Biogenesis and architecture of arterivirus replication organelles', *Virus Research*. Elsevier B.V., 220, pp. 70–90.

Hogue, B.G. and Machamer, C. E. (2008) 'Coronavirus structural proteins and virus assembly.', in *Nidoviruses*. American Society for Microbiology, pp. 179–200.

Holmes, K. V *et al* (2001) 'Receptor specificity and receptor-induced conformational changes in mouse hepatitis virus spike glycoprotein', *Adv Exp Med Biol*, 494, pp. 173–181.

Horger, K. S. *et al* (2009) 'NIH Public Access', *Jacs*, 131(5), pp. 1810–1819.

Hsieh, P. *et al* (2005) 'Assembly of Severe Acute Respiratory Syndrome Coronavirus RNA Packaging Signal into Virus-Like Particles Is Nucleocapsid Dependent Assembly of Severe Acute Respiratory Syndrome Coronavirus RNA Packaging Signal into Virus-Like Particles Is Nucleocapsid Dep', *Journal of Virology*, 79(22), pp. 13848–13855.

Hsu, N. Y. *et al* (2010) 'Viral reorganization of the secretory pathway generates distinct organelles for RNA replication', *Cell*. Elsevier Ltd, 141(5), pp. 799–811.

Hu, B. *et al* (2015) 'Bat origin of human coronaviruses Coronaviruses: Emerging and re-emerging pathogens in humans and animals Susanna Lau Positive-strand RNA viruses', *Virology Journal*, 12(1), pp. 1–10.

Huang, H. *et al* (2006) 'Human herpesvirus 6 envelope cholesterol is required for virus entry', *Journal of General Virology*, 87(2), pp. 277–285.

Hurst, K. *et al* (2005) 'A major determinant for membrane protein interaction localizes to the carboxy-terminal domain of the mouse coronavirus nucleocapsid protein.',

Journal of virology, 79(21), pp. 13285–97.

Imbert, Isabelle, Snijder EJ, Dimitrova M, Guillemot JC, Lecine P, C. B. (2007) 'The SARS-Coronavirus PLnc domain of nsp3 as a replication/transcription scaffolding protein', *Virus Research*, 133(2), pp. 136–148.

Israelachvili, J. N. (2011) 'Intermolecular and surface forces', *Academic Press*.

Jeon, J. H. and Lee, C. (2017) 'Cellular cholesterol is required for porcine nidovirus infection', *Archives of Virology*. Springer Vienna, 162(12), pp. 3753–3767.

Jiaming, L. *et al* (2017) 'The recombinant N-terminal domain of spike proteins is a potential vaccine against Middle East respiratory syndrome coronavirus (MERS-CoV) infection', *Vaccine*. Elsevier Ltd, 35(1), pp. 10–18.

Jones, I. and Morikawa, Y. (1996) 'Baculovirus vectors for expression in insect cells', *Current Opinion in Biotechnology*, pp. 512–516.

Joseph, M. and Nagaraj, R. (1995) 'Conformations of peptides corresponding to fatty acylation sites in proteins. A circular dichroism study', *Journal of Biological Chemistry*, pp. 19439–19445.

Kanjanahaluethai, A. *et al* (2007) 'Membrane topology of murine coronavirus replicase nonstructural protein 3', *Virology*, 361(2), pp. 391–401.

Kawase, M. *et al* (2009) 'Protease-mediated entry via the endosome of human coronavirus 229E.', *Journal of virology*, 83(2), pp. 712–721.

Kienzle, T. E. *et al* (1990) 'Structure and orientation of expressed bovine coronavirus hemagglutinin-esterase protein.', *Journal of virology*, 64(4), pp. 1834–8.

Kirchdoerfer, R. N. *et al* (2016) 'Pre-fusion structure of a human coronavirus spike

protein', *Nature*. Nature Publishing Group, 531(7592), pp. 118–121.

Kirchhausen, T. (2012) 'Bending membranes', *Nature Cell Biology*. Nature Publishing Group, 14(9), pp. 906–908. doi: 10.1038/ncb2570.

Kitts, P. A., Ayres, M. D. and Possee, R. D. (1990) 'Linearization of baculovirus DNA enhances the recovery of recombinant virus expression vectors', *Nucleic Acids Research*, 18(19), pp. 5667–5672. doi: 10.1093/nar/18.19.5667.

Kitts PA, P. R. (1993) 'A method for producing recombinant baculovirus expression vectors at high frequency', *BioTechniques*, 14(5), pp. 810–7.

Klumperman, J. *et al* (1994) 'Coronavirus M proteins accumulate in the Golgi complex beyond the site of virion budding.', *Journal of virology*, 68(10), pp. 6523–34.

Knoops, Kikkert, M., Worm, S. H. E. Van Den and Zevenhoven-dobbe, J. C. (2008) 'SARS-Coronavirus Replication Is Supported by a Reticulovesicular Network of Modified Endoplasmic Reticulum', *PLoS Biology*, 6(9), p. e226.

Kooijman, E. E. *et al* (2005) 'Spontaneous curvature of phosphatidic acid and lysophosphatidic acid', *Biochemistry*, 44(6), pp. 2097–2102.

Koynova, R. and Caffrey, M. (1998) 'Phases and phase transitions of the phosphatidylcholines', *Biochimica et Biophysica Acta - Reviews on Biomembranes*, pp. 91–145.

Kralj-Iglič, V. *et al* (2001) 'Myelin-like protrusions of giant phospholipid vesicles prepared by electroformation', *Colloids and Surfaces A: Physicochemical and Engineering Aspects*, 181(1–3), pp. 315–318.

Krishnan, K. *et al* (2009) 'Profilin interaction with phosphatidylinositol (4,5)-

bisphosphate destabilizes the membrane of giant unilamellar vesicles', *Biophysical Journal*. Biophysical Society, 96(12), pp. 5112–5121.

Krogh, A. *et al* (2001) 'Predicting transmembrane protein topology with a hidden Markov model: Application to complete genomes', *Journal of Molecular Biology*, 305(3), pp. 567–580.

Krueger, D. K. *et al*. (2001) 'Variations in Disparate Regions of the Murine Coronavirus Spike Protein Impact the Initiation of Membrane Fusion', *Journal of Virology*, 75(6), pp. 2792–2802.

Kuo, L. *et al* (2000) 'Retargeting of coronavirus by substitution of the spike glycoprotein ectodomain: crossing the host cell species barrier.', *Journal of virology*, 74(3), pp. 1393–1406.

Kuo, L. *et al* (2016) 'Analyses of Coronavirus Assembly Interactions with Interspecies Membrane and Nucleocapsid Protein Chimeras', *Journal of Virology*, 90(9), pp. 4357–4368.

Kuo, L. and Masters, P. S. (2002) 'Genetic Evidence for a Structural Interaction between the Carboxy Termini of the Membrane and Nucleocapsid Proteins of Mouse Hepatitis Virus Genetic Evidence for a Structural Interaction between the Carboxy Termini of the Membrane and Nucleocapsid Protein', *Journal of Virology*, 76(10), pp. 4987–4999.

Kyte, J. and Doolittle, R. F. (1982) 'A simple method for displaying the hydropathic character of a protein', *Journal of Molecular Biology*, 157(1), pp. 105–132.

De La Serna, J. B. *et al* (2004) 'Cholesterol rules: Direct observation of the

coexistence of two fluid phases in native pulmonary surfactant membranes at physiological temperatures', *Journal of Biological Chemistry*, 279(39), pp. 40715–40722.

Lai, Alex L.,Li, Y. and L. K. T. (2005) 'Interplay of proteins and lipids in virus entry by membrane fusion', in *Protein- lipid interactions*. Germany: Wiley-VCH Verlag GmbH, pp. 279–303.

Lai, A. L. *et al* (2017) 'The SARS-CoV Fusion Peptide Forms an Extended Bipartite Fusion Platform that Perturbs Membrane Order in a Calcium-Dependent Manner', *Journal of Molecular Biology*. Elsevier Ltd, 429(24), pp. 3875–3892.

Latham, T. and Galarza, J. M. (2001) 'Formation of wild-type and chimeric influenza virus-like particles following simultaneous expression of only four structural proteins.', *Journal of virology*, 75(13), pp. 6154–6165.

Lau, S. K. P. *et al* (2013) 'Genetic Characterization of Betacoronavirus Lineage C Viruses in Bats Reveals Marked Sequence Divergence in the Spike Protein of Pipistrellus Bat Coronavirus HKU5 in Japanese Pipistrelle: Implications for the Origin of the Novel Middle East Respiratory Sy', *Journal of Virology*, 87(15), pp. 8638–8650.

Lee, Hee Jung, Shieh,C,K., Gorbalenya, A.E., Koonin, E.V., La Monica, N., Tuler, J., Bagdzhadzhyan, A. and Lai, M. M. (1991) 'The complete sequence (22 kilobases) of murine coronavirus gene 1 encoding the putative proteases and RNA polymerase.', *Virology*, 180(2), pp. 567–582.

Lee, M. C. S. *et al* (2005) 'Sar1p N-terminal helix initiates membrane curvature and completes the fission of a COPII vesicle', *Cell*, 122(4), pp. 605–617.

Lei, J., Kusov, Y. and Hilgenfeld, R. (2018) 'Nsp3 of coronaviruses: Structures and functions of a large multi-domain protein', *Antiviral Research*. Elsevier, pp. 58–74. doi: 10.1016/j.antiviral.2017.11.001.

Li, F. *et al* (2006) 'Conformational States of the Severe Acute Respiratory Syndrome Coronavirus Spike Protein Ectodomain', *Journal of Virology*, 80(14), pp. 6794–6800.

Li, F. (2015) 'Receptor Recognition Mechanisms of Coronaviruses: a Decade of Structural Studies', *Journal of Virology*, 89(4), pp. 1954–1964.

Li, F. (2016) 'Structure, Function, and Evolution of Coronavirus Spike Proteins', *Annual Review of Virology*, 3(1), pp. 237–261.

Li, W. *et al* (2003) 'Angiotensin-converting enzyme 2 is a functional receptor for the SARS coronavirus', *Nature*. Macmillan Magazines Ltd., 426, p. 450.

Li, W. *et al* (2015) 'The EMBL-EBI bioinformatics web and programmatic tools framework', *Nucleic Acids Research*, 43(W1), pp. W580–W584.

Li, W. *et al* (2017) 'Identification of sialic acid-binding function for the Middle East respiratory syndrome coronavirus spike glycoprotein', *Proceedings of the National Academy of Sciences*, p. 201712592.

Li, Y. *et al* (2014) 'Structure of a conserved golgi complex-targeting signal in coronavirus envelope proteins', *Journal of Biological Chemistry*, 289(18), pp. 12535–12549.

Liao, Y. *et al* (2004) 'Expression of SARS-coronavirus envelope protein in Escherichia coli cells alters membrane permeability', *Biomedical and biophysical communications*, 325(1), pp. 374–380.

Liao, Y. *et al* (2006) 'Biochemical and functional characterization of the membrane association and membrane permeabilizing activity of the severe acute respiratory syndrome coronavirus envelope protein', *Virology*, 349(2), pp. 264–275.

Liao, Z. *et al* (2001) 'Lipid Rafts and HIV Pathogenesis : Host Membrane Cholesterol Is Required for Infection by HIV Type 1', *AIDS research and human retrovirses*, 17(11), pp. 1009–1019.

Lim, K. P. and Liu, D. X. (2001) 'The missing link in coronavirus assembly. Retention of the avian coronavirus infectious bronchitis virus envelope protein in the pre-Golgi compartments and physical interaction between the envelope and membrane proteins', *Journal of Biological Chemistry*, 276(20), pp. 17515–17523.

Lin, S. Y. *et al* (2014) 'Structural basis for the identification of the N-terminal domain of coronavirus nucleocapsid protein as an antiviral target', *Journal of Medicinal Chemistry*, 57(6), pp. 2247–2257.

Lopez, L. A. *et al* (2008) 'Importance of Conserved Cysteine Residues in the Coronavirus Envelope Protein', *Journal of Virology*, 82(6), pp. 3000–3010.

Lopez, Lisa A *et al* (2008) 'Importance of Conserved Cysteine Residues in the Coronavirus Envelope Protein', *Journal of Virology*, 82(6), pp. 3000–3010.

Lu, G., Hu, Y., Wang, Q., Qi, J., Gao, F., Li, Y., Zhang, Y., Zhang, W., Yuan, Y., Bao, J.and Zhang, B. (2013) 'Molecular basis of binding between novel human coronavirus MERS-CoV and its receptor CD26.', *Nature*, 500(7461), p. 227.

Lu, L. *et al* (2014) 'Structure-based discovery of Middle East respiratory syndrome coronavirus fusion inhibitor', *Nature Communications*, 5, p. 3067.

Lu, W. *et al* (2002) ‘Characterization of a truncated soluble form of the baculovirus (AcMNPV) major envelope protein Gp64’, *Protein Expression and Purification*, 24(2), pp. 196–201.

Luckow, V. a *et al* (1993) ‘Efficient generation of infectious recombinant baculoviruses by site-specific transposon-mediated insertion of foreign genes into a baculovirus genome propagated in Escherichia coli.’, *Journal of virology*, 67(8), pp. 4566–4579.

Luisi, P. L., Walde, P. and Oberholzer, T. (1999) ‘Lipid vesicles as possible intermediates in the origin of life’, *Current Opinion in Colloid and Interface Science*, 4(1), pp. 33–39. doi: 10.1016/S1359-0294(99)00012-6.

Lundin, A. *et al* (2014) ‘Targeting Membrane-Bound Viral RNA Synthesis Reveals Potent Inhibition of Diverse Coronaviruses Including the Middle East Respiratory Syndrome Virus’, *PLoS Pathogens*, 10(5).

Luo, Z., Matthews, A. M. and Weiss, S. R. (1999) ‘Amino Acid Substitutions within the Leucine Zipper Domain of the Murine Coronavirus Spike Protein Cause Defects in Oligomerization and the Ability To Induce Cell-to-Cell Fusion’, *Journal of Virology*, 73(10), pp. 8152–8159.

Luo, Z. and Weiss, S. R. (1998) ‘Roles in Cell-to-Cell Fusion of Two Conserved Hydrophobic Regions in the Murine Coronavirus Spike Protein’, *Virology*, 244(2), pp. 483–494.

Ma-Lauer, Y. *et al* (2016) ‘p53 down-regulates SARS coronavirus replication and is targeted by the SARS-unique domain and PL ^{pro} via E3 ubiquitin ligase RCHY1’, *Proceedings of the National Academy of Sciences*, p. 201603435.

Ma, C. *et al* (2014) 'Intranasal vaccination with recombinant receptor-binding domain of MERS-CoV spike protein induces much stronger local mucosal immune responses than subcutaneous immunization: Implication for designing novel mucosal MERS vaccines', *Vaccine*, 32(18), pp. 2100–2108.

Madan, V. *et al* (2005) 'Viroporin activity of murine hepatitis virus E protein', *FEBS Lett*, 579(17), pp. 3607–3612.

Madu, I. G. *et al* (2009) 'Characterization of a Highly Conserved Domain within the Severe Acute Respiratory Syndrome Coronavirus Spike Protein S2 Domain with Characteristics of a Viral Fusion Peptide', *Journal of Virology*, 83(15), pp. 7411–7421.

Madu, Ikenna G *et al* (2009) 'Characterization of a Highly Conserved Domain within the Severe Acute Respiratory Syndrome Coronavirus Spike Protein S2 Domain with Characteristics of a Viral Fusion Peptide', *Journal of Virology*, 83(15), pp. 7411–7421.

Maier, H. J. *et al* (2013) 'Infectious bronchitis virus generates spherules from zippered endoplasmic reticulum membranes', *mBio*, 4(5), pp. 1–12.

Maier, H. J. *et al* (2016) 'Extensive coronavirus-induced membrane rearrangements are not a determinant of pathogenicity', *Nature Publishing Group*. Nature Publishing Group, (June), pp. 1–12.

Malik, E. *et al* (2016) 'PH dependent antimicrobial peptides and proteins, their mechanisms of action and potential as therapeutic agents', *Pharmaceuticals*, pp. 1–35.

Martin, I. and Ruysschaert, J. M. (2000) 'Common properties of fusion peptides from

diverse systems', *Bioscience Reports*, 20(6), pp. 483–500.

Masters, P. (1992) 'Localization of an RNA-binding domain in the nucleocapsid protein of the coronavirus mouse hepatitis virus.', *Arch virol*, 125(1–4), pp. 141–160.

Masters, P. S. (2006) 'the Molecular Biology of coronaviruses', *advances in virus research*, (66), pp. 193–292.

Mateos-Gomez, P. A. *et al* (2011) 'Gene N Proximal and Distal RNA Motifs Regulate Coronavirus Nucleocapsid mRNA Transcription', *Journal of Virology*, 85(17), pp. 8968–8980.

Matsuyama, S. *et al* (2005) 'Protease-mediated enhancement of severe acute respiratory syndrome coronavirus infection.', *Proceedings of the National Academy of Sciences of the United States of America*, 102(35), pp. 12543–7.

Matsuzaki, K. *et al* (1998) 'Relationship of membrane curvature to the formation of pores by magainin 2', *Biochemistry*, 37(34), pp. 11856–11863.

Matsuzaki, K., Yoneyama, S. and Miyajima, K. (1997) 'Pore formation and translocation of melittin', *Biophysical Journal*, 73(2), pp. 831–838.

McMahon, H. T. and Gallop, J. L. (2005) 'Membrane curvature and mechanisms of dynamic cell membrane remodelling.', *Nature*, 438(7068), pp. 590–596.

McMahon, H. T., Kozlov, M. M. and Martens, S. (2010) 'Membrane Curvature in Synaptic Vesicle Fusion and Beyond', *Cell*, 140(5), pp. 601–605.

McWilliam, H. *et al* (2013) 'Analysis Tool Web Services from the EMBL-EBI.', *Nucleic acids research*, 41(Web Server issue), pp. 597–600.

van Meer, G. (2008) 'Membrane lipids, where they are and how they behave:

Sphingolipids on the move', *Nature Reviews Molecular Cell Biology*, 9(2), pp. 112–124.

Miller, S. and Krijnse-Locker, J. (2008) 'Modification of intracellular membrane structures for virus replication', *Nature Reviews Microbiology*, pp. 363–374.

Millet, J. K. *et al* (2016) 'A camel-derived MERS-CoV with a variant spike protein cleavage site and distinct fusion activation properties', *Emerging Microbes and Infections*. Nature Publishing Group, 5(12), pp. e126-9.

Millet, J. K. and Whittaker, G. R. (2015) 'Host cell proteases: Critical determinants of coronavirus tropism and pathogenesis', *Virus Research*. Elsevier B.V., 202, pp. 120–134.

Millet, J. K. and Whittaker, G. R. (2018) 'Physiological and molecular triggers for SARS-CoV membrane fusion and entry into host cells', *Virology*. Elsevier Inc., 517(December 2017), pp. 3–8.

Mironov, A. A. *et al* (2001) 'Small cargo proteins and large aggregates can traverse the Golgi by a common mechanism without leaving the lumen of cisternae', *Journal of Cell Biology*, 155(7), pp. 1225–1238.

Misumi, Y. *et al* (1991) 'Functional expression of furin demonstrating its intracellular localization and endoprotease activity for processing of proalbumin and complement pro-C3', *Journal of Biological Chemistry*, 266(25), pp. 16954–16959.

Mohd, H. A., Al-Tawfiq, J. A. and Memish, Z. A. (2016) 'Middle East Respiratory Syndrome Coronavirus (MERS-CoV) origin and animal reservoir Susanna Lau', *Virology Journal*. Virology Journal, 13(1), pp. 1–7.

Molina, S. *et al* (2007) 'The low-density lipoprotein receptor plays a role in the infection of primary human hepatocytes by hepatitis C virus', *Journal of Hepatology*, 46(3), pp. 411–419.

Monsma, S. A., Oomens, A. G. and Blissard, G. W. (1996) 'The GP64 envelope fusion protein is an essential baculovirus protein required for cell-to-cell transmission of infection.', *Journal of virology*, 70(7), pp. 4607–16.

Morré, D. J. and Ovtracht, L. (1977) 'Dynamics of the Golgi apparatus: membrane differentiation and membrane flow.', *International review of cytology. Supplement*, 5(5), pp. 61–188.

Mortola, E. and Roy, P. (2004) 'Efficient assembly and release of SARS coronavirus-like particles by a heterologous expression system', *FEBS Letters*, 576(1–2), pp. 174–178.

Mou, H. *et al* (2013) 'The Receptor Binding Domain of the New Middle East Respiratory Syndrome Coronavirus Maps to a 231-Residue Region in the Spike Protein That Efficiently Elicits Neutralizing Antibodies', *Journal of Virology*, 87(16), pp. 9379–9383.

Mourez, T. *et al* (2007) 'Baculovirus expression of HCoV-OC43 nucleocapsid protein and development of a Western blot assay for detection of human antibodies against HCoV-OC43', *Journal of Virological Methods*, 139(2), pp. 175–180.

Munger, J. *et al* (2008) 'Synthesis As a Target for Antiviral Therapy', *Nature biotechnology*, 26(10), pp. 1179–1186. doi: 10.1038/nbt.1500.Systems-level.

Nagy, P. D. and Pogany, J. (2012) 'The dependence of viral RNA replication on co-opted host factors', *Nature Reviews Microbiology*. Nature Publishing Group, 10(2),

pp. 137–149.

Naito, A. *et al* (2000) ‘Conformation and dynamics of melittin bound to magnetically oriented lipid bilayers by solid-state31P and13C NMR spectroscopy’, *Biophysical Journal*, 78(5), pp. 2405–2417.

Nal, B. *et al*. (2005) ‘Differential maturation and subcellular localization of severe acute respiratory syndrome coronavirus surface proteins S, M and E’, *Journal of General Virology*, 86(5), pp. 1423–1434.

Narayanan, K. *et al* (2000) ‘Characterization of the coronavirus M protein and nucleocapsid interaction in infected cells.’, *Journal of virology*, 74(17), pp. 8127–8134.

Netherton, C. L. and Wileman, T. (2011) ‘Virus factories, double membrane vesicles and viroplasm generated in animal cells’, *Current Opinion in Virology*. Elsevier B.V., 1(5), pp. 381–387.

Neufeldt, C. J. *et al* (2016) ‘The Hepatitis C Virus-Induced Membranous Web and Associated Nuclear Transport Machinery Limit Access of Pattern Recognition Receptors to Viral Replication Sites’, *PLoS Pathogens*, 12(2), pp. 1–28.

Neuman, B. W. *et al* (2011) ‘A structural analysis of M protein in coronavirus assembly and morphology’, *Journal of Structural Biology*. Elsevier Inc., 174(1), pp. 11–22.

Neuman, B. W. *et al* (2014) ‘Atlas of coronavirus replicase structure’, *Virus Research*. Elsevier B.V., 194, pp. 49–66.

Neuman, B. W. (2016) ‘Bioinformatics and functional analyses of coronavirus

nonstructural proteins involved in the formation of replicative organelles', *Antiviral Research*. Elsevier B.V., pp. 97–107.

Neuman, B. W. and Buchmeier, M. J. (2016) 'Supramolecular Architecture of the Coronavirus Particle', in *Advances in Virus Research*, pp. 1–27.

Nguyen, D. H. and Hildreth, J. E. K. (2000) 'Evidence for Budding of Human Immunodeficiency Virus Type 1 Selectively from Glycolipid-Enriched Membrane Lipid Rafts', *Journal of Virology*, 74(7), pp. 3264–3272.

Nieva, J. L., Madan, V. and Carrasco, L. (2012) 'Viroporins: Structure and biological functions', *Nature Reviews Microbiology*. Nature Publishing Group, 10(8), pp. 563–574.

Ohki, S., & Arnold, K. (2000) 'A mechanism for ion-induced lipid vesicle fusion. Colloids and Surfaces B', *Biointerfaces*, 18(2), pp. 83–97.

Ohnuma, K. *et al* (2013) 'Inhibition of Middle East Respiratory Syndrome Coronavirus Infection by Anti-CD26 Monoclonal Antibody', *Journal of Virology*, 87(24), pp. 13892–13899.

Oostra, M. *et al* (2006) 'Glycosylation of the severe acute respiratory syndrome coronavirus triple-spanning membrane proteins 3a and M.', *Journal of virology*, 80(5), pp. 2326–36.

Ou, X. *et al* (2016) 'Identification of the Fusion Peptide-Containing Region in Betacoronavirus Spike Glycoproteins', *Journal of Virology*, 90(March), p. JVI.00015-16.

Oudshoorn, D. *et al* (2017) 'Expression and cleavage of middle east respiratory

syndrome coronavirus nsp3-4 polyprotein induce the formation of double-membrane vesicles that mimic those associated with coronaviral RNA replication', *mBio*. American Society for Microbiology, 8(6), pp. e01658-17.

Pan, J. *et al* (2008) 'Genome-wide analysis of protein-protein interactions and involvement of viral proteins in SARS-CoV replication', *PLoS ONE*, 3(10).

Park, J. E., Cruz, D. J. M. and Shin, H. J. (2011) 'Receptor-bound porcine epidemic diarrhea virus spike protein cleaved by trypsin induces membrane fusion', *Archives of Virology*, 156(10), pp. 1749–1756.

Parthasarathy, K. *et al* (2012) 'Expression and purification of coronavirus envelope proteins using a modified β-barrel construct', *Protein Expression and Purification*. Elsevier Inc., 85(1), pp. 133–141.

Paul, D. (2013) 'Architecture and biogenesis of plus-strand RNA virus replication factories', *World Journal of Virology*, 2(2), p. 32.

Pautot, S., Frisken, B. J. and Weitz, D. a (2003) 'Production of Unilamellar Vesicles Usingan Inverted Emulsion', *Langmuir : the ACS journal of surfaces and colloids*, (10), pp. 2870–2879.

Pear, W. S. *et al* (1993) 'Production of high-titer helper-free retroviruses by transient transfection.', *Proceedings of the National Academy of Sciences*, 90(18), pp. 8392–8396.

Pécheur, E. I. *et al* (1998) 'Membrane fusion induced by 11-mer anionic and cationic peptides: A structure-function study', *Biochemistry*, 37(8), pp. 2361–2371.

Peng, G. *et al* (2011) 'Crystal structure of mouse coronavirus receptor-binding

domain complexed with its murine receptor', *Proceedings of the National Academy of Sciences*, 108(26), pp. 10696–10701.

Peng, T. Y., Lee, K. R. and Tarn, W. Y. (2008) 'Phosphorylation of the arginine/serine dipeptide-rich motif of the severe acute respiratory syndrome coronavirus nucleocapsid protein modulates its multimerization, translation inhibitory activity and cellular localization', *FEBS Journal*, 275(16), pp. 4152–4163.

Perlman, S. and Netland, J. (2009) 'Coronaviruses post-SARS: update on replication and pathogenesis.', *Nature reviews. Microbiology*, 7(6), pp. 439–50.

Pervushin, K. *et al* (2009) 'Structure and inhibition of the SARS coronavirus envelope protein ion channel', *PLoS Pathogens*, 5(7).

Peter, B. J. *et al* (2004) 'BAR domains as sensors of membrane curvature: the amphiphysin BAR structure.', *Science (New York, N.Y.)*, 303(5657), pp. 495–499.

Pfefferle, S. *et al* (2011) 'The SARS-Coronavirus-host interactome: Identification of cyclophilins as target for pan-Coronavirus inhibitors', *PLoS Pathogens*, 7(10).

Pijlman, G. P. *et al* (2001) 'Autographa californica baculoviruses with large genomic deletions are rapidly generated in infected insect cells', *Virology*, 283(1), pp. 132–138.

Pijlman, G. P., van Schinjndel, J. E. and Vlak, J. M. (2003) 'Spontaneous excision of BAC vector sequences from bacmid-derived baculovirus expression vectors upon passage in insect cells', *Journal of General Virology*, 84(10), pp. 2669–2678.

Popova, R. and Zhang, X. (2002) 'The spike but not the hemagglutinin/esterase protein of bovine coronavirus is necessary and sufficient for viral infection', *Virology*,

294(1), pp. 222–236.

Prentice, E., Jerome, W. G., *et al* (2004) ‘Coronavirus Replication Complex Formation Utilizes Components of Cellular Autophagy’, *Journal of Biological Chemistry*, 279(11), pp. 10136–10141.

Prentice, E., Mcauliffe, J., *et al* (2004) ‘Identification and characterization of severe acute respiratory syndrome coronavirus replicase proteins’, *Journal of virology*, 78(18), pp. 9977–9986.

Qian, M. *et al* (2009) ‘A Lipid Receptor Sorts Polyomavirus from the Endolysosome to the Endoplasmic Reticulum to Cause Infection’, *PLoS Pathogens*, 5(6), p. e1000465.

Qian, Z., Dominguez, S. R. and Holmes, K. V (2013) ‘Role of the Spike Glycoprotein of Human Middle East Respiratory Syndrome Coronavirus (MERS-CoV) in Virus Entry and Syncytia Formation’, *PLoS ONE*, 8(10), p. e7469.

Qiu, Z. *et al* (2006) ‘Endosomal proteolysis by cathepsins is necessary for murine coronavirus mouse hepatitis virus type 2 spike-mediated entry.’, *Journal of virology*, 80(12), pp. 5768–5776.

Quinteros, J. A. *et al* (2015) ‘Analysis of the complete genomic sequences of two virus subpopulations of the Australian infectious bronchitis virus vaccine VicS’, *Avian Pathology*. Taylor & Francis, 44(3), pp. 182–191.

Raamsman, M. J. B. *et al* (2000) ‘Characterization of the Coronavirus Mouse Hepatitis Virus Strain A59 Small Membrane Protein E’, 74(5), pp. 2333–2342.

Raj, V. S. *et al* (2013) ‘Dipeptidyl peptidase 4 is a functional receptor for the

emerging human coronavirus-EMC', *Nature*, 495(7440), pp. 251–254.

Rawlings, N. D., & Barrett, A. J. (2013) 'ntroduction: the clans and families of cysteine peptidases', in *In Handbook of Proteolytic Enzymes*, pp. 1743–1773.

Reeves, P., John & Dowben, M., R. (1969) 'Formation and properties of thin- walled phospholipid vesicles', *Cellualr Physiology*, 73(1), pp. 49–60.

Regan, A. D. *et al* (2008) 'Differential role for low pH and cathepsin-mediated cleavage of the viral spike protein during entry of serotype II feline coronaviruses', *Veterinary Microbiology*, 132(3–4), pp. 235–248.

Reggiori, F. *et al* (2010) 'Coronaviruses hijack the LC3-I-positive EDEMosomes, ER-derived vesicles exporting short-lived ERAD regulators, for replication', *Cell Host and Microbe*, 7(6), pp. 500–508.

Regla-Nava, J. a. *et al* (2015) 'Severe Acute Respiratory Syndrome Coronaviruses with Mutations in the E Protein Are Attenuated and Promising Vaccine Candidates', *Journal of Virology*, 89(7), pp. 3870–3887.

Reguera, J. *et al* (2014) 'A structural view of coronavirus-receptor interactions', *Virus Research*. Elsevier B.V., 194, pp. 3–15.

Rigaud, J. L., Pitard, B. and Levy, D. (1995) 'Reconstitution of membrane proteins into liposomes: application to energy-transducing membrane proteins', *BBA - Bioenergetics*, 1231(3), pp. 223–246.

Risco, C. *et al* (1995) 'Membrane protein molecules of transmissible gastroenteritis coronavirus also expose the carboxy-terminal region on the external surface of the virion', *J Virol*, 69(9), pp. 5269–5277.

Rosen, E., Stapleton, J. T. and McLinden, J. (1993) ‘Synthesis of immunogenic hepatitis A virus particles by recombinant baculoviruses’, *Vaccine*, 11(7), pp. 706–712.

Rossman, J. S. *et al* (2010) ‘Influenza Virus M2 Protein Mediates ESCRT-Independent Membrane Scission’, *Cell*. Elsevier Ltd, 142(6), pp. 902–913.

Ruch, T. R. and Machamer, C. E. (2011) ‘The Hydrophobic Domain of Infectious Bronchitis Virus E Protein Alters the Host Secretory Pathway and Is Important for Release of Infectious Virus’, *Journal of Virology*, 85(2), pp. 675–685.

Ruch, T. R. and Machamer, C. E. (2012) ‘The Coronavirus E Protein: Assembly and Beyond’, *Viruses*, 4(3), pp. 363–382.

Saad, J. S. *et al* (2006) ‘Structural basis for targeting HIV-1 Gag proteins to the plasma membrane for virus assembly.’, *Proceedings of the National Academy of Sciences of the United States of America*, 103(30), pp. 11364–9.

Sainz, B. *et al* (2005) ‘The Aromatic Domain of the Coronavirus Class I Viral Fusion Protein Induces Membrane Permeabilization: Putative Role during Viral Entry ’, *Biochemistry*, 44(3), pp. 947–958.

Sainz, B. *et al* (2006) ‘Inhibition of severe acute respiratory syndrome-associated coronavirus (SARS-CoV) infectivity by peptides analogous to the viral spike protein’, *Virus Research*, 120(1–2), pp. 146–155.

Sakai, Y. *et al* (2017) ‘Two-amino acids change in the nsp4 of SARS coronavirus abolishes viral replication’, *Virology*. Elsevier Inc., 510(June), pp. 165–174.

Salzwedel, K., West, J. T. and Hunter, E. (1999) ‘A Conserved Tryptophan-Rich

Motif in the Membrane-Proximal Region of the Human Immunodeficiency Virus Type 1 gp41 Ectodomain Is Important for Env-Mediated Fusion and Virus Infectivity', *Journal of virology*, 73(3), pp. 2469–2480.

Sapay, N., Guermeur, Y. and Deléage, G. (2006) 'Prediction of amphipathic in-plane membrane anchors in monotopic proteins using a SVM classifier', *BMC Bioinformatics*, 7, pp. 1–11.

Sawicki, S. G., & Sawicki, D. L. (1995) 'Coronaviruses use discontinuous extension for synthesis of subgenome-length negative strands. In Corona-and Related Viruses', pp. 499–506.

Sawicki, S. G., Sawicki, D. L. and Siddell, S. G. (2007) 'A contemporary view of coronavirus transcription.', *Journal of virology*, 81(1), pp. 20–9.

Schmitt, A. P., & Lamb, R. A. (2005) 'Influenza Virus Assembly and Budding at the Viral Budozone', *Virus Structure and Assembly*, 64, pp. 383–416.

Schmitt, a P. and Lamb, R. a (2004) 'Escaping from the cell: assembly and budding of negative-strand RNA viruses.', *Current topics in microbiology and immunology*, 283, pp. 145–196.

Schneider, C. A., Rasband, W. S. and Eliceiri, K. W. (2012) 'NIH Image to ImageJ: 25 years of image Analysis', *Nature Methods*, 9(7), pp. 671–675.

Seidah, N. G. and Prat, A. (2012) 'The biology and therapeutic targeting of the proprotein convertases', *Nature Reviews Drug Discovery*. Nature Publishing Group, 11(5), pp. 367–383.

Shaklee, P. M. *et al* (2010) 'Protein incorporation in giant lipid vesicles under

physiological conditions', *ChemBioChem*, 11(2), pp. 175–179.

Shimanouchi, T. *et al* (2007) 'Permeation of a ??-heptapeptide derivative across phospholipid bilayers', *Biochimica et Biophysica Acta - Biomembranes*, 1768(11), pp. 2726–2736.

Shirato, K., Kawase, M. and Matsuyama, S. (2013) 'Middle East Respiratory Syndrome Coronavirus Infection Mediated by the Transmembrane Serine Protease TMPRSS2', *Journal of Virology*, 87(23), pp. 12552–12561.

Sievers, F. *et al* (2011) 'Fast, scalable generation of high-quality protein multiple sequence alignments using Clustal Omega', *Molecular Systems Biology*, 7(539).

Simmons, G. *et al* (2004) 'Characterization of severe acute respiratory syndrome-associated coronavirus (SARS-CoV) spike glycoprotein-mediated viral entry', *Proceedings of the National Academy of Sciences*, 101(12), pp. 4240–4245.

Simmons, G. *et al* (2005) 'Inhibitors of cathepsin L prevent severe acute respiratory syndrome coronavirus entry.', *Proceedings of the National Academy of Sciences*, 102(33), pp. 11876–11881.

Skehel, J. J. and Wiley, D. C. (1998) 'Coiled coils in both intracellular vesicle and viral membrane fusion', *Cell*, pp. 871–874. doi: 10.1016/S0092-8674(00)81710-9.

Smith, G. E., Summers, M. D. and Fraser, M. J. (1983) 'Production of human beta interferon in insect cells infected with a baculovirus expression vector . Production of Human Beta Interferon in Insect Cells Infected with a Baculovirus Expression Vector', *Molecular and Cellular Biology*, 3(12), pp. 2156–2165.

Smits, S. L. *et al* (2005) 'Nidovirus sialate-O-acetylesterases: Evolution and

substrate specificity of coronaviral and toroviral receptor-destroying enzymes', *Journal of Biological Chemistry*, 280(8), pp. 6933–6941.

Snijder, E. J. *et al* (2006) 'Ultrastructure and Origin of Membrane Vesicles Associated with the Severe Acute Respiratory Syndrome Coronavirus Replication Complex', *Journal of Virology*, 80(12), pp. 5927–5940.

Sparks, J. S., Lu, X. and Denison, M. R. (2007) 'Genetic Analysis of Murine Hepatitis Virus nsp4 in Virus Replication', *Journal of Virology*, 81(22), pp. 12554–12563.

Stachowiak, J. C. *et al* (2012) 'Membrane bending by protein–protein crowding', *Nature Cell Biology*. Nature Publishing Group, 14(9), pp. 944–949.

Stertz, S. *et al* (2007) 'The intracellular sites of early replication and budding of SARS-coronavirus', *Virology*, 361(2), pp. 304–315. doi: 10.1016/j.virol.2006.11.027.

Strating, J. R. and van Kuppeveld, F. J. (2017) 'Viral rewiring of cellular lipid metabolism to create membranous replication compartments', *Current Opinion in Cell Biology*. Elsevier Ltd, 47, pp. 24–33.

Streicher, P. *et al* (2009) 'Integrin reconstituted in GUVs: A biomimetic system to study initial steps of cell spreading', *Biochimica et Biophysica Acta - Biomembranes*. Elsevier B.V., 1788(10), pp. 2291–2300.

Sturman, L. S., Ricard, C. S. and Holmes, K. V (1990) 'Conformational change of the coronavirus peplomer glycoprotein at pH 8.0 and 37 degrees C correlates with virus aggregation and virus-induced cell fusion.', *Journal of virology*, 64(6), pp. 3042–50.

Suarez, T. *et al* (2000) 'Membrane Interface-Interacting Sequences within the Ectodomain of the Human Immunodeficiency Virus Type 1 Envelope Glycoprotein:

Putative Role during Viral Fusion', *Journal of Virology*, 74(17), pp. 8038–8047.

Sun, Y. *et al* (2017) 'Identification of a novel inhibitor against middle east respiratory syndrome coronavirus', *Viruses*, 9(9), pp. 1–12.

Supekar, V. M. *et al* (2004) 'Structure of a proteolytically resistant core from the severe acute respiratory syndrome coronavirus S2 fusion protein', *Proceedings of the National Academy of Sciences*, 101(52), pp. 17958–17963.

Surjit, M. *et al* (2005) 'The Severe Acute Respiratory Syndrome Coronavirus Nucleocapsid Protein Is Phosphorylated and Localizes in the Cytoplasm by 14-3-3-Mediated Translocation The Severe Acute Respiratory Syndrome Coronavirus Nucleocapsid Protein Is Phosphorylated and Localizes', *Society*, 79(17), pp. 11476–11486.

Surjit, M. *et al* (2006) 'The nucleocapsid protein of severe acute respiratory syndrome-coronavirus inhibits the activity of cyclin-cyclin-dependent kinase complex and blocks S phase progression in mammalian cells.', *The Journal of biological chemistry*, 281(16), pp. 10669–81.

Suzuki, K. and Ohsumi, Y. (2007) 'Molecular machinery of autophagosome formation in yeast, Saccharomyces cerevisiae', *FEBS Letters*, 581(11), pp. 2156–2161.

Sweitzer, S. M. and Hinshaw, J. E. (1998) 'Dynamin undergoes a GTP-dependent conformational change causing vesiculation', *Cell*, 93(6), pp. 1021–1029.

Swift, G. H. *et al* (1989) 'Differential requirements for cell-specific elastase I enhancer domains in transfected cells and transgenic mice.', *Genes & development*, 3(5), pp. 687–696.

Szostak, J. W., Bartel, D. P. and Luisi, P. L. (2001) ‘Synthesizing LIfe’, *Nature*, 409, pp. 387–390.

Taguchi, F. and Hirai-Yuki, A. (2012) ‘Mouse hepatitis virus receptor as a determinant of the mouse susceptibility to MHV infection’, *Frontiers in Microbiology*, 3(FEB), pp. 1999–2002.

Takahashi, T. *et al* (2013) ‘Multiple membrane interactions and versatile vesicle deformations elicited by melittin’, *Toxins*, 5(4), pp. 637–664.

Tang, T. K. *et al* (2005) ‘Biochemical and immunological studies of nucleocapsid proteins of severe acute respiratory syndrome and 229E human coronaviruses’, *Proteomics*, 5(4), pp. 925–937.

Taube, S., Jiang, M. and Wobus, C. E. (2010) ‘Glycosphingolipids as Receptors for Non-Enveloped Viruses’, *Viruses*, 2(4), pp. 1011–1049.

Teoh, K.-T. *et al* (2010) ‘The SARS Coronavirus E Protein Interacts with PALS1 and Alters Tight Junction Formation and Epithelial Morphogenesis’, *Molecular Biology of the Cell*. Edited by A. Nusrat. The American Society for Cell Biology, 21(22), pp. 3838–3852.

Thorp, E. B. *et al* (2006) ‘Palmitoylations on murine coronavirus spike proteins are essential for virion assembly and infectivity’, *J Virol*, 80(3), pp. 1280–1289.

Thorp, E. B. and Gallagher, T. M. (2004) ‘Requirements for CEACAMs and Cholesterol during Murine Coronavirus Cell Entry’, *Journal of Virology*, 78(6), pp. 2682–2692.

Torres, J. *et al* (2006) ‘Model of a Putative Pore : The Pentameric a -Helical Bundle

of SARS Coronavirus E Protein in Lipid Bilayers', *Biophysical Journal*. Elsevier, 91(3), pp. 938–947.

Torres, J. *et al* (2007) 'Conductance and amantadine binding of a pore formed by a lysine-flanked transmembrane domain of SARS coronavirus envelope protein.', *Protein science : a publication of the Protein Society*, 16, pp. 2065–2071.

Torres, J., Briggs, J. A. G. and Arkin, I. T. (2002) 'Multiple site-specific infrared dichroism of CD3-ζ, a transmembrane helix bundle', *Journal of Molecular Biology*, 316(2), pp. 365–374.

Treanor, J. J. *et al* (2006) 'Virus Hemagglutinin Vaccine in Elderly Adults Linked references are available on JSTOR for this article : Dose-Related Safety and Immunogenicity of a Trivalent Baculovirus-Expressed Influenza-V Hemagglutinin Vaccine in Elderly Adults', *The journal of infecoius diseases*, 193(9), pp. 1223–1228.

Trincone, A. and Schwegmann-Weßels, C. (2015) 'Looking for a needle in a haystack: Cellular proteins that may interact with the tyrosine-based sorting signal of the TGEV S protein', *Virus Research*. Elsevier B.V., 202, pp. 3–11.

Tsai, B. *et al* (2003) 'Gangliosides are receptors for murine polyoma virus and SV40', *EMBO Journal*, 22(17), pp. 4346–4355.

Tseng, Y.-T. *et al* (2010) 'Self-assembly of Severe Acute Respiratory Syndrome Coronavirus Membrane Protein', *Journal of Biological Chemistry*, 285(17), pp. 12862–12872.

Tseng, Y. *et al* (2014) 'SARS-CoV envelope protein palmitoylation or nucleocapid association is not required for promoting virus-like particle production', *Journal of biomedical science*, 21(1), p. 34.

Tsumoto, K. *et al* (2009) ‘Efficient formation of giant liposomes through the gentle hydration of phosphatidylcholine films doped with sugar’, *Colloids and Surfaces B: Biointerfaces*, 68(1), pp. 98–105.

Ujike, M. and Taguchi, F. (2015) ‘Incorporation of spike and membrane glycoproteins into coronavirus virions’, *Viruses*, 7(4), pp. 1700–1725.

Ulasli, M. *et al* (2010) ‘Qualitative and quantitative ultrastructural analysis of the membrane rearrangements induced by coronavirus’, *Cellular microbiology*, 12(6), pp. 844–861.

Venkatagopalan, P. *et al* (2015) ‘Coronavirus envelope (E) protein remains at the site of assembly’, *Virology*, 478, pp. 75–85. doi: 10.1016/j.virol.2015.02.005.

Vennema, H. *et al* (1996) ‘Nucleocapsid-independent assembly of coronavirus-like particles by co-expression of viral envelope protein genes.’, *The EMBO journal*, 15(8), pp. 2020–2028.

Verheije, M. H. *et al* (2007) ‘Localization and Membrane Topology of Coronavirus Nonstructural Protein 4: Involvement of the Early Secretory Pathway in Replication’, *Journal of Virology*, 81(22), pp. 12323–12336.

Volchuk, A. *et al* (2000) ‘Megavesicles implicated in the rapid transport of intracisternal aggregates across the Golgi stack’, *Cell*, 102(3), pp. 335–348.

Volz, A. *et al* (2015) ‘Protective Efficacy of Recombinant Modified Vaccinia Virus Ankara Delivering Middle East Respiratory Syndrome Coronavirus Spike Glycoprotein’, *Journal of Virology*, 89(16), pp. 8651–8656.

Voß, D. *et al* (2009) ‘Studies on membrane topology , N-glycosylation and

functionality of SARS-CoV membrane protein', *Journal of virology*, 13(1), p. 79.

Walde, P. *et al* (2010) 'Giant Vesicles: Preparations and Applications', *ChemBioChem*, 11(7), pp. 848–865.

Walls, Alexandra C *et al* (2016) 'Cryo-electron microscopy structure of a coronavirus spike glycoprotein trimer', *Nature*. Nature Publishing Group, 531(7592), pp. 114–117.

Walls, Alexandra C. *et al* (2016) 'Glycan shield and epitope masking of a coronavirus spike protein observed by cryo-electron microscopy', *Nature Structural and Molecular Biology*, 23(10), pp. 899–905.

Walls, Alexandra C. *et al*. (2017) 'Tectonic conformational changes of a coronavirus spike glycoprotein promote membrane fusion', *Proceedings of the National Academy of Sciences*, 114(42), pp. 11157–11162.

Wang, N. *et al* (2013) 'Structure of MERS-CoV spike receptor-binding domain complexed with human receptor DPP4', *Cell Research*. Nature Publishing Group, 23(8), pp. 986–993.

Waterhouse, A. M. *et al* (2009) 'Jalview Version 2-A multiple sequence alignment editor and analysis workbench', *Bioinformatics*, 25(9), pp. 1189–1191.

Weiss, S. R. and Navas-martin, S. (2005) 'Coronavirus Pathogenesis and the Emerging Pathogen Severe Acute Respiratory Syndrome Coronavirus Coronavirus Pathogenesis and the Emerging Pathogen Severe Acute Respiratory Syndrome Coronavirus', *Microbiology and Molecular Biology Reviews*, 69(4), pp. 635–664.

Weisz, O. A., Swift, A. M. and Machamer, C. E. (1993) 'Oligomerization of a membrane protein correlates with its retention in the Golgi complex', *Journal of Cell*

Biology, 122(6), pp. 1185–1196.

Welsch, S. *et al* (2007) ‘More than one door - Budding of enveloped viruses through cellular membranes’, *FEBS Letters*, 581(11), pp. 2089–2097.

Wessman, P. *et al* (2010) ‘Effect of α-helical peptides on liposome structure: A comparative study of melittin and alamethicin’, *Journal of Colloid and Interface Science*. Elsevier Inc., 346(1), pp. 127–135.

Wheeler, D. L. *et al* (2005) ‘Database resources of the National Center for Biotechnology Information’, *Nucleic Acids Research*, 33(DATABASE ISS.), pp. 39–45.

White, Judith M. *et al* (2008) ‘Structures and mechanisms of viral membrane fusion proteins: Multiple variations on a common theme’, *Critical Reviews in Biochemistry and Molecular Biology*, 43(3), pp. 189–219.

White, Judith M *et al* (2008) ‘Structures and Mechanisms of Viral Membrane Fusion Proteins’, *Critical Reviews in Biochemistry and Molecular Biology*, 43(3), pp. 189–219.

White, J. M. and Whittaker, G. R. (2016) ‘Fusion of Enveloped Viruses in Endosomes’, *Traffic*, 17(6), pp. 593–614. doi: 10.1111/tra.12389.

de Wilde, A. H. *et al* (2013) ‘MERS-coronavirus replication induces severe in vitro cytopathology and is strongly inhibited by cyclosporin A or interferon-α treatment’, *Journal of General Virology*, 94(PART8), pp. 1749–1760.

De Wilde, A. H. *et al* (2014) ‘Screening of an FDA-approved compound library identifies four small-molecule inhibitors of Middle East respiratory syndrome

coronavirus replication in cell culture', *Antimicrobial Agents and Chemotherapy*, 58(8), pp. 4875–4884.

Williams, R. K., Jiang, G. S. and Holmes, K. V (1991) 'Receptor for mouse hepatitis virus is a member of the carcinoembryonic antigen family of glycoproteins.', *Pnas*, 88(13), pp. 5533–5536.

Wilschut, J. *et al* (1980) 'Studies on the Mechanism of Membrane Fusion: Kinetics of Calcium Ion Induced Fusion of Phosphatidylserine Vesicles Followed by a New Assay for Mixing of Aqueous Vesicle Contents', *Biochemistry*, 19(26), pp. 6011–6021.

Wilson, L. *et al* (2004) 'SARS coronavirus E protein forms cation-selective ion channels', *Virology*, 330(1), pp. 322–331.

Wilson, L., Gage, P. and Ewart, G. (2006) 'Hexamethylene amiloride blocks E protein ion channels and inhibits coronavirus replication.', *Virology*, 353(2), pp. 294–306. doi: 10.1016/j.virol.2006.05.028.

Wirblich, C. *et al* (2017) 'One-Health: a Safe, Efficient, Dual-Use Vaccine for Humans and Animals against Middle East Respiratory Syndrome Coronavirus and Rabies Virus.', *Journal of virology*, 91(2), pp. 584–594.

Wissink, E. H. J. *et al* (2004) 'Significance of the oligosaccharides of the porcine reproductive and respiratory syndrome virus glycoproteins GP2a and GP5 for infectious virus production', *Journal of General Virology*, 85(12), pp. 3715–3723.

Wong, S. K. *et al* (2004) 'A 193-Amino Acid Fragment of the SARS Coronavirus S Protein Efficiently Binds Angiotensin-converting Enzyme 2', *Journal of Biological Chemistry*, 279(5), pp. 3197–3201.

Woo, P. C. Y. *et al* (2012) 'Discovery of Seven Novel Mammalian and Avian Coronaviruses in the Genus Deltacoronavirus Supports Bat Coronaviruses as the Gene Source of Alphacoronavirus and Betacoronavirus and Avian Coronaviruses as the Gene Source of Gammacoronavirus and Deltacoronavi', *Journal of Virology*, 86(7), pp. 3995–4008.

Woo, P. C. Y. *et al* (2014) 'Discovery of a novel bottlenose dolphin coronavirus reveals a distinct species of marine mammal coronavirus in Gammacoronavirus.', *Journal of virology*, 88(2), pp. 1318–31.

Wu, C. H. *et al* (2009) 'Glycogen synthase kinase-3 regulates the phosphorylation of severe acute respiratory syndrome coronavirus mucleocapsid protein and viral replication', *Journal of Biological Chemistry*, 284(8), pp. 5229–5239.

Xia, S. *et al* (2014) 'Middle East respiratory syndrome coronavirus (MERS-CoV) entry inhibitors targeting spike protein', *Virus Research*, 194, pp. 200–210.

Xie, Q. *et al* (2018) 'Analysis of the genome sequence and prediction of B-cell epitopes of the envelope protein of Middle East respiratory syndrome-coronavirus', *IEEE/ACM Transactions on Computational Biology and Bioinformatics*, pp. 1344–1350.

Xu, X. *et al* (2009) 'Crystal structure of the C-terminal cytoplasmic domain of non-structural protein 4 from mouse hepatitis virus A59', *PLoS ONE*, 4(7), p. e6217.

Xu, Y., Lou, Z., *et al* (2004) 'Crystal structure of severe acute respiratory syndrome coronavirus spike protein fusion core', *Journal of Biological Chemistry*, 279(47), pp. 49414–49419.

Xu, Y., Liu, Y., *et al* (2004) 'Structural basis for coronavirus-mediated membrane

fusion: Crystal structure of mouse hepatitis virus spike protein fusion core', *Journal of Biological Chemistry*, 279(29), pp. 30514–30522.

Yamada, A. *et al* (2006) 'Spontaneous Transfer of Phospholipid-Coated Oil-in-Oil and Water-in-Oil Micro-Droplets through an Oil / Water Interface Spontaneous Transfer of Phospholipid-Coated Oil-in-Oil and Water-in-Oil Micro-Droplets through an Oil / Water Interface', *Langmuir*, 22(29), pp. 9824–9828.

Yamada, Y. and Liu, D. X. (2009) 'Proteolytic Activation of the Spike Protein at a Novel RRRR/S Motif Is Implicated in Furin-Dependent Entry, Syncytium Formation, and Infectivity of Coronavirus Infectious Bronchitis Virus in Cultured Cells', *Journal of Virology*, 83(17), pp. 8744–8758.

Yamashita, Y. *et al* (2002) 'Shape changes of giant unilamellar vesicles of phosphatidylcholine induced by a de novo designed peptide interacting with their membrane interface', *Langmuir*, 18(25), pp. 9638–9641.

Yamashita, Y., Kinoshita, K. and Yamazaki, M. (2000) 'Low concentration of DMSO stabilizes the bilayer gel phase rather than the interdigitated gel phase in dihexadecylphosphatidylcholine membrane', *Biochimica et Biophysica Acta - Biomembranes*, 1467(2), pp. 395–405.

Yang, J. *et al* (2012) 'Replication of murine coronavirus requires multiple cysteines in the endodomain of spike protein', *Virology*, 427(2), pp. 98–106.

Yang, Y. *et al* (2014) 'Receptor usage and cell entry of bat coronavirus HKU4 provide insight into bat-to-human transmission of MERS coronavirus', *Proceedings of the National Academy of Sciences*, 111(34), pp. 12516–12521.

Yang, Y. *et al* (2015) 'Two Mutations Were Critical for Bat-to-Human Transmission of

Middle East Respiratory Syndrome Coronavirus', *Journal of Virology*, 89(17), pp. 9119–9123.

Yao, Q., Masters, P. S. and Ye, R. (2013) 'Negatively charged residues in the endodomain are critical for specific assembly of spike protein into murine coronavirus', *Virology*. Elsevier, 442(1), pp. 74–81.

Yeaman, M. R. and Yount, N. Y. (2003). Mechanisms of Antimicrobial Peptide Action and Resistance. *Pharmacological reviews*. 55(1), pp. 27–55.

Ye, R., Montalto-Morrison, C. and Masters, P. S. (2004) 'Genetic analysis of determinants for spike glycoprotein assembly into murine coronavirus virions: distinct roles for charge-rich and cysteine-rich regions of the endodomain', *J Virol*, 78(18), pp. 9904–9917.

Ye, Y. and Hogue, B. G. (2007) 'Role of the Coronavirus E Viroporin Protein Transmembrane Domain in Virus Assembly', *Journal of Virology*, 81(7), pp. 3597–3607.

Yeaman, M. R. and Yount, N. Y. (2003) 'Mechanisms of Antimicrobial Peptide Action and Resistance', 55(1), pp. 27–55. doi: 10.1124/pr.55.1.2.27.

Yin, J. *et al* (2010) 'Cholesterol is important for a post-adsorption step in the entry process of transmissible gastroenteritis virus', *Antiviral Research*. Elsevier B.V., 88(3), pp. 311–316.

Ying, T. *et al* (2014) 'Exceptionally Potent Neutralization of Middle East Respiratory Syndrome Coronavirus by Human Monoclonal Antibodies', *Journal of Virology*, 88(14), pp. 7796–7805.

Yokomori, K., Stohlman, S.A, & Lai, M. . (1993) ‘The detection and characterization of multiple hemagglutinin-esterase (HE)-defective viruses in the mouse brain during subacute demyelination induced by mouse hepatitis virus’, *Virology*, 192(1), pp. 170–178.

Yu, Y., & Quinn, P. J. (1994) ‘Dimethyl sulphoxide: a review of its applications in cell biology’, *Bioscience Reports*, 14(6), pp. 259–281.

Yu, Y. *et al* (2009) ‘Vesicle budding induced by a pore-forming peptide’, *Journal of the American Chemical Society*, 132(1), pp. 195–201.

Yu, Z. and Q. P. (2004) ‘Structure of the N-terminal RNA-binding domain of the SARS CoV nucleocapsid protein’, *Bioscience Reports*, 14(6), pp. 259–281.

Yuan, Y. *et al* (2017) ‘Cryo-EM structures of MERS-CoV and SARS-CoV spike glycoproteins reveal the dynamic receptor binding domains’, *Nature Communications*. Nature Publishing Group, 8(China CDC), pp. 1–9.

Zaki, A. M. *et al* (2012) ‘Isolation of a Novel Coronavirus from a Man with Pneumonia in Saudi Arabia’, *New England Journal of Medicine*, 367(19), pp. 1814–1820.

Zaki AM1, van Boheemen S, Bestebroer TM, Osterhaus AD, F. R. (2012) ‘Isolation of a Novel Coronavirus from a Man with Pneumonia in Saudi Arabia’, *New England Journal of Medicince*, 367(19), pp. 1814–20.

Zalinger, Z. B. *et al* (2015) ‘MDA5 Is Critical to Host Defense during Infection with Murine Coronavirus’, *Journal of Virology*. Edited by S. Perlman, 89(24), pp. 12330–12340.

Zelus, B. D. *et al* (2003) ‘Conformational changes in the spike glycoprotein of murine

coronavirus are induced at 37 degrees C either by soluble murine CEACAM1 receptors or by pH 8.', *Journal of virology*, 77(2), pp. 830–40.

Zhao, G. *et al* (2006) 'M and N proteins of SARS coronavirus induce apoptosis in HPF cells', *Cell Biology and Toxicology*, 22(5), pp. 313–322.

Zhao, Y. (2003) 'Improving baculovirus recombination', *Nucleic Acids Research*, 31(2), pp. 6e – 6.

Zheng, J. *et al* (2018) 'Identification of N-linked glycosylation sites in the spike protein and their functional impact on the replication and infectivity of coronavirus infectious bronchitis virus in cell culture', *Virology*. Elsevier Inc., 513(July 2017), pp. 65–74.

Zheng, Y.-H. *et al* (2003) 'Nef increases the synthesis of and transports cholesterol to lipid rafts and HIV-1 progeny virions.', *Proceedings of the National Academy of Sciences of the United States of America*, 100(14), pp. 8460–5.

Zhou, B. *et al* (2008) 'The nucleocapsid protein of severe acute respiratory syndrome coronavirus inhibits cell cytokinesis and proliferation by interacting with translation elongation factor 1alpha.', *Journal of virology*, 82(14), pp. 6962–71.

Zhou, X. *et al* (2017) 'Ultrastructural characterization of membrane rearrangements induced by porcine epidemic diarrhea virus infection', *Viruses*, 9(9), p. 251.

Zhu, J. *et al* (2004) 'Following the rule: Formation of the 6-helix bundle of the fusion core from severe acute respiratory syndrome coronavirus spike protein and identification of potent peptide inhibitors', *Biochemical and Biophysical Research Communications*, 319(1), pp. 283–288.

Ziebuhr, J., Snijder, E. J. and Gorbalenya, A. E. (2000) 'Virus-encoded proeteinases and proteolytic processing in the Nidovirales', *Journal of General Virology*, 81(2000), pp. 853–879.

Ziebuhr, J., Thiel, V. and Gorbalenya, A. E. (2001) 'The Autocatalytic Release of a Putative RNA Virus Transcription Factor from Its Polyprotein Precursor Involves Two Paralogous Papain-like Proteases that Cleave the Same Peptide Bond', *Journal of Biological Chemistry*, 276(35), pp. 33220–33232.

Zúñiga, S. *et al* (2004) 'Sequence Motifs Involved in the Regulation of Discontinuous Coronavirus Subgenomic RNA Synthesis', *Journal of Virology*, 78(2), pp. 980–994.

Zúñiga, S. *et al* (2010) 'Coronavirus nucleocapsid protein facilitates template switching and is required for efficient transcription.', *Journal of virology*, 84(4), pp. 2169–75.